A Thesis
entitled

"INFRA-RED SENSITIVE PHOTOCATHODES FOR STREAK CAMERA APPLICATIONS"

b y

CHRISTOPHER CLEMENT PHILLIPS, B.A.

Submitted for the

Degree of Doctor of Philosophy
of the
University of London

Imperial College of Science and Technology

London, 1983

ABSTRACT

A detailed investigation has been conducted into the chemical, structural and photoemission properties of both Sl and GaAs NEA photocathodes, the two classes of photocathode material with potential for NIR streak camera use.

The photocathodes were chemically analysed using XPS, and the electron spectrometer was accurately calibrated with a specially designed electron gun, thereby permitting accurate quantitative chemical analyses of the photocathode films.

The XPS analysis of the GaAs-(Cs-O) films showed a well defined Cs_2O overlayer stoichiometry and substrate peak attenuation measurements indicated that this Cs_2O layer was $\sim$1.2 nm thick. A dipole surface layer work function lowering model is advanced to explain both these results and the XPS binding energy shifts observed in the Cs:O overlayer.

XPS analysis of a large number of Sl photocathodes showed a mean Cs:O ratio of 2:1. In spite of the cathode to cathode variation in this ratio, for each cathode it was constant during processing and independent of the XPS take-off direction. The Ols peak was split into two peaks and the higher binding energy peak was shown to be due to oxygen in contact with silver, and not oxygen in $Cs_{11}O_3$ as proposed by other workers. Measurements of the $Cs3d^{5/2}$ peak widths for both photocathode materials demonstrated the absence of band bending effects in the Sl, and this information was used to construct a revised band structure model for the cathode.

The Sl EDC's showed cathode work function values of $\sim$1.4eV after caesiation, $\sim$1.5eV after the second silver evaporation and 1.2eV finally. The EDCs from the GaAs photocathodes were found for the first time to be the "thermalised" electron distributions characteristic of true NEA surfaces.

Temporal response times of the NEA photocathodes were directly measured with a UHV-compatible streak camera and a mode-locked dye laser. The results showed response times which were dependent on the cathode film thickness, and which could be made as low as 8 psec.

TABLE OF CONTENTS

		Page Number
CHAPTER 1	INTRODUCTION	13.
CHAPTER 2	THE DESIGN AND PERFORMANCE OF THE UHV PHOTOCHRON IV STREAK TUBE	18.
2.1	Introduction	18.
2.2	Principles of operation of the streak camera	18.
2.3	Factors affecting streak camera temporal resolution	19.
2.3.1	Static Spatial Resolution	20.
2.3.2	Dynamic Spatial Resolution	23.
2.3.3	Temporal effects	24.
2.3.4	Calculating the limiting temporal resolution of a particular tube design	26.
2.4	Features of the Streak Tube design used in this study	29.
2.4.1	Electron optical design and predicted performance	29.
2.4.2	Constructional Details	33.
2.4.3	Static Resolution tests	38.
2.4.4	Dynamic Testing	39.
2.5	Conclusion	45.

Page Number

CHAPTER 3 INFRARED PHOTOCATHODE MATERIALS

3.1 Introduction 47.

3.2 III- V Semiconductor Photocathodes 48.

3.2.1 III-V Photocathode production 48.

3.2.2 III-V Photocathode photoemission mechanism 49.

3.2.3 Suitability of NEA cathodes for streak camera work 54.

3.3 The S1 Ag-O-Cs Photocathode

3.3.1 S1 Photocathode Production 57.

a) Formation of the silver base 58.
b) Oxidation of the silver base 62.
c) Second silver evaporation 63.
d) Caesiation or "activation" 63.
e) Final silver evaporation 65.

3.3.2 Basic properties of the S1 Photocathode 67.

3.3.3 Models for the structure and Photoemission mechanisms of the S1 Photocathode 68.

3.3.4 Suitability of the S1 Photocathode for streak camera work 84.

CHAPTER 4 EXPERIMENTAL TECHNIQUE AND APPARATUS

4.1 General Description of apparatus 87.

4.2 Spectral Photosensitivity Measurement 94.

4.3 Photocathode Processing

4.3.1 S1 Photocathode Processing

4.3.1a) S1 Processing Equipment 96.

4.3.1b) S1 Processing Technique 102.

a) Initial Silver Evaporation 105.
b) Oxidation 105.
c) Caesiation 105.
d) Second Silver evaporation 106.
e) Final Bake 106.

Page Number

CHAPTER 4 (continued)

4.3.2 NEA GaAs Photocathode Processing

4.3.2(a) NEA GaAs Photocathode Processing Equipment 106.

4.3.2(b) NEA GaAs Photocathode Processing Technique 109.

4.4 Recording XPS Spectra 112.

4.5 Auger Analysis of Substrates

4.5.1 Description of the Auger Process 115.

4.5.2 Recording AES Spectra 118.

4.6 Recording Photoelectron Energy Distribution Curves (EDCs) 118.

CHAPTER 5 QUANTITATIVE SURFACE ANALYSIS FROM XPS SPECTRA

5.1 Introduction 123.

5.2 Description of the Principles of X-Ray Photoelectron Spectroscopy 125.

5.3 Description of the factors affecting measured peak intensities in XPS 127.

5.3.1 Excitation of Electrons within the sample 127.

5.3.2 Transport of Electrons from the emitting atoms to the energy analyser 131.

5.3.3 Energy Analysis of the emitted electrons 135.

5.3.3a) Characteristics of the analyser: theory and direct measurement 135.

5.3.3b) Peak area Determination 146.

5.4 Routes to Quantitative Surface Analysis from XPS

5.4.1 Introduction 153.

5.4.2 Internal calibration using reference samples 154.

5.4.3 Quantification using reference data sets from other workers 157.

Page Number

CHAPTER 5 (continued)

5.4.4 Choosing the quantification procedures most applicable to the Ag-O-Cs system 162.

5.5 Conclusion. 163.

CHAPTER 6 RESULTS OF PHOTOCATHODE EXPERIMENTS

6.1 Introduction 167.

6.2 Experimental Results on GaAs Photocathodes

6.2.1 Spectral Sensitivity Measurements 169.

6.2.2 Photoelectron E.D.C.s of GaAs Photocathodes 169.

6.2.3 GaAs NEA Photocathode Temporal Response Results 173.

6.2.4 GaAs NEA Photocathode XPS Results 177.

6.3 Si Photocathode Experimental Results

6.3.1 Spectral Sensitivities of Si Photocathodes 182.

6.3.2 Si Photocathode EDCs 184.

6.3.3 Polarisation Dependence of Si Cathode Photosensitivity 195.

6.3.4 Si Photocathode XPS Results 199.

6.4 Conclusion 205.

CHAPTER 7 CONCLUSIONS DRAWN FROM EXPERIMENTAL DATA

7.1 Introduction 207.

7.2 Conclusions as to the nature of the GaAs Photocathodes produced in these experiments 207.

CHAPTER 7 (continued)

		Page Number
7.3	Conclusions as to the nature of the S1 Photocathodes produced in this study	
7.3.1	Evidence concerning the Physical structure of the S1 Photocathodes	216.
7.3.2	Evidence concerning the Electronic structure of the S1 Photocathodes produced in this study.	224.
7.3.3	Evidence concerning the photoemissive mechanism of the S1 Photocathodes produced in this study	231.
7.4	Conclusions as to the Best type of Photocathode for future use in Infra-red Ultrafast Imaging Devices	234.
APPENDIX I	Enhancement of Photoemission from Small Spheres.	238.
APPENDIX II	Calculated Cs:O XPS Ratios in the S1 Photocathode $Cs_{11}O_3$ Overlayer model.	245.
APPENDIX III	Colloidal Silver Particle Size Calculated from S1 XPS Results.	249.
REFERENCES.		253.
ACKNOWLEDGEMENTS		267.
PUBLICATION	"An Experimental and Theoretical Study of the Transmission Function of a Commercial Hemispherical Electron Energy Analyser."	269.

GLOSSARY OF ACRONYMS AND ABBRIEVIATIONS

AES	Auger Electron Spectroscopy
ATF	Analyser Transmission Function
CAE	Constant Analyser Energy
CRR	Constant Retarding Ratio
EDC	(photoelectron) Energy Distribution Curve
EESF	Experimental Elemental Sensitivity Factor
FWHM	Full Width Half Maximum
HBE	Higher Binding Energy
HT	High Tension
IETU	Intrinsic Emission Time Uncertainty
IMFP	Inelastic Mean Free Path
LBE	Lower Binding Energy
MTF	Modulation Transfer Function
NEA	Negative Electron Affinity
NIR	Near Infra-Red
OMA	Optical Multichannel Analyser
QCO	Quartz Crystal Oscillator
RF	Radio Frequency
SPC	Subshell Photoionisation Cross-section
SPW	Surface Plasmon Wave
TMTF	Temporal Modulation Transfer Function
UHV	Ultra High Vacuum
UPS	Ultraviolet-Photoelectron Spectroscopy
USAF	United States Air Force
UV	Ultra Violet
XPS	X-Ray Photoelectron Spectroscopy

CHAPTER 1

INTRODUCTION

Image tube devices are the only devices known today capable of recording linear temporal intensity measurements of events on a sub-picosecond time scale. Although the ∿0.8psec (Sibbett et al., 1983) temporal resolution of the fastest streak tubes available has been eclipsed by the temporal resolutions of second order auto-correlation methods such as two-photon fluorescence and second harmonic generation, the non-linear nature of these latter techniques limits their applicability to experiments in which comparitively high light intensities are available and in which a measurement of the shape of the optical pulse under investigation is subordinate to a measure of its width.

For experiments in which only low light levels are available for investigation, and where the details of the temporal intensity profile of the optical event are of interest (e.g. transient fluorescene spectroscopy, plasma diagnostics in laser fusion experiments, semi-conductor fluorescence experiments etc.) the streak camera remains a research tool without peer.

The spectral range in which a streak camera can be used is determined entirely by the properties of the photocathode with which it is fitted. In particular the spectral sensitivity, intrinsic emission time uncertainty and the photoelectron energy distribution emitted by a particular cathode serve to limit the spectral range over which a specified time resolution can be achieved in practice. At present these factors place a wavelength limit of ∿ 1μm on the useful spectral range of streak camera operation.

With the current interest in optical fibre telecommunications

technology however, with its emphasis on the development of infra-red LEDs, lasers and detectors working at wavelengths close to the 1.4 μm absorption minimum (Midwinter, 1979) and the 1.3 μm material dispersion minimum (Payne and Gambling, 1975) in optical fibres, a streak camera with an extended infra-red operational range would find numerous applications in the temporal diagnostics of high speed optical components and transmission systems.

With this fact in mind the present study was initiated to evaluate the potential for streak camera use of the two types of photocathode material currently available with usable photoresponse in this spectral region, the S1 (Ag-O-Cs) photocathode, and the newer 3-5 compound family of "negative electron affinity" (NEA) photocathodes.

The following chapter describes the design, construction and testing of the UHV-compatible streak tube which was specially fabricated to compare the temporal performance of both types of photocathodes inside the UHV equipment in which they were processed. The details of the streak tube design used in this study are preceded by a brief description of the general principles of operation of streak camera systems, and a discussion of the effects of various photocathode characteristics on streak camera performance.

Chapter 3 is an overview of the existing knowledge concerning the properties, structures and photoemission mechanisms of the two types of photocathode material. In it the models and methods of previous workers are reviewed and the potential suitability of both types of photocathode material for streak camera applications is assessed in view of this work. The fourth chapter describes in detail the equipment and experimental techniques which were developed in the course of this project, resulting in the successful processing, photo-emissive characterisation, chemical analysis and temporal testing of both types of photocathodes within a large volume all-metal UHV apparatus.

The surface sensitive techniques of X-ray photoelectron spectroscopy (XPS), although established as a powerful research tool capable of yielding a variety of qualitative information on the surface composition of a solid in UHV, has only comparitively recently been refined to the stage where quantitative analysis of a surface of unknown structure can be attempted with a degree of confidence in the results. Chapter 5 consists of a brief description of the various factors which combine to complicate the task of extracting surface composition data from measured XPS spectra, together with an account of the experiments performed with the UHV apparatus as part of the quantification framework.

These experiments consisted of a direct measurement of the transmission of the electron energy analyser as a function of electron energy, and trials using a range of stoichiometric compounds in an attempt to measure experimental subshell photoionisation cross-sections for the Ag-O-Cs system in the S1 photocathodes under study. The chapter concludes with a description of the quantification scheme adopted (in the light of the results of these experiments) for application to the experimental XPS spectra obtained from the photocathodes at various stages in their processing schedules.

Chapter 6 contains the body of the experimental results obtained from the photocathode experiments. These results include details of the XPS studies of a large number of S1 photocathodes, the measurements for the first time of "thermalised" photo electron energy distribution curves (EDCs) from the NEA photocathodes, and new direct measurements of the response times of various GaAs NEA photocathodes measured with the UHV compatible streak camera. Chapter 7, the final chapter, contains a discussion of the significance of the experimental data, and in it conclusions are drawn concerning the modes of operation of both types of infra-red sensitive photocathode.

It concludes with a reassessment of the potential spheres of application of either type of photocathode material in the light of the discoveries made in this project.

CHAPTER 2

THE DESIGN AND PERFORMANCE OF THE UHV PHOTOCHRON IV STREAK TUBE

2.1 Introduction

This chapter describes the construction and design of a uniquely flexible UHV-compatible version of the Photochron IV-M sub-picosecond streak tube which was especially built for this infra-red photocathode study.

The design details of the streak tube are introduced with a brief resumé of the principles of operation of general streak camera systems and an outline of the various factors affecting the ultimate temporal resolution of such systems.

2.2 Principles of operation of the streak camera

In a typical electron-optical chronoscopy experiment, light from some luminous event is imaged onto the photocathode of a streak tube with an optical transfer lens. Assuming that the cathode is sufficiently sensitive at the wavelength of interest and that no saturation effects are occurring, the photoelectrons emitted from the cathode will faithfully reproduce the characteristics of the light image both spatially and temporally. These photoelectrons are then accelerated quickly to a high velocity by means of a high extraction field and pass through an electron-optical lens system which focusses the image onto a high resolution phosphor screen. The incorporation of an electrostatic deflection system into the tube enables this image to be streaked across the phosphor screen at high speed (of the order of 3×10^8 m sec^{-1}) so that temporal variations in the

light input intensity are translated into spatial intensity variations on the phosphor. The phosphor image can then be either photographed and microdensitometered or measured directly with an optical multichannel analyser (OMA) to yield a truly linear (in contrast to the other correlation-based methods of ultra short pulse measurement) record of the temporal variation of the intensity of the light striking the photocathode.

Tube designs on which the cathode image is scanned in a circle (Butslov et al., 1972) can record only temporal information about the light input, whereas designs which scan a thin slit in a straight line across the screen (Bradley and Sibbett, 1975) can also record spatial information in one dimension, and can for example be used in conjunction with spectrometers to record spectral information of transient optical events. A further refinement of the same principle is the framing tube (Sibbett, Baggs and Niu, 1982) which produces a series of two dimensional 100 ps "snapshots" of the cathode image by sweeping the electron image across an aperture plate.

In such streak camera systems optical gain is normally present by virtue of the high accelerating potential between the cathode and the screen, but for some applications it is advantageous to build extra image intensification into the system. This can be achieved either with a standard image intensifier optically coupled to the phosphor screen (e.g. Bradley et al., 1978) or with a microchannel plate built into the streak camera body (Sibbettet al., 1982). The resulting intensified system is frequently capable of single photoelectron detection.

2.3 Factors Affecting Streak Camera Temporal Resolution

The limiting temporal resolution is clearly dependent on the static image spatial resolution, accuracy of synchronism of the electrical deflection signal with the optical event and on any temporal effects which may occur to introduce differences in the times of arrival at the deflectors of electrons which originated at the same time and place in

the photocathode. The complex manner in which these effects combine to produce a limit to the temporal resolution attainable can only be calculated accurately using numerical computer ray-tracing methods, and consequently the following description is largely qualitative in character.

2.3.1 Static Spatial Resolution

The static resolution of a streak tube is generally empirically defined as the maximum number of line pairs per millimetre in a resolution test pattern at the cathode which result in a similar pattern, distinguishable by eye, at the screen. Limits to the static resolution lie principally in the aberration characteristics of the lensing system. Spherical aberration in the electon lens will result in electrons leaving a point on the photocathode at different emission angles being focussed to different parts of the screen, and chromatic aberration will produce blurring of the image as a result of the finite velocity spread of the photoelectrons as they are emitted.

Although it is possible for the screen phosphor grain size (Piedmont and Pollehn, 1976), inaccuracies in the positions and potentials of the streak tube electrodes, the extraction mesh pitch and light scattering in the photocathode all to reduce the static spatial resolution, the effects of these factors are difficult to predict quantitatively and are experimentally not found to be important for designs with static resolutions worse than $\sim$ 60 lpmm^{-1} at the photocathode.

As the cathode illumination level is increased from a low value there are a number of effects which can combine to reduce the spatial resolution, and thereby reduce the useful dynamic range of the tube. Mutual repulsion within the bunch of electrons travelling the length of the tube body will defocus the beam if the transit down the tube includes relatively long stretches of travelling through low potential regions (Niu and Sibbett, 1981). Moreover if the photocathode film has a particularly high resistance, the ohmic voltage drop across its surface as the photocurrent

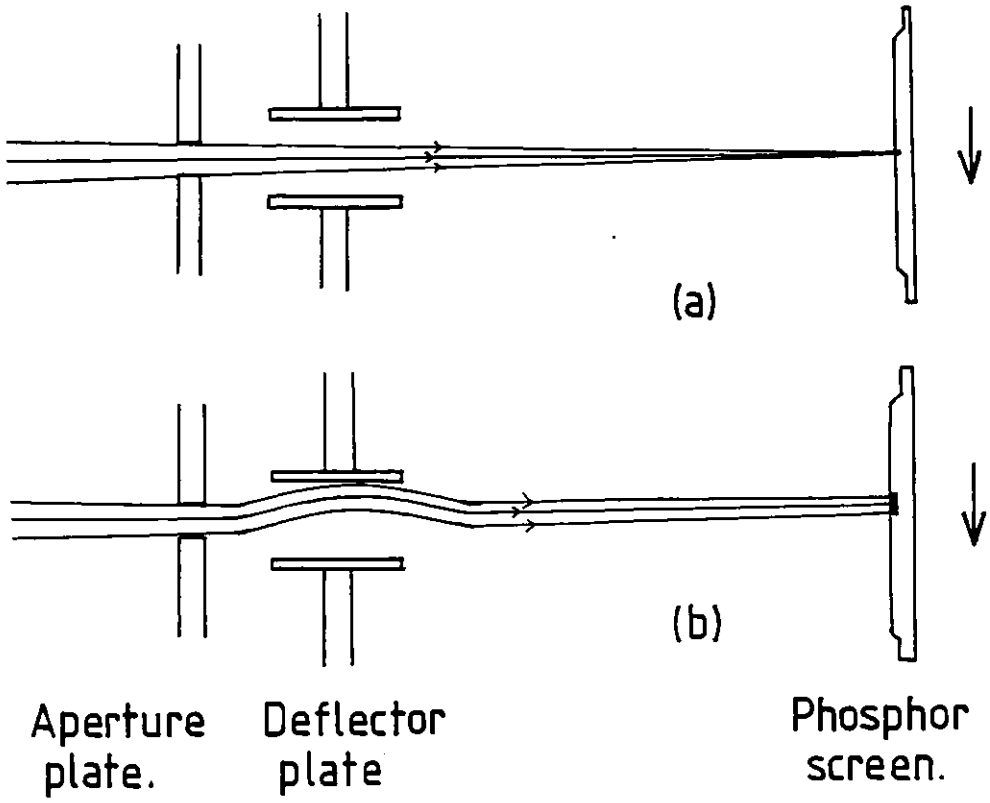


Fig 2·1

Trajectories of Photoelectrons Emitted from a Single point on the Photocathode at such a Time as to arrive at the Phosphor at a Point on the Tube Axis. At low Streak Speeds (a) the Electrons Come to a Sharp Focus at the Screen, but at High Streak Speeds the Image is Defocussed by the Aberrating Fields in the Deflector Region (b).

is drawn from its centre can give rise to an electrostatic lens in the cathode-mesh region which will defocus the image of the phosphor screen (Kalibjian, 1975). In the case of negative electron affinity cathodes it is also possible that the surface photovoltaic effect will tend to straighten the (bent) electron bands at the surface of brightly illuminated cathodes, resulting in changes in sensitivity and a surface potential shift of up to 0.6 eV, which again may produce a "microlensing" effect between the photocathode and the mesh (Kalibjian, 1975) resulting in intensity dependent image defocussing and a reduceddynamic range.

2.3.2 Dynamic Spatial Resolution

When the image is streaked across the screen its spatial resolution, ignoring other temporal effects, tends to be degraded by the aberrating fields which are present in and around the deflection system. Because practical deflecting plates have to have a finite length the photoelectrons are subjected to a temporally varying field as they traverse the deflection region. This field will defocus the streaked image even if the phase of the deflection voltage is arranged so that the image still strikes the screen in the position corresponding to zero deflection, as shown in Figure 2.1 (normally only the central linear portion of the deflection voltage ramp is used in streak camera systems to ensure temporal linearity on the screen and to optimise the temporal resolution of the system). This dynamic defocussing effect is thus dependent on the ratio of the rate of change of the deflecting field to the amount of time spent by the photoelectrons in the deflecting region, and will result in decreasing spatial resolution as the streak speed is increased.

The limits to camera temporal resolution arising from this effect are normally somewhat crudely calculated by estimating a "dynamic spatial resolution", R lpmm^{-1}, and calculating the streak tube "technical time resolution", $\Delta\tau_T$, from the formula

$$\Delta\tau_T = \frac{1}{vR} \qquad (2.1)$$

where v is the streak speed.

2.3.3 Temporal effects

The above analysis of streak camera temporal resolution has thus far tacitly assumed that the photoelectrons leave the photocathode-vacuum surface at the same instant that the incident photon is absorbed, and that all photoelectrons are emitted with identical kinetic energies. In reality photons absorbed simultaneously throughout the thickness of the photocathode will give rise to a pulse of photoelectrons with a finite spread of emission energies (typically $\sim$ 0.5eV for visible light), and moreover differences in transit times of the photoelctrons from their points of excitation to the cathode-vacuum interface introduce a further "intrinsic emission time uncertainty" when photoelectrons excited throughout the cathode thickness are considered. This latter quantity is not known with certainty , but is regarded as being an insignificant $\sim 10^{-14}$s (Bulgyin et al., 1976) for an Sl photocathode, as compared with up to 10^{-9} sec (but see Chapter 6), for some of the III-V NEA photocathode materials (Bell, 1973).

The fact that photoelectrons are emitted with a range of velocities also means that they will take a range of times to travel between the cathode and the deflectors, and thereby degrade the streak camera temporal resolution further. This "transit time spread" can be minimised by designing the streak tube so as to minimise the transit time itself, i.e. maintaining the photoelectron kinetic energy

as high as possible over as much as possible of the tube axis. This consideration is particularly important in the cathode-mesh region where the photoelectrons start with very low energies, and large transit time speads, as given by the following formula, can arise if insufficiently high extraction fields are used (Csorba, 1971).

$$\Delta\tau = \sqrt{\frac{2m}{e}}\ \frac{\sqrt{\Delta\varepsilon}}{E} \qquad (2.2)$$

where m = rest mass of the electron

e = electronic charge

$\Delta\varepsilon$ = emission energy spread of photoelectrons in eV

E = cathode-mesh extraction field in V m^{-1}

With the extraction fields of $\sim$ 50 KV cm^{-1} typically achieved in practical devices, and an initial energy spread of 0.2 eV for an S20 cathode near photoelectric threshold, this transit time spread can be reduced to values of $\sim$ 0.2 ps (Sibbett, Niu and Baggs, 1982). This transit time spread can of course be much larger for streak tubes used in spectral regions where a much larger initial energy spread results e.g. the 5eV photoelectron energy distribution observed with 1 kV X-rays (Attwood and Coleman, 1976), and is frequently the factor which limits the final temporal resolution attainable with a particular tube design.

A further difficulty arises when the effect of a finite slit height is taken into account. Photoelectrons emanating from extremes of the slit length will travel in a longer trajectory before striking the phosphor, and will consequently arrive slightly later. The result is that at high streak speeds the streak image becomes curved and, since the image analysing techniques employed are generally only capable of integrating over a straight strip of the phosphor

this "dynamic streak curvature" (or "temporal distortion") will serve to reduce the effective camera temporal resolution.

The streak tube can be used in the synchroscan mode (as opposed to the single-shot mode), where the optical event under investigation is being repeated and the results integrated at a typical rate of tens or hundreds of megahertz (e.g. experiments in which the optical event is being excited by pulses from a repetitive source such as a c.w. mode-locked laser). In this case the deflection signal is a sinusoidal RF voltage, and clearly inaccuracies in the synchronisation between the deflection signal and the optical pulses will result in degradation of the temporal resolution. Such phase jitter problems are particularly encountered in synchronously pumped mode-locked dye laser systems (e.g. see 2.4.3).

2.3.4 Calculating the limiting temporal resolution of a particular tube design

The simplest method for calculating the tube temporal resolution is to consider each of the resolution degrading effects in turn, and calculate the amount, $\Delta\tau_i$, by which each would broaden the record of an infinitely short light pulse in the absence of all the other temporal resolution degrading effects. Assuming an independent gaussian broadening effect, the total camera temporal resolution ΔT can be calculated from the $\Delta\tau_i$ arising from all the resolution degrading effects mentioned previously by the formula ...

$$(\Delta T)^2 = \sum_i (\Delta\tau_i)^2 \qquad (2.3)$$

A more sophisticated approach to the problem, however, takes into account the fact that many of these resolution degrading effects are interdependent (e.g. increasing streak speed will

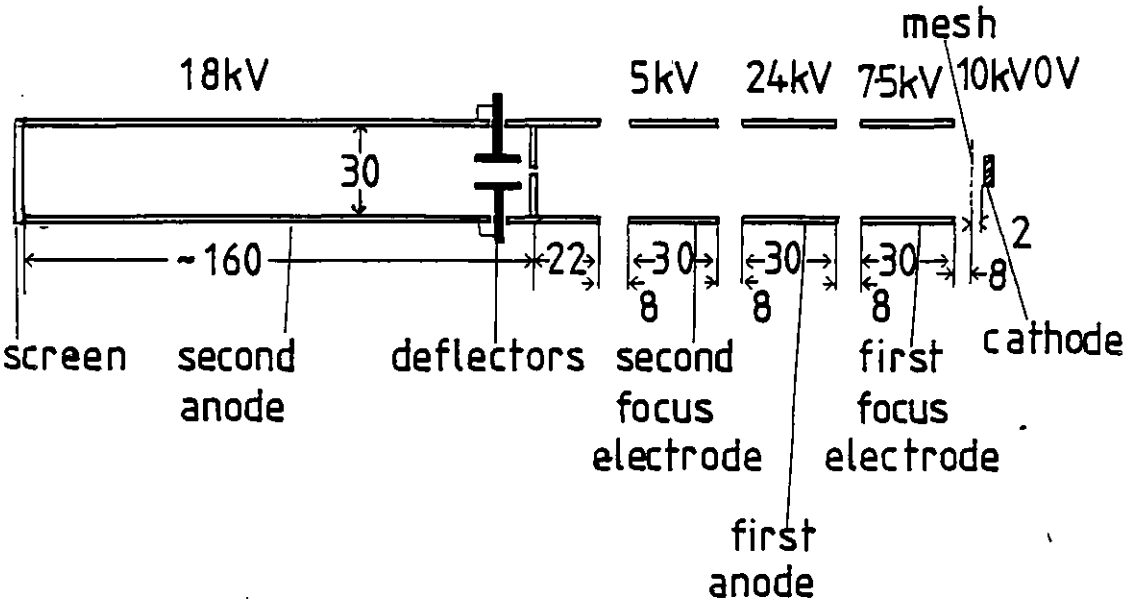


Fig. 2·2

PHOTOCHRON IV-M

Photochron IV-M Schematic.Dimensions in millimetres.

inevitably degrade spatial resolution), and that the actual temporal resolution can only be calculated numerically with a complex computer program to calculate a "temporal modulation transfer function" (TMTF) for the tube design (Niu, Sibbett and Baggs, 1982).

2.4 Features of the Streak Tube Design used in this study

2.4.1 Electron-optical design and predicted performance

The electron optical design used in this study is the Photochron IV-M, as developed by Sibbett et al. (1982), Figure 2.2, and is basically a scaled-down version of the Photochron IV, to fit in the restricted space available in the UHV analysis chamber. The tube features an electrostatic focussing system cosnsisting of four co-axial cylindrical electrodes of equal diameters, and therefore lent itself to cheap and accurate fabrication. The four electrodes constituted two interacting electrostatic lenses, allowing optimisation of both static and dynamic tube resolution, and the electrode potentials chosen resulted in a high electrostatic potential down the entire tube axis (Sibbett et al., 1982), which in turn resulted in a minimised transit time spread and a large dynamic range.

The performance characteristics of the Photochron IV tube design, in particular its "temporal modulation transfer function" and its static spatial resolution have been evaluated numerically by Niu et al. (1982), using a suite of computer ray tracing programmes which avoid the simplifications of the Gaussian approximation method (described in 2.3.4) which is more commonly used to tackle this problem. The results of their calculations are reproduced in Figures 2.3 - 2.5.

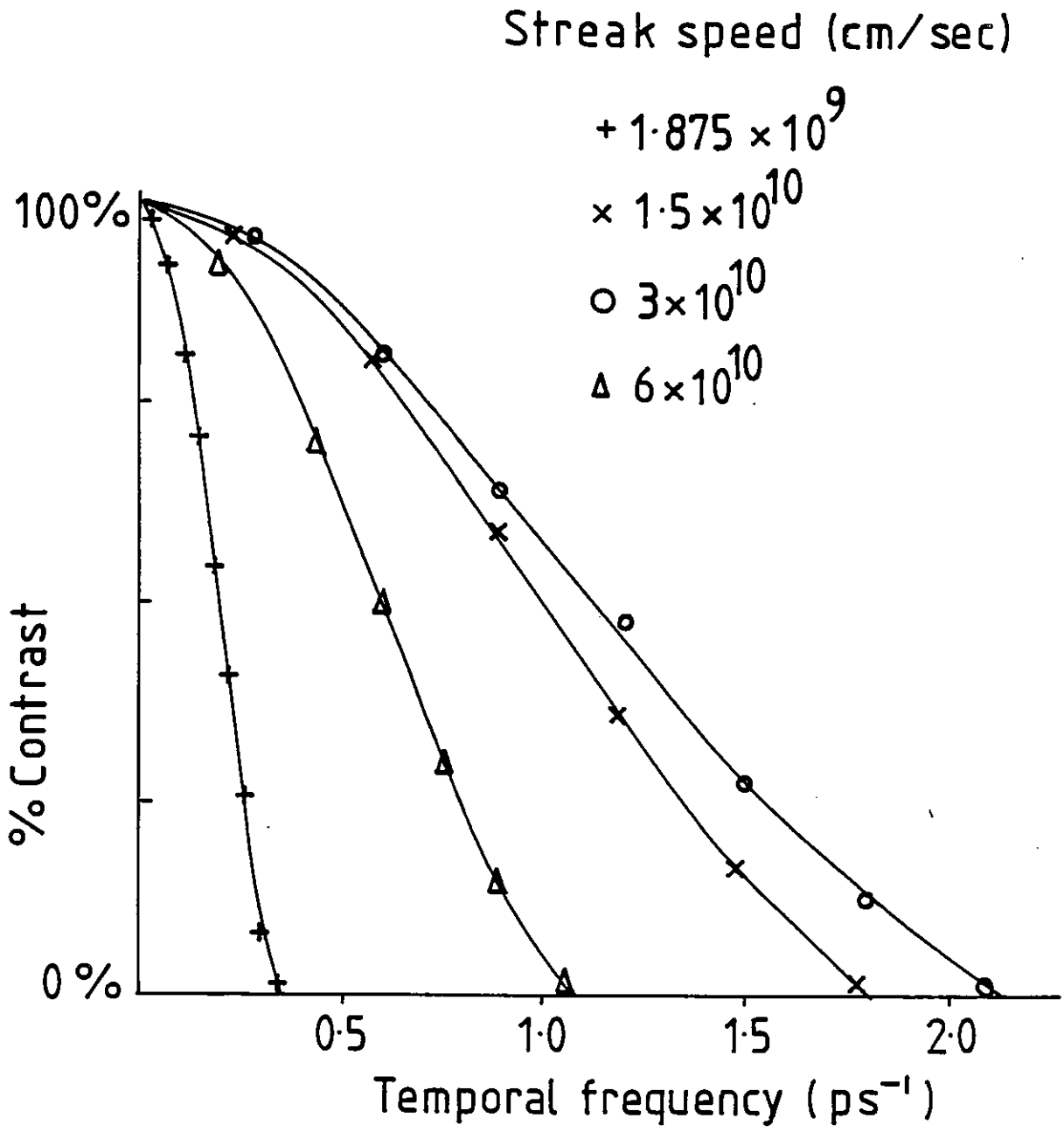


Fig.2·3.
Temporal Modulation Transfer Function (TMTF) of the Photochron IV after Niu et al.,1982.

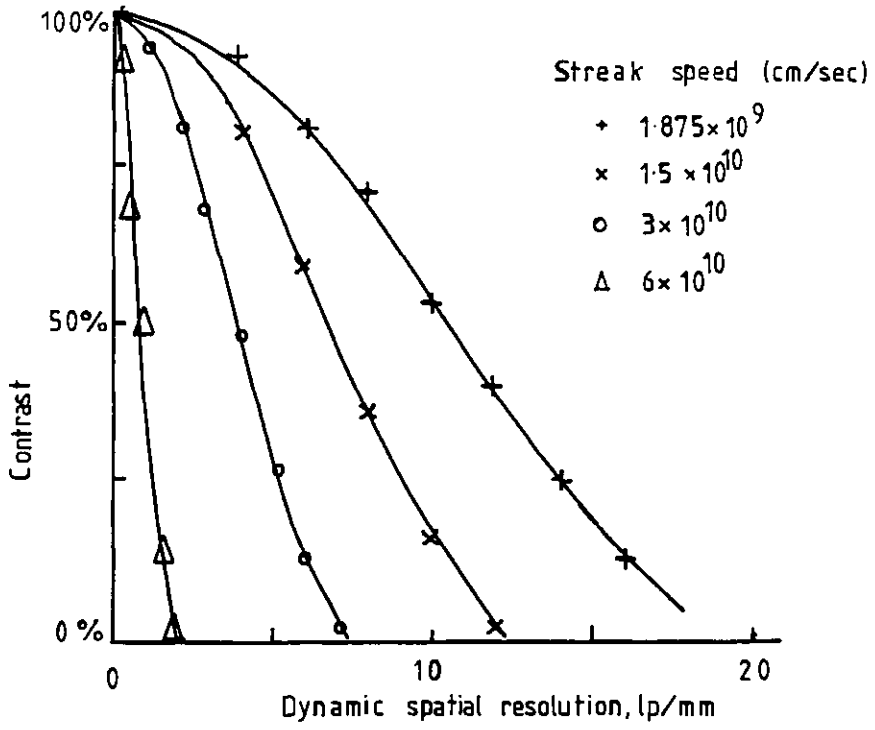


Fig. 2·4

Dynamic Spatial Resolution of the Photochron IV after Niu et al.,(1982)

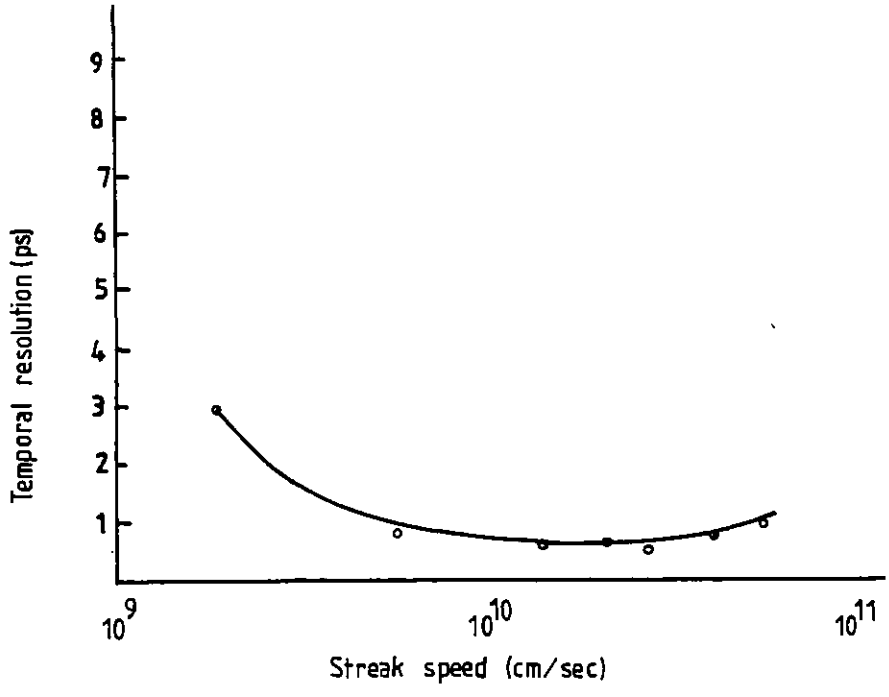


Fig. 2·5.

Optimum Streak Speed of the Photochron IV after Niu et al.,(1982)

For this tube design the static spatial resolution would seem in principle to be limited not by the electron optics of the lensing system, but by factors such as the phosphor resolution, mesh cell size etc. (Sibbett et al., SPIE Conf. Proc., 1982), to a value of $\sim$ 60 lpmm at the photocathode. When the image is streaked however, the effects of electron optical aberrations serve to limit the dynamic spatial resolution and the effects of finite phosphor resolution etc. become less important.

One of the most interesting aspects of these calculations is shown in Figure 2.5 where the effects of increasing aberrations in the tube deflection region as the streaking speed is increased result in the existence of an optimum streak speed, above which the tube temporal resolution begins to degrade.

Sibbett et al. also calculated the changes in tube characteristics which resulted from the scaling down and slight geometrical differences between the Photochron IV and IV-M (SPIE Conference Proceedings, 1982). The results, summarised in the tables below, indicate that although the miniaturised version is, in theory at least, capable of slightly superior temporal resolution, if suffers more markedly from the effects of temporal distortion (dynamic slit curvature), which would mean that in practice the optimum resolution could only be achieved with very small slit heights.

		Photochron IV	Photochron IV-M
Overall length		395 mm	274 mm
Image Magnification		- 2	-2.2
Deflection sensitivity		3cmKV^{-1}	2.5cmKV^{-1}
Static Spatial Resolution		>60 lpmm^{-1}	>60 lpmm^{-1}
Dynamic Spatial Resolution (optimum)		>50 lpmm^{-1}	>50 lpmm^{-1}
Dynamic Range		911	1700
Temporal distortion at various			
slit heights	h = 1 mm	0.2psec.	0.28psec.
	2 mm	0.77psec.	1.1psec.
	3 mm	1.72psec.	2.4psec.
	4 mm	3.08psec.	4.3psec.
	5 mm	4.76psec.	6.8psec.

2.4.2 Constructional Details

The cylindrical electrodes were turned from a single piece of stainless steel tubing and, after careful jigging, they were spot welded to the tungsten pins in the glass support rods (Figure 2.6). An adjustable section was built into the drift space region of the tube body to enable final fine adjustments to the tube body length to be made thereby ensuring that correct photocathode alignment inside the UHV system was possible.

The end of the drift space electrode was threaded and screwed into a custom "Kovar" flange which itself was glass/metal sealed to an FC 200 UHV conflat flange. Electrical feed throughs to carry the various electrode voltages and deflection signals were sealed into the glass wall. A P11 phosphor-coated glass disc (with a segment removed to allow pumping of the screen-window volume) was spot-welded onto the end of the drift space electrode with nickel wire clips. Connections between the Kovar pin electrical

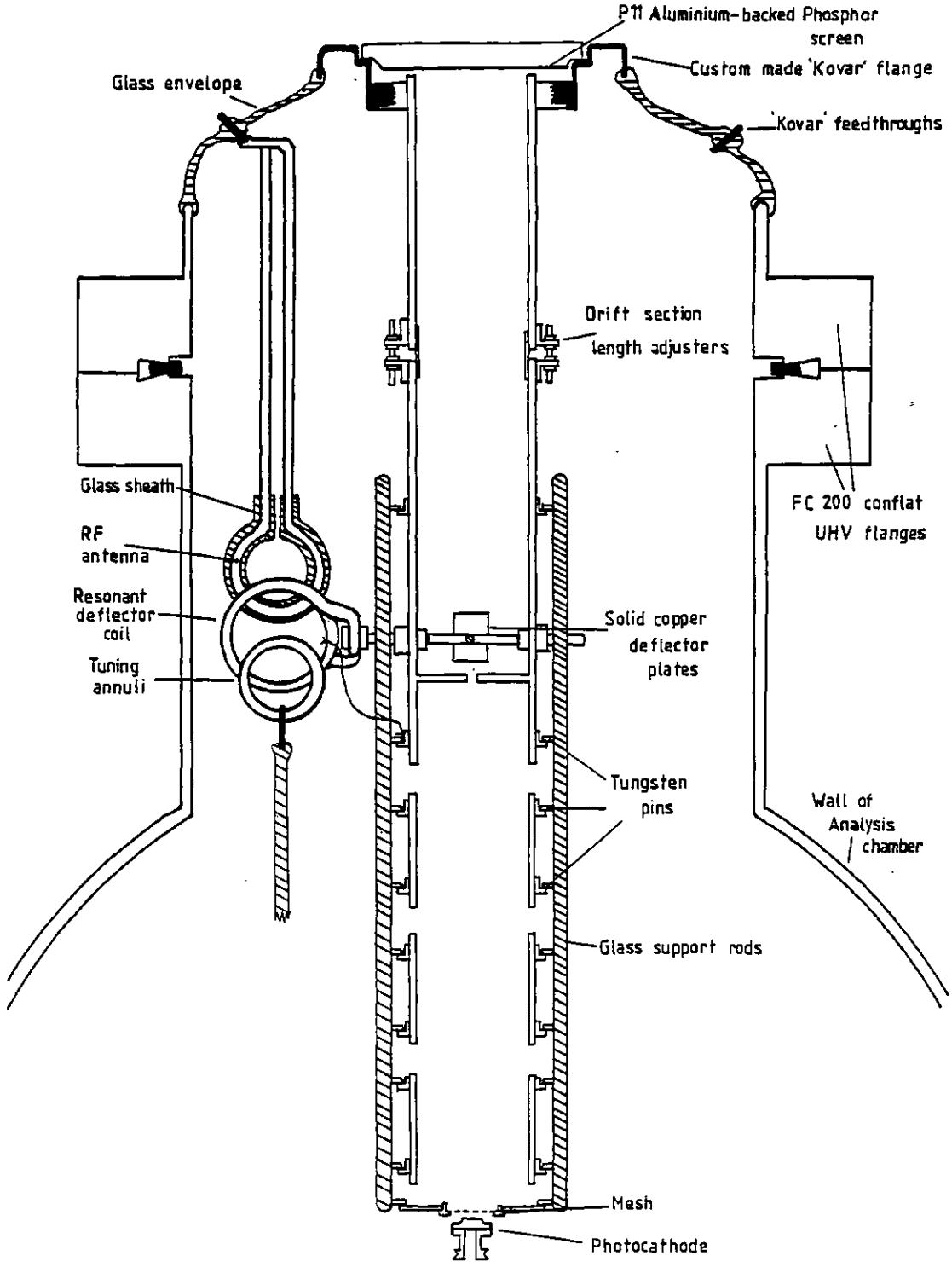


Fig. 26.

Constructional Details of UHV Streak Tube.



Photograph of the UHV Streak Camera.

feedthroughs and the various lens electrodes were made with nickel wire insulated with glass tubing.

The deflection plates used were all copper and measured 10mmx7mm, with a 3mm separation. They were mounted in a "straight through" configuration (Figure 2.7), which allowed for the easy incorporation of the rest of the deflection circuitry with the minimum of stray inductance. The streak tube was to be tested in the synchroscan mode at 138.3 MHz, accordingly an inductor, fashioned from four turns of 15 s.w.g. (1.8 mm dia.) polished copper wire wrapped around a 25mm diameter cylindrical former, was bolted onto the deflector plate support rods. The electrical centre of this inductor was connected to the anode electrode to ensure that a symmetrical deflection voltage appeared on the plates, and that they did not charge up during static resolution testing.

The deflection circuit was thus entirely formed from high conductivity polished copper and as such showed a very high quality factor at resonance, and very little of the phase drift problems encountered in the sealed-off streak tube deflection circuits, where a Kovar section is used to go through the glass envelope introducing large losses at the RF frequencies used.

The RF signal was inductively coupled into the deflection circuit using a 25 mm diameter single loop antenna which had been insulated with bent glass tubing so that it was capable of isolating the RF amplification electronics from the -18KV d.c. level of the deflection circuit.

The deflection circuit resonant frequency was coarsely tuned to the synchroscan frequency by deforming the deflector coil before the tube was bolted on to the UHV system. Once on the UHV system the deflector coil was straddled by two copper annuli (19 mm UHV copper gaskets) mounted on glass insulating mounts on a UHV "wobble stick". By moving the wobble stick around and thereby changing the

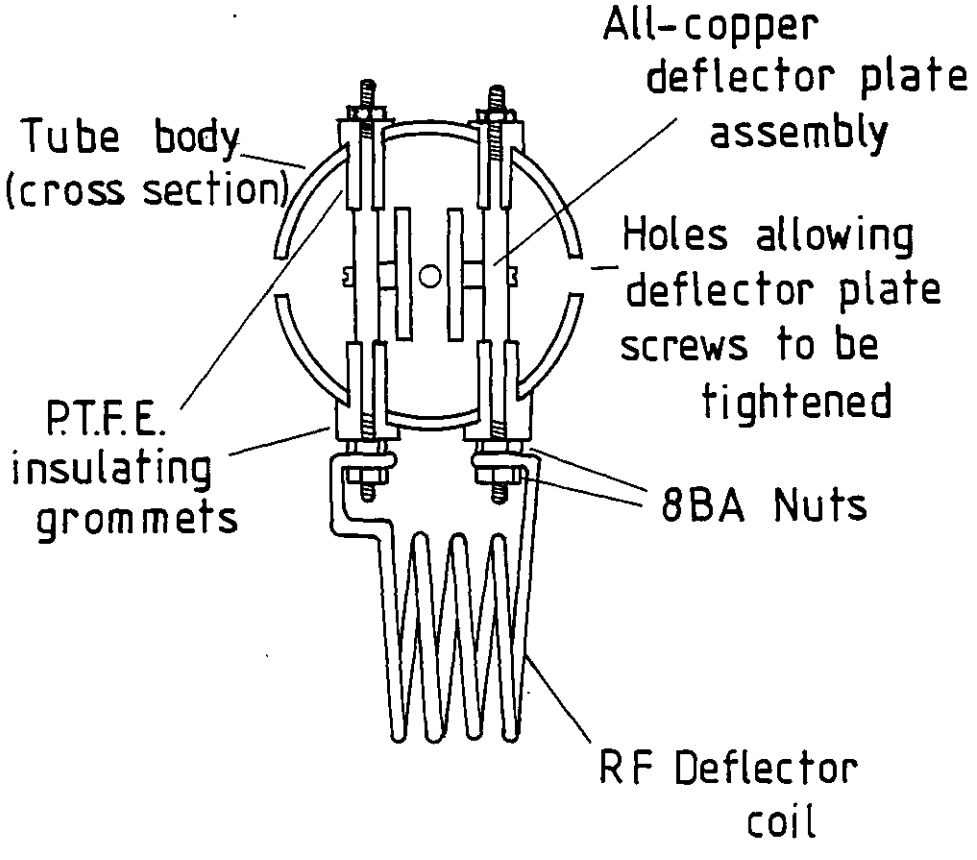


Fig. 2·7.

Constructional Details of the High-Q Resonant Deflector Circuit.

effective inductance of the deflector coil/annuli combination, the deflection circuit could be fine tuned over ∿ 5 MHz, and be made to resonate at the correct synchroscan frequency.

The 60 meshes per mm copper mesh (E.M.I. Electron Tubes Limited) was held into the mesh holder with three stainless steel clips, and was easily replacable if damaged. Once processed and tested, photocathodes were mounted onto the high precision spectrometer manipulator where they could be aligned at the correct distance from, and parallel to the mesh, and be illuminated through a UHV window on the opposite side of the spherical analysis chamber.

The entire streak camera structure therefore, was UHV compatible, usable with a variety of photocathode materials, easily demountable for modification, and bakeable to well in excess of the 200C normally used for equipment bakeouts.

2.4.3 Static Resolution Tests

In order to experimentally test the static resolution of the assembled streak tube an S1 photocathode (fabricated as described in 4.3.1) was mounted on to the spectrometer manipulator and checked for parallelism with the mesh by observing the beam of a He-Ne laser reflected off its back-surface.

A 1951 USAF resolution chart was illuminated with a white lamp and imaged onto the photocathode with a 135 mm f/3.5 NIKKOR-Q SLR camera lens. The various d.c. focus electrode potentials were derived from a variable high voltage resistive potential divider network to minimise the effects on observed resolution of ripple present on the E.H.T. power supply output. The streak tube was biassed with the cathode at earth potential and the screen at + 18KV, in order to minimise the stray electrostatic fields which would otherwise be present in the photocathode region due to the proximity of other items of UHV equipment at earth potential.

After optimisation of the electrode potentials the limiting static resolution was judged by eye, and the magnification of the resolution chart imaging optics was calculated by using the same lens resolution chart assembly to project an image onto a diffusing screen and measuring its dimensions.

Under these conditions it was possible to resolve all the elements on the USAF resolution chart, corresponding to an experimentally determined minimum static resolution of 51 $lpmm^{-1}$ at the photocathode. This figure compares well with the thoretically determined 60 $lpmm^{-1}$ (Sibbett, Niu and Baggs, 1982) and was quite adequate for the experiments planned in this study. A more accurate static resolution measurement (with the considerable experimental difficulties which would arise from the fact that the closest distance of approach to the photocathode from outside the UHV system was $\sim$ 30 cm) was therefore deemed unnecessary.

2.4.4 Dynamic Testing

For dynamic testing of the streak tube, picosecond pulses from a mode-locked dye laser were used as a test source. The photocathode used was the same S1 which had been used to test the static resolution, and all the d.c. electrode potentials were left at the same values as for the static test.

The USAF resolution chart was replaced with a 5μm wide slit which had been produced photolithographically in an evaporated aluminium film. The static slit image on the phosphor screen was focussed with unity magnification onto the target of a Princeton Applied Research model 1205H optical multichannel analyser (OMA), using a 135 mm f/5.6 Rodenstock enlarger lens. Under these conditions the static image of the slit was illuminating 6 channels of the OMA at FWHM, corresponding to a phosphor image 140μm wide.

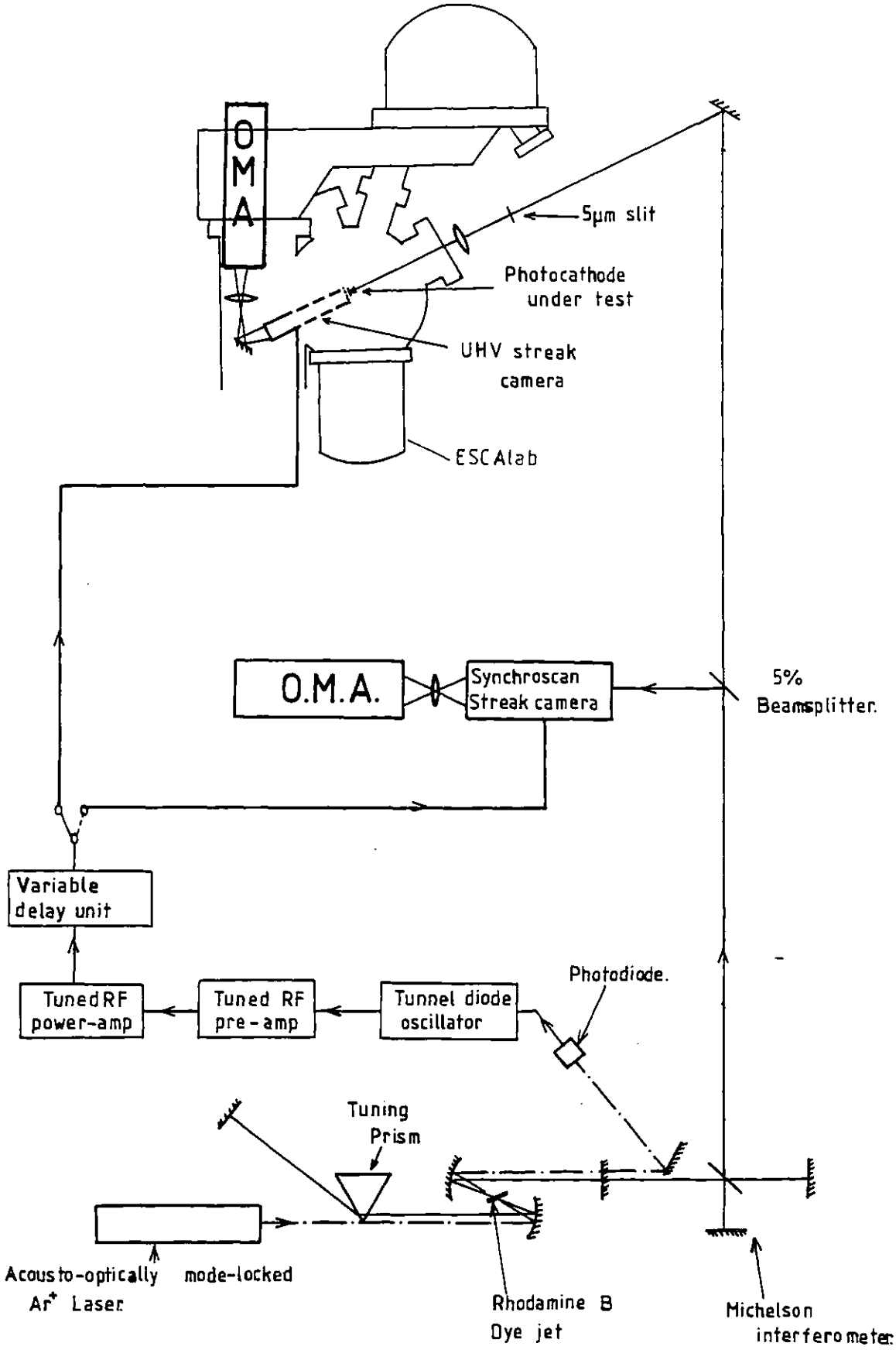


Fig. 2·8.

Schematic Diagram of the Mode-Locked Dye Laser used to Test the Streak Camera.

The laser used as a test source was an astigmatically-compensated folded cavity dye laser, working at $\sim$ 630 nm using Rhodamine B dye. The dye laser was synchronously pumped with $\sim$ 70 psec pulses at an average power of $\sim$ 400 mW from an acousto-optically mode-locked Spectra Physics model 164 Ar ion laser. The laser system used (Figure 2.8) and its principal characteristics are described in greater detail by May et al. (1982).

The 138.8 MHz RF deflection signal is derived from the mode locked pulse train output of the laser using a photodiode/tunnel-diode oscillator circuit (Willson, 1982). The $\sim$ 5 mW output from the tunnel diode oscillator was amplified up to $\sim$ 5 W through a tuned RF pre-amplifier and poweramplifier combination before being applied to the loop antenna on the streak tube.

Pulses from the laser were passed through a Michelson interferometer arrangement which split each dye laser pulse into two equal intensity pulses separated by a calibrated delay of 100 ps. The amplitude and phase of the RF deflection signal was adjusted to bring the images of the pulses to the centre of the phosphor screen, and to ensure that the separation of the pulses was adequate to be measured with the OMA, this resulted in a streak speed of $\sim 1.8 \times 10^7$ m s^{-1} being used.

Figure 2.9 is a typical OMA trace produced under these experimental conditions. The FWHM pulse widths of $\sim$ 18 psec obtained this way were the same as obtained simultaneously on a separate streak camera system with a sealed off streak tube, even although this second streak camera system had already been demonstrated to have temporal resolution of $\sim$ 1 ps with a passively mode-locked ring dye laser system (Willson et al., 1982). Previous experience had shown that whereas the synch-pumped dye laser typically generated pulses of $\sim$ 1 ps FWHM as measured by second harmonic generation (SHG) autocorrelation techniques (May et al., 1982), the smallest streak width ever recorded



Fig. 2·9

Photograph of a Typical Display on the Optical Multichannel Analyser.

with a synchroscan streak camera on the system was 7 psec FWHM.

It seems therefore that the figure of 18 psec obtained was principally due to jitter between the times of arrival at the streak camera of the mode-locked pulses and the phase of the RF deflection signal, and represented only an upper limit to the temporal resolution of the streak camera on the UHV system. Such jitter problems are a common feature of synchronously mode-locked laser systems which rely on saturation of the modulated gain in the dye laser cavity as the main pulse compression mechanism (May et al., 1982). Pulse to pulse variation in the Ar^+ ion pumping pulses means that the dye laser pulse tends to shift to a phase position either slightly earlier (for a relatively intense Ar^+ pump pulse) or slightly later (for a relatively weaker Ar^+ pump pulse) than the mean phase position (Figure 2.10). Moreover the pulse to pulse amplitude variation of the dye laser pulses will also increase due to this effect and the triggering point on the tunnel diode oscillator will therefore also suffer from a pulse to pulse phase variation. In recording a trace on the OMA this jitter in the streak image is integrated over at least $\sim 10^5$ pulses and results in a broadened streak image.

Of the $\sim$ 17 ps jitter observed in these experiments therefore $\sim$ 7 ps can be attributed to jitter in the dye laser pulse train and the remainder due to the jitter in the RF electronics. Attempts to improve on these jitter figures and achieve the previously attained 7 ps optimum synchroscan pulse width with this system were thwarted by the relatively low output powers available from the ageing plasma tube in the Ar^+ ion laser at the time of these experiments, which meant that the dye laser was operating closer to threshold than usual.

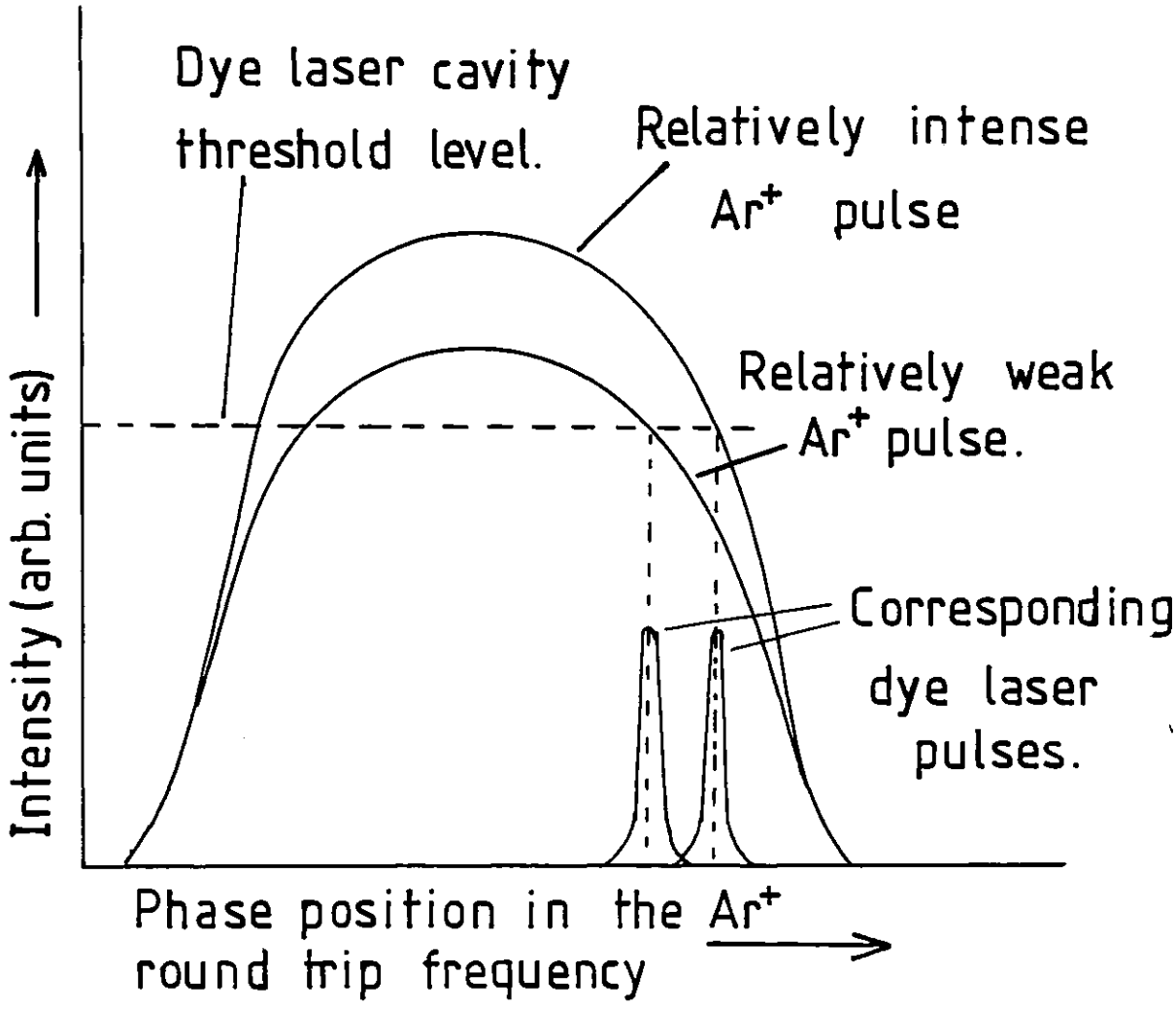


Fig. 2·10.

The Effect of Ar^+ Pulse-to-Pulse Intensity Variation on Dye Laser Pulse Phase Jitter.

2.5 Conclusion

The design, construction and testing of a unique UHV demountable streak tube have been described. The resulting instrument for the first time allows for the direct comparative testing of different photocathode materials with all other experimental parameters remaining unchanged, thereby allowing for e.g. a direct measurement of the intrinsic emission time uncertainty of NEA III-V photocathodes as compared to Si photocathodes.

Although the streak camera so far has only been tested down to a temporal resolution of <18 psec, theoretical studies predict a resolution in the sub-picosecond range, and the flexibility of the constructional design employed, in conjunction with the facility of the UHV system to process a dozen photocathodes at a time should mean that any future minor modifications necessary to realise this ultimate target can be made with the minimum of delay and expense.

CHAPTER 3

INFRARED PHOTOCATHODE MATERIALS

3.1 Introduction

With the current interest in extending the application of streak camera pulse measurement techniques from the visible into the near infrared region of the spectrum, the choice of known suitable photocathode materials becomes limited to the S1 photocathode and the more recent generation of single crystal III-V semiconductor photocathodes.

The S1 cathode, as used in streak tubes is a thin semi-transparent film formed from the elements silver, oxygen and caesium by vacuum deposition onto a glass substrate following an experimentally derived processing schedule, and has exhibited a photoresponse threshold of $\sim$ 1.5μm (Hou et al., 1981; Stahl, 1972).

The III-V cathodes comprise a family of semiconductors, containing elements from groups three and five of the periodic table deposited onto a substrate in such a manner as to produce a heavily doped single crystal film with low electron scattering, which is then coated with a caesium-oxygen overlayer to lower its surface work function and produce high photoelectron escape probabilities. Under the conditions of such a "negative electron affinity" (NEA) surface treatment, the long wavelength threshold can be made to be dependent only on the bandgap of the semiconductor used and thresholds of up to 2.1μm (Gregory et al., 1980) have been reported, with a theoretical limit of 3.35μm imposed by existing materials technology.

In this chapter the production, properties and theories of operation (as far as they are known) of the two types of cathode material are compared and contrasted, with particular reference to their potential for use in near infra-red streak cameras.

3.2 3.2 III-V Semiconductor Photocathodes.

3.2.1, III-V Semiconductor Photocathode Production.

One of the primary requirements for successful semiconductor cathode production is for high purity component materials and ultra-clean production conditions. In practice this means that all vacuum deposition must take place at pressures of less than 10^{-9} mbar (Chinen et al., 1980) in order that impurity incorporation at normal growth rates is insignificant compared with the normal intentional dopant concentrations of $\sim$ 100 ppm.

Opaque III-V bases for use in the reflection mode can be made either by cleaving a single crystal of the cathode material in UHV conditions (Spicer et al., 1978) or by heat cleaning the crystal at a temperature of between 585 C (Stocker, 1975) and 610 C (Arsen'eva-Geil' and Kask, 1965). The period of heating is chosen as a compromise between the conflicting interests of reducing surface dopant evaporation and reducing surface contamination. Cleaning by a mild argon ion bombardment has been found to produce a surface of adequate cleanliness, but the resulting cathodes showed reduced overall sensitivity due to electron-hole recombination at the damaged semiconductor surface (Garbe and Frank, 1969).

The clean semiconductor base is then subjected to an activation process, consisting of an exposure to caesium vapour which is terminated when the photosensitivity of the photocathode reaches a peak, followed by exposure to a controlled quantity (about 24L, James and Moll, 1969) of high purity oxygen. These two processing steps are sometimes repeated several times to form a cathode with

an optimised response in the chosen spectral region. The existing experimental evidence suggests that the caesium-oxygen overlayer formed in this process has a stoichiometry close to Cs_2O (Uebbing and James, 1970, and Section 6.2.4).

Production of thin semitransparent transmission photocathodes requires that the emitting film be epitaxially deposited onto a substrate which is closely lattice matched to it, and yet optically transparent in the wavelength region of interest. Allenson et al. (1972) deposited a 25μm lattice matching layer of $Ga_{0.25}\ Al_{0.75}$ As onto a GaP single crystal substrate using liquid phase epitaxy, thereby reducing the lattice mismatch with the 2μm GaAs photoemitting layer to less than 0.2%, and producing transmission photocathodes with sensitivities of up to ∿400 μA/lumen white light and a photoelectric threshold of ∿ 880 nm. A similar approach was adopted by Gregory et al. (1980) who used an InP substrate, a graded $In\ As_x\ P_{1-x}$ lattice matching layer 15 μm thick, a 1.5 μm thick $In_{0.77}\ Ga_{0.23}$ As photo-emitting layer and a final 2nm Schottky layer of silver to produce a cathode which could be biassed to obtain a long wavelength threshold of 2.1 μm,although for reasons they could not explain this required that the photocathode be cooled to 125K.

Semiconductor substrates can also be thermocompression bonded to glass (Antypas et al., 1978; Antypas and Edgecumbe 1975), thereby facilitating their incorporation into practical imaging devices. The resulting substrate can be cleaned and processed in a similar manner to a single crystal substrate (Chinen et al., 1980).

3.2.2 III-V Photocathode photoemission mechanism

The photoemissive mechanism in the III-V near infra-red photocathodes, being a bulk excitation process can be accurately described by the "three step model", as originally propounded by

Spicer (1958). In this model the probability of an electron being photoemitted is consdered as the product of the probabilities associated with three discrete steps in the photoemissive process, namely

1) The probability per unit volume of bulk photoelectron excitation, in this case by direct interband transitions (James and Moll, 1969).

2) The probability that the excited photoelectron will reach the vacuum interface, taking into account the various electron scattering losses.

3) The probability that the electron, arriving at the vacuum interface will cross it and be photoemitted.

For NEA cathodes the theory of steps 1), 2) and 3) is well understood, being based on the electron transport properties and band structures of the materials concerned, both of which have been extensively investigated with a variety of techniques (James and Moll, 1969; Arsen'eva-Geiland Kask 1965; Bell, 1973; Dinan et al., 1971 and Blakemore,1982)

It is at step 3) that the negative electron affinity surfaces exhibit marked enhancement over their positive electron affinity counterparts. At the surface of a III-V semiconductor there exist surface states ("dangling bonds") which, in the case of an intrinsic crystal, are occupied up to the level of the bulk Fermi level, i.e. up to the middle of the band gap. If one imagines this intrinsic crystal being gradually doped, the bulk Fermi level becomes

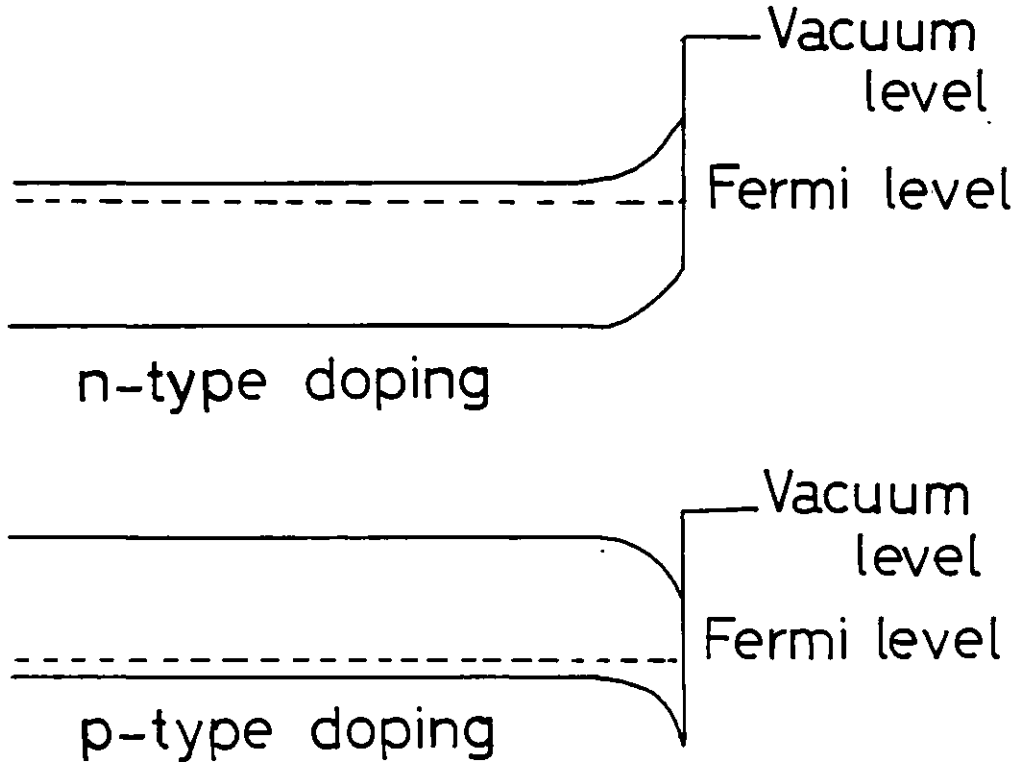


Fig 3.1

Band Bending in a Doped Semi-Conductor.

displaced from its position in the centre of the band gap (upwards in the case of n-type doping, downwards in the case of p-type doping), and charge flows to or from the surface until the bulk and surface Fermi levels are once again coincident. If the surface density of states is sufficiently high, one can think of the Fermi level being effectively "pinned" at the surface and band bending will occur at the surface over a distance which is dependent on the free carrier density (Bell, 1973), but which can be made small compared with both the photoelectron escape depth and the photon absorption depth (Spicer, 1977), Figure 3.1.

If the work function of the surface is further reduced by the addition of a Cs-O overlayer, as in Figure 3.2, the effective electron affinity for photoelectrons excited within the bulk of the material becomes negative. Hence for NEA photocathodes the photoelectric threshold is limited only by the band gap of the semiconductor and such devices show sharp emission thresholds and flat quantum efficiency curves (Figure 3.3). Moreover, because interest is no longer confined to those "hot" conduction band photoelectrons with sufficient energy to clear an energy barrier at the vacuum interface, electrons which have been scattered down into the metastable conduction band minima can be emitted, consequently the escape depth characteristic of step (2) becomes the 1-10 μm (James and Moll, 1969) minority carrier diffusion length (limited principally by defect scattering in the thin film) as opposed to the "hot" electron scattering length (determined principally by electron-electron scattering) of 10-30 nm (James and Moll, 1969; Spicer and Wooten, 1963). The narrow wavelength-independent thermal electron energy distributions predicted for these cathodes (see also 6.2.2) would result in very low electron transit time dispersion in a streak tube.

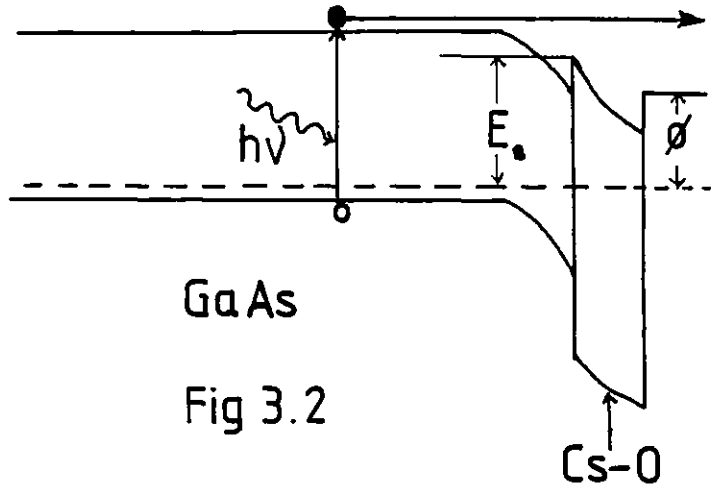


Fig 3.2

Schematic Band Bending Diagram of a NEA Photocathode.

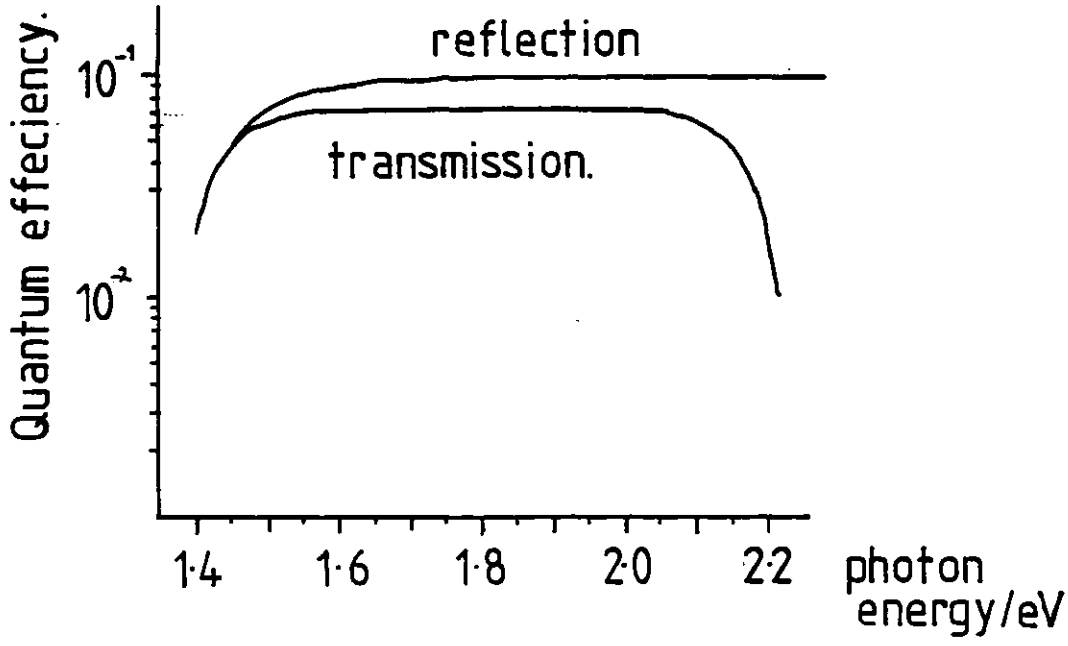


Fig 3.3

Quantum Efficiency Curve for a GaAs NEA Photocathode (after Allenson et al.,1972)

In the case of very long wavelength threshold cathode materials the height of the junction between the semiconductor and the Cs-O overlayer, and the thickness of the overlayer itself can become important (Figure 3.4). As one considers materials with smaller (3.4a-3.4b) bandgaps, this interfacial barrier remains approximately fixed with respect to the bulk valance band (Spicer, 1977), until there comes a point when the energy of the conduction band minimum lies below the interfacial barrier and in the absence of assisting applied fields, the photoelectrons have to tunnel through the Cs-O overlayer. This behaviour is manifest in the shapes of the spectral sensitivity curves of decreasing bandgap NEA photo-emitters (Figure 3.5).

In order, then, to realise the full potential of the NEA photocathodes the emitting film must be of very high crystallographic quality (to maintain the long minority carrier diffusion length), its boundaries must be as strain-free as possible to minimise electron-hole recombination at the surfaces, and it must have a thickness of the same order as the minority carrier diffusion length (Allen, 1971).

3.2.3 Suitability of NEA cathodes for streak camera work

The facts outlined above have unfortunate consequences if the use of such cathode materials in ultrafast streak tube devices is contemplated. Electron-optic design considerations require that cathodes in such devices operate in the transmissive mode, and this typically reduces the sensitivity available by a factor of ~ 3 (Gregory et al., 1980), due to the technical difficulties in growing an epitaxial thin film of equivalent crystallographic quality to a piece of bulk material and eliminating the surface strains at the interfaces of the film.

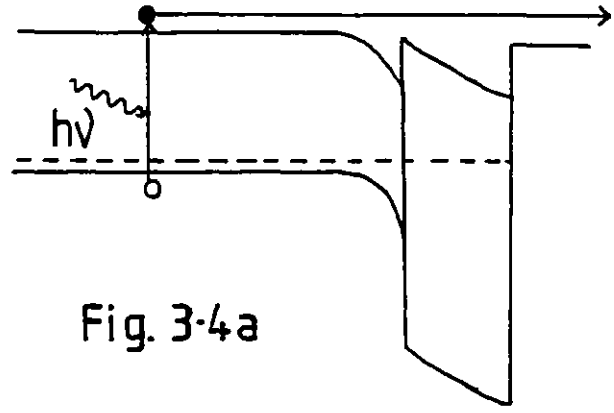


Fig. 3·4a

The Effect of Interfacial Barrier Height on Photoemission from Narrow Band Gap Semiconductors.

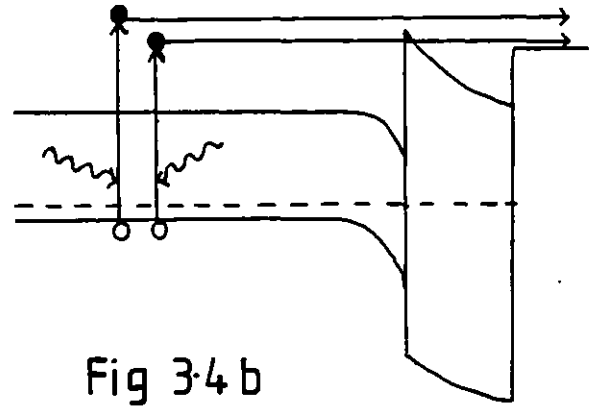


Fig 3·4 b

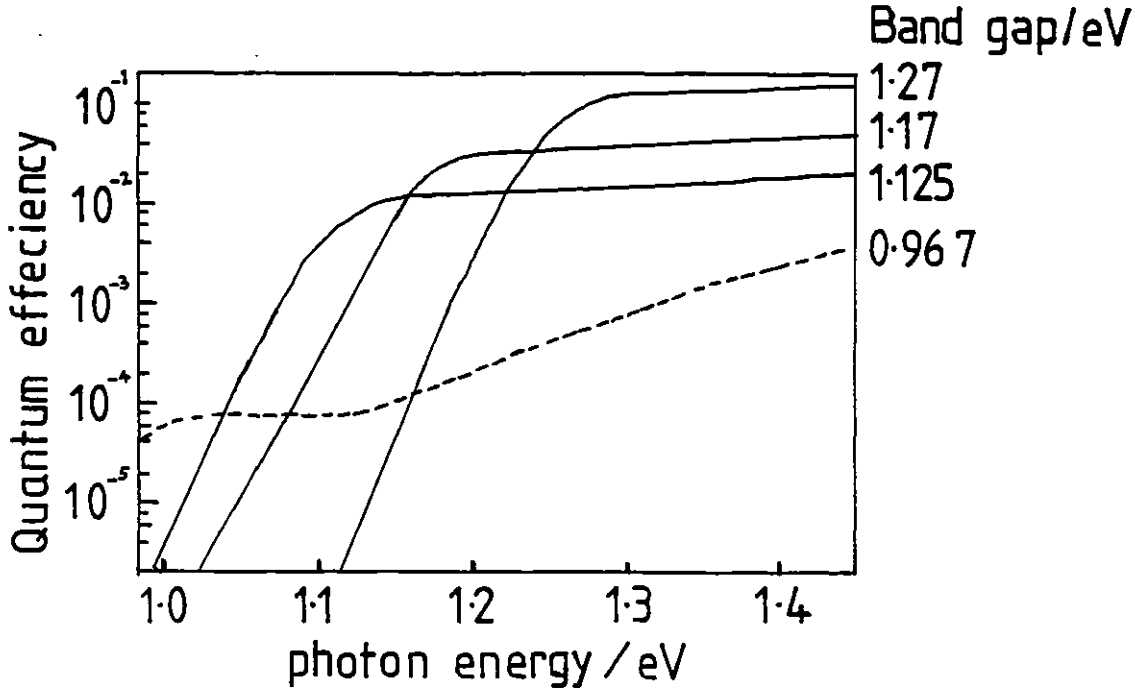


Fig 3·5

Quantum Efficiency curves for Narrow Bandgap Semiconductors (after Spicer,1977)

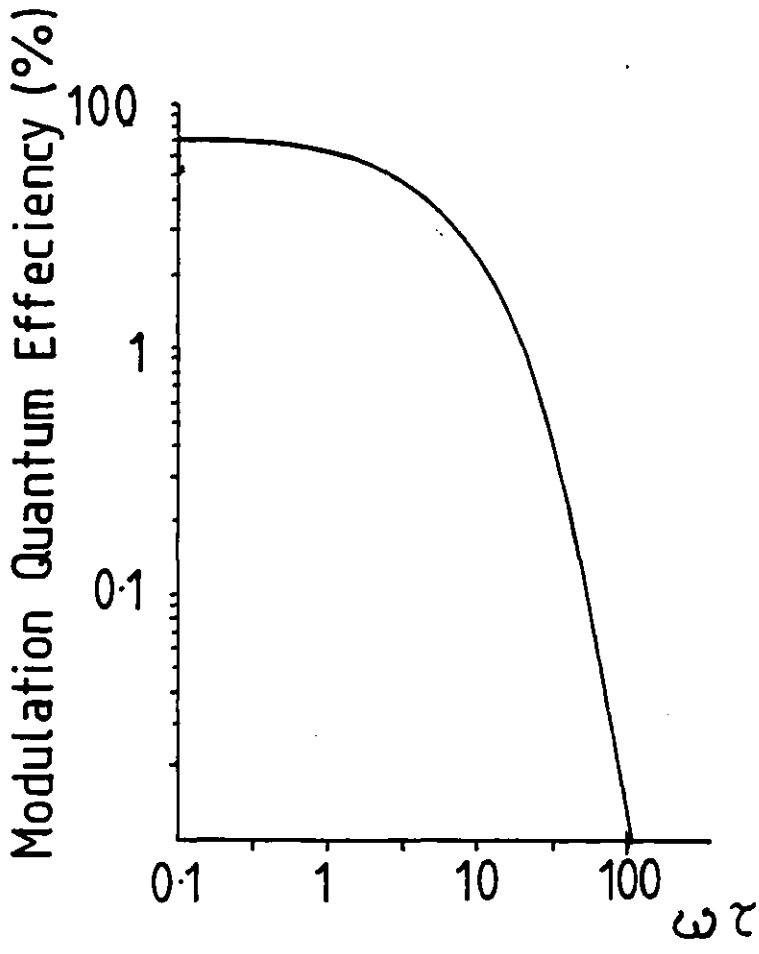


Fig 3·6

Calculated Temporal Modulation Transfer Function for a Transmission Photocathode of Thickness Equal to one Diffusion Length L, and with an Optical Absorption Coeffecient α such that $\alpha L=10$. (After Bell, 1973)

At the start of this study, however, it seemed that the main drawback of such cathode materials was likely to be their comparatively long "intrinsic temporal emission uncertainty" (see 2.3.3). Although there were no experimental results, theory suggested that for a cathode of thickness equal to the minority carrier diffusion length the difference between the times of emission of photoelectrons excited simultaneously at the front and rear surfaces of the active film is likely to be of the same order of magnitude as the minority carrier diffusion lifetime τ, i.e. $\sim 10^{-9}$s.

Calculations by Bell (1969) predicted a temporal modulation transfer function (Figure 3.6) which dropped to a value of 50% at a radian frequency ω where $\omega\tau \simeq 1.5$ for a transmissive cathode of thickness equal to the minority carrier diffusion length. Such a temporal response would clearly be inadequate for the majority of streak camera applications, although such a cathode might suit some framing cameras. It did seem conceivable however that experimentation with thinner active films and field-assisted photoemission (a high extraction field is of course a common feature of most streak tube designs), could yield an improvement in temporal response at the expense of a considerable loss of sensitivity, and for the results of such experiments the reader is referred to Chapter 6.

3.3 The S1 Ag-O-Cs Photocathode

3.3.1 S1 Photocathode production

In sharp contrast to the systematic development of the III-V semiconductor cathodes, the production techniques employed for the fabrication of S1 photocathode materials were arrived at in an entirely empirical fashion by an apparent combination of luck and experimental ingenuity in which a detailed understanding of the chemistry and physics of the cathode film was largely absent.

In a study of the photoemissive properties of thin films of caesium adsorbed on metals (inspired by the earlier work of Campbell (1928) with potassium on oxidised copper), Koller (1930) discovered that if a layer of silver was first oxidised "in such a manner as to give a layer of silver oxide several hundred molecules deep" and then caesium was distilled onto its surface, and its temperature was raised to 250°C "a reaction takes place and a compound is formed which is remarkably photosensitive".

Since this early work many variations on the basic process have been tried, notably a final evaporation of silver followed by baking was found to considerably enhance the photocathode sensitivity (Asao and Suzuki, 1930), but the following steps form the basic core of all these processes.

a) Formation of the silver base

For photocathodes which are to be used in the reflection mode the silver base can be formed in a variety of ways. It can be a sheet of pure silver, a film of silver electrolytically deposited on glass by the reduction of silver nitrate, an evaporated opaque layer of silver on glass, or even a single silver crystal (Hoene and Saggau, 1966). The initial form of the silver base does not seem to have a first order effect on the photocathode sensitivity, although Koller believed that a slightly roughened silver base was beneficial.

For transmission photocathodes the character of the silver base is fundamentally important and it is universally formed by evaporating a thin semitransparent layer of silver on to a transparent (usually glass) substrate. The amount of silver deposited is usually controlled by monitoring the change in the optical transmission of the substrate during deposition. Silver is known however to have a strong tendency towards aggregation when the evaporated layer is thin,

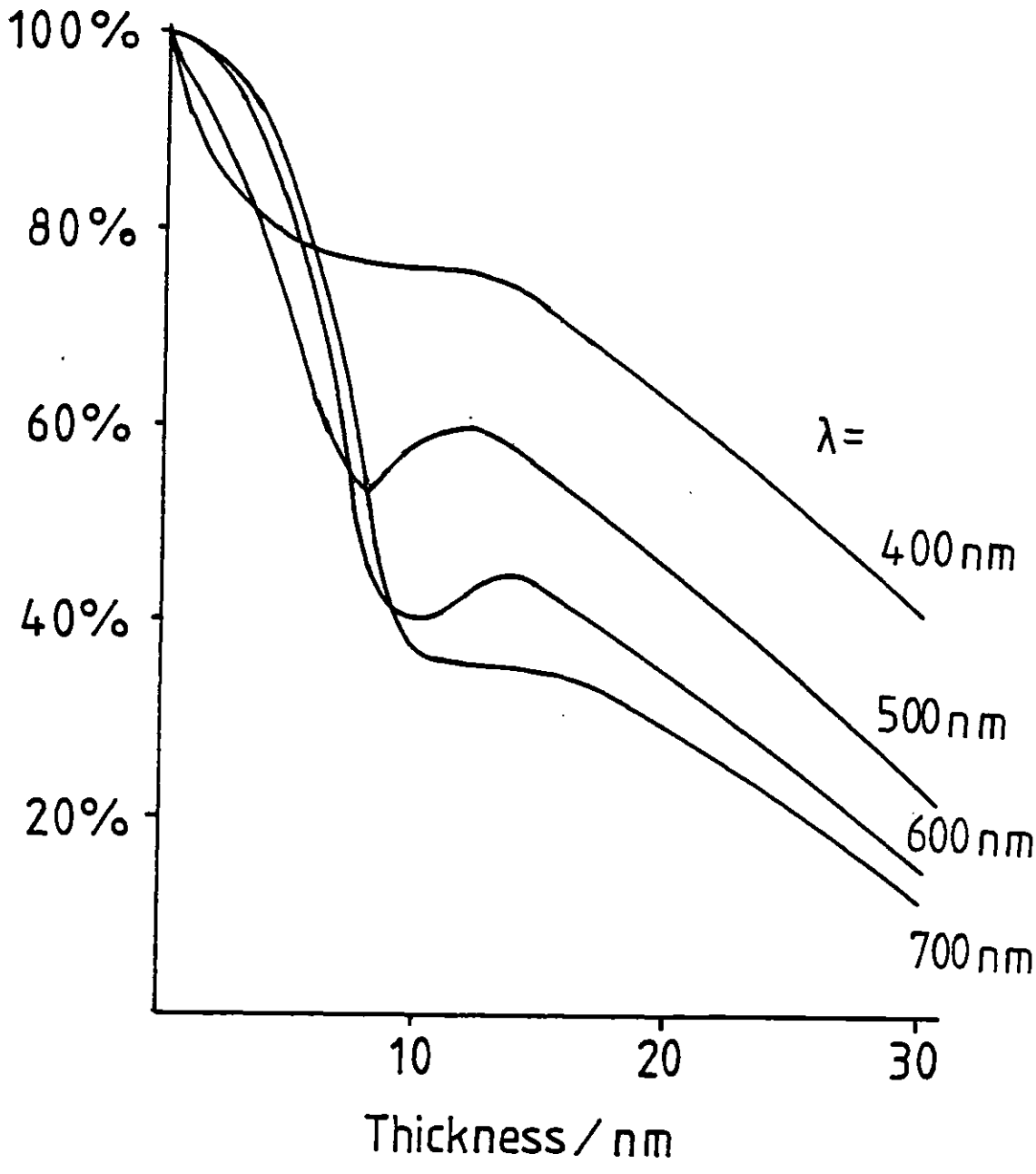


Fig. 3·7

Transmission versus Thickness Curves for Silver Films Evaporated in 2 Seconds. (From Sennett and Scott, 1950)

consequently the optical transmission alone does not provide a reliable and reproducible means of monitoring either the thickness or the structure of the evaporated silver base.

As an example of this Faust (1958) showed that for films evaporated in the same time interval there was a kink in the transmission versus thickness curve, even when measured with monochromatic light, so that some values of transmission corresponded to three different film thicknesses. Sennett and Scott (1950) showed that these transmission versus thickness curves, although independent of evaporation angle, were sensitive to evaporation rate, with quickly evaporated films showing pronounced kinks in the transmission-thickness curves (Figure 3.7). Electron microscopy carried out by the same workers showed that in the case of slowly evaporated ($\sim$ 20 minutes) films the aggregates tended to "grow more in height i.e. become thicker before joining together than do the aggregates of the rapidly ($\sim$ 2 sec) formed films which tend to remain thin and grow out over the substrate".

Since the evaporation of the first silver base is always done with the substrate at room temperature it would seem that control of the evaporation rate, together with optical transmission measurement will probably define both the structure and thickness of the silver base film.

Soboleva et al. (1962) established a correlation between smoothness of the evaporated silver base and the ultimate longwavelength threshold of the complete cathode, and they obtained the longest threshold wavelength by creating a very smooth initial silver base by evaporating it very slowly. In practice however, semitransparent bases are normally made by evaporating until the white light optical transmission drops by about 50%, at such a rate that the whole evaporation takes about two minutes.

b) Oxidation of the Silver base

Silver will react with oxygen to form the normal oxide Ag_2O, but only at relatively high pressures and temperatures, viz. 160 C with oxygen present in pressures in excess of ∿550 mbar (Benton and Drake, 1932). A more controlled and convenient way of achieving the oxidation is by oxygen ion bombardment in a glow discharge.

For opaque cathodes the silver base is made the negative electrode in a d.c. discharge, excited in a pressure of ∿ 0.1 mbar of oxygen, and the process is terminated when the interference colours generated by the thin optically transparent oxide layer reach an empirically determined hue. The same process can be applied to semitransparent base films, although in this case the process is terminated when the white light transmission of the film reaches a maximum.

With some transmission cathodes however the resistance of the base film is either too high initially or more commonly it rises to an excessive value as the oxidation progresses, whereupon the base film charges up and oxidation ceases. Such an unevenly oxidised base layer results in a poor cathode sensitivity and so this problem is often circumvented by using an R.F. a.c. discharge.

Provided oxidation is even and proceeds to the correct degree no-one has reported any dependence of the final cathode sensitivity on either the oxygen pressure, the discharge electrode geometry, or the discharge voltage (be it a.c. or d.c.) in spite of the fact that the R.F. discharge may well result in the silver being bombarded with negative as well as positive ions.

c) Second Silver evaporation

When the cathodeis being formed in the presence of a silver evaporator, a second layer of silver is sometimes evaporated at this stage, with generally beneficial results on the final cathode photosensitivity. In the case of opaque photocathodes this evaporation is terminated when the oxide colour changes to a dark purple hue, whereas in semitransparent cathodes the evaporation is usually continued until the while light transmission has dropped to half its value after stage (b).

d) Caesiation or "activation"

It is generally agreed that caesiation is the most crucial stage in Sl cathode processing. It is only at this stage that significant photo- and thermionic emission develops, and these quantities are normally used to monitor the progress of the caesiation reaction. For successful cathode formation it is essential that the cathode temperature is maintained in the range 120 ∿ 250 C, where the desired reaction can take place (Sommer, 1968; Koller, 1930). Moreover if excess caesium is allowed to react with the cathode film an irreversible fall in photocathode sensitivity is observed (Sommer, 1968). Although this behaviour is unique to the Sl, and remains largely unexplained, it seems to have been observed by the majority of workers in the field, and it results in considerable care and experience being necessary to terminate the caesiation at the correct stage.

Two methods have been developed to ensure the correct dosage of caesium. In the first, the whole of the vacuum device is heated to 150 ∿ 200 C(Sommer, 1968), with the exception of the cathode which is kept close to room temperature, and caesium vapour, either from a vacuum distilled ampoule or from a chromate channel, is distilled onto the cathode until its colour changes to one determined by previous experimentation. The cathode is then warmed up to the same

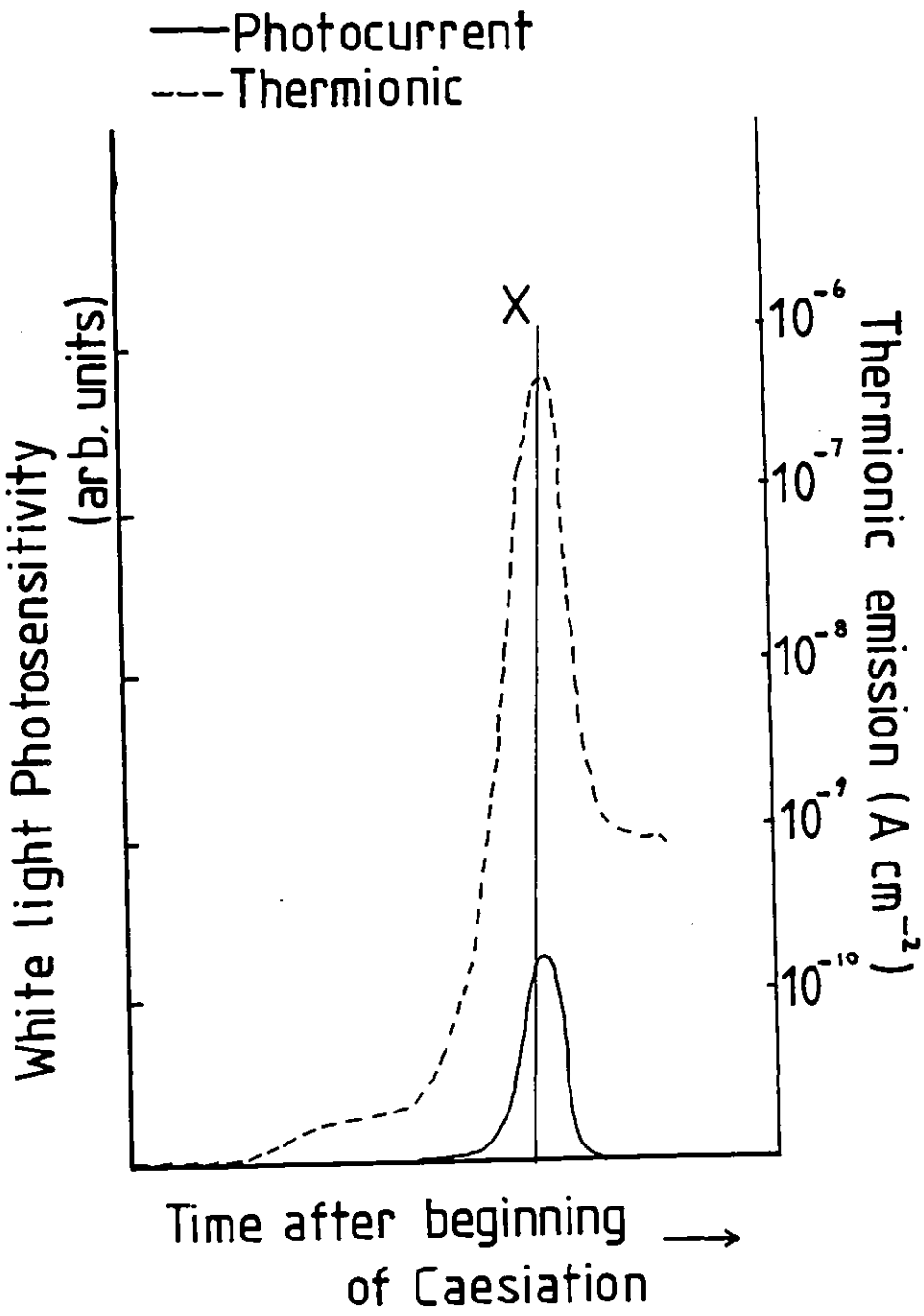


Fig 3·8

Development of Photocurrent and Thermionic Emission During Caesiation.(Sayama,1946)

temperature as the rest of the device whereupon photosensitivity develops.

The second method involves warming the whole device to 150 ∿ 200 C and slowly introducing caesium vapour whilst monitoring the thermionic and photocurrent. A typical progress of these quantities is shown in Figure 3.8. In this case the author (Sayama, 1946) found it best to stop the introduction of caesium at point X, but it must be recognised that the geometry, pumping speed and temperature distribution of the vacuum system under consideration can considerably alter these characteristics, and that almost always the only way to determine the optimum caesium dosage on a given system is by trial and error (see e.g. Section 4.3.1(b)).

e) Final Silver evaporation

If a silver evaporator is present, and particularly if stage (c) is omitted from the process, a slow final evaporation of silver, followed by a short bake at ∿ 250 C (Asao and Suzuki, 1930) is often found to increase the white light sensitivity of the tube by a factor of ∿ 4, with a disproportionately high increase in the infra-red sensitivity. The evaporation is typically terminated after the white light sensitivity has slowly peaked and fallen by a factor of ∿ 1/3 and is paced to take place over ∿ 15 minutes. The white light sensitivity typically increases by a factor of 2 ∿ 2.5 during this evaporation and increases again by a similar factor during the bake.

As mentioned already these steps form only the basis of a photocathode processing schedule. In many cases step (e) is followed by a controlled exposure to oxygen which can sometimes increase the threshold sensitivity. Hou et al. (1981) went further, using a "yo-yo" process consisting of repeated small doses of silver

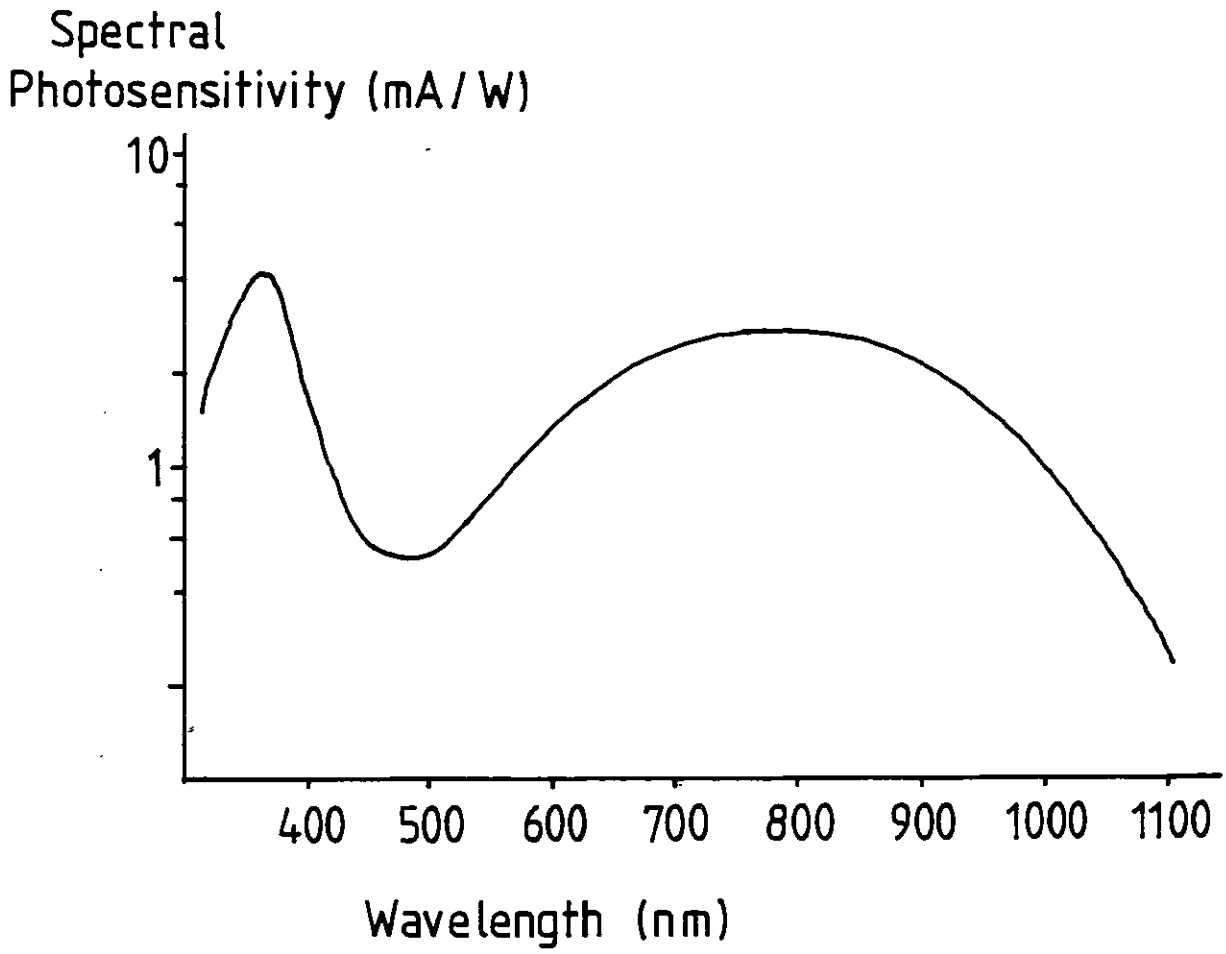


Fig 3·9
Spectral Photosensitivity Curve for a Commercial S1 Photocathode(RCA Wallchart).

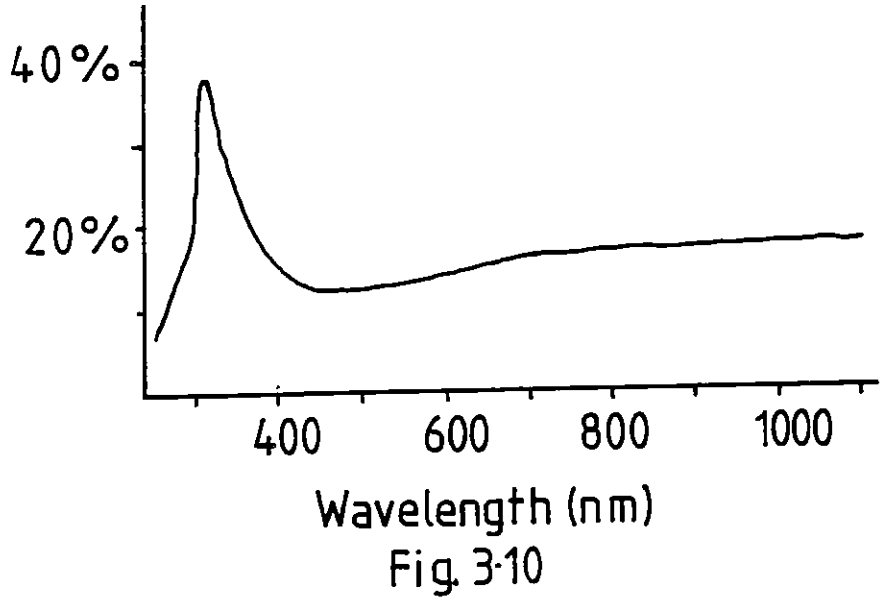


Fig. 3·10
Optical Transmission of an S1 Photocathode (Asao,1940)

and oxygen, terminated by a finely controlled oxygenation to selectively enhance the response in the threshold region, thereby extending the cutoff wavelength to 1.5 μm.

Other workers have employed altogether different processing techniques designed to eliminate other problems such as high cathode resistivity (Hou et al., 1982) and the need to excite glow discharges in all-metal UHV systems (Ebbinghaus et al., 1976).

Component cleanliness, low partial pressures of residual gases (particularly oxygen and methane) and thorough baking and outgassing of all channels and filaments used throughout the processing schedule have been found to be almost as essential for Sl photocathode production as for the ultra high purity III-V cathodes. In most cases the failure of a particular cathode processing attempt can be directly traced to the presence of small amounts of some contaminant.

3.3.2 Basic Properties of the Sl Photocathode

One of the first hints as to the complexity of the Sl cathode is provided by the presence of a large amount of structure in its spectral sensitivity curve (Figure 3.9). In the UV region the curve shows a sharp maximum near 350 nm followed by a sharp minimum at about 320 nm and a continued rising yield at shorter wavelengths thereafter (these features are normally only observed in the reflection mode of course due to the high absorption of most substrate materials in this spectral region). From about 450 nm out to the infra-red threshold of 1-1.3 μm the curve shows a very broad flat peak, with a maximum at a wavelength anywhere between 600 nm and 800 nm (Bates, 1981).

The optical transmission characteristics of a complete Sl are shown in Figure 3.10. The principle feature of these curves is a transmission maximum occurring at a wavelength of $\sim$ 320 nm, close to the transmission maximum observed by Asao (1940) in silver films.

Values reported for the photocathode surface resistivity, a parameter which can severely limit the dynamic range of a streak tube or framing camera (Kalibjian, 1975) vary over several orders of magnitude. In some cases high resistivities of the order of MΩ/□ and semiconducting properties have been reported (Harper and Choyke, 1956), whilst other workers observed low resistivities and metallic conduction properties (Asao, 1940). Hou et al. (1982) monitored the appearance of the low metallic-like resistivity with the progress of the final silver evaporation process stage, and showed that using the normal S1 process a low surface resistivity and an extended long wavelenth threshold were mutually exclusive, a problem which they avoided by developing a new processing schedule involving a base layer of palladium.

Thermionic emission at room temperature lies typically in the range 10^{-11} to 10^{-14} A cm^{-2} (Sommer, 1968), the highest value of any know photoemitter, and this tends to limit the dyanamic range attainable with this material. Measurements of the temperature dependence of this thermionic emission give values for the thermionic work function in the range 0.83 eV (Davey, 1957) to 0.91 eV (Eckhart, 1955).

3.3.3 Models for the structure and photoemission mechanisms of the S1 Photocathode

It is generally accepted that the details of the physical and chemical structure of the S1 cathode have not yet been established with certainty. The absence of this knowledge clearly makes hypotheses concerning the photoemission mechanisms difficult to formulate or test in a quantitative manner. Nevertheless over the years a variety of models have appeared in the literature, each combining assumptions about the cathode structure, and what follows is an approximately chronological attempt to summarise their main features.

Koller's (1930) initial experiments led him to explain the emission from his cathode as being entirely due to a thin film of caesium oxide, coated with a thin layer of elemental caesium. The silver was present solely to provide an oxide capable of being reduced by the caesium and thereby generating the correct caesium oxide layer. By making assumptions about the yield of the nickel pellets he used to generate the caesium vapour he decided that the optimum cathode (which was probably inferior to a present day S1, being heavily caesiated) had an atomic Cs:O ratio of 6.6:1. The relevance of this work to the conventional S1 cathodes produced today is questionable on account of the unusual processing schedule employed.

Campbell (1931) performed a series of experiments employing a basic S1 processing schedule, in which he correlated the amount of caesium necessary for optimum photoemission with the pressure drop observed during the oxygen discharge stage and deduced that the cathode contained caesium and oxygen in the atomic ratio of 2:1. He also discovered that if he stopped the caesium flux prematurely photosensitivity would vanish in time, but if he overcaesiated and sealed the cathode bulb off, the photosensitivity would stay at a constant low value. He interpreted these results as meaning that the oxidised silver base was reduced by the caesium according to the reaction

$$Ag_2O+2Cs \rightarrow Cs_2O+2Ag$$

and that this reaction would continue as the caesium was deposited until the Ag_2O was exhausted at which point the caesium would form a thin layer on the cathode surface corresponding to maximum photosensitivity. Excess caesium at this stage he imagined forming a thick layer on the cathode surface which would absorb photoelectrons

and kill the photosensitivity. Even at this early juncture, however, Campbell realised the inadequacies of this model. The fact that he could not reproduce an S1 type surface with caesium overlayers on either silver or caesium oxide alone led him to postulate a "complex produced by the merging of the Cs_2O and the silver (and possibly caesium) into one another".

In 1956 Borziak et al. published the results of a study of the optical absorption and photoemission of films of caesiated silver and caesium oxide (which they described as Cs_2O although they present no evidence to support this stoichiometry). They produced optical absorption data suggesting that the "Cs_2O" was a semiconductor with a band gap of approximately 2eV and an electron affinity which varied between 1.0 and 0.5 eV. Moreover they correlated the minimum in the S1 photoresponse curve at λ = 320 nm with the absorption minimum in a pure silver film, and by monitoring changes in the spectral response of the oxide film as silver was sputtered on to it they were able to show that the longwavelength response was associated with silver and not the hypothetical caesium impurity centres previously suggested by Klebnikov (1946), Dobretsov (1952) and Chechik (1954).

Comparison of the photoemissive characteristics of the caesium oxide film with the caesiated silver nonetheless made it clear that it was not simply excess caesium in the oxide film which was changing the properties of the added silver, and Borziak finally concluded that the cathode was probably best described as silver particles dispersed in a semiconducting caesium oxide matrix, with bandgap excitation in the caesium oxide being responsible for the cathode sensitivity in the UV and excitation from the silver particles (with a much lowered work function due to their caesium oxide coating) being responsible for the broad peak in the visible and near infra-red photosensitivity.

At about the same time Frimer and Gerasimova (1956) published results from the electron microscopy of quartz replicas of Sl photocathodes at various stages in processing. These results showed that silver films of the thicknesses commonly used as photocathode bases consisted of microcrystals of dimensions <20 nm (the limiting resolution of their quartz replica technique) and that the surface topology did not change during the oxidation process, provided that the silver film was not heated much above room temperature before oxidation. The smooth structure was maintained throughout the cathode processing provided the normal Sl process was followed and the final Sl therefore had surface roughness on a scale <20 nm. If the Sl process was departed from however, the surface morphology was found to change. In particular, overcaesiation led to the appearance of large irregular crystallites on the cathode surface, of dimensions $\sim$ 1μm with the accompanying loss of sensitivity.

Measurements of the photocathode surface resistivity, published almost simultaneously by Harper and Choyke (1956) showed that the thin films normally used for transmission photocathodes had a high resistivity of the order of MΩ/□, with a negative temperature coefficient characteristic of a semiconducting layer with an activation energy of 0.2 eV. This work agreed with the subsequent work of Davey (1957) in which a thermal conductivity activation energy of 0.2 eV was deduced from the temperature dependence of cathode resistivity. The results of both of these studies were of course consistent with the Borziak idea of the cathode being composed of isolated conducting particles in a semiconducting matrix.

In 1968 Sommer published a comprehensive review of the then current state of knowledge regarding the structure and emission mechanisms of the Sl. Drawing on his own experiments monitoring the onset of infra-red photosensitivity as silver was added to a caesium

oxide film and on the optical absorption data of Borziak (1956) and Asao (1940) on caesium-oxide and silver films, Sommer was able to advance convincing arguments in favour of a Borziak type cathode structure.

In the "Sommer-Borziak" model, then, the photocathode was conceived as an inhomogeneous structure of silver particles embedded in a predominantly Cs_2O matrix - the presence of small quantities of other oxides of caesium, or even atomic silver was not ruled out. Band gap excitation in the caesium oxide matrix was considered responsible for the steeply rising quantum efficiency of the cathode for wavelengths less than 300 nm, whereas bulk excitation in the silver particles followed by emission into the caesium oxide and thence into the vacuum (both interfaces were assumed to have low energy barriers and correspondingly high photo-electron transmission probabilities), was held responsible for photo-emission at wavelengths longer than ∿300 nm. In this model the cathode was also characterised by patches on its surface of very low work function, as deduced from abnormal current-voltage photoemission curves obtained by Soboleva (1959), which were largely responsible for the high thermionic emission observed in some S1's and whose disappearance during the final silvering stage was considered responsible for the shortening of the longwavelength threshold and the observed drop of two or three orders of magnitude in the thermionic emission at this stage.

With this model Sommer was able to explain,albeit in a qualitative fashion, nearly all of the experimentally observed properties of S1 photocathodes with the notable exception of the large enhancement of the visible and near infrared photosensitivity observed during the final silvering and baking processing stage.

From experiments measuring the spectral sensitivity of a caesiated silver film several tens of nanometers thick (Sommer, 1967)

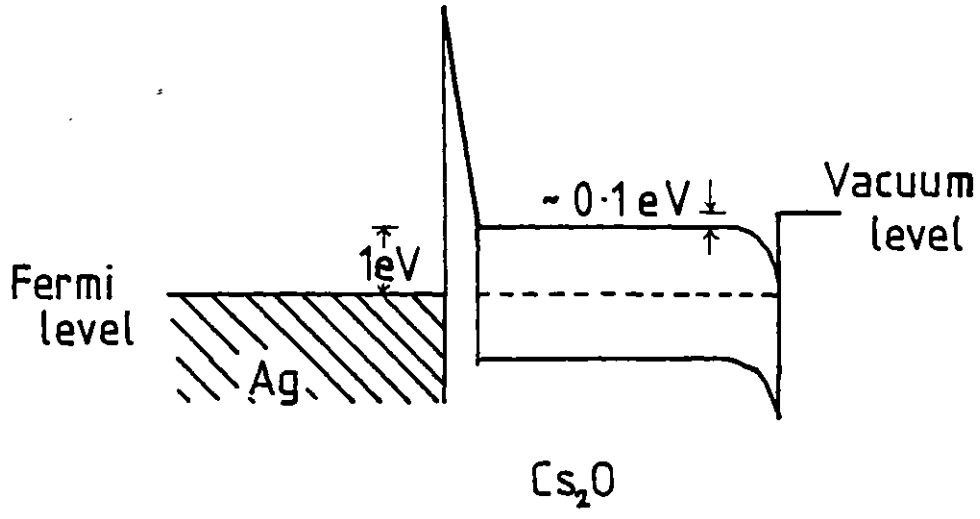


Fig. 3·11

Band Diagram for the S1 Photocathode as Postulated by Neil and Mee (1970).

in both the reflective and transissive mode, he was able to demonstrate a long photoelectron escape depth of 10's of nm for low energy photoelectrons in silver. This information, combined with the observed low optical reflection coefficient and consequent higher absorption per incident photon of an S1 as compared to bulk silver he adduced to explain the generally high quantum efficiency ($\sim 10^{-2}$) in the visible region of the spectrum of an S1 cathode as compared with bulk silver ($\sim 10^{-4}$). The broad flat peak in the visible region of the spectral response curve was tentatively explained as being due to the effect of rising photoelectron escape probability at the interfaces as the exciting radiation energy is increased above threshold being gradually balanced out and eventually defeated by the decreasing photoelectron escape depth at higher photoelectron energies in the silver particles.

The Sommer-Borziak model was put on a more quantitative footing when Neil and Mee (1970) published the results of a study of the photoelectron energy distribution curves (EDC's) from S1 cathodes with exciting radiation in the range 1.55 to 5.00 eV. The authors used data from Borziak's (1956) absorption and photoemission results from caesium oxide films, together with the known work function of bulk silver to draw a hypothetical energy band diagram for the silver particles embedded in the caesium oxide (Figure 3.11) which they used to explain features observed in the E.D.C.'s. In particular for a range of photon-energies, they identified a peak in the E.D.C.'s 0.3eV below the maximum photoelectron energy which corresponded to a peak in the E.D.C. measured from bulk silver which results from a peak in the bulk density of states for silver 0.3eV below the Fermi level. This peak became more pronounced after the final silver evaporation stage of the cathode processing schedule. The broad slow electron peak observed at photoelectron kinetic energies of $\sim$ 0.4 eV for incident radiation of energy>3.4 eV they tentatively attributed to

pair production in the caesium oxide matrix.

As a further refinement to the Sommer-Borziak model, Sommer (1980) suggested that a donor level 0.2 eV below the conduction band minimum in Cs_2O might be responsible for the low work function ($\sim$ 1eV) generally measured for S1 cathodes, as compared with the electron affinity of 0.8 eV and bandgap of 2eV deduced by Borziak which alone would suggest an intrinsic work function of $\sim$1.8 eV. Sommer ascribed this donor level to the presence of Cs_2O_2 impurities based on a study by Gugel et al. (1977) of the thermodynamics of the reaction of caesium with silver oxide. It must be said, though, that the existence of this species in an S1 cathode is still no more than a hypothesis. The deduction of its presence by Gugel et al. involved a number of arguments of dubious plausibility, including the somewhat arbitraryassumption that the silver oxide cathode base would remain stable under UHV, but spontaneously dissociate into metallic silver and gaseous oxygen in the presence of caesium vapour so that the thermodynamics of caesium oxide formation could be calculated for reactions in the gas phase with a large excess of oxygen.

Bates (1981) and Bates and Yang (1980) considered a different caesium oxide responsible for the low work function exhibited by the S1. On the basis of XPS analysis of S1 surfaces they deduced a cathode structure consisting of silver particles dispersed throughout a matrix of Cs_2O, with a 1-2 nm thick layer of $Cs_{11}O_3$ on the surface reducing the effective electron affinity for photoelectrons from the bulk of the cathode to negative values. They also draw on the Maxwell-Garnett theory (1904, 1906) of optical absorption for a system consisting of small particles of linear dimensions much less than the wavelength of light embedded in an insulating matrix.

This theory as developed by Marton and Lemon (1971, 1977) and Yamaguchi et al. (1974) predicts an "optical conduction resonance" at a certain incident light wavelength when the dipoles induced on the small metallic particles oscillate collectively in a manner akin to the electrons in a bulk plasma resonance in an electron gas, and a peak in the optical absorption of the film occurs. Towards the limiting case where the size of the particles and their separations are both much smaller than the wavelength of the exciting radiation, the frequency of this optical conduction resonance is found to be dependent only on the intrinsic optical constants of the small particles and on their volume fraction in the material. This fact was used by Bates (1981) to explain the variation in the position of the "peak" in the visible portion of the spectral sensitivity curve as depending on the volume fraction of silver present in the cathode which in turn depends on the processing schedule employed.

Using the plausibility argument that increased light absorption by the silver particles would result in increased photoemission, Bates calculated the frequency of the "optical conduction resonance" for the type of silver particles believed to be present in the Sommer-Borziak S1, and concluded that this mechanism could account for the enhancement of the silver photoemission in the visible region over and above what one might expect for bulk silver.

As both Schmitt-Ott et al. (1980) and Sommer (1968) pointed out, one would expect a large increase in the photoemission from small silver particles anyway, due to the increased likelihood of photoelectron escape simply because the photoelectrons are likely to be excited closer to an interface. If one assumes a long escape depth for photoelectrons once they have left the silver particles and entered the oxide matrix (consistent with the low electron affinity for

the surface proposed by Bates, 1981) using the Neil and Mee (1970) type energy band diagram for the particle/matrix and matrix/vacuum interfaces, and electron escape depths found in the literature, one can calculate enhancement factors for this effect of about one order of magnitude. A more detailed description of this calculation is presented in the Appendix I.

Although it is capable of explaining most of the characteristics of the S1 cathode with a degree of success, the Sommer-Borziak model is not the only one which has appeared in the literature. An attempt to use classical semiconductor theory to explain the photo-emissive properties of an S1 resulted in Khlebnikov (1946), Dobretsov (1952) and Chechik et al. (1954) modelling the photocathode as a film of semiconducting Cs_2O containing atomic silver impurities producing narrow localised acceptor levels a fraction of an eV above the valence band maximum (responsible for the emission in the region of $\lambda \sim 360$ nm) and atomic caesium impurities producing donor levels a fraction of an eV below the conduction band minimum (responsible for the visible and infra-red response). Such a theory is of course at variance with the experimental evidence proving the necessity of silver for any long wavelength sensitivity.

Eckhart (1955) proposed an S1 band diagram with silver impurity levels ~ 0.3 eV below the conduction band minimum, and an electron affinity of ~ 0.8 eV on the basis of his photoelectric and thermionic measurements on photomultipliers. A similar scheme was adopted by Pakhomov (1969, 1971) and Pakhomov and Melamid (1971) who regarded silver donor levels as being responsible for the visible and infra-red sensitivity, and caesium impurity levels as being responsible for the photosensitivity in the UV. Although Pakhomov admits the likely existence of collidal silver particles in the cathode he maintains that silver in this form reduced the photosensitivity by absorbing light without photoemitting and that as such it was merely

an undesirable side effect of the normal S1 processing schedule. For this reason he introduced silver by diffusing it in from the edges of a caesium oxide film and was able to obtain a cathode with low infra red absorption but moderate infrared sensitivity, attributing this to having introduced the correct level of silver impurity doping and little or no colloidal silver.

Although such semiconductor models are attractive in their simplicity, as several authors have pointed out (e.g. Neil and Mee, 1970; Bates, 1981) describing silver as an impurity when it typically comprises at least 20% of the photocathode is unrealistic. Moreover the likelihood of reproducing the precise crystallographic structure and low doping levels necessary to result in the hypothetical band structure with its narrow impurity levels, with such a wide variety of S1 processing schedules seems slight. This is not to say of course that the caesium oxide matrix in the Sommer-Borziak model cannot be considered as a semiconductor with its associated band diagram. It is the narrowness and positions of the hypothetical impurity levels and their significance in the photoemissive process which initially seem doubtful.

A more recent mechanism, claimed to account for the visible and infra-red portion of the S1 photosensitivity curve has been proposed by Endritz (1974). By depositing an S1 cathode film on a glass diffraction grating substrate with a horizontal periodicity of $\sim$ 890 nm, and a vertical modulation of 10 $\sim$30 nm, he produced a photocathode with sharp peaks in the spectral sensitivity curve which appeared at different wavelengths for different angles of cathode illumination (Figure 3.12). These peaks were interpreted as being due to the resonant coupling of the incident radiation into surface plasmon waves (SPW's) on the cathode surface, the rules of energy and momentum conservation being satisfied by a momentum component supplied by virtue of the regular periodicity in the cathode surface

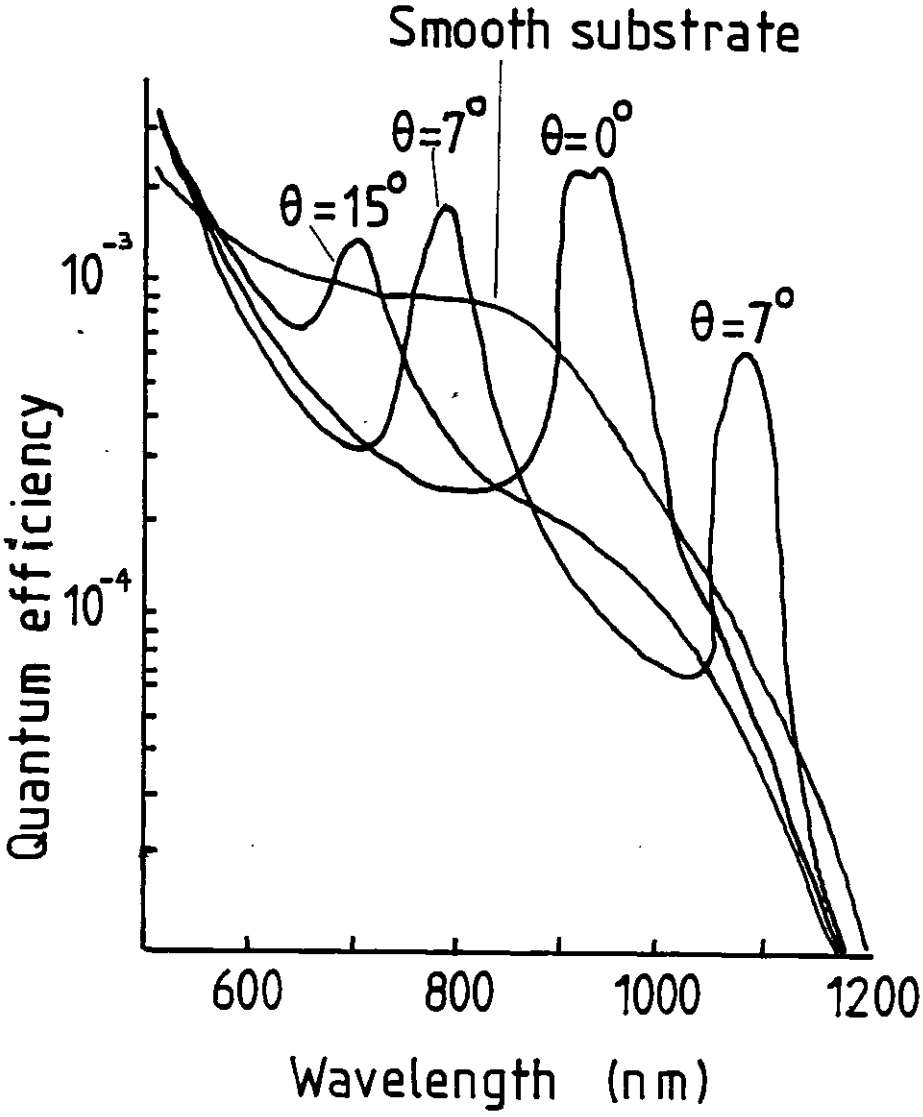


Fig. 3·12

Spectral Quantum Efficiency Curves for an S1 Cathode Deposited on a Diffraction Grating Substrate (After Endritz,1974)

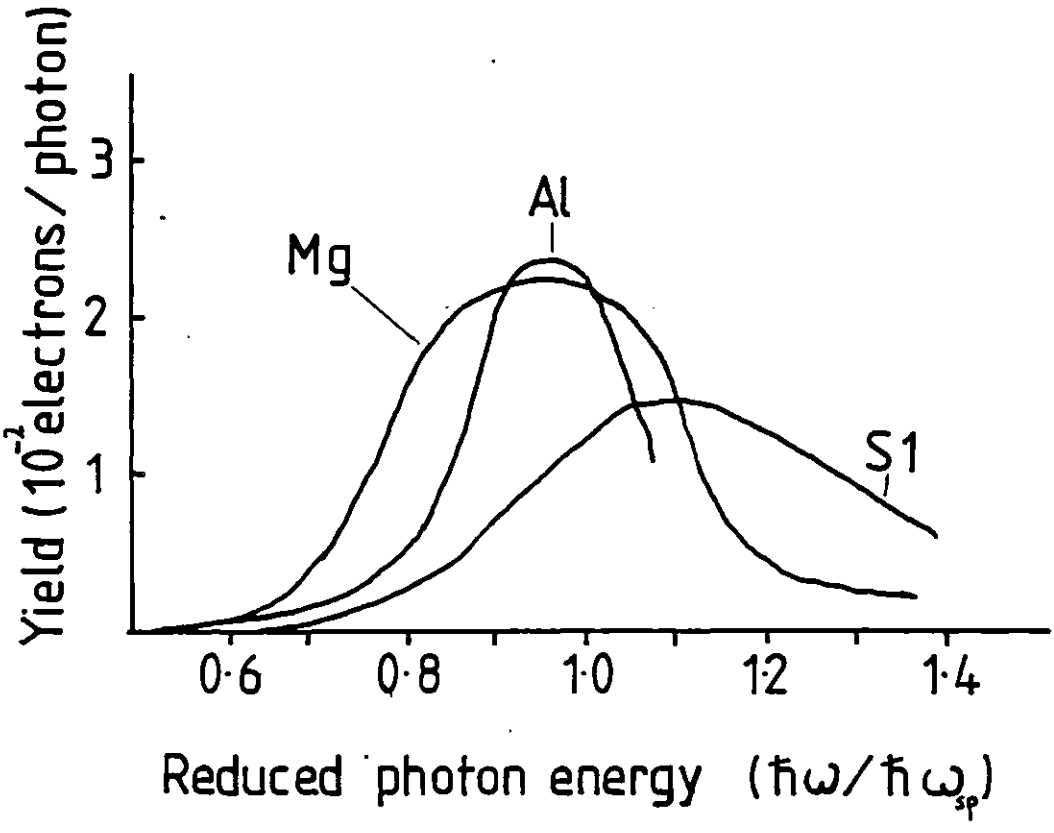


Fig. 3·13

Quantum Efficiency as a Function of Photon Energy Normalised to the SPW Frequency for Al and Mg Metals and an S1 Photocathode (Ebbinghaus et al., 1976)

roughness spectrum. Once these SPW's have been excited they can decay by the Landau damping mechanism, resulting in all their energy going into a single photoelectron which can then be photoemitted. Although Endritz's cathode had impressive angular tunability, the overall sensitivity even on the smooth substrate was down by a factor of 3 or 4 on the normal S1 sensitivity (R.C.A. wall chart, 1970) making the results of questionable relevance to normal S1 photocathodes (see also Chapter 6 for experimental results on this topic).

The SPW photoemission mechanism was also supported by a UPS study of S1-like surfaces produced in a UHV system by Ebbinghaus et al. (1976). The surfaces were produced by exposing a caesium coated semitransparent silver base to oxygen, and the authors concluded that the resulting structure had an overlayer of $Cs_{11}O_3$ clusters. Loss structures in their UPS spectra indicated a SPW energy of 1.55 eV for this material, which they correlated with the observed "peak" in the visible photoresponse for an S1 photocathode (Figure 3.13). Again however the relevance of this work is suspect on account of the absence of any photosensitivity information about the film they were analysing.

Since SPW's can only be excited by components of the $\underline{E}$ vector in an optical field normal to the cathode surface (Raether, 1977), a more convincing demonstration of the importance of this mechanism in a normal S1 would be a simple measurement of the polarisation dependence of cathode sensitivity for non-normal angles of illumination. Even in the presence of considerable surface roughness one would expect to see a significant difference between the yields (corrected for reflection losses) with "s" and "p" polarised light if the SPW mechanism were operating.

3.3.4 Suitability of the S1 photocathode for streak camera work

The semitransparent S1 is well suited to in situ fabrication inside self-contained streak camera tubes, since it requires only a source of caesium vapour, a glow discharge electrode and a silver evaporator to be built into the tube itself. This is in contrast to the complicated cathode transfer techniques which would be necessary to incorporate a NEA cathode into a streak tube, because of the difficulties which would be otherwise involved in warming up a substrate which had been built into a streak tube body to the 600 C or so required for sufficient substrate cleaning before activation.

The existing evidence suggests that on the whole the S1 cathode is more tolerant to background gas pressures than its NEA counterpart, with successful processing often taking place at pressures of 10^{-8} mbar compared with the 10^{-10} mbar considered essential for NEA work.

Although direct experimental evidence is absent, considerations of typical cathode thicknesses and electron Fermi velocities would suggest an intrinsic cathode emission uncertainty of $\sim 10^{-14}$ s (Zavoisky and Fanchenko, 1965), about four orders of magnitude faster than the predicted values for typical NEA cathodes (Bell, 1973).

The two main drawbacks of S1 cathodes are their potentially high surface resistivity (leading to image defocussing at high emission currents, thereby limiting the cathode dynamic range) and their comparatively poor photosensitivity to wavelengths in the 1.3μm region of the spectrum.

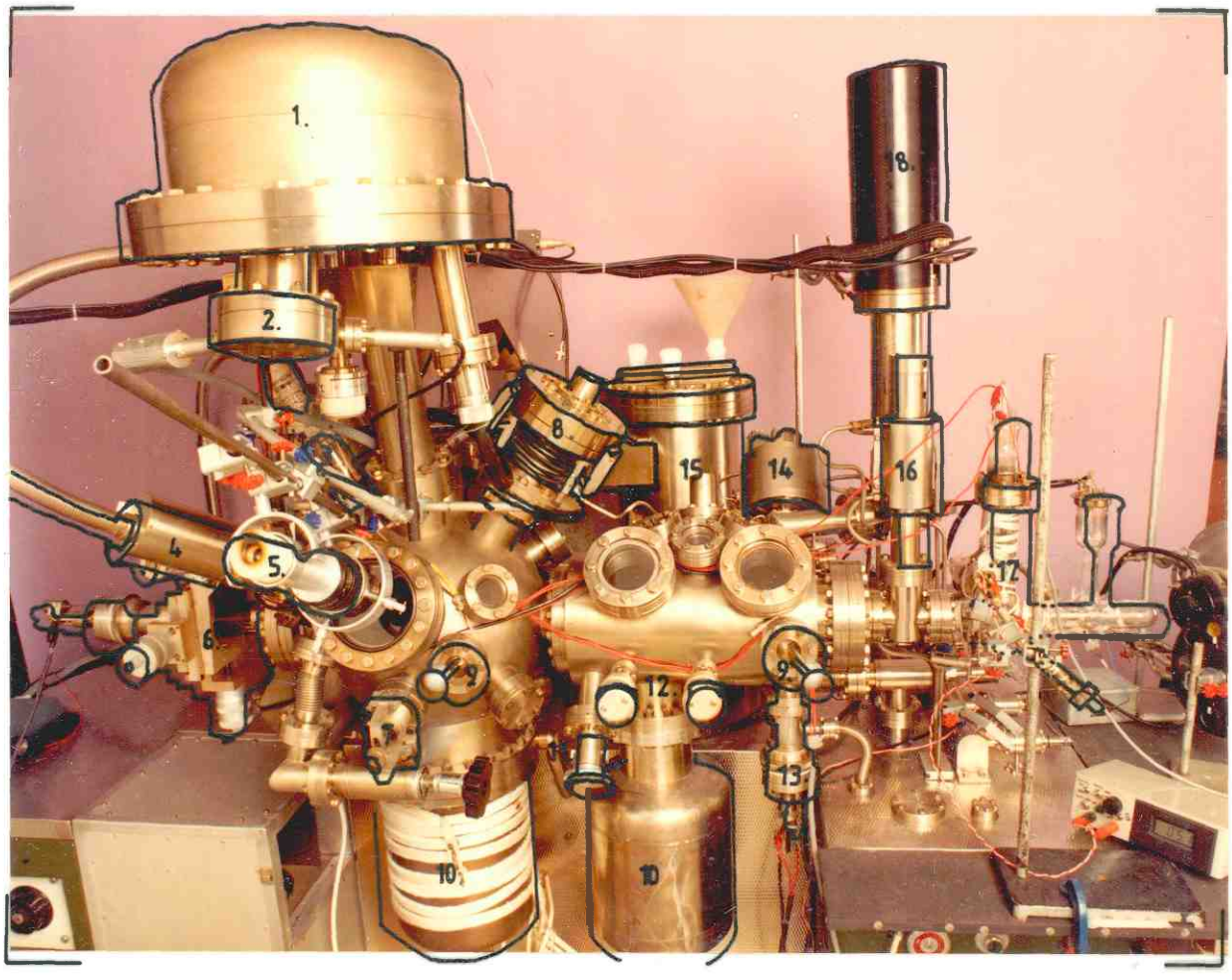


Fig.4·1.

1.Hemispherical Electron Energy Analyser
2.Channeltron Housing
3.Caesium Gun
4.X-Ray Source
5.135 mm Lens Imaging 5µm Slit onto Photocathode
6.Precision X,Y,Z Manipulator
7.Wobble stick for Tuning the RF Streak Camera
8.Electron Gun for AES
9.Sample Transport Mechanism Wobble sticks
10.Titanium Sublimation Pumps
11.Gate Valve.
12.Sample Transport Mechanism Actuators.
13. Preparation Chamber Heating Probe
14.High Energy Ar^+ Gun
15.LN_2 cooled cold Trap
16.Pneumatic Gate Valve.
17.Caesiation Chamber.
18.Mass Quadrupole Gas Analyser.

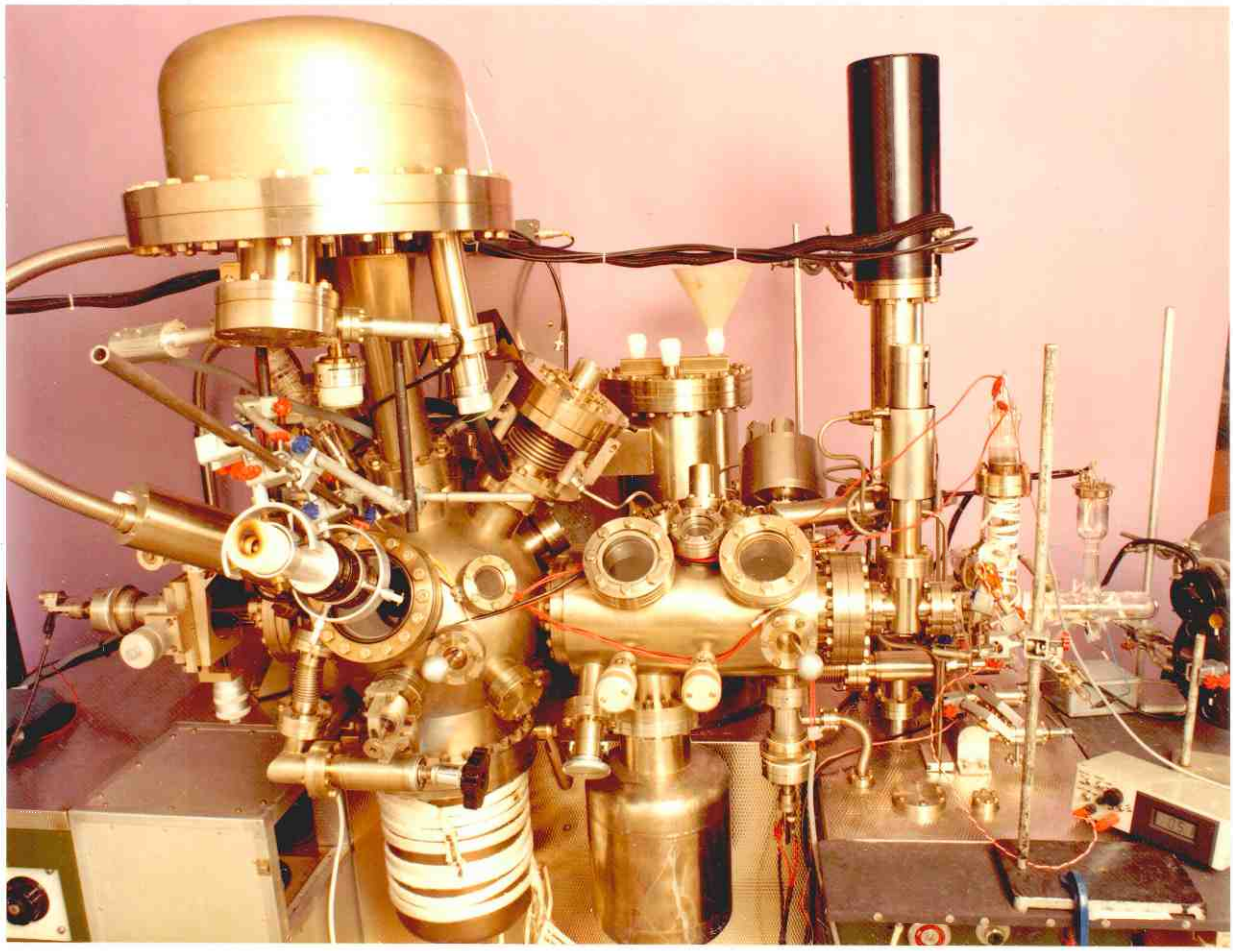


Fig.4·1.

CHAPTER 4

EXPERIMENTAL TECHNIQUE AND APPARATUS

4.1 General description of apparatus

All the experiments were carried out in a modified commercial UHV electron spectrometer (VG Scientific ESCAlab) as depicted in Figures 4.1 and 4.2. The equipment, as it was delivered, consisted of two stainless steel chambers, each pumped by a liquid nitrogen cooled oil diffusion pump and a titanium sublimination pump.

The preparation chamber was initially designed for general sample processing and was fitted with liquid nitrogen cooled evaporation sources, a quadrupole mass spectrometer for residual gas analysis and a sample probe on which samples could be heated up to temperatures of $\sim$400 C, or cooled to temperatures approaching 77K whilst remaining in electrical isolation from the chamber itself. This chamber was also equipped with two argon ion guns, one a high energy (up to 10kV) cold cathode discharge type, the other a low energy ($\sim$200eV) hot filament type. These were used to clean the substrates with varying degrees of force before attempting processing.

The analysis chamber took the form of a 30 cm diameter "mu-metal" sphere into which samples which had been treated in the preparation chamber could be transported and chemically analysed. It was fitted with a twin-anode X-ray source on a linear motion drive, which could be moved in close to the sample to provide intense X-ray illumination at the Mg$k\alpha$ (1253.6eV) or Al$k\alpha$ (1486.6eV) wavelengths.

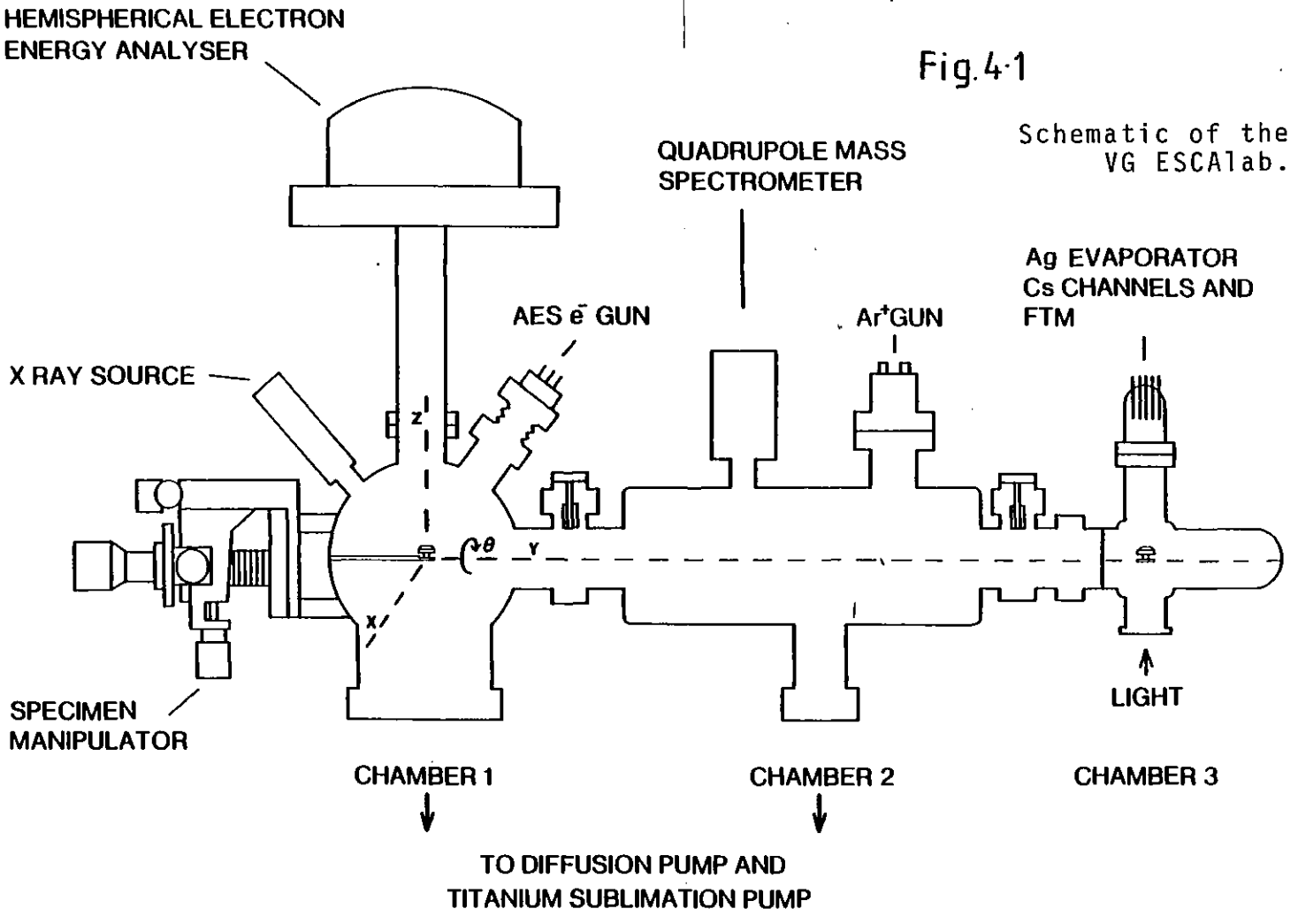


Fig.4·1

Schematic of the VG ESCAlab.

For Auger electron spectroscopy, a focussed electron gun (VG LEG 61) mounted on a steerable bellows flange was used. This produced a narrow focussed beam (of radius variable down to $\sim$0.5 μm) of 0.5-6kV electrons, which could be moved about in the sample plane without the defocussing problems introduced by electrostatic deflection.

The UHV demountable streak camera (Chapter 5) was also mounted on this chamber, on a flange diametrically opposite the main front window. An external projection lens was used to cast the test images through this window onto the back of the photocathodes when they were undergoing streak camera tests.

The cathode specimens could be mounted on a precision manipulator in this chamber which afforded movement in three dimensions over a range of $\sim$ 5 cm, with a positional accuracy $\sim$100 μm, and 360° rotation of the sample about the y axis (Figure 4.1). Whilst on the manipulator the sample temperature could be controlled in the range $\sim$300 C to 77K and the sample was kept in electrical isolation from the rest of the chamber.

The energy spectrum of the electrons emitted by the sample (in XPS, AES, or when measuring EDC's) was measured using a hemispherical sector electrostatic energy analyser fitted with a channeltron electron multiplier detector (see Section 5.3.3).

High purity gases could be admitted into either chamber from a gas handling line which could be evacuated separately from the rest of the system using one of the diffusion pumps (Figure 4.3). The two chambers were separated by a gate valve through which samples could be transported using a small "railway carriage" on a movable rail, both of which were operated by rotary motion feed throughs.

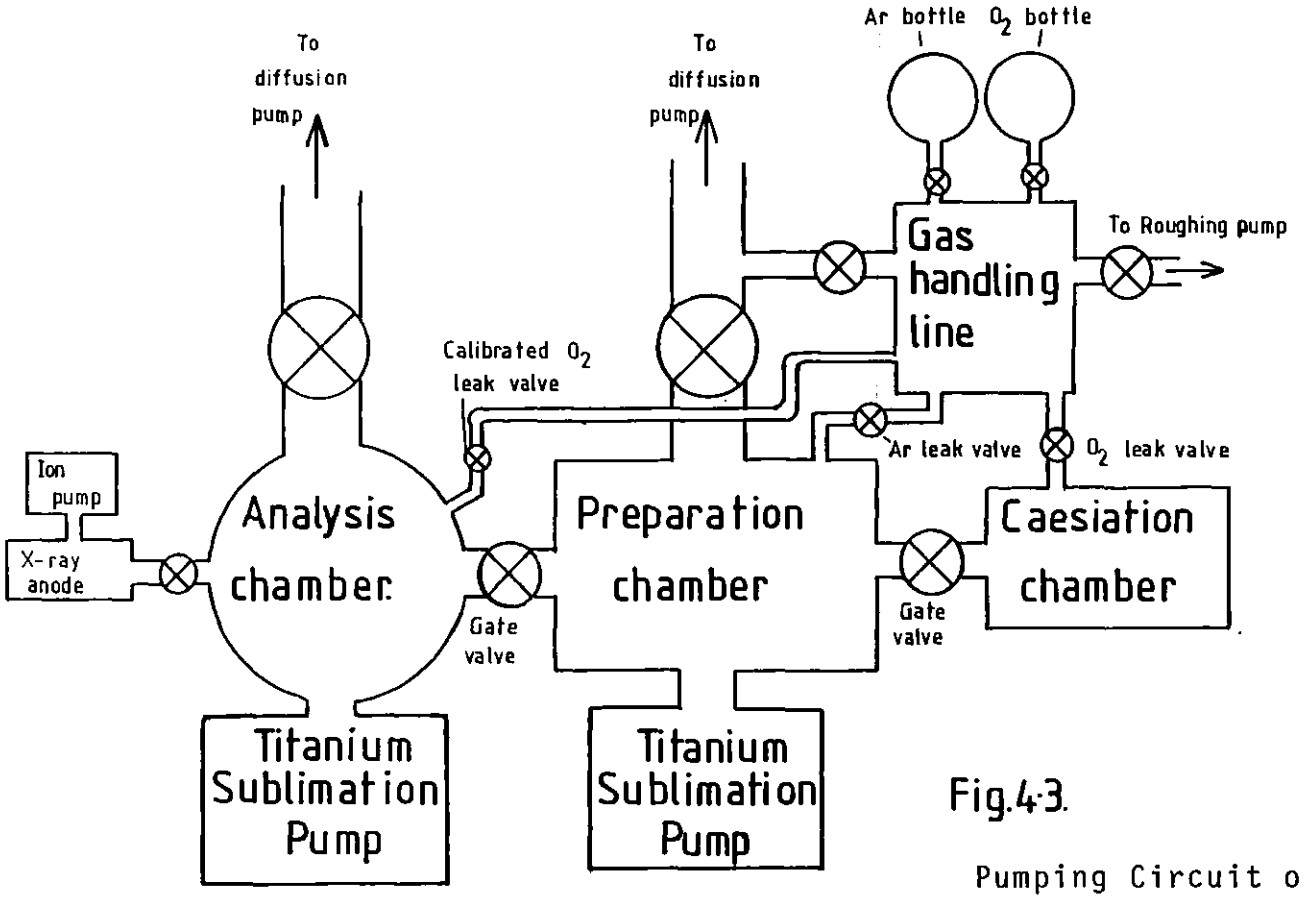


Fig.4-3.

Pumping Circuit of the ESCAlab.

At each end of the travel of the railway mechanism samples could be put on and taken off the railway carriage with small forks mounted on UHV "wobble sticks", and transferred to the storage carousels, heating post, specimen manipulator etc.

The "railway carriage" was modified, with the metal stub on which the sample would sit being replaced with a glass item. This simultaneously allowed for the sample to be illuminated from below whilst remaining electrically isolated from the rest of the system (Figure 4.4). This, in conjunction with an isolated springy wire contact allowed for photocurrent, ion bombardment current and transmission measurements to be made on the substrates whilst they were in the preparation chamber.

Similarly the specimen holder on the end of the precision manipulator in the analysis chamber was replaced with a redesigned version (Figure 4.5) having a smooth outer surface (to minimise discharge problems which can arise due to the high electric fields used with the streak camera) and a hollow tubular post on which the sample stub waslocated, with a small mirror underneath to direct light arriving through one of the chamber windows up onto the underside of the substrate. This arrangement allowed for transmissive photosensitivity measurements with the sample in the position normally used for XPS and AES.

The vacuum equipment was constructed entirely from stainless steel, copper, glass and PTFE and was thus bakeable at temperatures up to 250 C. After the normal 48 hour 200 C bakeout, followed by a thorough degassing of all the filaments, evaporators, X-ray anode etc., the analysis chamber would typically attain a pressure of $< 5 \times 10^{-11}$ mbar, and the preparation chamber $< 10^{-10}$ mbar. Residual gas analysis showed this background pressure to be mainly CO, CO_2 and H_2O vapour, with no detectable partial pressure of O_2.

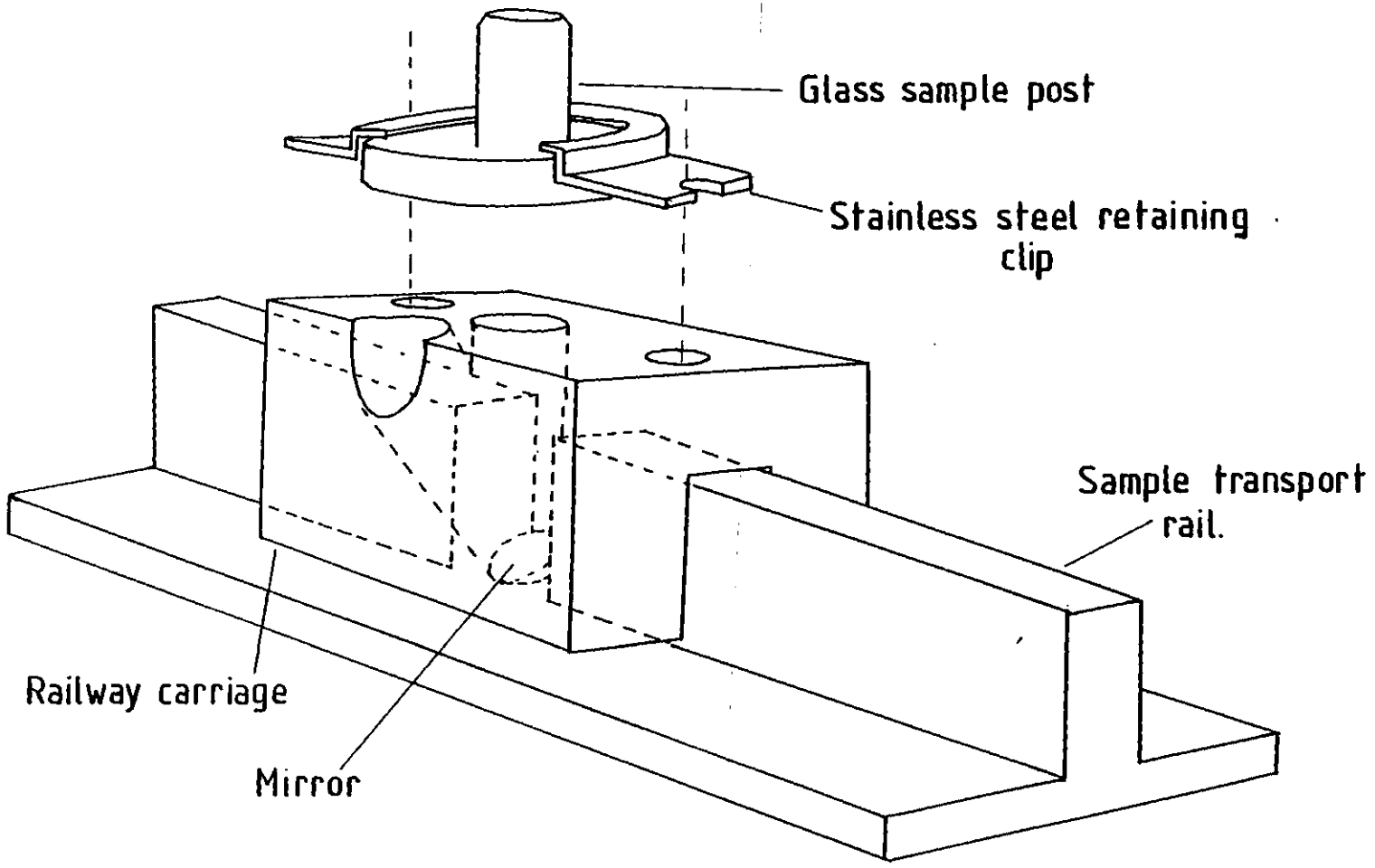


Fig.4.4.

Modifications to Sample Transport Mechanism.

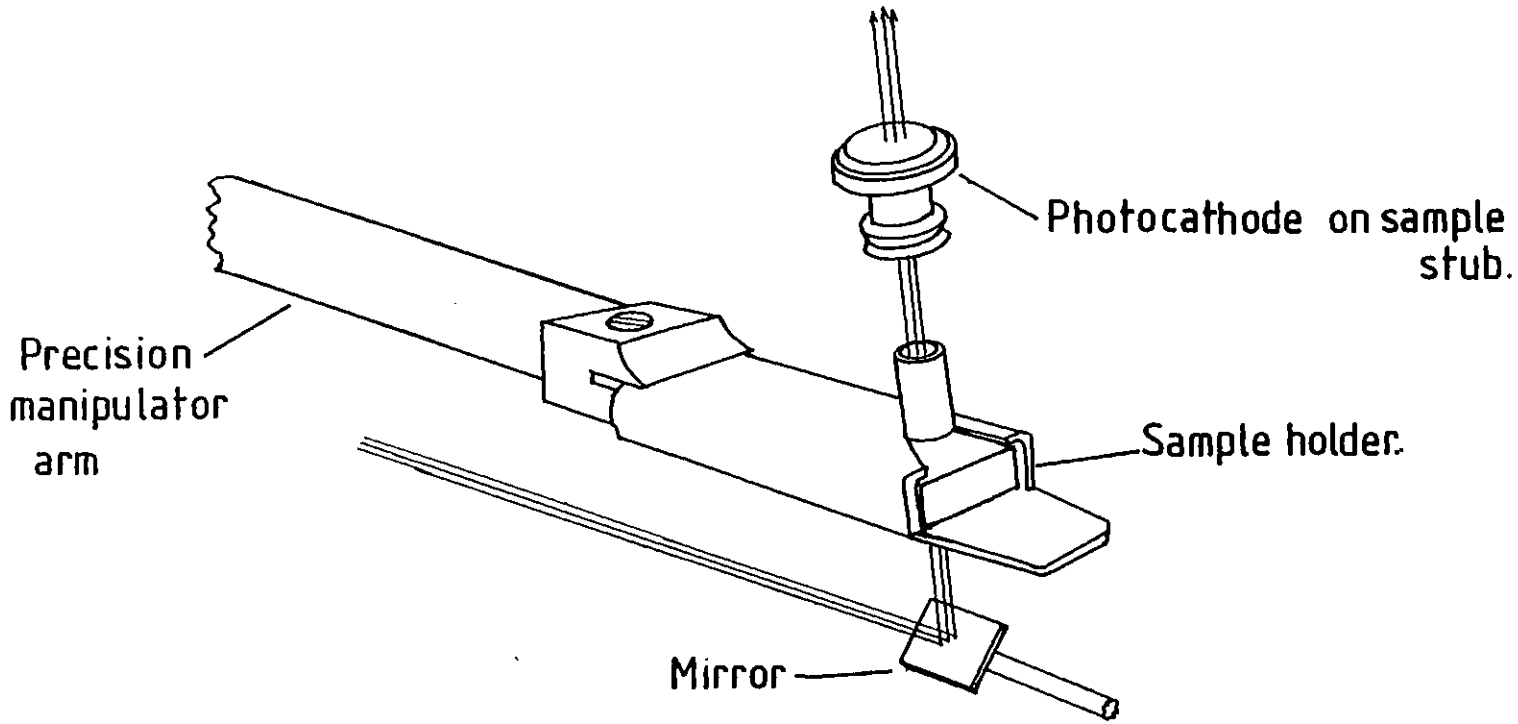


Fig.4.5. Modifications to the Analysis Chamber Sample Holder.

4.2 Spectral Photosensitivity Measurement

The equipment modifications outlined in Section 4.1 meant that photocurrent measurement could be measured in both chambers in the transmission and the reflection modes, with the photocathode electrically isolated from the metal chamber. This last point is important because, as initial trials showed, measuring the photocurrent with the sample earthed and an isolated collector biassed at a positive potential results in large errors from the photocurrent emitted from the chamber walls.

To eliminate the effects of sample thermionic emission (which at some stages in the process can be many times larger than the photocurrent), the light source was chopped at a frequency of ∿80 Hz with a chopper wheel and the photocurrent was measured with a Brookdeal type 9503-SC lock-in amplifier (Figure 4.5). The output of the lock-in amplifier was connected to a chart recorder to provide a permanent record of the development of photosensitivity during processing.

In order to arrive at an absolute spectral sensitivity curve for each photocathode the following procedure was adopted. The output (in mW) from a focussed white lamp filtered with one of a number of interference filters (each with a measured bandwidth ∿ 1% of their centre frequency) which spanned the wavelength range 555 nm →1.06 μm, was measured with a calibrated optical power meter (Photodyne 44XL). Care was taken to ensure that the lamp-filter-powermeter geometry was the same as that used when measuring photocurrents in the vacuum equipment. This measurement provided a series of "filter factors" which allowed the shape, but not the absolute magnitude of the photosensitivity curve for a particular cathode to be calculated from the photocurrent readings with the various filters. The absolute

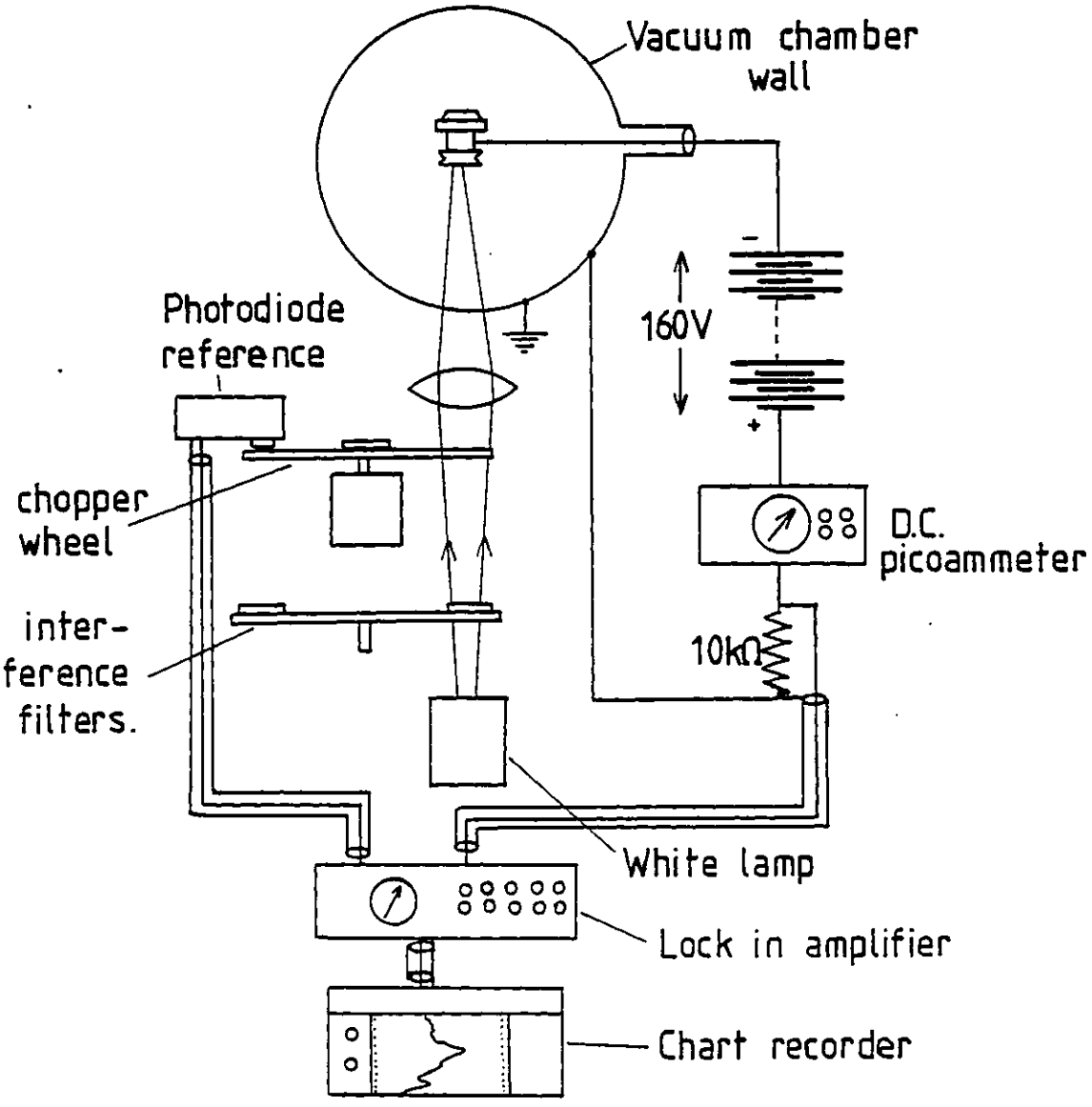


Fig.4·6.

Photocurrent Measurement Circuit.

magnitude of the photosensitivity at 633 nm was then measured using the known output of a low power ($\sim$0.4 mW) He-Ne laser which could be easily steered so that all of its output was illuminating the photocathode. The spectral sensitivity curve calculated from the filter readings was then scaled so as to give the same sensitivity as this at 633 nm.

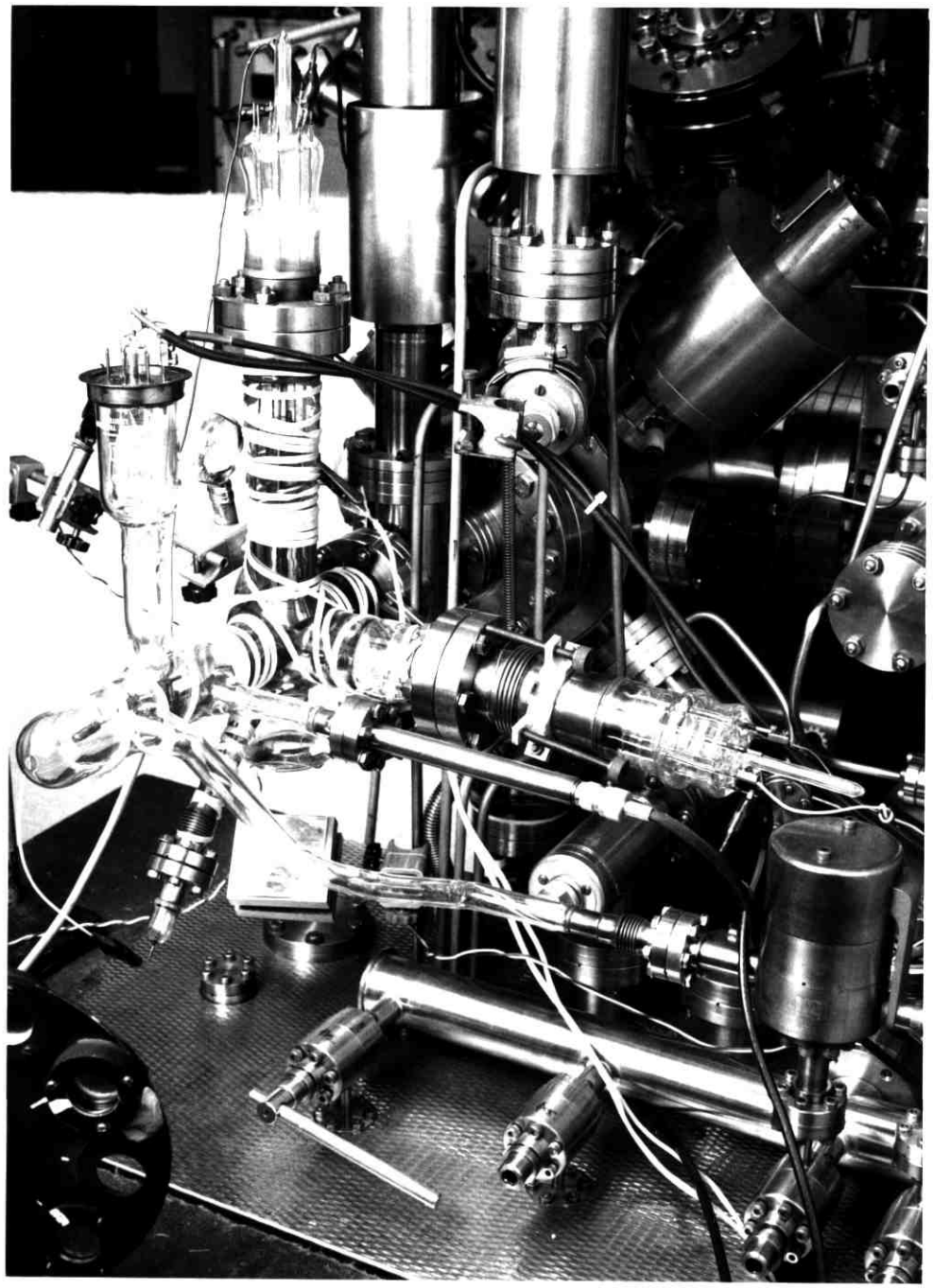
4.3 Photocathode Processing

4.3.1 S1 Photocathode processing

4.3.1a) S1 Processing equipment

Initial trials showed that S1 cathode processing in the large metal preparation chamber of the UHV system posed many problems. In particular the relatively high pressure oxygen discharge extended throughout the chamber, bombarding everything with oxygen ions and causing a permanant oxygen background pressure in the system, sufficient to cause the rapid decay of any photocathodes successfully produced. The same trials also indicated that some form of substrate heating was necessary at the caesiation stage, which in turn meant having to have the chamber walls hot to prevent the majority of caesium vapour from condensing on them in preference to the photocathode. All of these considerations combined to make the construction of a special S1 processing chamber essential.

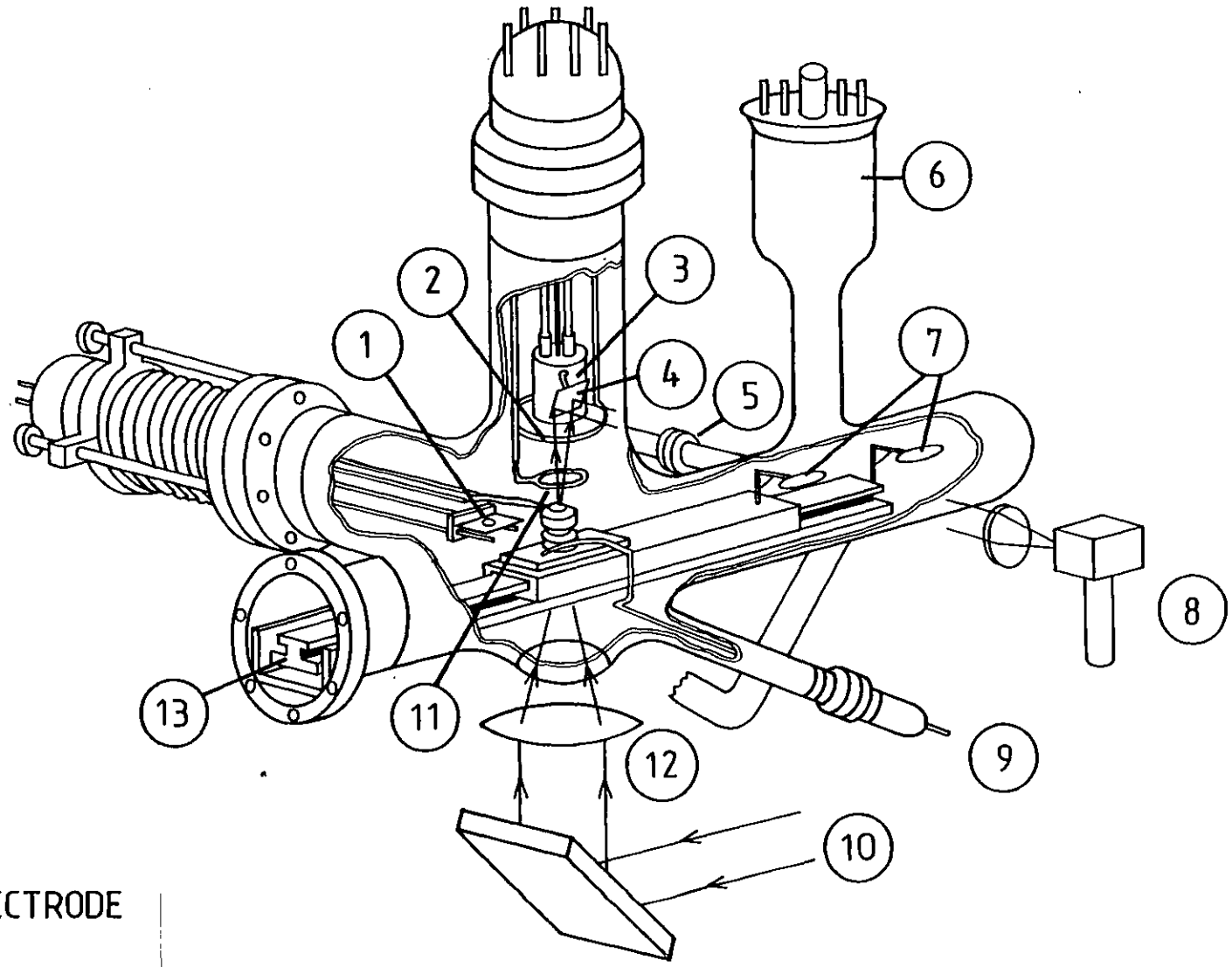
This chamber was made from pyrex glass and could be heated to $\sim$ 150 C by means of a nichrome wire heating element insulated with a flexible fibreglass sheathing and coiled over the chamber surface. The photocathode substrates entered the chamber, via a pneumatically operated gate valve, on a telescoping rail. The rail was activated by two spring loaded soft iron slugs which could be dragged over to the glass chamber walls with an external magnet and then dragged along the walls to slide the transport mechanism, springing back into place afterwards to allow the upper rail to pass



Photograph of the S1
Photocathode Processing
Chamber

SI PROCESSING CHAMBER

1. QUARTZ CRYSTAL
2. CAESIUM CHANNELS
3. EVAPORATOR SHIELD
4. MIRROR
5. PIRANI GUAGE
6. ION GUAGE
7. MAGNETIC SLUGS
8. SILICON PHOTOCELL
9. ELECTRICAL CONTACT TO PHOTOCATHODE
10. LIGHT
11. COLLECTOR/DISCHARGE ELECTRODE
12. LENS
13. TELESCOPING TRANSPORT RAIL



through the gate valve (Figure 4.7). The cathode substrates sat on a glass post screwed to the upper rail, permitting transmission photosensitivity to be monitored during processing, the electrical contact to the cathode being made with a springy contact on a bellows glass-to-metal seal.

Mounted above the cathode substrate on a 7-way glass pinch on a FC38 UHV glass-to-metal sealed flange there was a shielded silver evaporator, twin caesium chromate channels, a silver ring electrode which fulfilled the dual functions of glow discharge electrode and photocurrent collector, and a small mirror which deflected the light passing up through the cathode out through a clear section of the glass walls of the chamber into a silicon photocell detector for optical transmission measurements. By insulating the shaft of the silver discharge ring electrode with glass tubing, and by using a fully floating exciter supply (Figure 4.8) it was possible to confine the glow discharge to the region betwen the cathode and the discharge electrode, and thereby ensure an even oxidation of the cathode even with a d.c. exciting field (see Section 3.3.1(b)) whilst simultaneously minimising the oxygen bombardment and absorption of other parts of the apparatus.

Fixed to the side of the chamber, on a 6-way pinch on a FC38 bellows mounted glass-to-metal flange, there was a chromel-alumel thermocouple , and a 6 MHz quartz crystal housed in a specially constructed UHV-compatible mount. By means of two adjustment screws on the bellows flange the thermocouple could be brought into contact with the top surface of the photocathode to measure its temperature. The quartz crystal oscillator (QCO) was used to measure the silver deposition rate by noting the changing resonant frequency of the crystal as silver was deposited on its centre through a 5.5 mm diameter hole in the shield. The crystal was calibrated on the basis of the formulae to be found in Holland (1965).

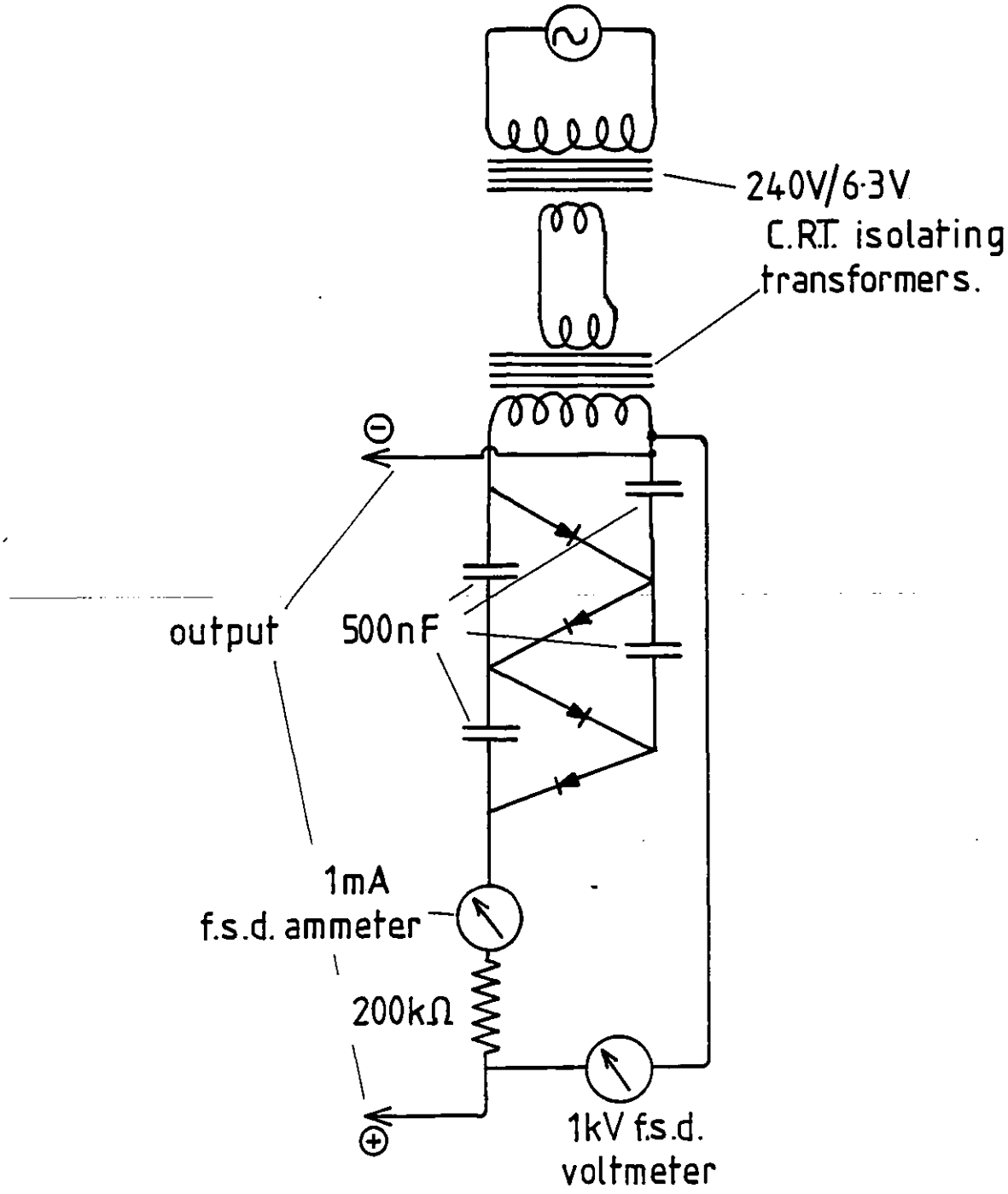


Fig.4·8.

Circuit Diagram of the Floating HT Power Supply used to Excite the Oxygen Gas Discharge.

The processing chamber was connected via a precision leak valve to the gas handling line and could, if necessary, be pumped through this connection independently of the other two chambers. After a normal system bakeout and with the caesium channels the evaporators and the ion gauge properly outgassed the chamber would reach a background pressure of $< 10^{-9}$ mbar.

4.3.1b) S1 Processing technique

The cathodes were prepared on a fused silica base (Spectrosil B), which was ground into a chamfered disc and retained on the hollow sample stub with a stainless steel ring as depicted in Figure 4.8. The silica discs were first cleaned by boiling for 15 minutes in a solution of 1 part saturated NaOH solution to 20 parts distilled water, followed by 15 minutes boiling in 5% HNO_3 solution. The discs were then placed on the sample stubs, the stainless steel retaining ring was spot-welded into place, and a broad stripe of conductive silver paint (Demetron type 620 000 02) was painted around the chamfered portion of the substrate to ensure a good electrical contact between the cathode film and the substrate holder. The stub assembly was then air-baked at 220 C to cure the paint, and this was followed by a vapour bath in iso-propyl alcohol just prior to insertion in the UHV system.

After the UHV system was baked and degassed a cathode substrate would be bombarded in the preparation chamber with a 6kV beam of argon ions at a current density of ~ 50 μA cm^{-2} for 10 minutes. The substrate cleanliness was then generally checked with XPS and AES and if there was no detectable carbon signal with either of these techniques it was transferred back to the analysis chamber for processing according to the following standard schedule (Figure 4.10).

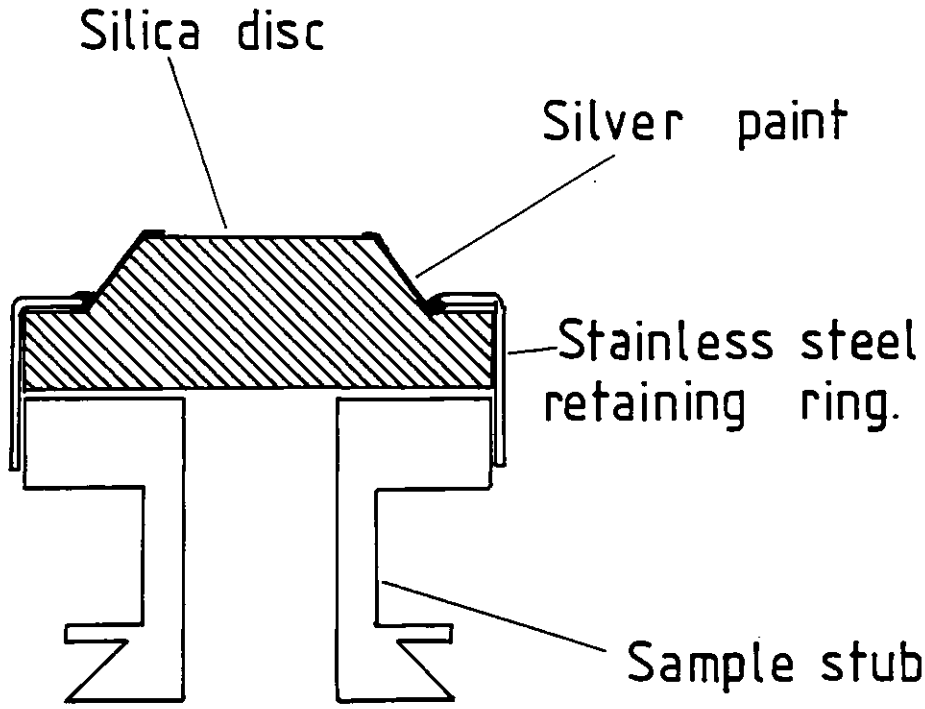


Fig. 4·9.

S1-Sample Stub Mounting Arrangement.

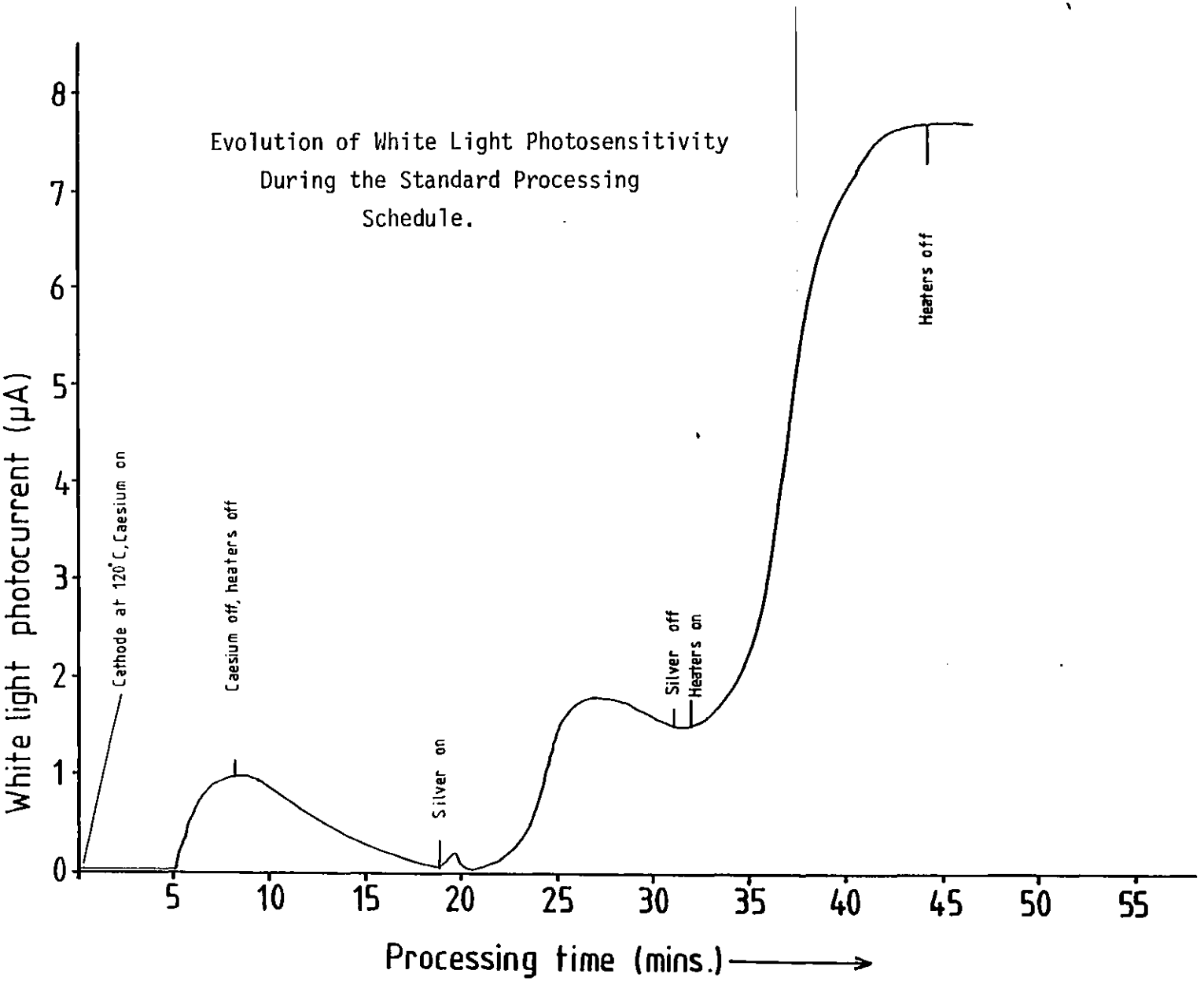

Evolution of White Light Photosensitivity
During the Standard Processing
Schedule.
White light photocurrent (μA)
Processing time (mins.)
Cathode at 120°C, Caesium on
Caesium off, heaters off
Silver on
Silver off
Heaters on
Heaters off
0
1
2
3
4
5
6
7
8
5
10
15
20
25
30
35
40
45
50
55

Fig. 4·10

a) Initial silver evaporation

Silver was evaporated at such a uniform rate that the white light optical transmission of the substrate fell by 50% in a period of ∿ 3 minutes, at which point deposition was stopped. At this point the QCO indicated that about 5.9 $\mu g/cm^2$ of silver had been deposited on the substrate.

b) Oxidation

The silver film was oxidised in a d.c. glow discharge struck in 0.1mbar of "specpure" oxygen. Oxidation would typically take ∿ 10 seconds, and was terminated when the white light transmission of the film reached a plateau of ∿ 95%. The oxygen was then pumped away and the processing chamber heating coil was switched on at such a power that the chamber attained a surface temperature of ∿ 150 C and the internal thermocouple indicated a cathode surface temperature of ∿ 115 C.

c) Caesiation

When the processing chamber pressure dropped below $5x10^{-8}$ mbar (typically one hour later) the current through one of the caesium channels was turned up gradually to a level at which previous experience had shown caesium vapour was being gently evolved (∿5.5 A in the case of the I.T.L. nickel channels used here). The thermionic current from the cathode would rise sharply to a value of several microamps, followed by the slow evolution of white light photosensivity. When the photocurrent reached an empirically determined value (corresponding to a cathode sensitivity of ∿5-10$\mu A\ Lm^{-1}$),

the current through the caesium channel was turned down to a quiescent level (3A) at which the channel was kept outgassed but did not evolve caesium, and the chamber heaters were switched off. At this point the white light photosensitivity would drop to a very low level.

d) Second Silver evaporation

When the thermocouple indicated that the cathode had cooled to close to room temperature, the silver evaporator current was turned up to a value which was known to result in the evaporation of silver at about one tenth of the rate used in the initial silver evaporation. Silver was deposited at this slow rate for about twenty minutes, during which time the photosensitivity quickly rose to a small peak and then fell (due to a small burst of caesium given off as the evaporator shields warmed up) before rising to a steady peak, falling slightly just before the silver was turned off at the point when the QCO indicated that the same amount of silver had been deposited as in the first evaporation.

e) Final Bake

The processing chamber heaters were turned up to the same temperature as was used for the caesiation. The cathode sensitivity slowly rose by a factor of three to four to a stable plateau, at which point the heaters were turned off and the cathode was allowed to cool to room temperature.

4.3.2 NEA Ga As Photocathode processing

4.3.2a) NEA Ga As photocathode processing equipment

In view of the ultra-high vacuum required it was decided to conduct the processing of the Ga As substrates in the analysis chamber. To avoid excessive caesium contaminating the various pieces

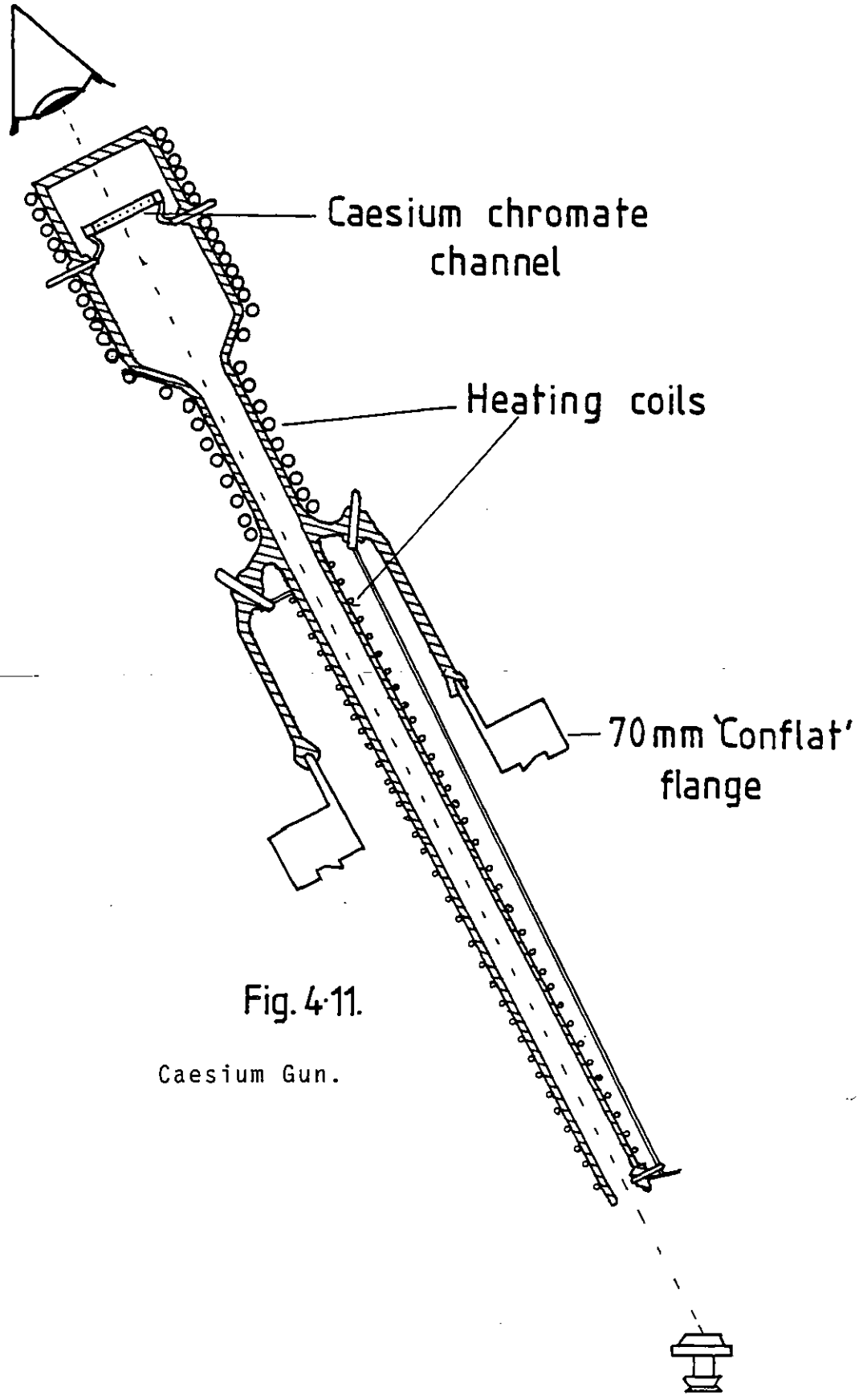


Fig. 4·11.

Caesium Gun.

of equipment present in this chamber and causing electrical discharge problems, a special "caesium gun" was developed and fabricated (Figure 4.11). This gun produced a controllable collimated beam of caesium atoms just broad enough to cover the photocathode substrate and it featured a flat window through which the sample could be sighted and lined up on the precision manipulator to ensure an even caesium coating over the entire cathode surface.

High purity oxygen could be admitted into the analysis chamber via a precision leak valve, which was calibrated against the analysis chamber ion gauge so that while processing cathodes, oxygen exposures could be made with the ion gauge switched off, ensuring that the cathode was only exposed to neutral oxygen atoms.

4.3.2b) NEA Ga As Photocathode processing technique

The substrates used consisted of 20 mm diameter discs of Corning 7056 glass onto which a single crystal strain matching layer of Ga_{1-x} Al_x As had been bonded, with the epitaxially grown highly Zn doped ($\sim 10^{18} cm^{-3}$) active Ga As layer on top. The emitting surface was (100).

The substrates were successively degreased in trichloroethylene, methanol and finally iso-propyl alcohol vapour baths. Just prior to attaching the substrates to the stainless steel sample stubs (Figure 4.12) and inserting them into the UHV system, approximately 0.3μm of the Ga As active layer on the surface of the substrate was removed by a 10 second etch in a room temperature mixture of 5 parts conc. H_2SO_4:1part H_2O_2(100 vol):1 part distilled water. The etch was terminated by washing the substrates in copious volumes of distilled water and blowing them dry.

After baking and degassing the UHV system the substrates, (following the work of Garbe and Frank, 1969) were subjected to a light 200eV argon ion bombardment at a current density of $\sim 0.5 \mu A\ cm^{-2}$

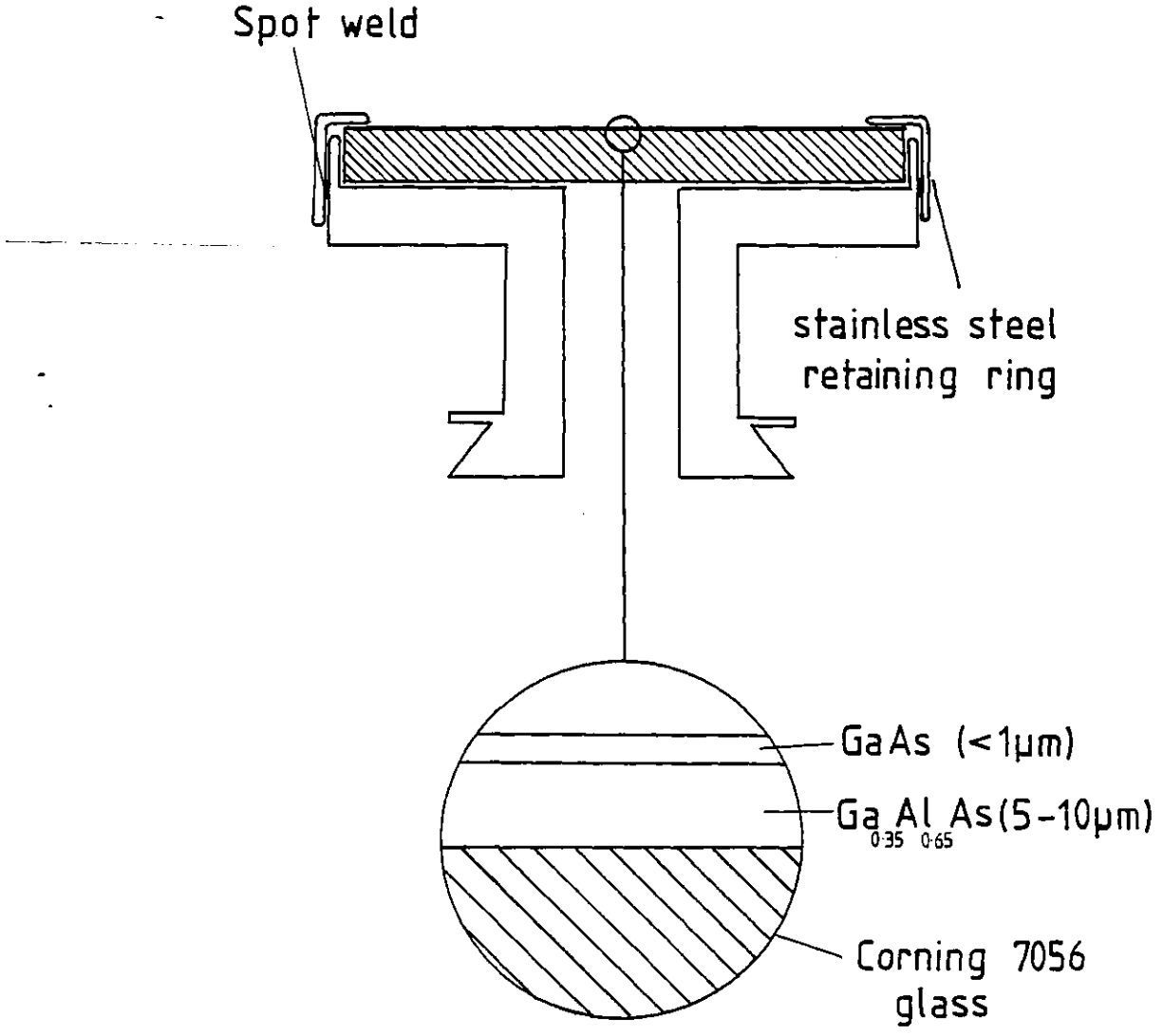


Fig. 4·12.

GaAs-Sample Stub Mounting Arrangement.

for ∿ 1 hour, and then annealed at a temperature of ∿400 C for 1 hour to remove as much as possible of the surface damage induced by the bombardment. Although it is recognised that this cleaning technique probably results in slightly inferior cathode photosensitivities (due to the higher electron-hole recombination velocities at the damaged Ga As surface), the normal method of heat cleaning the substrate by maintaining it at a temperature of 620 C ± 20 C for a few minutes involved prodigious experimental difficulties due to the poor thermal contact afforded by the transportable sample holders, (initial trials attempting to clean the substrates on the preparation chamber heating post met with no success).

The substrate was then transported to the analysis chamber and positioned under the caesium gun on the precision manipulator for activation. The cathodes were first caesiated to a peak in transmission photosensitivity and the caesium flux was continued until the photosensitivity dropped by ∿ 30% (see Figure 4.13) whereupon the caesium channel current was turned down to the quiescent level and a 10^{-9} mbar partial pressure of oxygen was leaked into the system. The white light photosensitivity would then peak and the oxygen leak was shut off when the photosensitivity dropped to 30% of this peak value. This caesium-oxygen cycle was repeated several times (typically 9) until the peak on caesiation was slightly less than the similar peak in the previous cycle. At this point the caesium gun heaters were turned off and the photosensitivity was finally re-optimised with a finely controlled oxygen exposure.

4.4 Recording XPS Spectra

At any stage in the processing of either type of photocathode the process could be interrupted and an XPS spectrum could be taken of the cathode. For this purpose the X-rays were generated by the electron bombardment of either magnesium or aluminium in a water-cooled

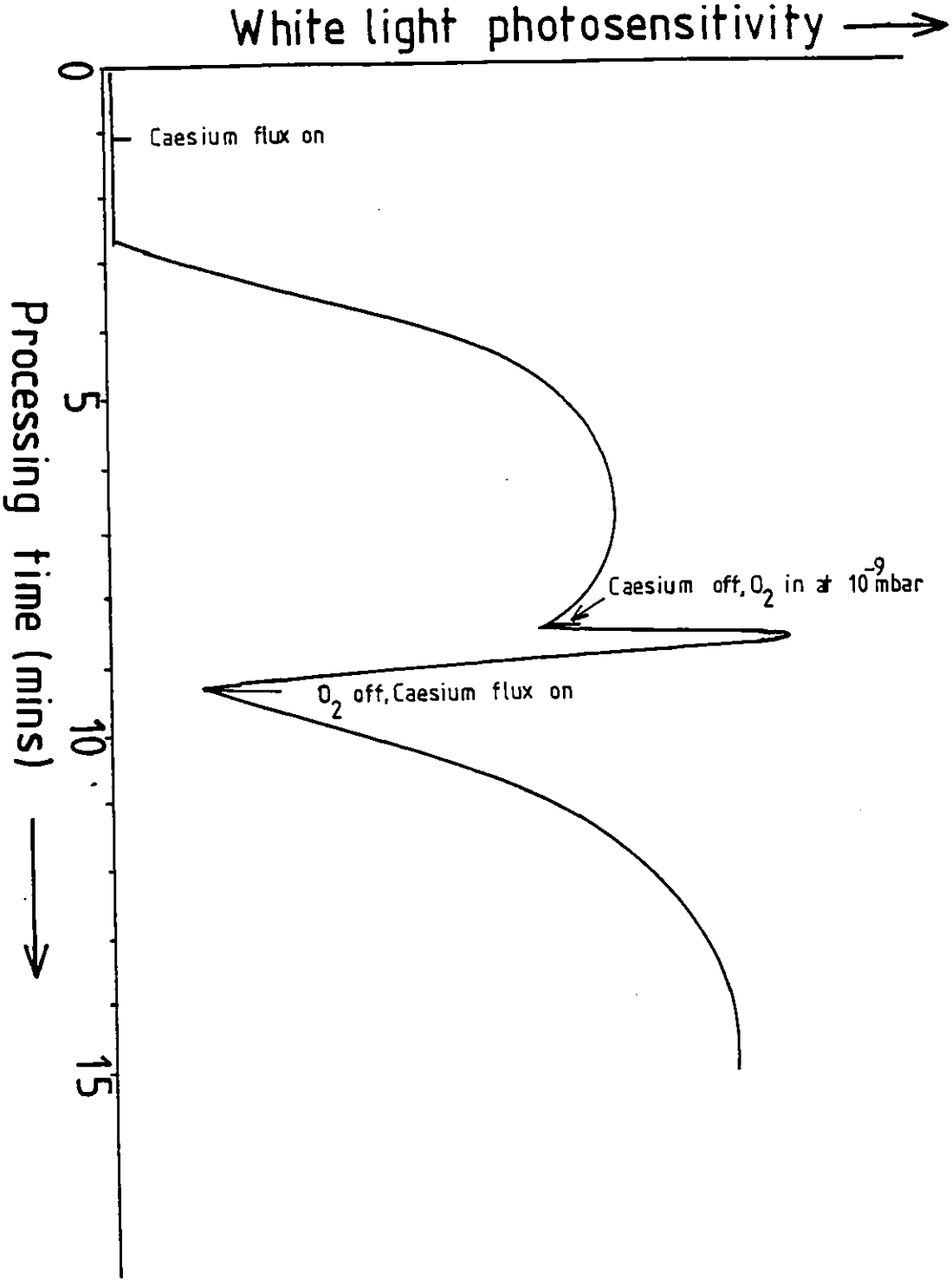


Fig. 4-13.

Evolution of Photosensitivity During one Cs-O cycle on the GaAs Photocathodes.

ion-pumped X-ray source (V.G. Scientific), and passed through a thin aluminium window which served both to reduce tbe Bremsstrahlung background in the otherwise unmonochromated Kα X-ray spectrum, and to isolate the anode and any gases it might produce under bombardment from the UHV of the analysis chamber.

In order to produce XPS spectra capable of yielding a quantitative chemical analysis of the photocathodes (see Chapter 5) it was important that all spectra were taken with the same X-ray intensity (i.e. the same electron bombardment energy and current), and at the same X-ray energy. In each case the X-ray energy was chosen to minimise the clashes betwen X-ray photoelectron and X-ray induced Auger electron peaks in the electron energy spectra. These considerations led to all the Si spectra being taken with Alkα radiation (15 kV, 5 mA bombardment) and all the Ga As traces being taken with Mgkα (10 kV 10mA bombardment).

The X-ray photoelectrons were energy analysed by the hemispherical electron energy analyser (see Section 5.3.3), the output of which was fed into the systems scanning electronics to emerge as a graph of counts per second against binding energy on an X-Y chart recorder. The electronics were capable of measuring peak positions to within 0.1 eV (after being calibrated against the Au 4f peaks in a test sample), and repeated traces of a chemically stable sample suggested an XPS peak intensity reproducibility of < 3%.

All the XPS spectra were taken with the analyser in the CAE mode with HV=20 eV, giving an analyser energy resolution of ∿0.5eV compared with the FWHM X-ray line widths of 0.68 eV (Mgkα) and 0.83 eV (Alkα) (Cardona and Ley, 1978). The variable aperture plate in the analyser was set so that electrons were collected from an approximately rectangular area of the sample 10mmx4mm. The substrate was angled so that X-ray photoelectrons leaving the sample in a small range of angles (a cone of ∿ 6°) around the surface normal were

collected by the analyser, and then it was moved around in three dimensions until the X-ray photoelectron signal detected by the analyser was maximised. For the XPS spectra at take-off angles of 30° and 60° to the sample normal the manipulator was adjusted so as to keep the position of the centre of the cathode surface unchanged whilst tilting the cathode.

For photosensitive cathodes the cathode sensitivity was found to degrade rapidly if the X-ray anode was used with bombardment powers in excess of 75 W @ 15kV. For this reason the spectra were taken as quickly as possible with the minimum photocathode X-ray exposure compatible with achieving an acceptable signal-to-noise ratio on the recorded spectra, and the cathode photosensitivities were checked between XPS runs to check that they were not varying by more than ± 10%.

During XPS measurements on photosensitive surfaces the analysis chamber windows were blacked out and the ion gauge was turned off to eliminate the possibility of excessive and variable sample charging due to photoemission from stray light.

4.5 Auger Analysis of Substrates

4.5.1 Description of the Auger Process

In the Auger decay process an ionised atom loses energy when a core vacancy is filled by an outer shell electron in a radiationless transition. The energy lost by the outer shell electron is transferred to a third electron which is ejected from the atom with a characteristic energy which is independent of the energy of the initial ionising source (Figure 4.14). To a first approximation the kinetic energy of this Auger electron, relative to the sample Fermi level is given by the expression

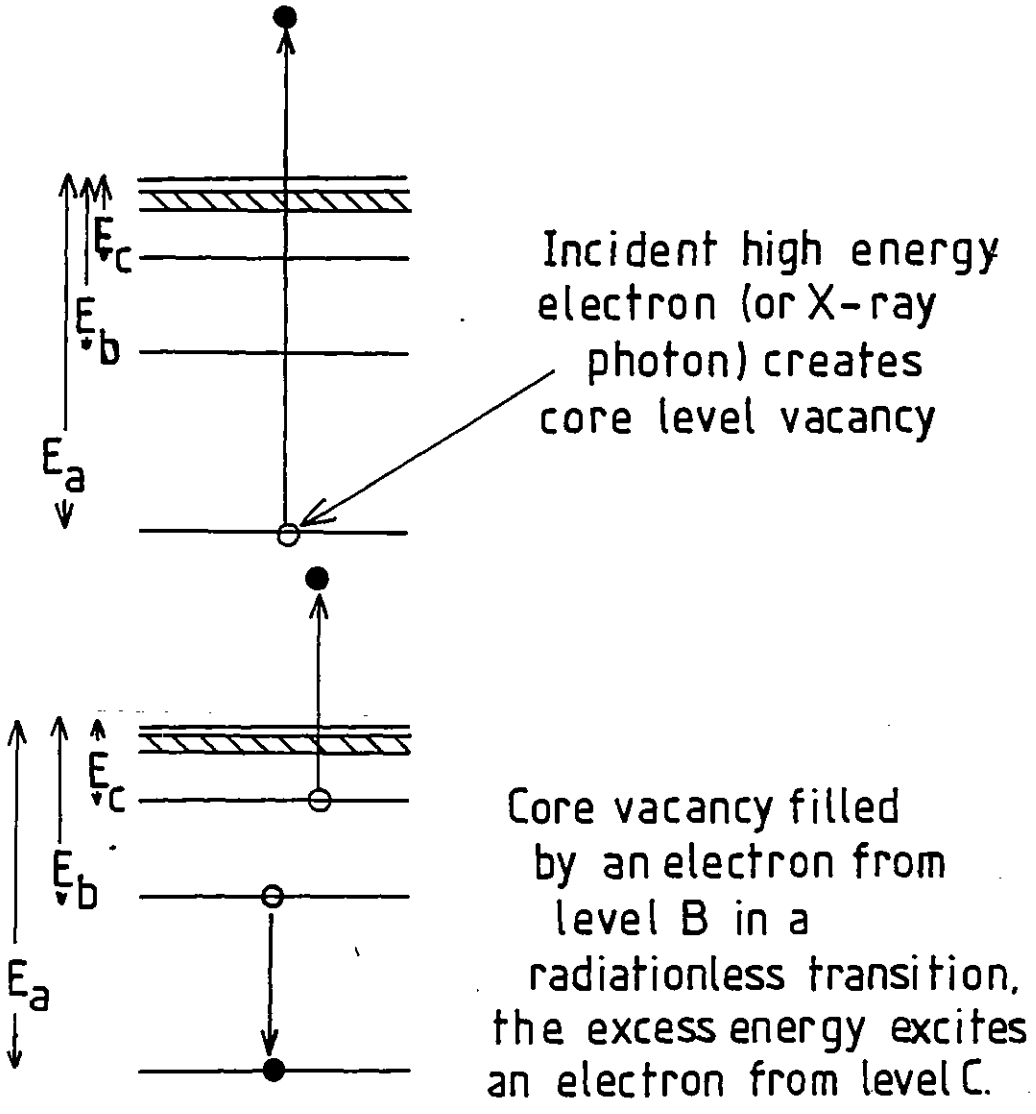


Fig. 4·14.

Diagram of the Auger Process.

$$E_K = E_A - E_B - E_C \qquad (4.1)$$

where the energies are the binding energies of the unperturbed atomic core level states relative to the Fermi level. More sophisticated formulae for the Auger energies attempt to take account of the fact that the binding energies actually involved are those of an ionised atom (Chang and Jenkins, 1970).

Because the Auger energy linewidth is the convolution of three lifetime-broadened linewidths the Auger electron peaks tend to be much broader than XPS peaks and the chemical state information is correspondingly poorer. The initial core vacancy can of course be generated by an X-ray photon, and Auger peaks are seen in XPS spectra, but it is more usual to produce the initial vacancy by bombardment with a beam of high energy electrons (2-5 keV), which can be finely focussed and result in a spatial resolution down to tens of nm.

Apart from the complexity and width of the peaks in Auger spectra, and the concomitant difficulty in interpreting them, the principal drawback is the uncertainty of the chemical effects of bombarding the sample with such a high energy electron beam (Madey and Yates 1971; and Menzel and Gomer, 1964).

The technique does not lend itself to quantitative surface analysis as well as XPS on account of the fact that a sufficiently general and accurate compilation of relative elemental Auger line intensities has not appeared in the literature to date, and that significant matrix dependent effects in the form of atomic backscattering of the primary electron beam as well as the uncertainty of the Auger electron inelastic mean free path would make such data difficult to use in practical cases.

4.5.2 Recording AES Spectra

To measure Auger spectra an unused substrate was placed on the precision manipulator and positioned at the co-ordinates which had been chosen by optimising the normal takeoff XPS signal (see Section 4.4), and the 3kV electron beam (produced in a V.G. Scientific LEG 61 electron gun) was steered to the centre of the substrate by using the mechanical steering mechanism and observing the electron beam induced fluorescence from the 4mm diameter beam spot on the glass substrate.

For routine AES spectra a beam current of 5 μA was used, and the spectra were recorded in the differential mode by applying a sinusoidal modulation of 5eV to the analyser and measuring the resultant modulation on the analyser channeltron detector signal with a lock-in amplifier. For these purposes the analyser was used in the CRR mode with a retard ratio of 4:1.

In spite of the large spot size and low beam currents used it was soon found that the electron beam rapidly degraded the photoresponse of an otherwise stable photocathode, inducing chemical changes in them which produced shifted peak positions and changed peak intensity ratios in the photocathode XPS spectra. As a result of this problem, AES was used principally as a means of determining substrate cleanliness, a role in which its increased sensitivity to carbon contamination made it a superior analytical technique to XPS.

4.6 Recording Photoelectron Energy Distribution Curves (EDC's)

For the recording of EDC's the cathodes were placed on the precision manipulator in the XPS normal take-off optimised position (as in 4.4) which corresponded to the cathode being on the axis of the analyser transfer lens. The electron energy analyser was

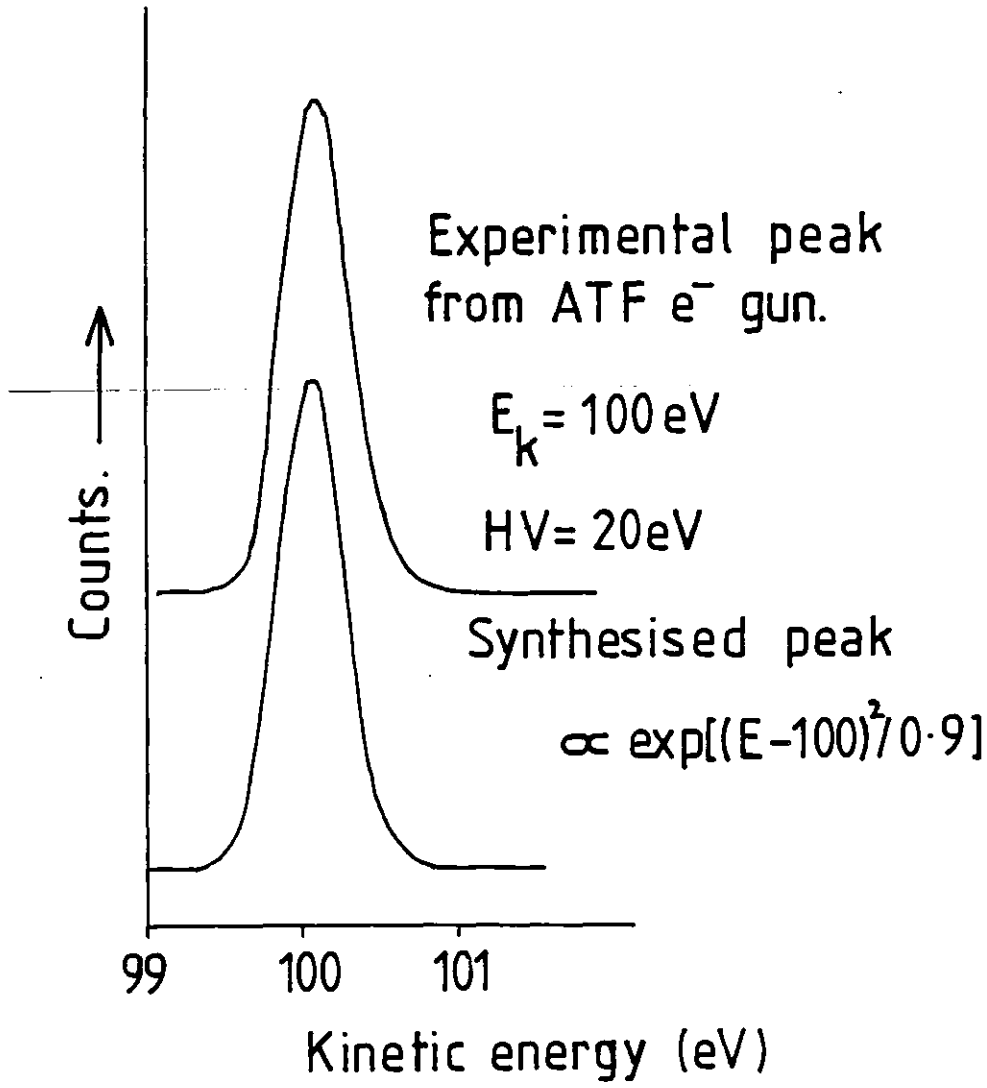


Fig. 4·15.

Comparison of Experimental and Computer Synthesized Instrumental Response Functions.

operated in the low energy CAE mode (originally designed for use in UPS analysis), and HV was set to 2eV since it was found that lower pass energies than this resulted in secondary electron production within the analyser due to the presence of stray magnetic fields.

The very low initial photoelectron energies of $\sim$ 0.5eV necessitated biassing the cathode at -9eV relative to earthwith a dry cell battery in order to increase the photoelectron kinetic energies to a point where they could be measured by the analyser.

The photocathodes were illuminated with a He/Ne laser, a 1.06 μm Nd:Yag laser,a 1.3 μm diode laser or the same filtered tungsten lamp as was used for the spectral photosensitivity measurements (see 4.2) heavily attenuated (by $\sim 10^3$) to avoid overloading the sensitive energy analysing equipment. All EDC traces had to be taken in a blacked-out labroatory with all sources of light in the UHV system (ion gauges etc.) turned off. The contribution of the background illumination to the measured EDC's was assessed by blanking off the interference filter with a metal disc, and re-running the energy scan with all other experimental parameters unchanged.

Under the experimental conditions described above, the analyser had an instrument response function (in the kinetic energy domain), which could be represented by a Gaussian function with a standard deviation σ = 21 meV. This latter conclusion was reached by comparing a computer synthesised Gaussian peak with the experimental peak shape of one of the electron peaks obtained with the miniature electron gun used for the ATF measurements (Section 5.3.3a), working at a kinetic energy of 100 eV. The actual linewidth of the electrons produced by the ATF gun was $\sim$ 75 meV i.e. $\sim$ kT where the temperature Tc of the thermionic cathode in the electron gun was $\sim$ 600 K (the HT supply used to bias the gun electrodes had a negligible output ripple figure of $<$ 1mV). At the time the analyser was being used with

HV=20eV and the 500 meV FWHM figure for the experimental peak in Figure 4.15 therefore results almost entirely from instrumental broadening and agrees well with the 460meV FWHM figure predicted by Equation 5.8. As can be seen from Figure 4.15 the experimental peakshape is described well by the synthesised Gaussian curve. On the basis of electrostatic scaling theory (e.g. Moss, 1968), using the same instrumental response function but with the energy scale attenuated by a factor of ten should accurately describe the response function of the analyser when it is used with HV=2eV to measure electrons with kinetic energies ∿10eV.

The filtered tungsten lamp exciting radiation had an energy width of ∿ 30 meV FWHM and this, coupled with the 50 meV analyser energy resolution meant that some of the features on the observed EDC's were close to the energy resolution limit of the system.

To assist in the interpretation of these curves they were therefore compared with curves synthesised by computer, in which the instrument response function was represented by the Gaussian function with δ = 21 meV described above. On the basis of this analysis the true widths of the EDC's were estimated at various stages in the cathode processing schedule, and values of the photoelectric work function were derived from them.

CHAPTER 5

QUANTITATIVE SURFACE ANALYSIS FROM XPS SPECTRA

5.1 Introduction

The past two decades have seen the rapid development of a number of techniques for the analysis of the chemical and physical composition of solid surfaces, each capable of supplying information on different aspects of the surface in a more or less quantitative manner (Roy and Carette, 1977 and Sevier, 1972). Since the pioneering work of Siegbahn (1967) the technique of X-ray photoelectron spectroscopy (XPS) has been developed into one of the more widespread of these methods for surface compositional analysis, and its potential for quantitative surface analysis of the top few monolayers of a solid is gradually being realised.

Auger electron spectroscopy (AES) has long been a qualitative surface analysis technique and in view of the similarities in the instrumentation required for the two spectroscopies they are frequently used simultaneously in surface compositional studies. Preliminary trials with S1 photocathode films however had shown that even light exposure of the cathode film to the electron beam used in AES resulted in rapid chemical degradation and loss of photosensitivity. For this reason the use of AES in this study was confined to checking the initial photocathode substrates for cleanliness and interest was confined to XPS for quantitative analytical work.

In this chapter the principles of XPS are briefly described, followed by a description of the procedures available to the experimentalist for a detailed quantitative evaluation of the technique. The chapter concludes with experimental details of the quantification procedures

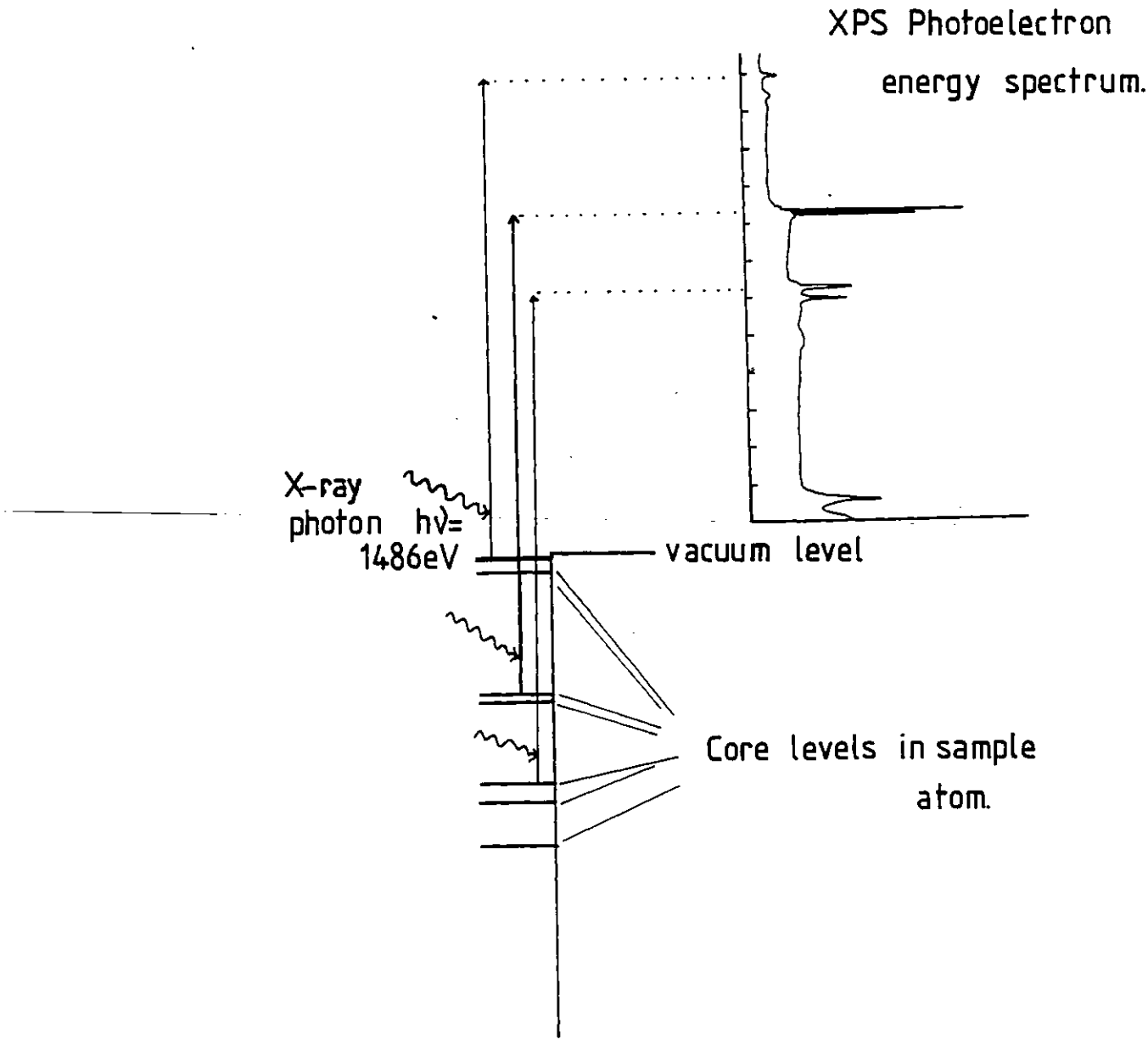


Fig. 5·1
Schematic Diagram of the XPS Process.

selected for use in this study, and the results and conclusions drawn from them.

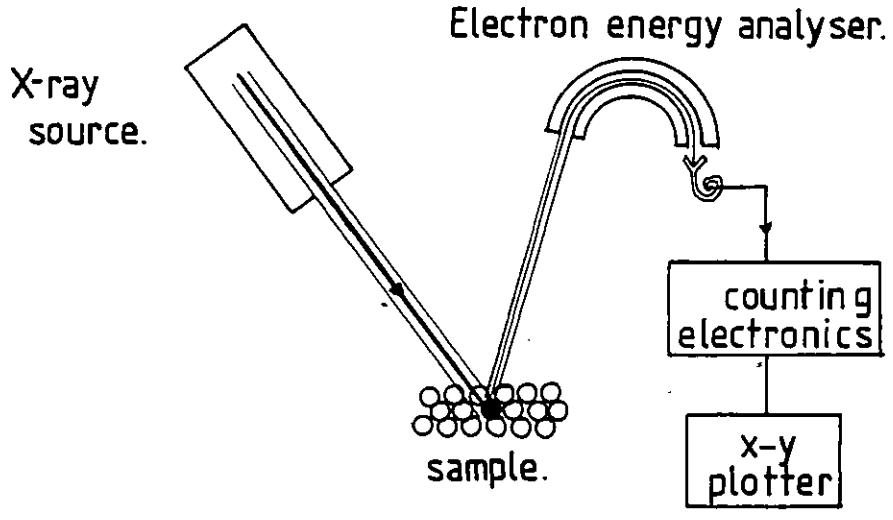
5.2 Description of the principles of X-ray Photoelectron Spectroscopy

In XPS a sample is irradiated with a source of soft X-rays with a known and preferably well-defined energy. Typically these are generated in aluminium (Al has an intense $k\alpha$ line $h\nu$ = 1486.6eV, ΔE = 0.83 eV) or magnesium (Mg$k\alpha$ $h\nu$ = 1253.6 eV, ΔE = 0.68 eV) anodesunder electron bombardment.

The incident X-ray photons can directly excite core electrons in the sampleinto states with sufficient energy to leave the solid (Figure 5.1). Analysis of the energy spectrum of the emitted photoelectrons yields information about the density and energies of the occupied electron states within the solid. The energies of the observed peaks in the photoelectron spectra can be interpreted in terms of the binding energies of the core electron states of the elements present in the sample, and small perturbations in these binding energies can be related directly to changes in the chemical environment of these elemental species.

Although the X-rays have a penetration depth of 100-1000 nm (Fadley, 1974), the inelastic mean free path of the emerging photo-electrons, although dependent on their energy, is typically several nanometers (Seah and Dench, 1979), and so the measured XPS spectra are representative of the sample composition up to this depth.

Detailed analysis of the relative photoelectron peak intensities coupled with a detailed knowledge of the characteristics of both the photoelectron energy analysing equipment and the electron scattering characteristics can thus yield information on the atomic percentages of the elements present in the first few monolayers of the sample. The technique can detect elements down to concentrations of $\sim$ 0.1



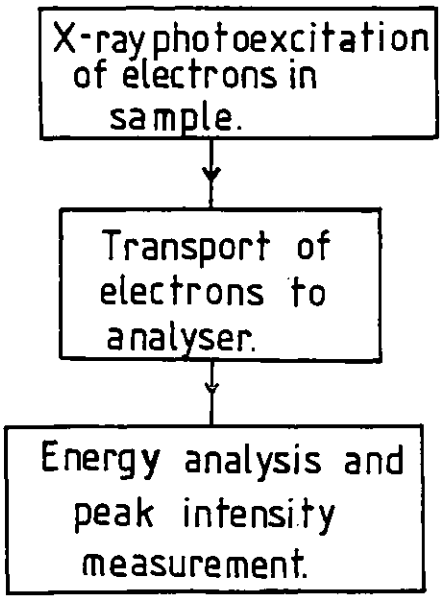


Fig.5·2
Schematic of the Chain of Events Leading to the Quantitative Chemical Analysis of a Surface by XPS.

atomic % and, if monochromated X-rays are used, elemental binding energy shifts can be measured with an accuracy of better than 0.1eV.

The principal drawback of XPS is the poor spatial resolution attainable. Signal-to-noise considerations and the difficulty in focussing X-ray beams dictate that XPS signals have to be averaged over a large sample area in order to obatin a sufficiently intense X-ray photoelectron spectrum.

5.3 Description of the factors affecting measured peak intensities in XPS

For the purposes of understanding quantitatively the factors affecting the relative intensities of the peaks observed in an XPS electron energy spectrum, the process can be conveniently described in terms of a simple chain of events, each with its own well defined but seldomly accurately calculable effect on the XPS peak intensity (Figure 5.2).

5.3.1 Excitation of electrons within the sample

In a typical XPS arrangement the sample will be illuminated with X-rays at an angle to the sample surface (Figure 5.3) and, since the X-ray source is normally close to the sample to achieve a high illumination level it is clear that there will be a degree of non-uniformity of the X-ray illumination intensity across the sample. This will not generally affect the measured XPS intensity ratios as long as the sample is homogeneous in composition across its surface.

As the X-rays penetrate into the sample they will be absorbed in a distance of $\sim$100-1000 nm (Fadley, 1974) and excite electrons from the various core levels present. Estimates of the subshell photoionisation cross sections (SPC's) for a number of different

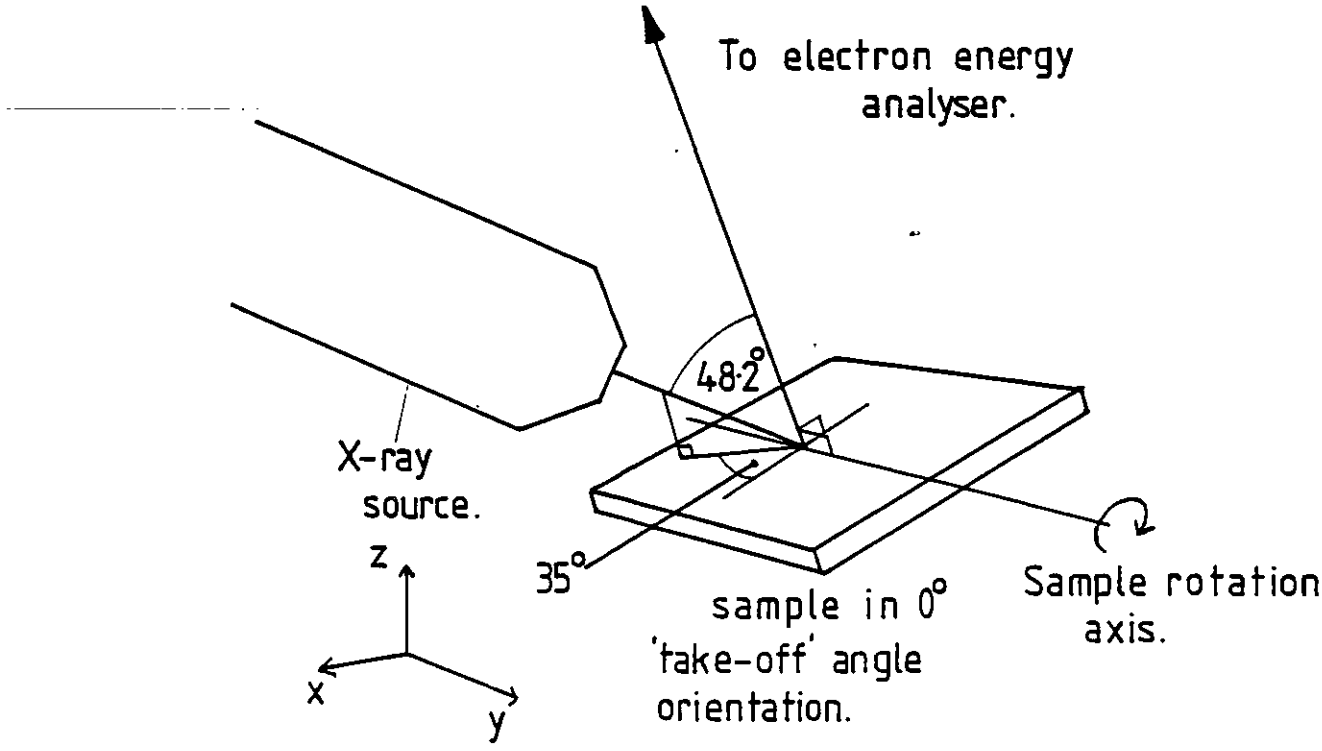


Fig. 5·3

XPS Geometry in the VG ESCAlab.

elements are available in the literature, some based on experimental studies, others based on theoretical calculations. Scofield (1976) presents a comprehensive list of SPC's calculated for the Mg kα and Al kα photon energies using a relatavistic Hartree-Slater self-consistent single potential atomic model. He mentions that the most significant inaccuracy in the calculations results from the approximations involved in calculating the electron-electron interactions in the atoms, and Evans et al. (1978) point out that these inaccuracies might be expected to become most important for photo-excitation near threshold.

Another limitation in using calculated SPC's is that within the "sudden approximation" employed to make such calculations tractable, the calculated SPC relates to the sum of all the primary electron ejection processes induced by the incident photon. Not all such electrons emerge with energies characteristic of single electron core excitation processes however. Some are involved in intrinsic multielectron loss processes during photoexcitation ("shake up" or "shake off" processes), in which they lose energy to one or more other electrons, and consequently would not be counted in a photoelectron peak intensity measurement.

At present the fraction of photoelectrons involved in such intrinsic losses is incalculable and experimentally it is difficult to separate these effects from those of extrinsic losses suffered by the photoelectrons during transport through the sample (Šunjic et al., 1974). There is nonetheless both theoretical and experimental evidence to suggest that these intrinsic losses are both small (<20%) and largely matrix independent (Krause, 1971 and Brillson and Caesar, 1976), with the exception of transition metals where multielectron loss processes can account for large and matrix dependent fractions of the photoexcitation intensity of between 50 and 70 percent (Wagner, 1977).

Experimental SPC's have been derived by a number of authors (e.g. Evans et al., 1978; Brillson and Caesar, 1976) by measuring XPS peak intensities in a number of stoichiometric compounds. The SPC's were calculated by making assumptions about the photoelectron IMFP, the energy transmission function of the analyser and the sample surface composition. The experimental results are characterised by large random errors, and it is only by careful statistical analysis (as performed by for example Seah, 1980 and Evans et al., 1978) that their worth can be established.

A further complication arises when the angular distribution of photoelectron emission by a particular atomic species is considered. Reilmann et al. (1976) pointed out that the photoelectrons are not emitted uniformly but follow an angular distribution given by

$$\frac{d\sigma_{nl}}{d\Omega} = \frac{\sigma_{nl}(\varepsilon)}{4\pi}\left[1 - \frac{\beta_{nl}(3\cos^2\theta - 1)}{4}\right] \qquad (5.1)$$

where ε is the photoelectron energy, σ_{nl} the SPC for the n,l electron, θ the angle between the X-ray photon direction and the photoelectron ejection direction and β_{nl} is a particular level-dependent parameter which Reilmann et al. calculated and tabulated for a range of elements using Hartree-Slater wavefunctions for the atoms. The form of Equation 5.1 is dependent only on the energy of the photoelectrons being low enough for the dipole transition approximation to hold good. At photoelectron energies of 1keV and below Reilmann et. al estimate that ignoring the quadrupole and higher terms introduces an error of $< 0.4\%$. The value of β_{nl} calculated however depends on the wavefunctions used, and the calculated values are generally accurate for photoemission well above threshold and for atomic-like core levels.

An inspection of Equation 5.1 reveals a "magic angle" of $54^{\circ}44'$ at which the value of β_{nl} is unimportant and the angular asymmetry parameter can effectively be ignored. Unfortunately the angle between the X-ray source and the electron spectrometer in commercial XPS instruments is usually determined by other geometrical considerations, and rarely coincides with this value.

5.3.2 Transport of electrons from the emitting atoms to the energy analyser

As the photoelectrons travel through the sample they will be scattered both elastically and inelastically by the core and valence electrons present. The effects of elastic scattering on the measured XPS spectrum are generally considered negligible (Fadley, 1974) as they are assumed only to average out the electron angular distributions which themselves have only a small effect on measured spectra for the majority of experimental geometries. A few instances of photoelectron diffraction ("channelling") in ordered crystalline substrates have been reported (Fadley et al. 1979) which themselves contain information on aspects of surface structure.

The effect of inelastic scattering is to move the energy of a photoelectron out of the range of the initial peak in the XPS spectrum into a broad background, consequently knowledge of the electron IMFP is crucial to both determining the significance of relative peak intensities in the XPS spectrum, and the effective sampling depth of the technique. Electron IMFP's are a strong function of electron kinetic energy, and are likely to show some matrix dependence.

Penn (1976) presented the results of a theoretical approach which predicted that the energy dependence of the electron IMFP's, λ, would take the form

$$\lambda(E) = \frac{E}{a(\ln(E)+b)} \qquad (5.2)$$

where the coefficients a and b depended on the valence electron concentration of the matrix and on the core level distributions of the matrix atoms. The calculations are based on a nearly free electron approximation for the valence electrons in the matrix, and Penn uses the expression to calculate electron IMFP's for the majority of elements from Z=3 to Z=83, claiming an accuracy of ∿5% in his estimate of λ for which this assumption holds good rising to ∿40% for non nearly free electron elements.

An empirically based formula for electron IMFP's was derived by Seah and Dench (1979). Based on a statistical analyis of 350 experimental IMFP's in the literature they presented evidence to suggest that the IMFP's showed a $\lambda \propto a^{3/2}$ matrix dependence (where a is the monolayer thickness) as well as an electron energy dependence, and that the best statistics were obtained when λ was expressed in monolayers for elemental materials, and when the results for elements and compounds were treated separately. As a result of their analysis they proposed the semi-universal expressions

$$\lambda_m(E) = \frac{538}{E^2} + 0.41(aE)^{\frac{1}{2}} \qquad (5.3)$$

for elements (where λ_m is the IMFP in monolayers and a is the monolayer thickness in nm) and

$$\lambda_m(E) = \frac{2170}{E^2} + 0.72(aE)^{\frac{1}{2}} \qquad (5.4)$$

for inorganic compounds.

An independent test of the relative merits of these two approaches to determining electron IMFP's resulted from the work of Hall and Morabito (1979), on matrix dependence of experimental Auger peak intensities. They obtained slightly tighter distributions for their "renormalised matrix correction factors" if they used the Seah and Dench IMFP's than if they used the work of Penn.

The effect of electron IMFP's on XPS peak intensities was explored by Fadley (1974) who used a simplified model with an atomically smooth surface and an X-ray penetration depth much greater than the electron IMFP to derive the following expressions for the XPS peak intensity attenuation for a thin layer of one material on top of another

$$N'_{t'}(\theta) = N'_{o}\left[1-\exp\left(\frac{-t'}{\lambda'(E')\cos\theta}\right)\right] \qquad (5.5)$$

$$N_{\infty,t'}(\theta) = N_{o}\exp\left[\frac{-t'}{\lambda'(E)\cos\theta}\right] \qquad (5.6)$$

Where the symbols have the following meanings

t' = the overlayer thickness

$\lambda'(E)$ = electron IMFP in the overlayer, as a function of electron kinetic energy

N_o = the intensity of the XPS peak which would result from a smooth infinitely thick piece of the sample

$N'_{t'}(\theta)$ = the peak intensity corresponding to the overlayer material, when the overlayer is t' thick, as a function of take-off angle

$N_{\infty,t'}(\theta)$ = the peak intensity corresponding to the base material, when it is covered by a layer t' thick in which the electron IMFP is $\lambda'(E)$.

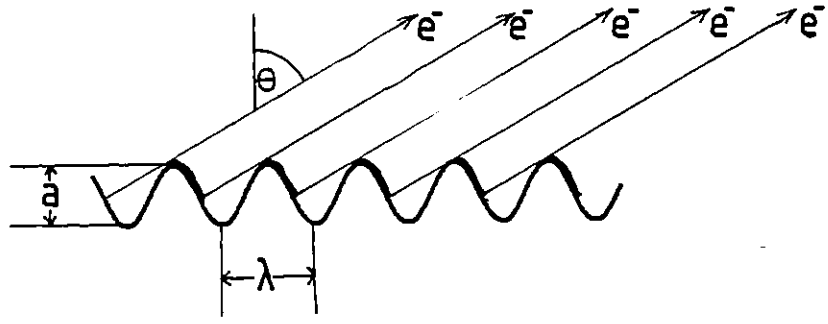


Fig.5·4

Photoelectron Shadowing Effects on a Rough Surface.

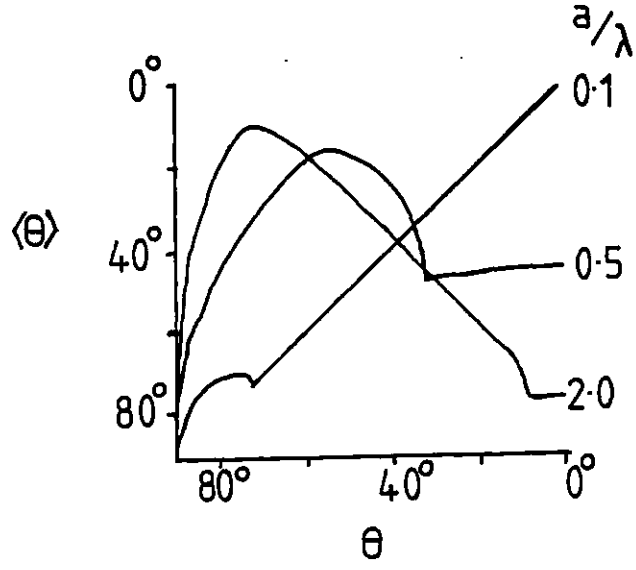


Fig. 5·5

Variation of ⟨θ⟩ with take-off angle θ for Sinusoidally Rough Surfaces.

Fadley also considers the problems introduced when the effect of sample surface roughness on the observed XPS peak intensities is taken into account. If surface roughness is extreme, then measuring spectra at very shallow take-off angles (Figure 5.4) can result in shadowing of portions of the surface. Even if θ is kept small enough to avoid this effect there is still the problem that the average angle of emission, $<\theta>$, from an unshadowed electron emitting rough surface will not in general be equal to θ (Figure 5.5). As Fadley points out, the average depth of emission at a take-off angle θ will vary as $\lambda < \cos\theta > \simeq \lambda \cos < \theta >$, and his calculations on some model surfaces showed that under certain conditions $< \theta >$ could actually increase as θ was decreased.

Although the effect of surface roughness is clearly impossible to calculate quantitatively under normal experimental conditions when the surface roughness characterisitics are largley unknown, Fadley does say that in general XPS spectra of rough surfaces accent the substrate compositionrelative to the surface at high θ values compared with an atomically smooth surface, and vice versa, and that all roughness effects are only likely to be important for cases when the scale of the vertical roughness is of the same order or greater than the horizontal roughness scale.

5.3.3 Energy Analysis of the emitted electrons

5.3.3a) Characteristics of the analyser: theory and direct measurement

Electron energy analysers have been extensively reviewed in the literature (Ballu, 1980; Seah, 1980, Roy and Carette, 1977), and only a brief description of their properties is presented here.

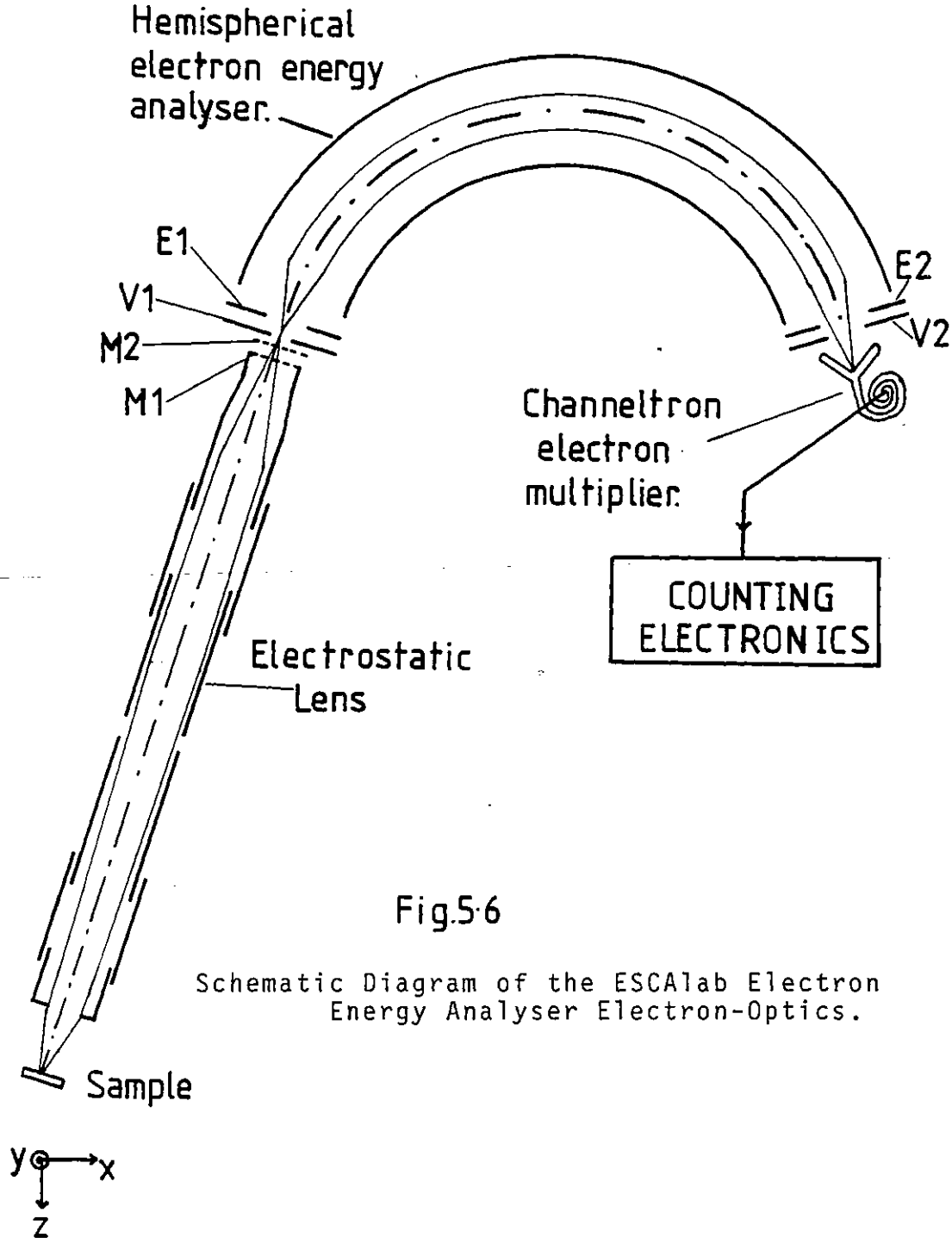


Fig.5·6

Schematic Diagram of the ESCAlab Electron Energy Analyser Electron-Optics.

At the electron energies encountered in XPS (and AES), electrostatically focussed energy analysers are generally used, as the effects of stray magnetic fields in wholly or partly magnetically focussed deflector systems at these relatively low electron energies of $\sim$ 100eV are difficult to eliminate.

For XPS the requirements of large analysed sample area, high signal-to-noise ratio and reasonable electron take-off angle resolution favour the choice of a hemispherical deflector energy analyser. Such analysers are usually used in conjunction with electron pre-retardation, as first suggested by Helmer and Weichert (1968), which can take place either in a pre-retarding lens or in a planar or spherical retarding mesh region, and which greatly enhances their sensitivity.

For these studies a V.G. Scientific ESCAlab, fitted with a 150° Hemispherical sector analyser, a planar mesh retarding region and a unity magnification electron optical transfer lens (Figure 5.6) was used to measure the XPS spectra from the photocathodes, with the aim of quantitative surface analysis.

With this system electrons excited in the sample are focussed by the transfer lens onto a planar earthed mesh (M1), and travel on into a planar retarding field (between M1 and M2), through a variable aperture (V1), through the fixed aperture (E1) and into the hemispherical sector analyser where they are deflected into a range of trajectories which pass through the exit aperture (E2) and pass from there through another variable aperture (V2) into a channeltron electron multiplier where they are counted by the counting electronics.

Energy scans can be taken in two modes using this sytem. In the constant analyser energy (CAE) mode, the voltages on the various electrodes are ramped so as to maintain a constant electron kinetic energy, E_o, for the central ray through the hemispherical analyser, while the retarding ratio (defined as the ratio of analysed

electron kinetic energies just before and just after the retarding region, E_k/E_o), is increased throughout the scan.

In the constant retarding ratio (CRR) mode, an energy scan is accomplished by ramping the voltages on the hemispheres so as to result in an E_o value which is a constant fraction of the analysed electron energy, so that the retarding ratio and the electron refraction effects in the mesh region are constant throughout the energy scan.

For both modes of operation the area of the sample from which electron flux is collected is determined almost exclusively by the shape and dimensions of the variable aperture V1, which lies close to the image plane of the transfer lens. As this lens terminates in an earthed mesh, and the potentials on the lens electrodes are ramped so as to be a constant fraction of the analysed kinetic energy, the "analysed electrons" (viz. those electrons emitted by the sample with the correct velocity and energy to reach the channeltron at a particular instant in the energy scan) will always be following the same trajectories through the lens in the course of an energy scan, and the lens therefore does not affect the transmission characteristics of the analysing system, and collects the same cone of electrons (of half angle 6°) throughout on energy scan.

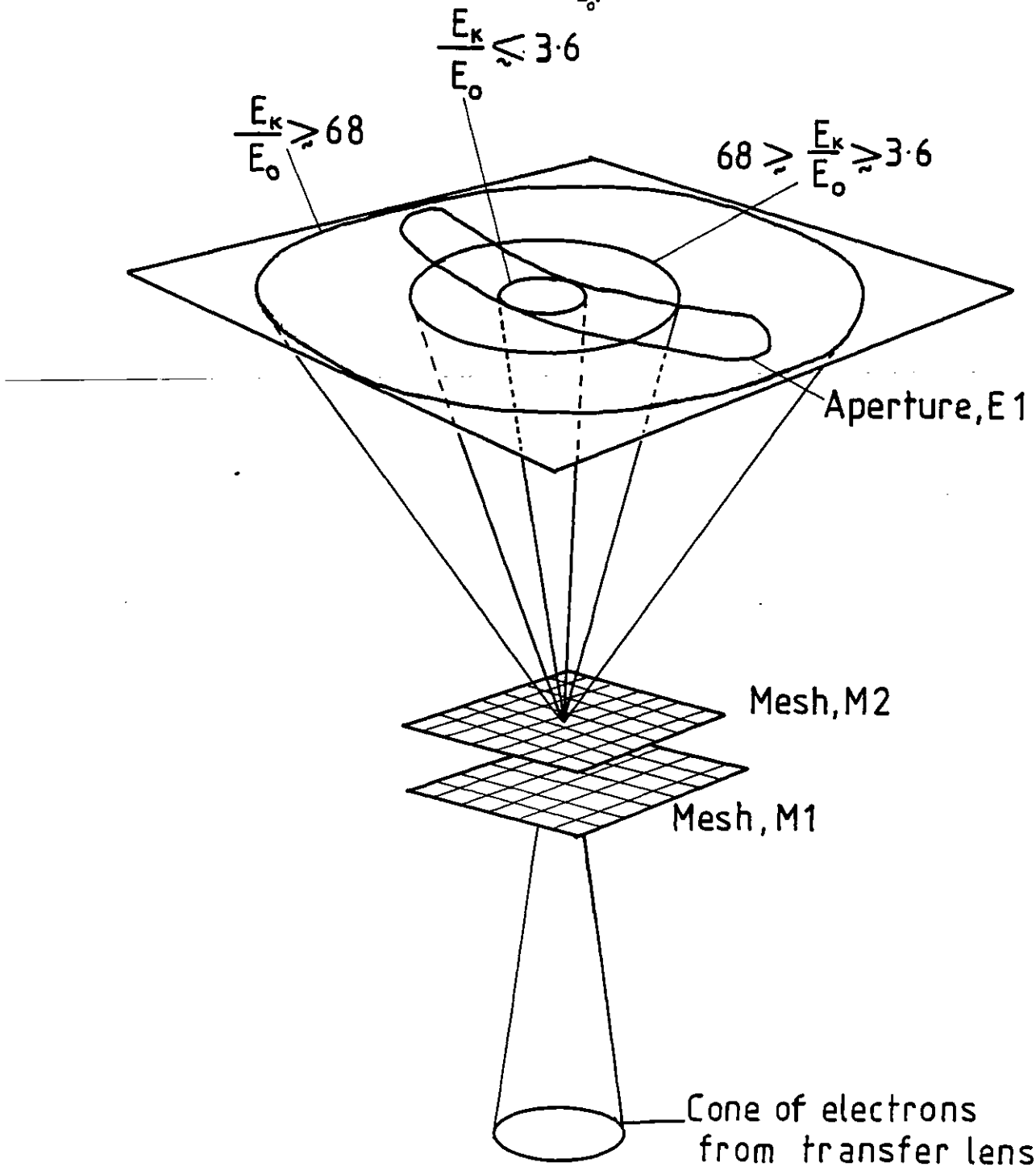
The energy resolution, ΔE, of the hemispherical analyser is given by Sevier (1972) as

$$\Delta E = \frac{E_o w}{2 r_o} \qquad (5.7)$$

where E_o is the kinetic energy of the central ray through the hemispheres, w the width of the analyser entrance and exit apertures (E1 and E2, equal in the case of the ESCAlab), and r_o is the radius of the central ray. Substitution of the values of

Fig.5·7.

Clipping of the XPS Photoelectron Beam by the Analyser Entrance aperture, E1, for different ranges of the Retard Ratio, E_K/E_o.



these parameters for the ESCALAB system gives

$$\Delta E = 0.023\ E_o \qquad (5.8)$$

Clearly the energy resolution ΔE will stay fixed during a CAE scan but increase linearly during a CRR scan.

The energy dependence of the electron transmission of this analyser system (defined as the area of the peak produced by the energy analysing system, in amp-eV units, for a source in the sample position emitting electrons uniformly in solid angle, and in a narrow energy range E, E+dE, divided by the current entering the analysing systemthrough the lens aperture), has been the subject of a preliminary theoretical treatment by Seah (1980). The form of the energy dependence of the analyser transmission function (ATF) will clearly depend on whether the system is used in the CAE or the CRR mode.

In the CAE mode the hemispherical analyser transmission is constant and all the energy dependence of the ATF is expected to arise from the effects of varying electron refraction in the retarding region. The ATF will therefore follow different power law dependencies on E_k according to whether or not the analyser entrance aperture E_1 clips the electron beam in either the radial or the tangential directions as the retarding ratio is increased in the course of an energy scan (figure 5.7)

In the CRR mode, electron refraction effects in the retarding region will remain constant throughout the scan, and the main energy dependence of the ATF will result from the broadening of the peaks in the XPS spectrum as the resolution of the system ΔE increases resulting in an ATF energy dependence

$$\propto E_k$$

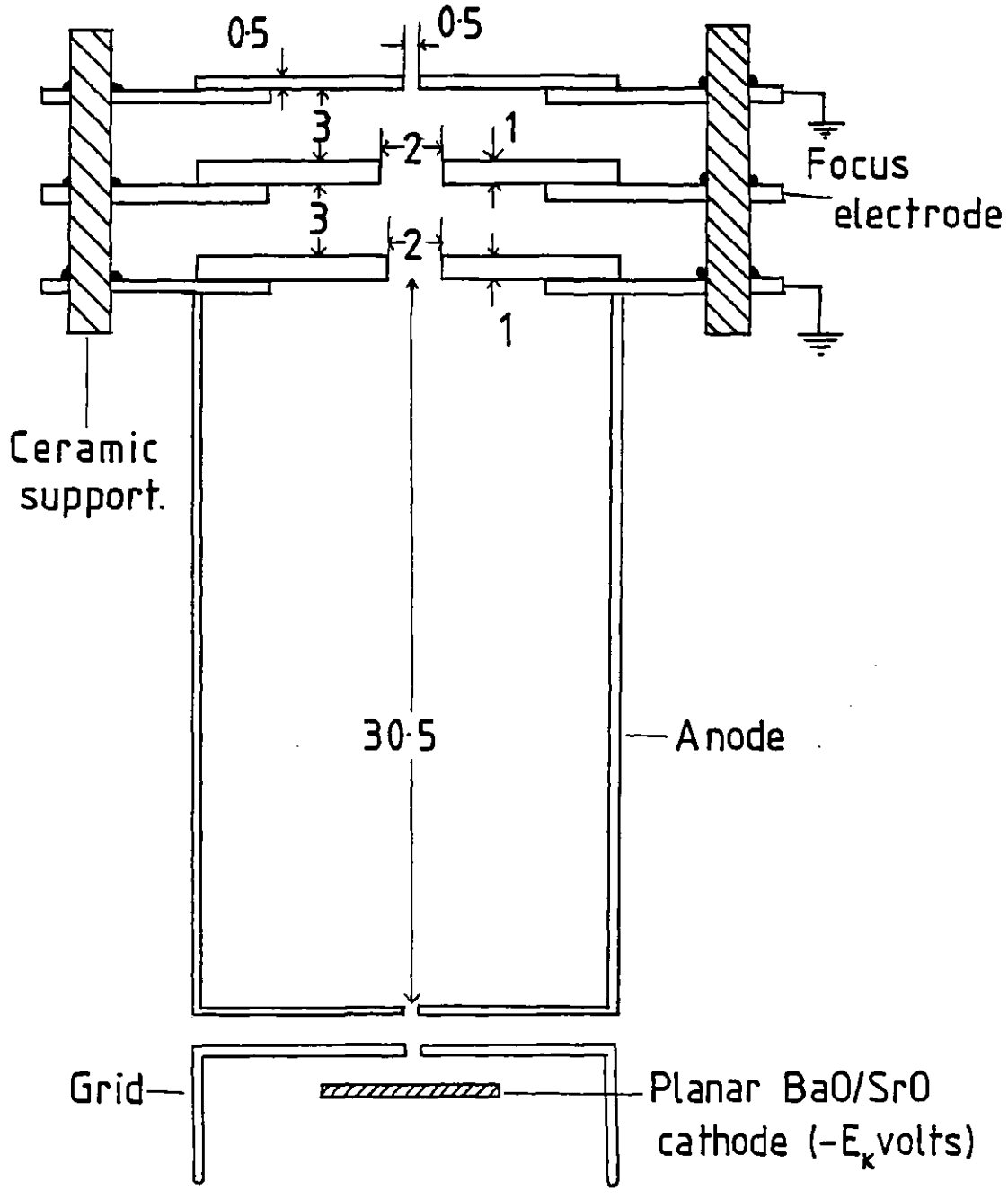


Fig.5·8.

Miniature Electron Gun Constructed for the ATF Measurements. Dimensions in mm.

These energy dependencies of the ATF are only approximate, being based on calculations which necessarily simplify the effects of lens aberrations fringing fields and manufacturing tolerances, and for accurate quantitative work it was thought desirable to measure the ATF experimentally. For this purpose a special miniature electron gun was designed and constructed which could be fitted onto the precision specimen manipulator.

The electron optics of this gun were designed with the aid of a computer ray tracing program to produce a crossover of electron trajectories a few millimeters in front of the final focus electrode (Figure 5.8) which accurately mimicked a point source of electrons, emitting uniformly in solid angle, and situated in the plane normally occupied by a sample. The beam current and profile produced by this gun could be measured with a Faraday cup collector and a phosphor screen respectively. By measuring the gun emission current with the Faraday cup, and then rotating the gun to face the analyser lens and measuring the electron peak intensity recorded by the analyser electronics, it proved possible to measure the ATF of the system directly for a variety of analyser settings and electron source positions over the range of electron kinetic energies encountered in XPS/AES. The results of these experiments are summarised in Figure 5.9 where the absolute experimentally measured ATF is plotted as a function of the electron kinetic energy (for the spectrometer settings used in this study) for both the CAE and CRR modes of spectrometer operation. Also plotted are the results of a detailed theoretical treatment of the transmission of the analyser system (using numerical computational methods), the details of which together with a complete description of the ATF experiments, have been published elsewhere (Hughes and Phillips, 1982). For the purposes of quantitative surface analysis the experimentally measured ATF was used throughout this work.

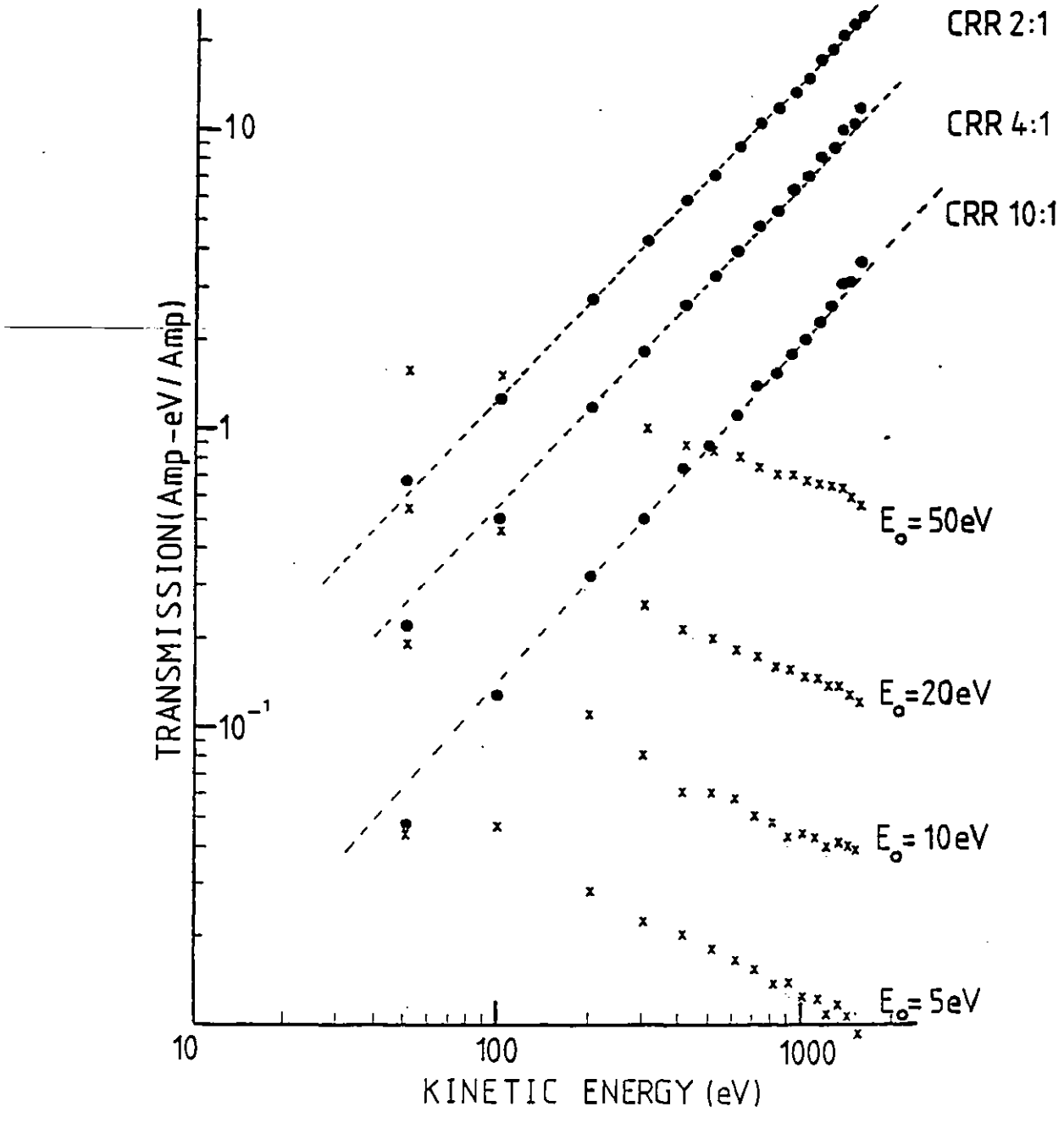


Fig 5·9

Results of the Experimental Measurement of the ATF of the Electron Energy Analyser in both the CRR (dots) and CAE (crosses) modes.

5.3.3.b) Peak area determination

The final stage in the electron energy measurement consists in the determination of what is to be considered as a measure of the intensity of XPS peaks and obtaining an accurate estimate of their peak position in energy. A typical XPS peak (Figure 5.10) appears on top of a broad background resulting from all the electrons which were initially emitted at higher kinetic energies but have suffered inelastic collsions, as well as electrons which have been excited by the Bremstrahlung background in the X-ray spectrum. It is clear that in the absence of detailed knowledge of all the scattering mechanisms and of the exact form of the spectrum at higher kinetic energies than the peak of interest, peak area determination must involve a degree of approximation.

A commonly used method is simply to draw a plausible-looking straight line background between two points on either side of the peak which are chosen by eye to approximately represent the limits of the peak (Figure 5.11a). A variation on this method is based on the idea that every photoelectron in a peak is associated with a contribution to the background level extending uniformly towards the lower kinetic energy region. As a result the height of the background line at any stage in the kinetic energy range spanning the peak is taken as being proportional to the area of the peak towards higher energies above the background, the constant of proportionality being adjusted so that the background level is coincident with the two end points of the peak (which are themselves determined by eye), as in Figure 5.11b.

Using the second method makes most difference on broad weak XPS peaks but although no comprehensive comparisons on the two methods have been published, there is reason to suppose that the difference in peak area estimates between the two techniques is $\sim$ 3% (Seah, 1980) and therefore small compared with other

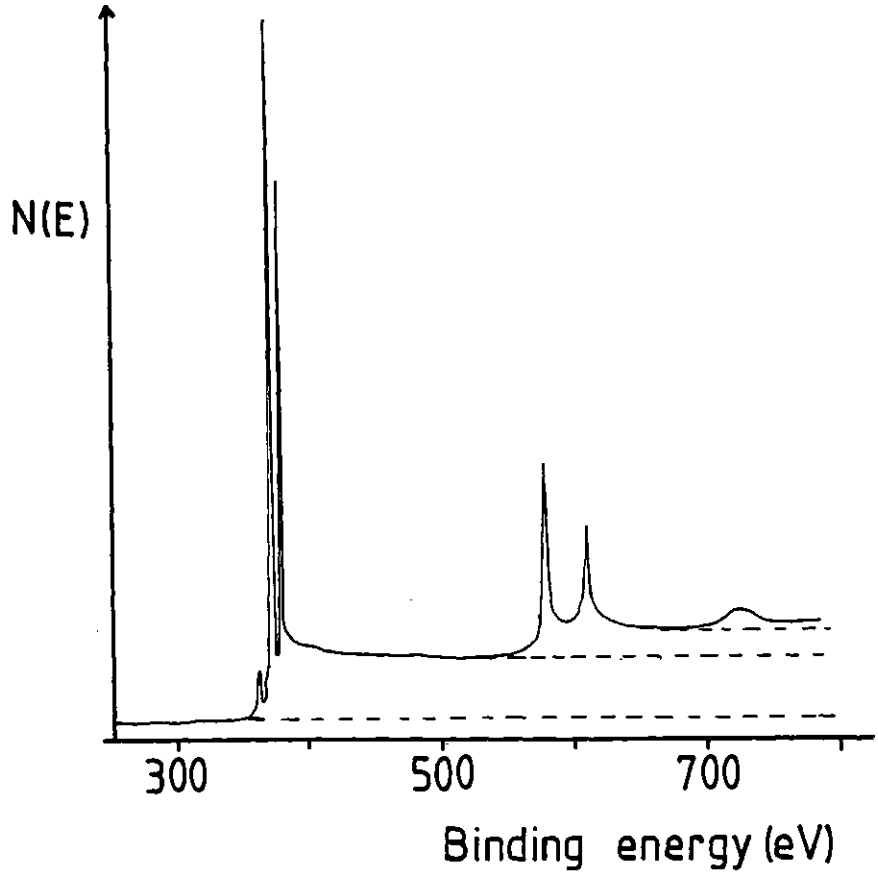


Fig.5·10

Schematic Representation of the Shape of the Inelastically Scattered Background Associated with each Peak in the XPS Spectrum of Pure Silver.

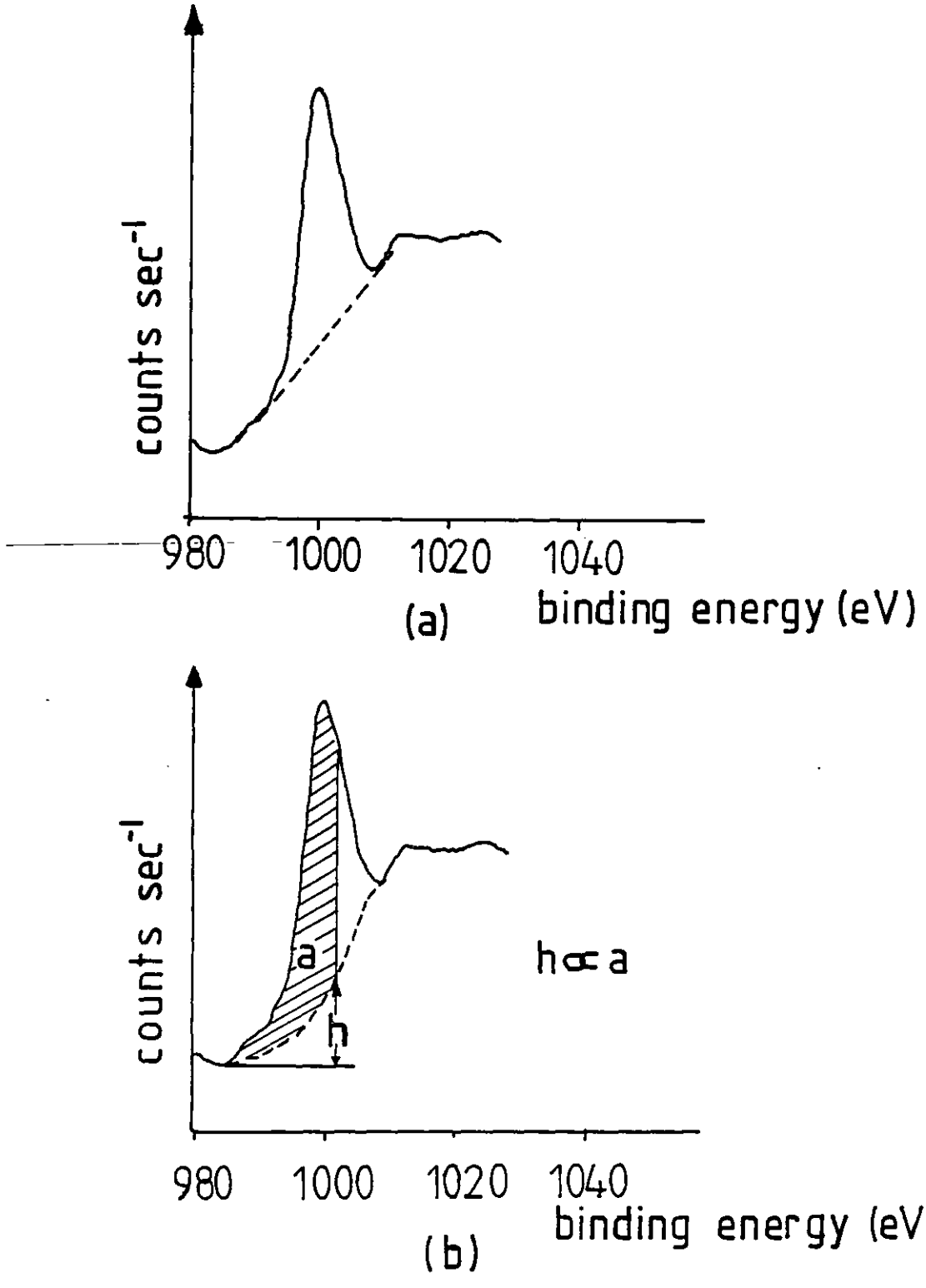


Fig 5·11

Schematic Representation of two types of Background Subtraction on a Cs $3p_{3/2}$ XPS peak.

uncertainties in the quantification process. The aim of both techniques is clearly not to attempt to count every electron associated with the XPS peak, but rather to ignore a fraction of the peak electrons which is independent of peak shape and to ignore all photoelectrons which may have suffered inelastic collisions on their way out of the sample. The latter scattered photoelectrons will not on the whole be representative of the surface composition and are in any case accounted for in the λ term in the equation used to obtain elemental concentrations from XPS peak areas.

In an effort to avoid the degree of subjectivity in choosing the peak integration limits in the above two procedures Powell and Larson (1978) tried two different peak intensity measuring techniques. In the first they selected end integration points equidistant from the peak centre, adjusted so that the integration limit on the low kinetic energy side was close to the minimum which occurred between the principal peak and the loss peaks arising from plasmon excitations. In the second procedure they chose their integration limits to be a fixed multiple of the FWHM of the peak. With the materials they were examining (Pb and In) they found the most consistent peak intensity measurements resulted from the second method of determining the integration limits.

An alternative approach to the problem was suggested by Seah (1979), who pointed out that the shape of the high kinetic energy side of an Auger peak is only slightly affected by loss events, and that consequently estimates of peak areas based only on the high kinetic energy side of the peak may show more consistency from one sample to another. Although Seah suggested this technique for differential AES spectra, the approach is just as valid for XPS N(E) type spectra, and can be a particular help when attempting to evaluate the intensities of two peaks which are close enough for

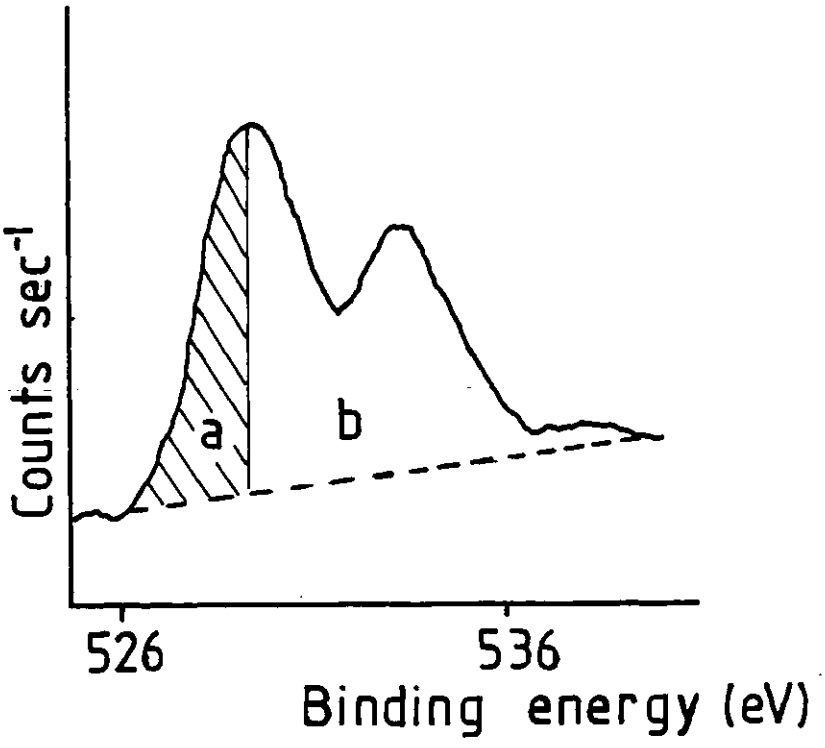


Fig.5·12.

Separating the Intensity Contributions of two Overlapping peaks:

Low Binding Energy Peak Intensity=2a

High Binding Energy Peak Intensity= (b-a)

their wings to overlap (Figure 5.12).

On occasions when the peak shape stays constant from one sample to another, the peak height above background may alone be a sufficient parameter on which to base a quantitative analytical result. For such an approach to hold good, however, all spectra must be taken under identical experimental conditions to avoid changing instrumental broadening, moreover if the peak of interest is of a width comparable to the analyser resolution, significant and incalculable deviations from the normal form of the ATF will result (Hughes and Phillips, 1982).

In order to obtain an accurate estimate of the kinetic energy of a peak, the binding energy scale of the spectrometer must be calibrated accurately against two known reference points in order to determine both its work function and, in the case of the hemispherical analyser, the constant H where

$$E_o = HV \qquad (5.9)$$

V being the voltage difference applied between the hemispheres and E_o being the energy of the central ray through them. This calibration is usually achieved by calibrating the spectrometer against the XPS peaks from a film of gold (or some other similarly inert conducting material) freshly evaporated in UHV onto a metallic substrate with good electrical contact with the spectrometer electronics.

A major obstacle to obtaining accurate binding energy values, particularly with highly insulating samples, is the effect of sample charging. If there is a net electron flux F away from the sample (taking into account any incident flux of stray electrons which may be present inside the spectrometer, as well as the emitted X-ray photoelectrons) and a resistance R

between the sample surface and the spectrometer, then the potential of the sample surface will clearly rise by a voltage

$$V = e\,FR \tag{5.10}$$

and the kinetic energy of the peaks in the XPS spectrum will shift by a similar amount. This problem has been studied by Lewis and Kelly (1980) who derived expressions for the shifts in measured peak energy for the limiting cases of a sample in good contact with the spectrometer electronics and a sample totally isolated from the spectrometer but bombarded by a large flux of electrons with a well-defined energy from an electron flood gun.

If sample charging is uniform over the surface the peak shape will remain the same and only their positions will shift when compared to spectra from an uncharged sample. In such cases chemical binding energy shifts can often still be calculated by referencing all the peak energies in a spectrum to that of a peak which one has reason to believe will show no chemical binding energy shift. If sample charging is non-uniform however, (as may well be the case with say very thin insulating films deposited on glass, where a voltage gradient develops across the surface as the electrons travel inward from the edge of the sample to replace electrons emitted from its centre), then the measured peaks become very broad, and although peak intensity information is often retained, measurement of chemical binding energy shifts is not possible without recourse to flood gun bombardment.

5.4 Routes to Quantitative Surface Analysis from XPS

5.4.1 Introduction

The quantification of the technique can be achieved by one of two methods. One can use other workers' data sets (both experimental and theoretical) on such parameters as subshell photoionisation cross sections, electron IMFP's, analyser transmission function, binding energy shift etc. or alternatively one can internally calibrate one's instrument using reference samples of known stoichiometry.

The reference sample method has the advantage that most of the experimental unknowns (surface roughness, analyser transmission function, analysis geometry, electron IMFP etc.) can be made to cancel in the quantification factor equations, allowing for simple and accurate sample analyses. On the other hand, using reference data sets distilled from a large number of workers should, in theory at least, produce a more reliable and accurate analysis because of the better statistics and more detailed knowledge of the analytical process.

In practice the method chosen will depend on the availability or otherwise of reference samples of known surface composition. For work in some chemical systems (e.g. some binary alloys) where the surface stoichiometry of a reference sample can be well defined and even may be stable enough to allow some form of etching cleaning process to be applied, the choice of calibration method is clear. In many chemical systems, however, the effects of surface contamination, surface segration or even surface chemical decomposition in the reference samples can combine to produce errors in quantification of comparable magnitude to the uncertainty in the reference data sets.

For the present study, with interest focussed on the elements silver, oxygen and caesium the position was not clear, and both methods of quantification were investigated. The contents of this section describe the procedures which were pursued and the results which were obtained for both these routes to quantiative surface analysis.

5.4.2 Internal calibration using reference samples

In choosing samples for spectrometer calibration one generally has a choice between using pure elemental reference samples or compound reference samples of known bulk composition. In the case of elemental reference samples the surface composition is of course well defined, but the electron IMFP's, surface roughness effects and surface contamination layers can all vary between reference samples and between the reference samples and the analysed sample. On the other hand, with compound reference samples although the effects of surface roughness and to an extent surface contamination cancel out, the surface composition may well be different from the known bulk stoichiometry.

For this study interest was confined to silver oxygen and caesium, for which elemental samples were clearly unsuitable. Accordingly the method of using freshly pressed and abraded samples of stoichiometric compounds, as used by Evans et al. (1977, 1978) was chosen. Laboratory reagent grade powder samples of Ag_2O, Ag O, Ag_2CO_3, and Cs_2CO_3 were pressed into 10 mm diameter pellets with a stainless steel press in an oxygen-free-nitrogen glove box with a pressing force of $\sim 3 \times 10^{8}$ Nm^{-2}. The spectrometer, previously at a pressure of $< 10^{-10}$ mbar was let up to dry nitrogen and the pellets were attached to the spectrometer sample slabs with stainless steel clips. Each sample surface was abraded with a stainless steel

scalpel blade just prior to insertion into the spectrometer to expose a fresh surface.

XPS spectra were taken at a background presure of $<10^{-8}$ mbar, which was reached without any subsequent baking of the equipment. At this stage residual gas analysis showed that the background pressure was largely water vapour with approximately 5% CO.

Spectra were taken at normal take-off angle, with Al kα radiation, and all the other spectrometer settings were as outlined in Section 4.4. Peak areas were measured by visually judging the limits to each peak and drawing a straight line background. The resulting peak shape was then traced out onto tracing paper, cut out and weighed (repetition trials suggested that this method measured the area of the peak shape with an accuracy of ∿1%). In the case of peaks with large inelastic loss tails or ones which overlapped with other peaks, peak areas were based on the half of the peak which was least affected by the unknown background level.

Some of the compounds showed evidence of chemical degradation (in particular the $Ag_2 CO_3$, which changed colour on pressing), and where this resulted in split XPS peaks only the larger undissociated peak was counted, in an effort to restrict the analysis to the portion of the sample with known stoichiometry. The results, corrected for the scaling factors involved in the plotting conditions, and normalised to the O1s peak intensity in each compound are tabulated in Figure 5.13 as a series of "experimental elemental sensitivity factors" (EESF's).

Apart from the normal experimental errors in peak area measurement, most of the compound to compound variation in these figures seems to arise from the unknown effects of sample contamination and chemical degradation. With the small number of compounds available it is clearly not possible to make precise

XPS Peak \ Compound	Cs_2CO_3	Ag_2CO_3	Ag_2O	AgO
O1s	1.0	1.0	1.0	1.0
Ag3p$^{3/2}$		2.08	2.35	2.60
Ag3p$^{1/2}$		1.11	1.20	1.37
Ag3d$^{5/2}$		3.42	4.36	4.00
Ag3d$^{3/2}$		2.19	3.02	2.93
Cs4d	2.67			
Cs4p$^{3/2}$	0.671			
Cs3d$^{3/2}$	6.79			
Cs3d$^{5/2}$	10.5			

Figure 5.13 Table of "Experimental Elemental Sensitivity Factors" (EESFs) obtained from various compounds

estimates of the value of these EESF's on quantitative analysis, but some idea can be gained by comparing the EESF's for two different XPS peaks which occur in more than one compound. For instance, looking at the ratio of the EESF's for Ag $3d^{3/2}$ and for Ag $3P^{3/2}$, we find a ± 3% variation in this quantity for all the silver containing compounds, whereas the ratio of the ESSF's for Ag $3d^{3/2}$ and O1s (which occur in the same compounds) varies by ± 16%. The O1s line occurs at a kinetic energy closer to that of Ag $3d^{3/2}$ than the Ag $3p^{3/2}$ line and one would therefore expect the effects of matrix dependant electron IMFPs and surface contamination to affect the Ag $3d^{3/2}$:O1s EESF ratio slightly less than the Ag $3d^{3/2}$:Ag $3p^{3/2}$ EESF ratio. It would seem therefore that the principal sources of error in this experiment stem from deviations away from the bulk stoichiometry at the reference sample surfaces.

The effects of this surface decomposition became more apparent in a second set of XPS traces which were taken two days later, the reference samples having spent the intervening period in the spectrometer under a vacuum of better than 10^{-8} mbar. The EESFs were seen to change by quite large factors between these two sets of traces. For example in the case of the AgO, the ratio of the O1s:Ag $3p^{3/2}$ peak intensities increased by a factor of 6.9 and the surface of the sample was clearly oxygen enriched.

5.4.3 Quantification using reference data sets from other workers

In principle the use of results obtained with different samples and in many cases with different types of spectrometer requires a detailed knowledge of the spectrometers' ATF, the photoelectron IMFPs and the subshell photoionisation cross sections.

	Brillson and Caesar (1976) $\lambda \propto E^{0.5}$	Szaman et al. (1980) $\lambda = mE+C$	Evans et al. (1978) $\lambda \propto E^{0.5}$	Wagner et al. $\lambda \propto E^{0.66}$	Berthou and Jørgensen (1975) $\lambda \propto \frac{1}{ATF}$	Scofield (1976) (theoretical)
$Ag3d^{5/2}$	1.79		2.82	3.47	2.43	2.40
$Ag3d^{3/2}$			2.04	2.35		1.67
$Ag3p^{3/2}$			2.02		0.79	1.81
$Ag3p^{1/2}$				1.59		0.91
$Cs4d^{5/2}$		1.46	1.59	1.45 / 2.42	0.62	0.70 / 1.20
$Cs4d^{3/2}$				0.97		0.49
$Cs3d^{5/2}$		5.70		7.08	6.50	5.36
$Cs3d^{3/2}$		3.63		4.76		3.71
O1s			0.55	0.70	0.70	0.66

Figure 5.14 Subshell photoionisation cross sections, relative to the F1s level, from the literature

In practice however, even if the ATF is known accurately it is often impossible to separate the effects of the energy dependence in the electron IMFPs from the actual experimental subshell photoionisation cross-section, and most experiments purporting to measure either of these quantities do so at the expense of assumptions about the other. Direct measurements of electron IMFP's can be made by evaporating thin overlayers of materials over other compounds and measuring XPS peak attenuation ratios, but this approach is unsuitable for the majority of inorganic compounds, and in any case can be subject to large errors (e.g. Powell, 1974).

The experimental SPCs for the elements of interest in this study which have appeared in the literature to date are tabulated in Figure 5.14, together with the assumptions about the energy dependence of the electron IMFPs involved in deriving these figures. Although the data are sparse it can be readily seen that the disagreement between different sets of experimentalists (not surprisingly) exceeds the inter-compound errors noted in Section 5.4.2, being ±50% in the case of the Ag $3d^{5/2}$ level, and moreover exceeds both the authors' estimates of their own accuracy (e.g. ±12%, Evans et al. 1978) and the average disagreement between experiment and theory).

One of the most promising approaches to solving this discrepancy would seem to be that adopted by Seah and Dench (1979) who performed a statistical analysis on the results of electron IMFPs establishing a matrix independent "universal curve" (see Section 5.3.2) with the adoption of a set of empirical equations to give the energy dependence of the electron IMFP in a variety of classes of material. The assertion that such a "universal curve"

exists for, say, all inorganic compounds clearly involves a degree of approximation, but in most cases the information on matrix band structure etc. which would be necessary to use any of the theoretical calculations on electron IMFPs is simply not available. In comparison the theory involved in calculating SPCs is relatively well established, and moreover the actual SPC (ignoring the shakeup / shake off fraction) is less likely to show matrix dependence than the electron IMFPs. It would seem more appropriate therefore to use theoretical SPCs in conjunction with experimental data to produce tables of experimental electron IMFPs for quantitative surface analysis rather than vice versa.

Confining our attention to inorganic compounds, Seah and Dench (1979) derived the following universal expression from an analysis of 52 IMFP results in the literature,

$$\lambda_n = \frac{641}{E^2} + 0.096\ E^{\frac{1}{2}} \qquad (5.11)$$

where λ_n is the electron IMFP expressed in nanometers and E is the electron kinetic energy in eV above the Fermi level. The applicability of this equation to the Ag-O-Cs chemical system can, to an extent, be tested using the compound data presented in Section 5.4.2. To do this, the ratio of the Seah and Dench IMFP to an electron IMFP, λ_e, derived from the experimental results was calculated using the expression

$$\frac{\lambda_n}{\lambda_e} = \frac{\left[\frac{641}{E_i^2} + 0.096\ E_i^{\frac{1}{2}}\right] \times \sum_i \times T(E_i)}{A_c\ (EESF_i)} \qquad (5.12)$$

where the symbols have the following meanings ...

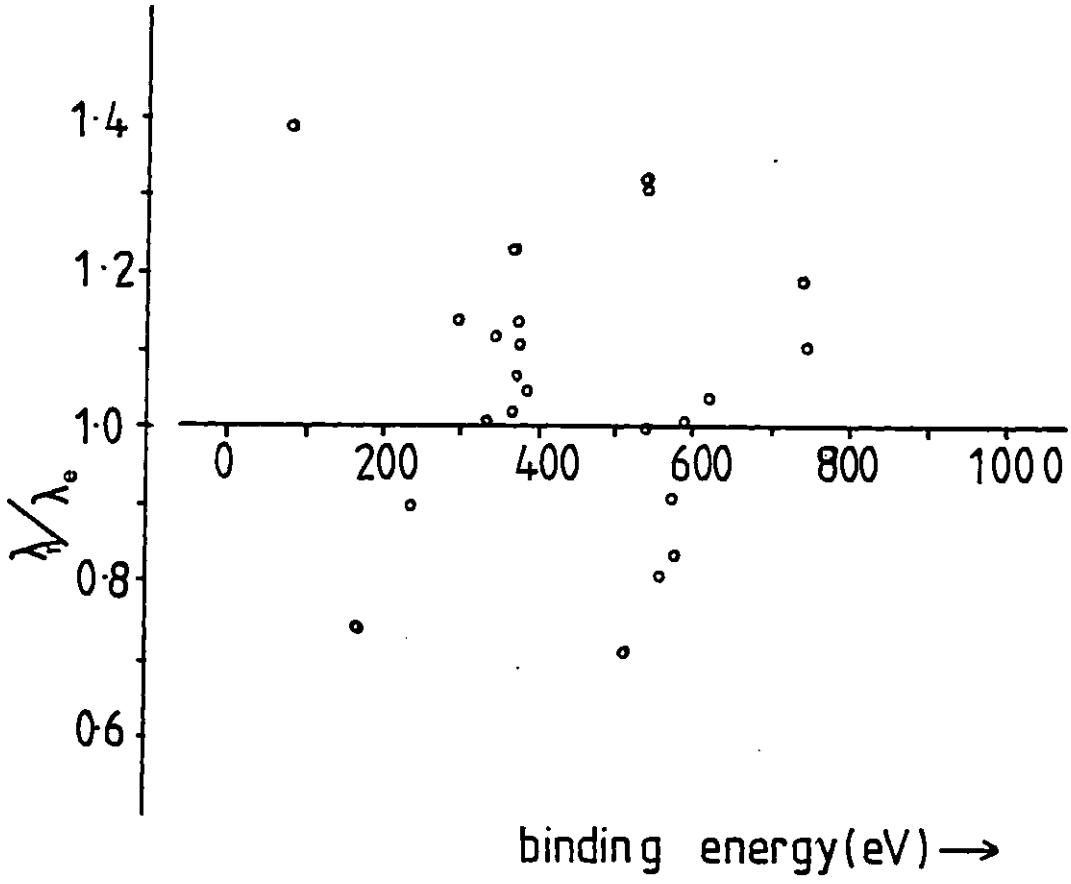


Fig. 5·15

A Plot of the Quantity λ_0/λ_e against XPS Peak Binding Energy (Peak Kinetic Energy =1486.6- B.E.)

E_i :- The kinetic energy of a particular XPS peak with, in this case, Alkα radiation

$\sum_i$:- The theoretical SPC for the XPS peak, taken from Scofield (1976)

$T(E_i)$:- The experimentally measured ATF at kinetic energy E_i, as published in Hughes and Phillips (1982), and Figure 5.9

$EESF_i$:- The experimental elemental sensitivity factor for the peak as defined in Section 5.4.2

A_c :- A scaling factor for each compound which was chosen so that the mean of the $\lambda_n:\lambda_e$ ratios for each compound was unity. This was done to avoid the undue emphasis that would be placed on the reliability of one XPS peak by normalising all the results from one compound to it, and was considered prudent in view of the fact that all the measurements from each compound spanned a similar kinetic energy range.

Plotting the quality λ_n/λ_e against kinetic energy (Figure 5.15) should reveal any systematic kinetic energy dependence in the electron IMFP in the experimental results not accounted for in the Seah and Dench expression for λ_n. Linear regression analysis confirms the initial visual impression that there is no residual IMFP dependence present in these results.

5.4.4 Choosing the Quantification procedures most applicable to the Ag-O-Cs system

In view of the chemical degradation problems encountered in the compound measurements of Section 5.4.2, and considering the

errors apparent in the experimentally derived SPC results, it was decided to use the theoretical SPC calculations presented by Scofield (1976), corrected for angular asymmetry effects using the work of Reilman et al. (1976). The ATF figures used were those which had been directly measured experimentally (Section 5.3.3a) with a miniature electron gun in the spectrometer, and the electron IMFPs were taken from Equation 5.10 as derived by Seah and Dench from a statistical analysis of a large number of IMFP measurements appearing in the literature, as the data on the Si matrix electronic structure which would have been necessary to use the theoretical IMFP work of Penn (1976) were unavailable.

5.5 Conclusion

The problems involved in extracting quantitative elemental concentrations from measured XPS spectra of an unknown sample have been described in detail, together with the procedures which were adopted to circumvent these problems in this work.

One of the major unknowns was the analyser transmission function (ATF) of the electron spectrometer, consequently this was directly measured for the first time using a miniature electron gun which was specially designed for this purpose and accurately imitated the emission from an XPS sample. This gun allowed for the determination of the ATF for the energy range used in XPS with an accuracy (based on the scatter of experimental data) of less than 5%.

The accuracy of the theoretical SPCs (Scofield, 1976) which were chosen for this work is a little more difficult to assess since the experimental data published so far is unsufficiently accurate to either prove or disprove the validity of Scofield's predictions with any degree of statistical significance. The effects

of shake-up and shake-off processes, although possibly reducing the calculated SPC by ∿20% would appear to be largely matrix independent (Krause, 1971 and Brillson and Caesar, 1976). Insofar as the quantitative analytical results are dealing with elemental ratios and not absolute atomic number densities a figure of ± 10% for the combined effects of inaccuracies in the theoretical SPCs and of atomic shake-up/off seems a reasonable estimate.

Equation 5.10 for the electron IMFP in inorganic compounds which was chosen for this work (Seah and Dench, 1979) is quoted as having an accuracy of ± 70%. This large figure results from the scatter observed by Seah and Dench in the large volume of experimental data they used to derive their equation and they present evidence to suggest that ∿ 30% of this scatter is due to random experimental errors, the remainder being due to genuine matrix dependencies in the electron IMFPs. In the case of the present analysis though, with all the measurements being done on similar S1 photocathode films one would expect the matrix dependence of the IMFP to become insignificant. Moreover for the elemental concentration ratio measurements only the kinetic energy dependence of the electron IMFP is important, although of course its absolute value is useful as a means of providing an estimate of the sampling depth of the technique. An estimate of the actual energy variation of the IMFP in particular chemical systems emerged from the work of Wagner et al. (1980) who, on the basis of a statistical analysis of IMFP results in the literature proposed a kinetic energy dependence $\lambda \propto E^m$ where m varied between extremes of 0.53 and 0.80 for different chemical systems. As all the quantitative analyses in this project were performed on photoelectron lines with kinetic energies in the narrow range 750→960 eV, the uncertainty in the deduced elemental ratios as a result of errors in the IMFP data used is likely to be

no more than $\sim$ 4%.

Combining all these error estimates together with the $\sim$ 3% error in peak area measurement (Seah, 1980), it can be seen that the procedures outlined in this chapter have resulted in the ability to measure elemental ratios in Sl photocathodes to an accuracy of $\sim$ 12%, the majority of this uncertainty arising from the possibility of inaccuracies in the Scofield SPCs used. Since one would expect SPCs to be fairly similar from one photocathode to another the percentage changes in elemental ratios between one photocathode and another are probably accurate to better than $\sim$ 7%.

CHAPTER 6

RESULTS OF PHOTOCATHODE EXPERIMENTS

6.1 Introduction

Because of the large number of different experiments performed in this work, and the complementary manner in which the results combine to allow conclusions concerning the nature of the cathodes studied to be drawn, it was decided to present the results in the form of a self-contained chapter.

This chapter consists therefore of two main sections containing the experimental results on the two types of infra-red sensitive photocathodes, with only a minimum of discussion of their significance. The results of the XPS analysis of a number of GaAs cathodes are presented, in conjunction with spectral sensitivity measurements, EDC data, and direct measurements of photocathode intrinsic emission time uncertainties. The results of a large number of S1 photocathode XPS analyses are also presented, together with EDC and photosensitivity data. The polarisation dependence of S1 cathode photosensitivity was also investigated, and results of measurements of the wavelength dependence of the yield ratio for "s" and "p" polarisations are also presented.

The contents of this chapter are intended primarily to be used in conjunction with the cross-references in Chapter 7 to illustrate the discussion therein.

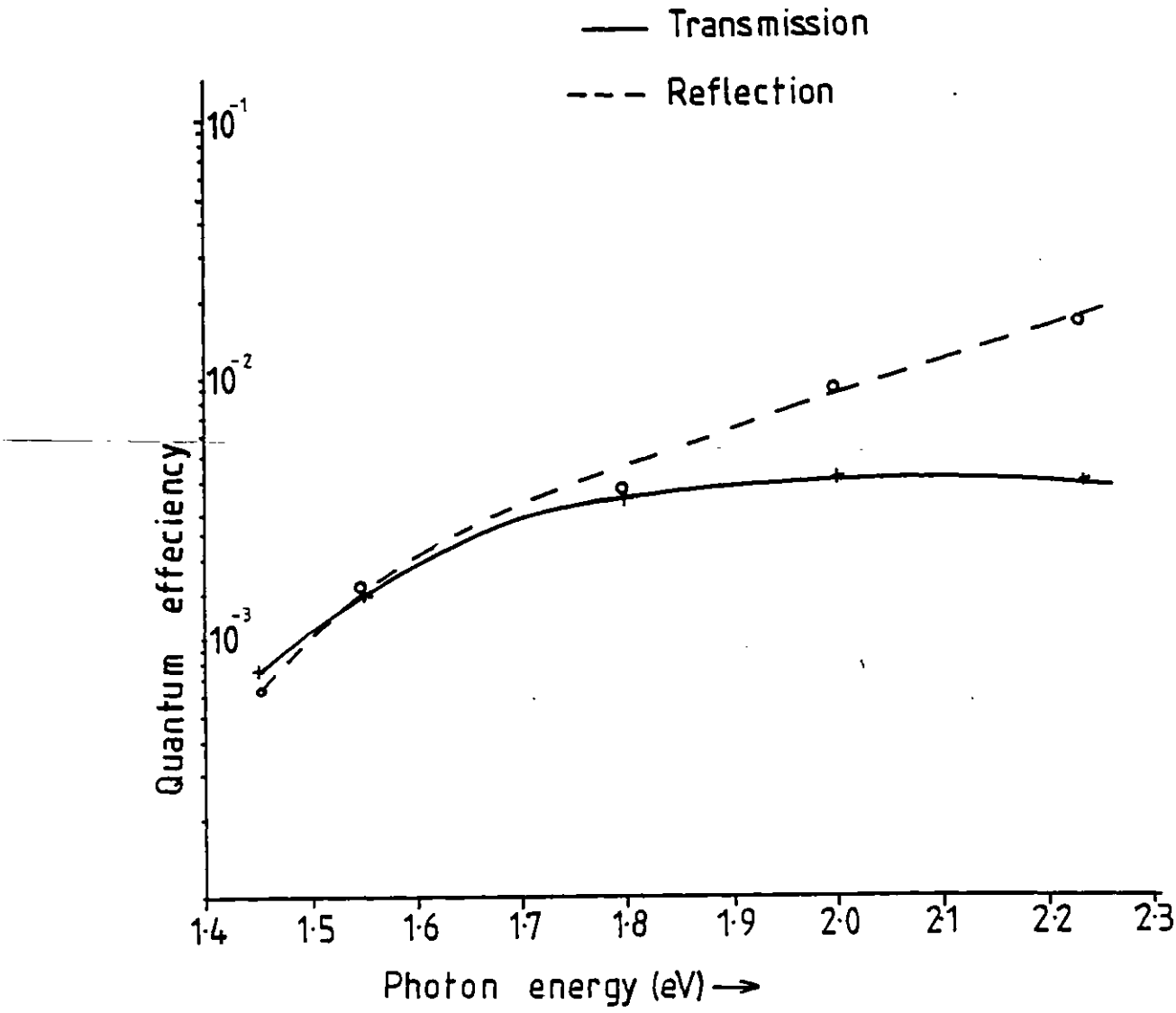


Fig.6·1
Quantum Effeciency of a GaAs Photocathode Produced in this Study.

6.2 Experimental Results on GaAs Photocathodes

6.2.1 Spectral Sensitivity Measurements

Figure 6.1 depicts the spectral quantum efficiency (measured as described in Section 4.2) in the reflection and the transmission mode of a typical GaAs film produced in the present work. As can be seen the transmission sensitivity takes the form of a broad flat curve which extends throughout the visible range of the spectrum, limited at one extreme by the 1.4eV direct band gap photoemission threshold of the GaAs active film, and at the other extreme by the heavy bandgap absorption in the strain matching $Ga_xAl_{1-x}As$ layer for photon energies in excess of 2.2 eV.

The reflection mode sensitivity is of course not affected by substrate absorption and consequently diverges from the transmissive mode curve at high photon enegies. The shapes of both these curves closely agree with those measured by Allenson et al. (1972) for a similar cathode structure, but the absolute magnitude of the cathode sensitivity in this work is less by about one order of magnitude.

6.2.2 Photoelectron EDC's from GaAs Photocathodes

The results of the EDC measurements (as described in Section 4.6) of a representative GaAs photocathode are reproduced in Figures 6.2 and 6.3. Their shapes provide direct evidence for the diffusion model of NEA photocathode operation, showing very little photon energy dependence over a photon energy range of $\sim$1 eV, with hot electron structure (in the form of a slight high kinetic energy "tail") only appearing at photon energies in excess of $\sim$ 2eV.

Clearly in many of these curves the 50 meV FWHM energy resolution function of the analyser (Section 4.6) was making a significant

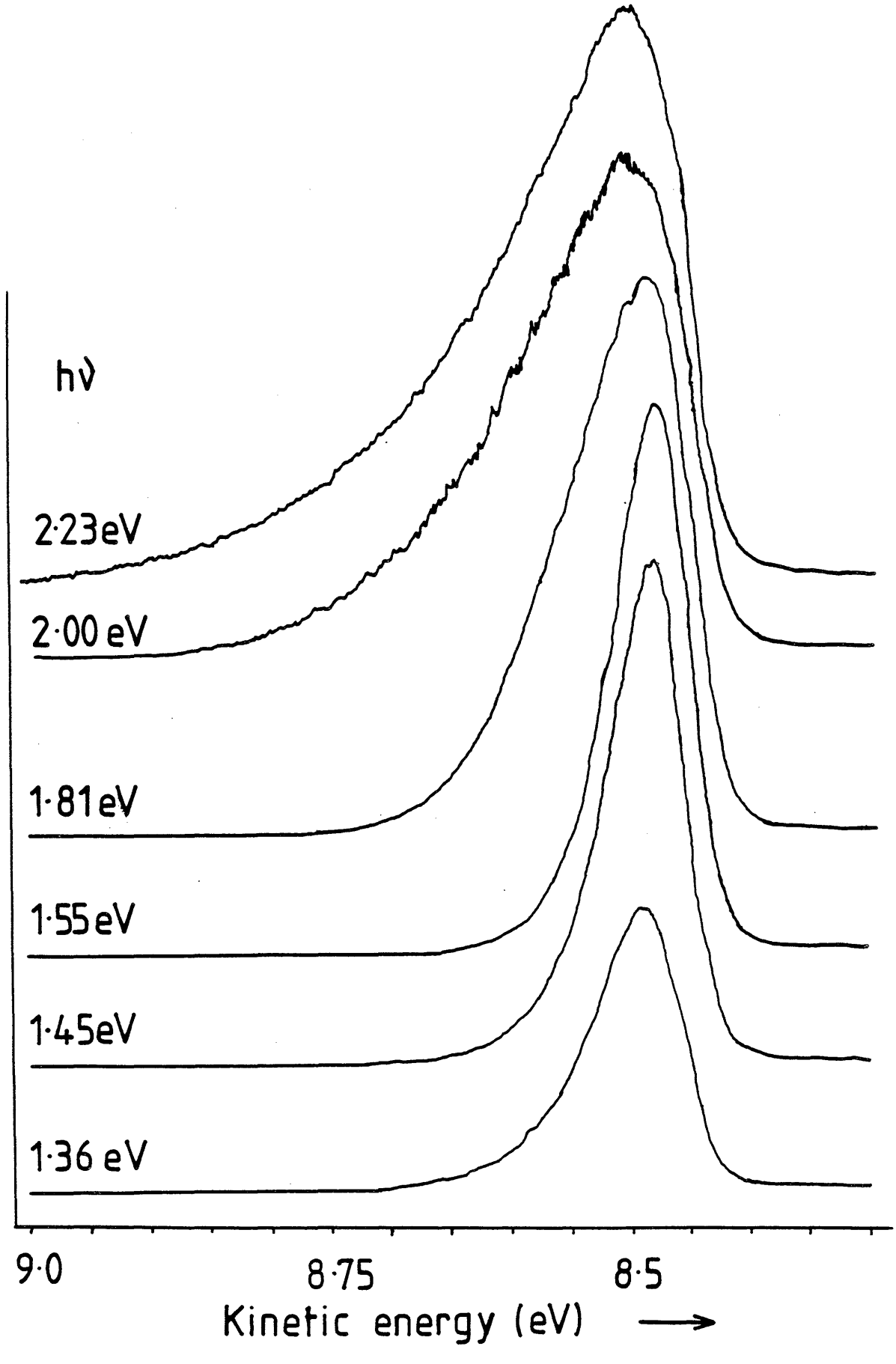


Fig. 6·2

Reflection Mode EDC's from a Typical GaAs NEA Photocathode.

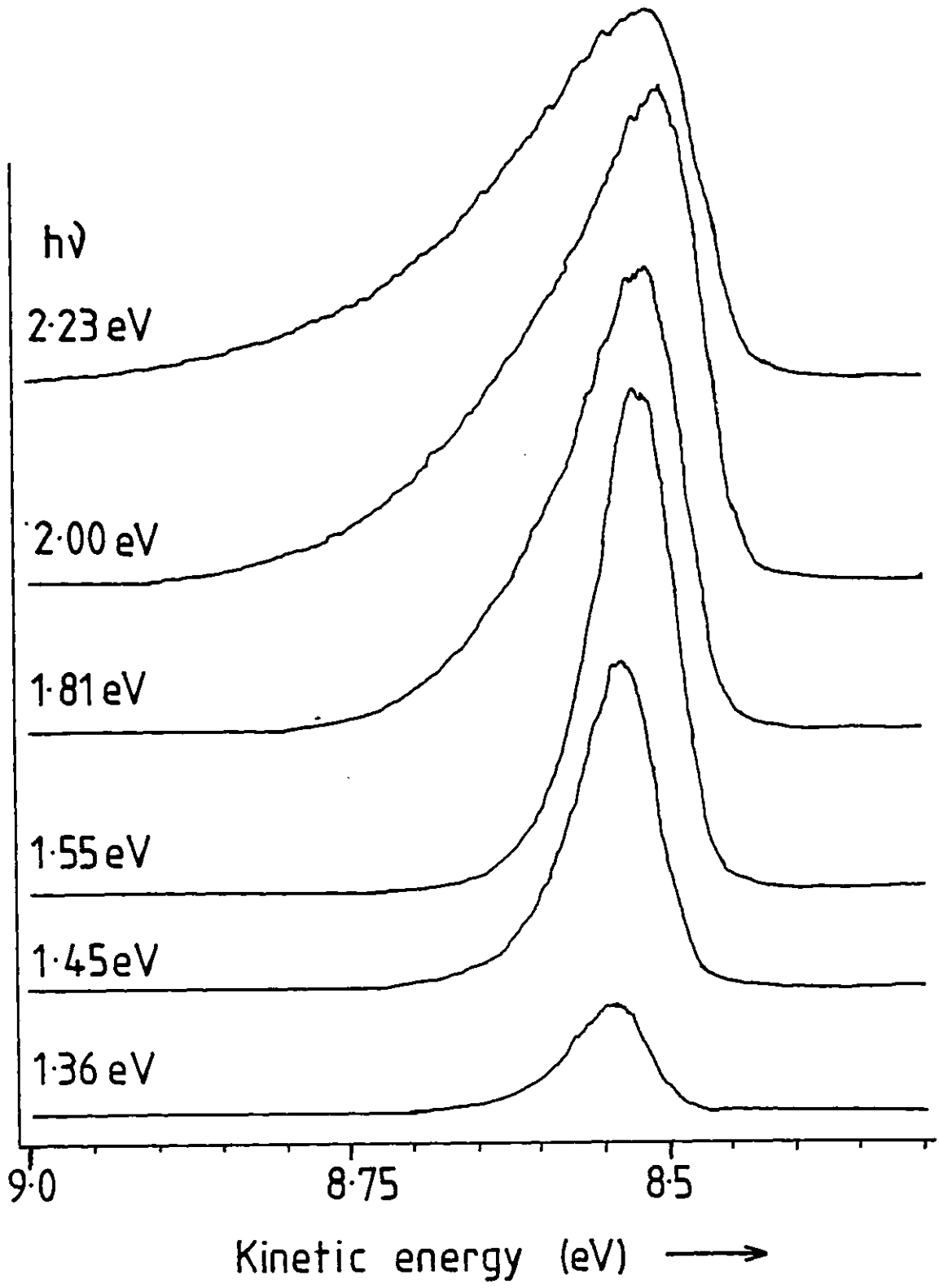


Fig. 6·3

Transmission Mode EDC's from a Typical GaAs NEA Photocathode.

contribution to the observed EDC width, and so the analyser instrumental response was de-convolved from the experimental FWHM EDC peak widths using the Gaussian deconvolution formula ..

$$\Delta E_m^2 = \Delta E_E^2 + \Delta E_A^2$$

where ΔE_m is the FWHM of the measured peak

ΔE_E is the FWHM of the actual EDC

and ΔE_A is the 50 meV FWHM of the analyser resolution function

The results of this analysis are given below in Figure 6.5, together with the energy bandwidth of the filters (measured with a Beckmann Spectrometer) used to monochromate the white light for the EDC measurements

$h\nu$	Filter bandwidth	Reflection Mode experimental FWHM($=\Delta E_m$)	Reflection Mode deconvolved FWHM($=\Delta E_E$)	Transmission Mode experimental FWHM($=\Delta E_m$)	Transmission Mode deconvolved FWHM($=\Delta E_E$)
1.36eV	30meV	92meV	77meV	75meV	60meV
1.45eV	34meV	78meV	60meV	75meV	60meV
1.55eV	38meV	97meV	83meV	75meV	60meV
1.81eV	13meV	125meV	114meV	110meV	98meV
2.00eV	16meV	160meV	152meV	140meV	131meV
2.23eV	22meV	175meV	168meV	175meV	168mev

Figure 6.5 EDC with data for NEA Photocathodes

Clearly these EDC's represent almost totally "thermalised" electron distributions with FWHM figures which are on the limits of resolution of the analysing system, and which would give very low transit time dispersion figures in a streak tube.

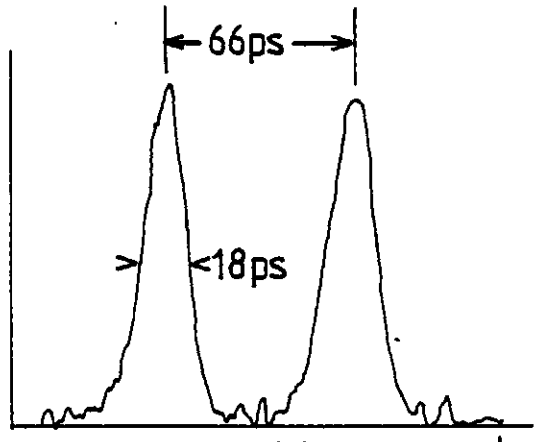
6.2.3 GaAs NEA Photocathode Temporal response results

The incorporation of the UHV compatible streak camera (described in detail in Chapter 2) into the vacuum system made it possible for the first time to accurately and directly measure the temporal performance of a number of NEA photocathode films in conditions similar to those which would occur if such cathodes were to be used in sealed off streak tubes.

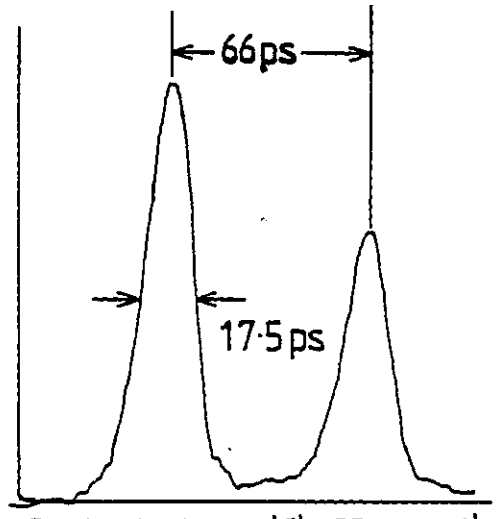
To do this the streak camera and dye laser system were first optimised as described in Sections 2.4.3 and 2.4.4, with an S1 photocathode in the UHV system streak camera. The separate sealed-off streak camera was then used to monitor the width of the pulses produced by the dye laser system and its associated electronics in the synchroscan mode, thereby providing a continuous measure of the effects of laser pulse width and RF electronic jitter which could be deconvolved from the pulses recorded by the UHV streak camera with the NEA photocathode under test. During all these tests the laser system and its associated electronics produced streak widths of 13$\sim$18ps FWHM on the sealed off streak tube.

In Figure 6.6 the streak results from three separate GaAs photocathode bases obtained in this way are presented. Although there were considerable differences in temporal response between one photocathode base and another, each base gave a similar streak trace each time it was argon-ion cleaned and reprocessed.

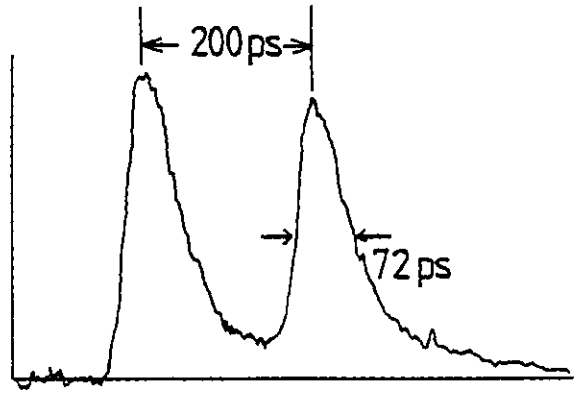
There was a correlation apparent between the recorded pulse width for a photocathode and its photosensitivity, faster photocathodes repeatedly producing lower photosensitivity figures on activation. Photocathode "A" for example, from which the photosensitivity data in Figure 6.1 was obtained, was approximately an order of magnitude faster than the diffusion model (Section 3.2.2) would predict for a cathode film of optimum thickness, whilst being about an order



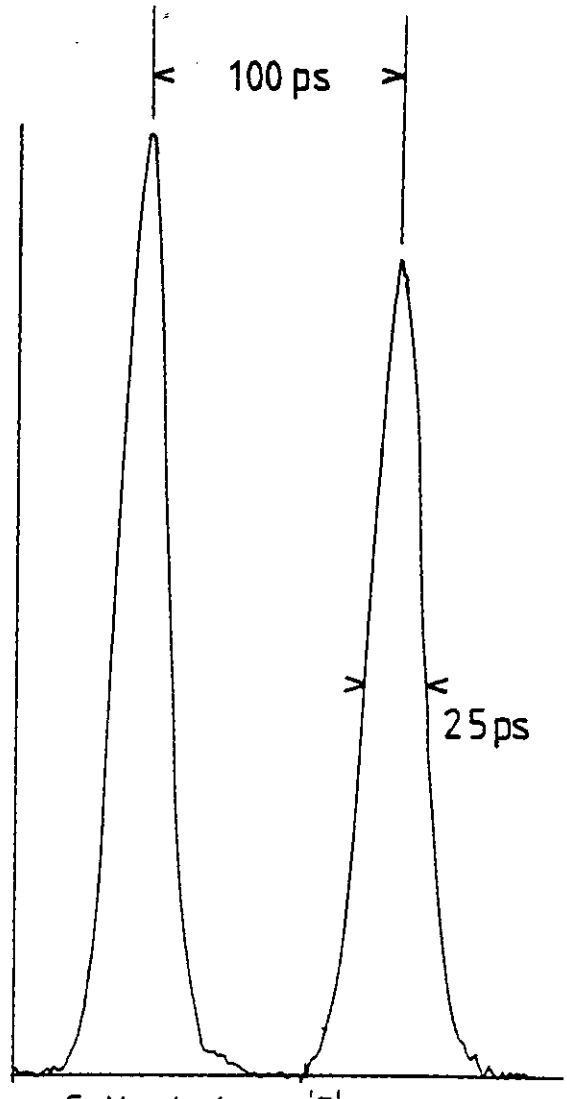
Cathode base 'C', 20 kv cm^{-1}



Cathode base 'C', 33kv cm^{-1}



Cathode base 'A'



Cathode base 'B'

Fig.6·6

Streak Widths obtained with various NEA Cathodes in this Study.

of magnitude less sensitive. A similar relationship between sensitivity and temporal response was obeyed by all the other photocathodes.

As part of the investigations into the reasons for the fast temporal response observed with these photocathodes, the extraction field in between the photocathode and the mesh was varied (by changing the cathode-mesh distance) to check if a field assisted photoemission mechanism existed. As can be seen from the streak traces for cathode base "c", it was found that changing the extraction field did not affect the measured photocathode response time.

Deconvolving the pulse widths observed on the sealed off streak camera from those measured on the UHV streak camera with the NEA cathode yielded a direct measurement of the "intrinsic emission time uncertainty" for these photocathodes, the factor which would ultimately limit the temporal resolution of any device in which they may be fitted (see 2.3.3). The results are tabulated in Figure 6.7.

GaAs Cathode Base	UHV streak Camera streak width	Sealed-off streak camera streak width	IETU
"A"	72psec	13psec	71psec
"B"	25psec	18psec	17psec
"C"	18.8psec	17psec	8psec

Figure 6.7 Temporal response data for NEA photocathodes

It can be seen that even the slowest of these three cathode films was almost an order of magnitude faster than the $\sim$800ps FWHM streak widths one would expect from the diffusion model based

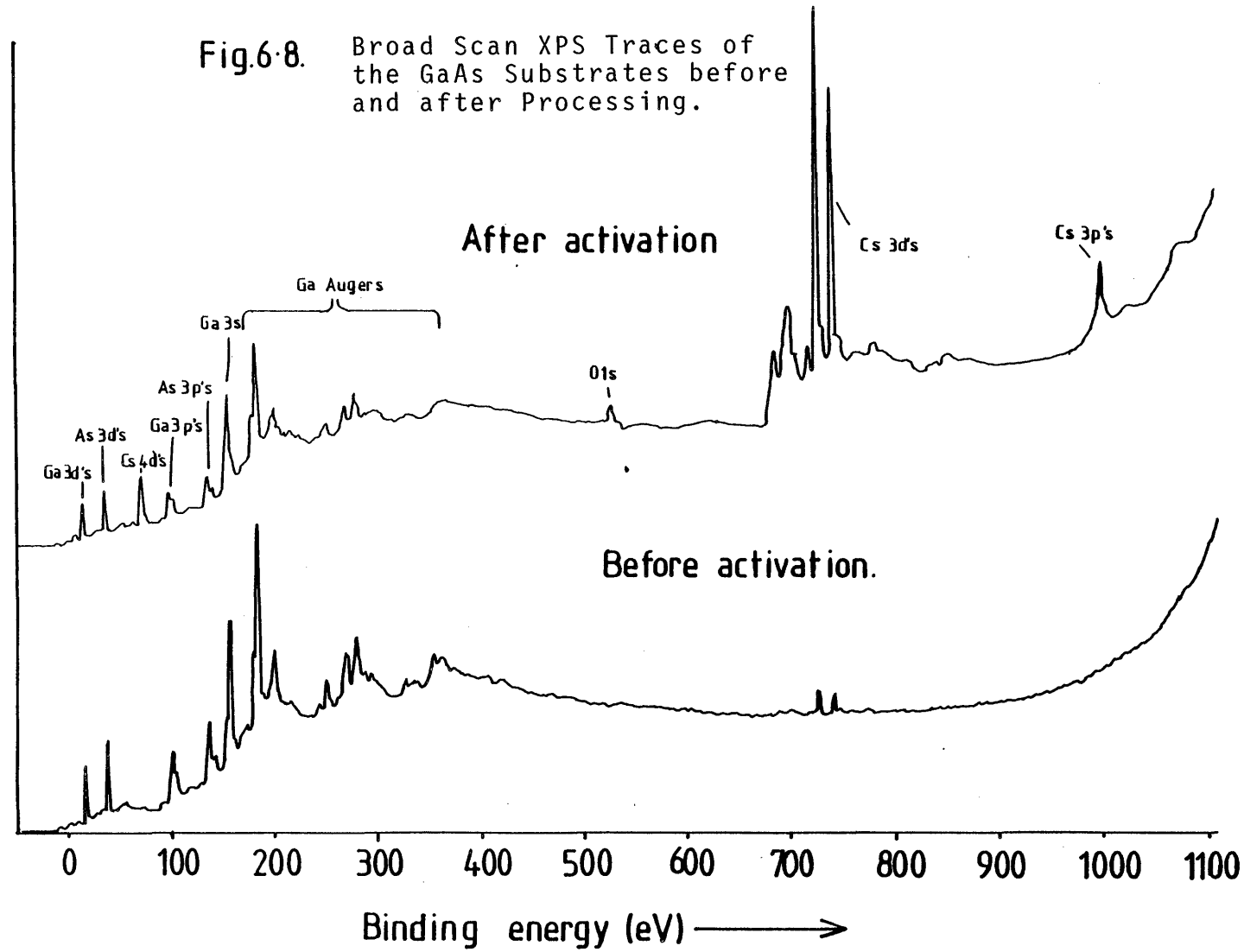


Fig.6·8. Broad Scan XPS Traces of the GaAs Substrates before and after Processing.

TMTF calculations made by Bell (1973, see Section 3.2.3) for NEA photocathodes of $\sim$1.5 μm thickness. Moreover the performance of the fastest one suggests exciting prospects for NEA applications in infra-red framing cameras and moderate temporal resolution streak tubes.

6.2.4 GaAs NEA Photocathode XPS results

The wide-scan Mgkα induced XPS spectra (Figure 6.8) from both the clean Ga As base and the fully processed photocathode film show a large binding energy range (between $\sim$170eV and $\sim$350 eV) in which the spectrum is dominated by gallium Auger transitions, making quantitative deductions from XPS peaks in that region difficult.

For this reason interest was confined to Cs3d$^{3/2}$, O1s, Ga3p and As3p type XPS transitions for quantitative analysis, and the quantification framework discussed in Chapter 5 was used to evaluate the surface Ga:As ratio on the substrate from the combined 3p$^{3/2}$ and 3p$^{\frac{1}{2}}$ peak areas. As can be seen from the XPS traces reproduced in Figure 6.9, activation of the GaAs substrate did not produce any measurable change in either the binding energy or the shape of the Ga and As substrate peaks, but merely affected their intensities.

Using the ratio of the substrate peak intensities before activation to the substrate peak intensities after activation, in conjunction with equations 5.6 and 5.11 (the overlayer attentuation equation and the Seah and Dench electron IMFP equation) estimates of the Cs-O overlayer thickness corresponding to the optimumm photosensitivity were calculated. The results of this analysis for the cathode base "B" (from which the photosensitivity data in Figure 6.1 were obtained) are tabulated in Figures 6.10 and 6.11.

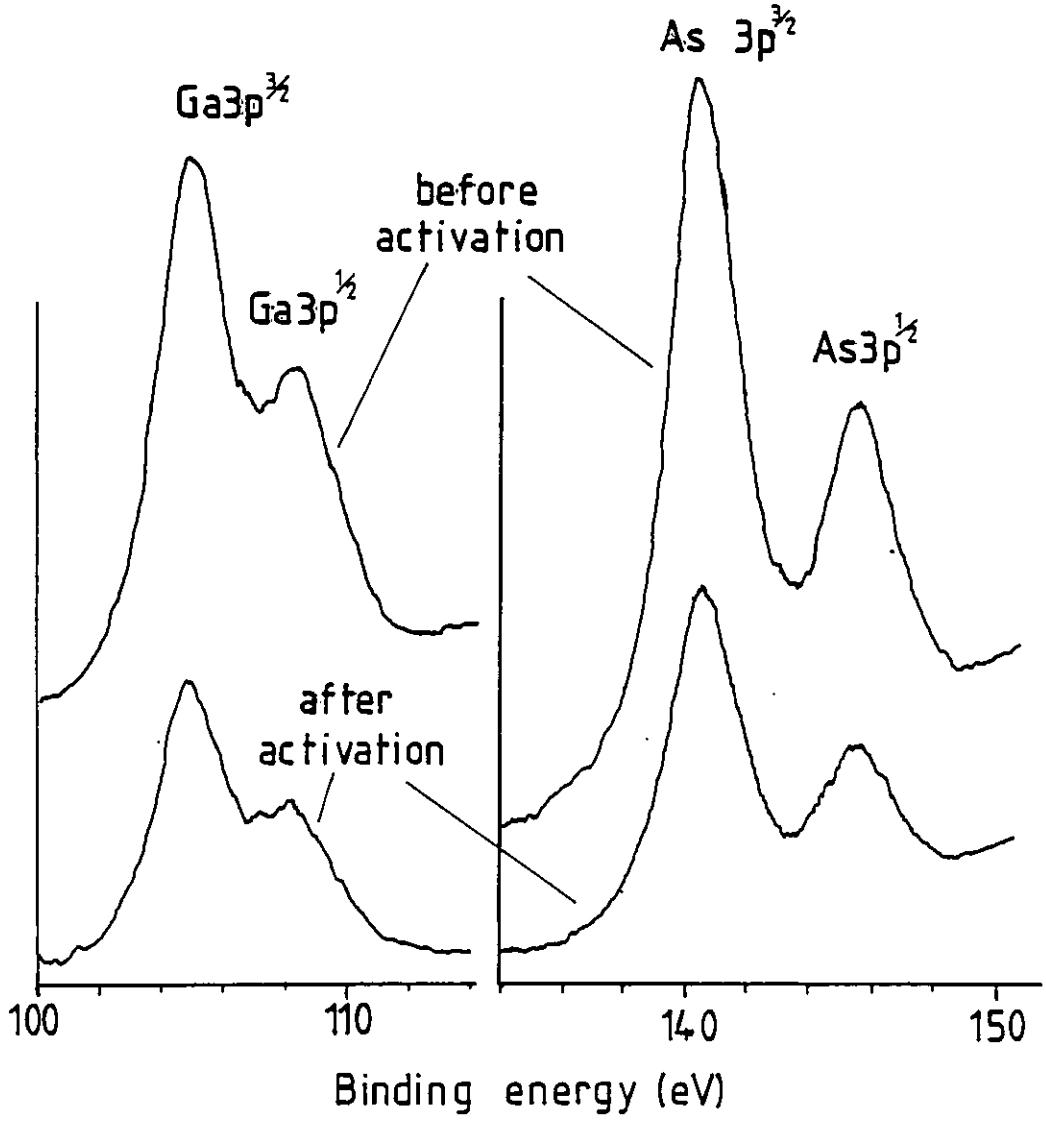


Fig.6·9
Ga and As XPS Peaks before and after the activation of the Substrate to NEA.

XPS peak	Take-off angle	$3p^{3/2}$ Binding Energy/eV Before activation	After activation	Intensity attenuation	Calculated Cs-O over-layer thickness/ nm
$Ga3p^{3/2,1/2}$	0°	104.5	104.5	0.59	1.7
	30°	104.5	104.5	0.68	1.1
	60°	104.5	104.5	0.52	1.06
$As3p^{1/2,3/2}$	0°	141.3	141.3	0.65	1.37
	30°	141.3	141.3	0.61	1.38
	60°	141.3	141.3	0.53	1.01
					mean = 1.27±0.26

Figure 6.10 Ga and As XPS peak data for NEA photocathodes

Cs:O (using the $Cs3d^{3/2}$ and O1s XPS peaks)

Takeoff angle	Cs:O Ratio
0°	1.99
30°	2.20
60°	1.95

Ga:As ratio (based on the $Ga3p^{3/2,5/2}$ and the $As3p^{3/2,5/2}$ peak)

Takeoff angle	Before activation	After activation
0°	1.36	1.23
30°	1.08	1.23
60°	1.28	1.26

Figure 6.11 Elemental ratios deduced from XPS peak intensities from NEA photocathodes

The accuracy of these overlayer thickness results is primarily limited by the accuracy of the IMFP equation used to obtain the electron IMFP in the Cs-Ooverlayer. Seah and Dench's own estimate of the absolute accuracy of this equation is ± 70% (with especially large uncertainties at kinetic energies of ∿ 100 eV, hence the decision not to include the Ga2p peak attenuation ratios when calculating the Cs-O overlayer thickness).

The measured elemental ratios from the cathode base "B" are tabulated in Figure 6.11, and they were typical of the elemental ratios found on all the GaAs cathodes processed. The results show a measured caesium to oxygen ratio very close to two with no surface segregation or caesium overlayer effects apparent in the takeoff angle variation of this ratio, suggesting a homogeneous Cs-O overlayer with a stoichiometry very close to Cs_2O. The measured Ga:As ratio however does deviate from the known bulk stoichiometry being on average ∿ 20% gallium rich.

This surface enrichment probably occurs during the annealing stage of the substrate cleaning process where, although Ga and As are evaporating congruently, evaporation is limited by the Ga evaporation rate from Ga "steps" on the (100) surface (Foxon et al., 1972). Similar Ga surface enrichment probably also occurs in the heat cleaning procedure normally employed for substrate preparation, but in either case the ultimate photocathode sensitivity does not seem to be adversely affected.

Typical XPS spectra (again from cathode "B") of the Cs_2O overlayer are reproduced in Figure 6.12 for three different angles of take-off, in the region of the Cs3d peaks and the O1s peak. No take-off angle dependence of any of the peak binding energies was measurable to within the 0.1eV accuracy of the instrument. The O1s signal took the form of a single symmetrical peak at 530.1±0.1eV,

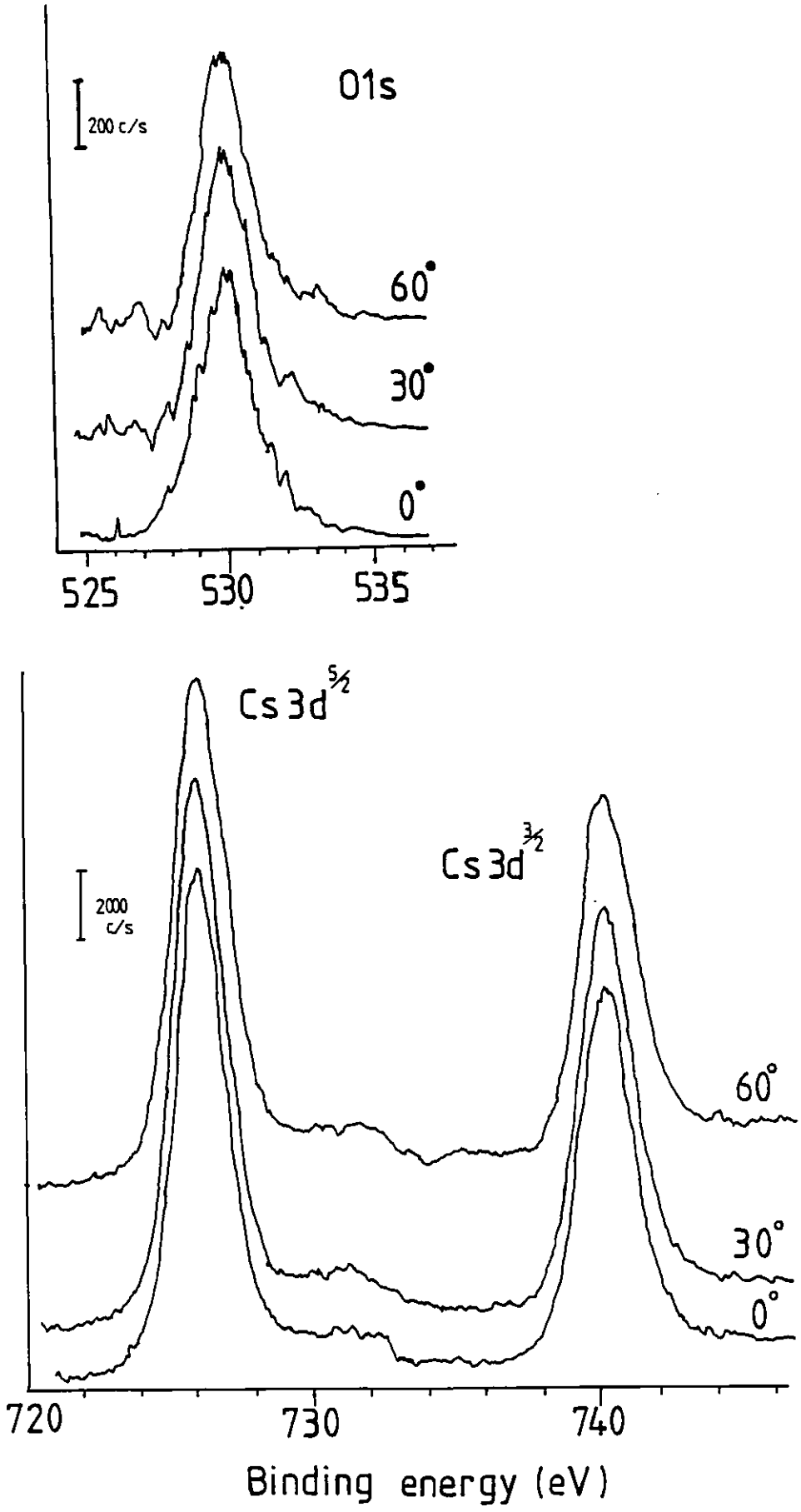


Fig.6·12.

Cs and O XPS Peaks for a Variety of take-off angles from from a Typical GaAs NEA Photocathode.

in contrast to the complicated oxide structure which was observed in the S1 XPS results (6.3.3). Measurements of the FWHM figures for the $Cs3d^{5/2}$ peak (the most intense and therefore easily measurable of the oxide peaks) from XPS spectra of seven different photocathode surfaces gave a mean value of 2.10±0.10eV, using the Mgkα radiation.

6.3 S1 Photocathode Experimental Results

6.3.1 Spectral Sensitivies of S1 Photocathodes

The actual spectral sensitivies of the S1 photocathodes produced were subject to considerable variation, but when the results from a large number (> 130) of photocathodes were analysed, it became apparent that all the cathodes could be divided into three main groups, a,b and c, according to their behaviour on processing.

Group "a" photocathodes had the highest photosensitivity and proved to be stable over many days in UHV. They were characterised by a processing photosensitivity profile similar to that described in 4.3.1(b). The spectral sensitivity measurements (carried out as described in 4.2), showed these cathodes to have a spectral sensitivity curve similar to those quoted for commercial phototubes, with a broad flat maximum in the region of λ = 800 nm, and a threshold in excess of 1.3μm. The absolute spectral sensitivity of a typical group "a" cathode in the transmission mode is reproduced in Figure 6.13.

Group "b" photocathodes were characterised by a stable photo-sensitivity (of $\sim 5\mu A\ lm^{-1}$) after the caesiation stage, a somewhat unpredictable variation of photosensitivity thereafter and a final photosensivity $\sim$ 50% of their group "a" counterparts. Group "c" cathodes were the ones which for one reason or another (generally carbon contamination problems with the processing equipment, or straightforward processing errors) resulted in very low and unstable photosensitivity. Unless otherwise

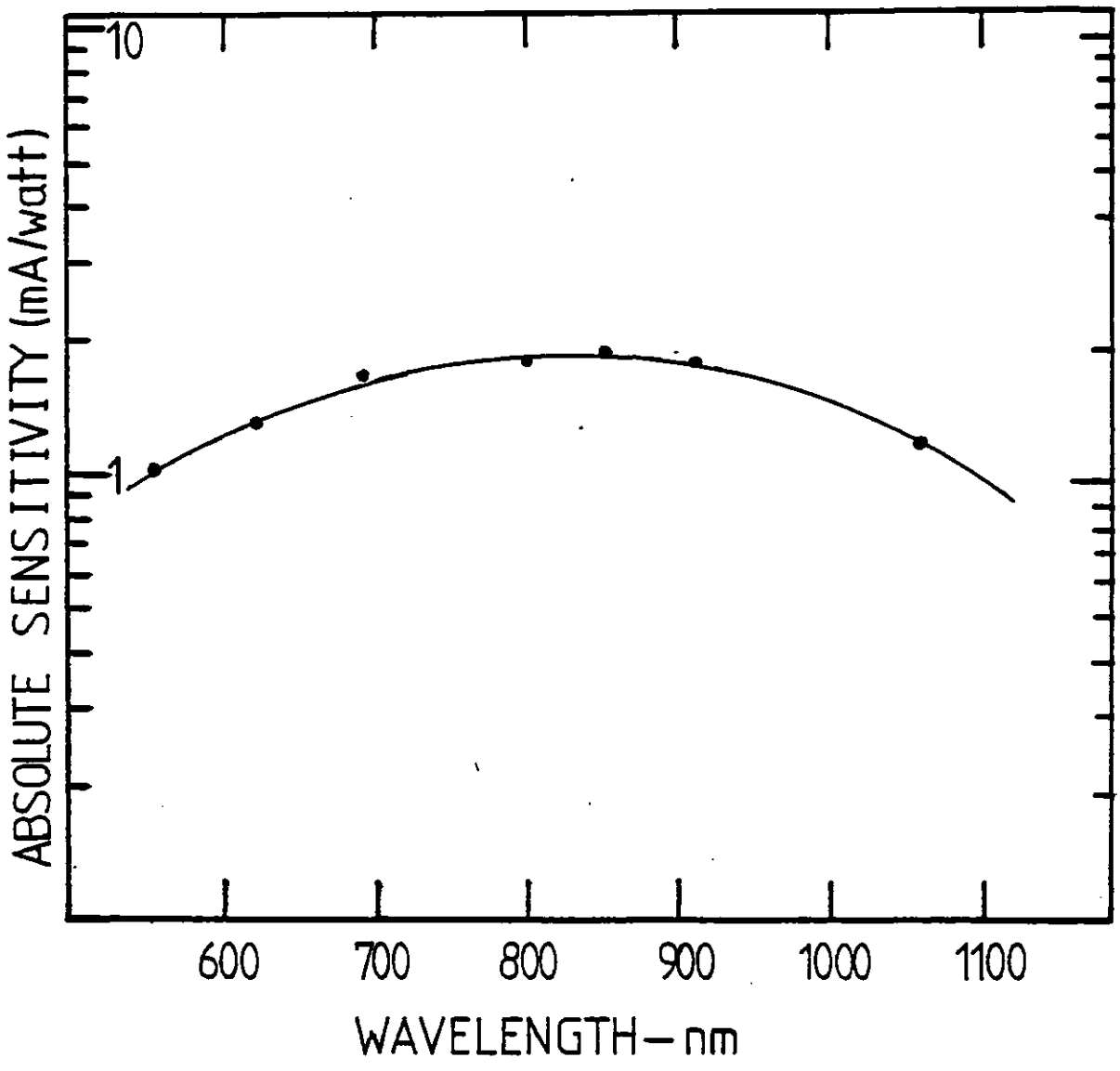


Fig.6·13

Transmission Spectral Sensitivity for a Typical Sl Photocathode Produced in this Study.

stated, all the XPS analytical studies and EDC analyses presented in this work were obtained from group "a" type photocathodes.

If at any stage there was a decay in the sensitivity of an S1 cathode, whether due to electron bombardment in AES, X-ray bombardment in XPS or a decay over a few hours in the UHV system, due to intrinsic cathode instability, it was always the photosensivity in the infra-red and threshold regions of the spectrum which decayed first, leaving the sensitivity at wavelengths less than ∿700nm virtually unchanged.

6.3.2 S1 Photocathode EDC's

The EDC's obtained from a typical group "a" type S1 cathode in the transmissive mode, with a range of wavelengths throughout the visible and near infra-red and at three different stages in the processing schedule are presented in Figure 6.14.

These curves were obtained under the same experimental conditions as the GaAs EDC's in Section 6.2.2, and to test for the effects of instrumental resolution on them, they were visually compared with computer synthesised curves. The curves "f" in Figure 6.14 (dashed lines) were synthesised from a room temperature Fermi function convolved with a Gaussian peak with σ=21meV(representing the 50 meV FWHM analyser resolution function, as described in Section 4.6), and scaled to the height of the experimental EDC. The curves "s" (dotted lines in Figure 6.14) were synthesised from a step function convolved with the analyser energy response function.

As can be seen in Figure 6.14, at all stages in the processing schedule and for the majority of incident photon wavelengths, the low kinetic energy sides of the EDC's show a more gradual tail off than can be explained by the instrumental resolution alone. The only

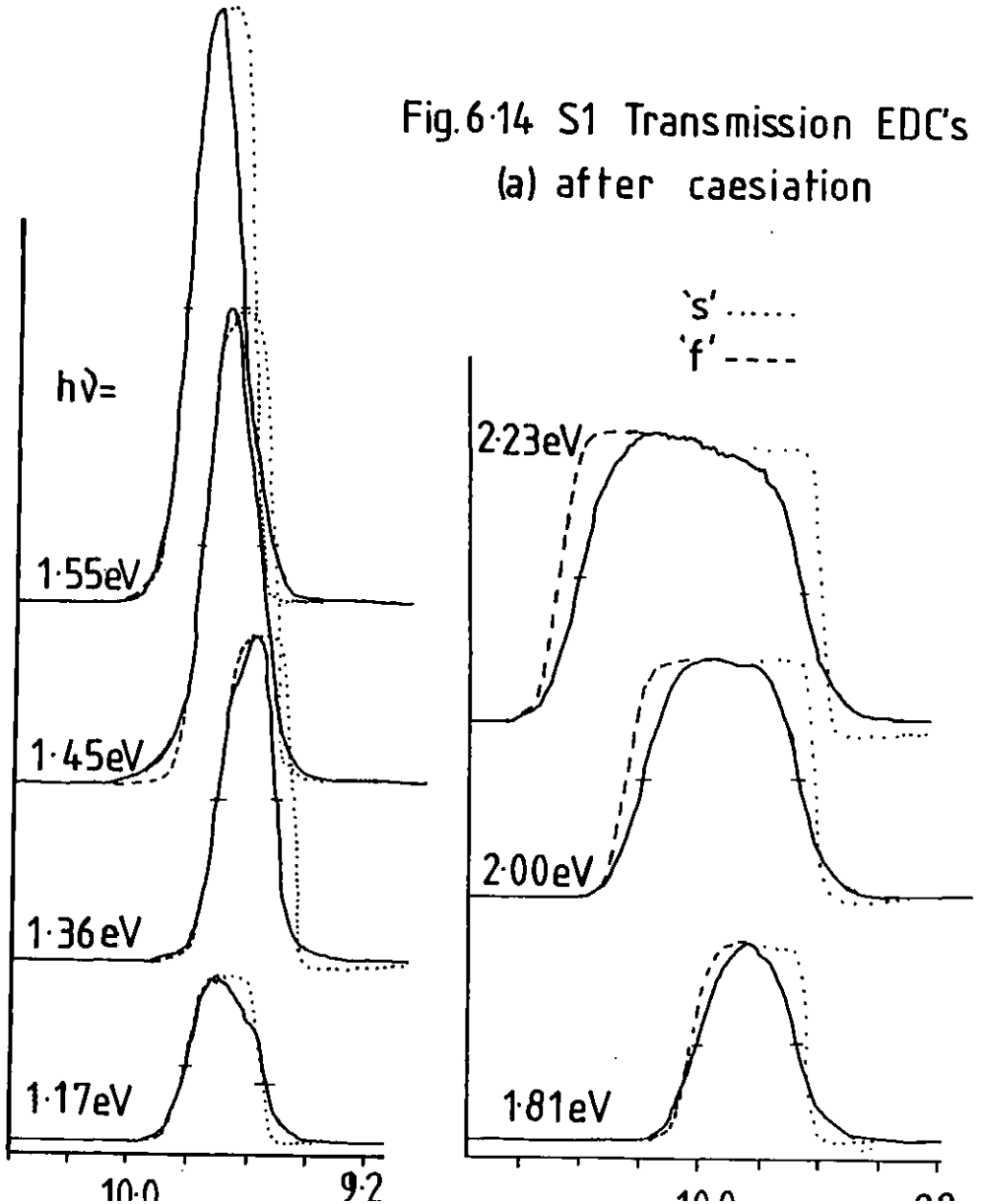


Fig. 6·14 S1 Transmission EDC's
(a) after caesiation

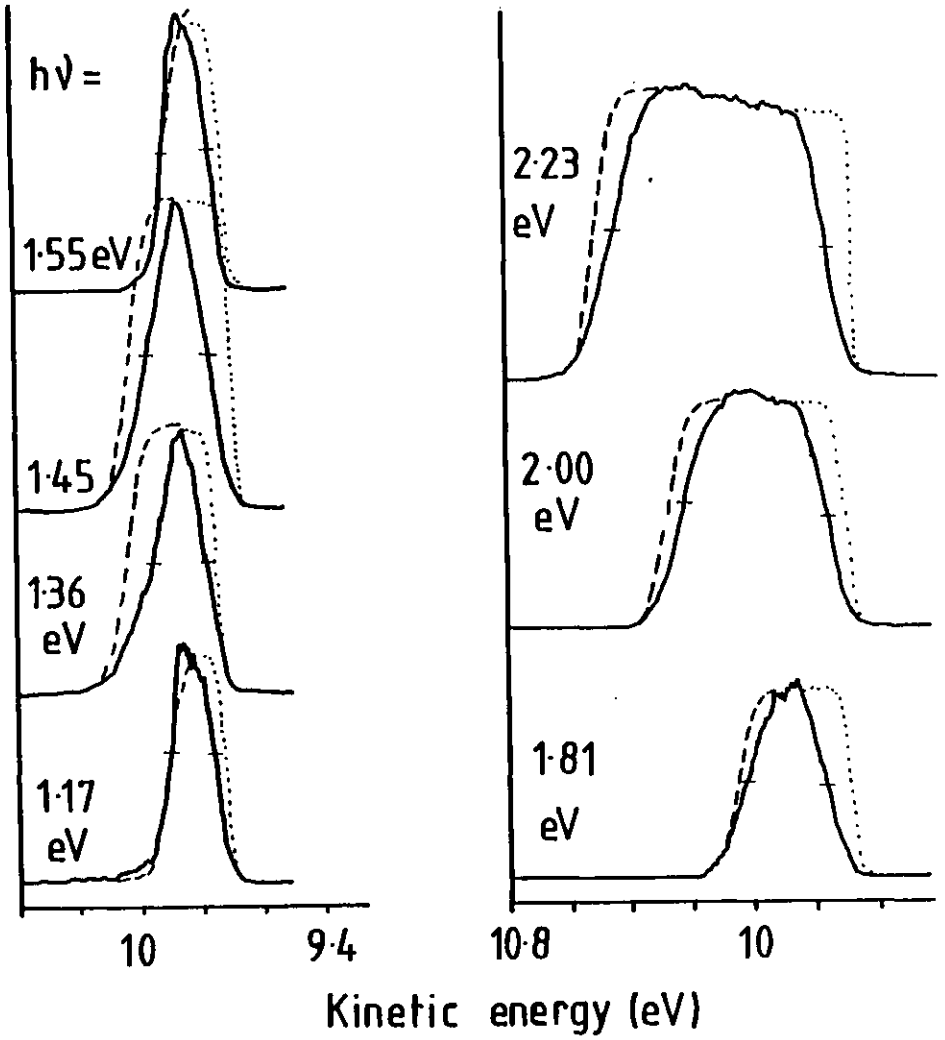
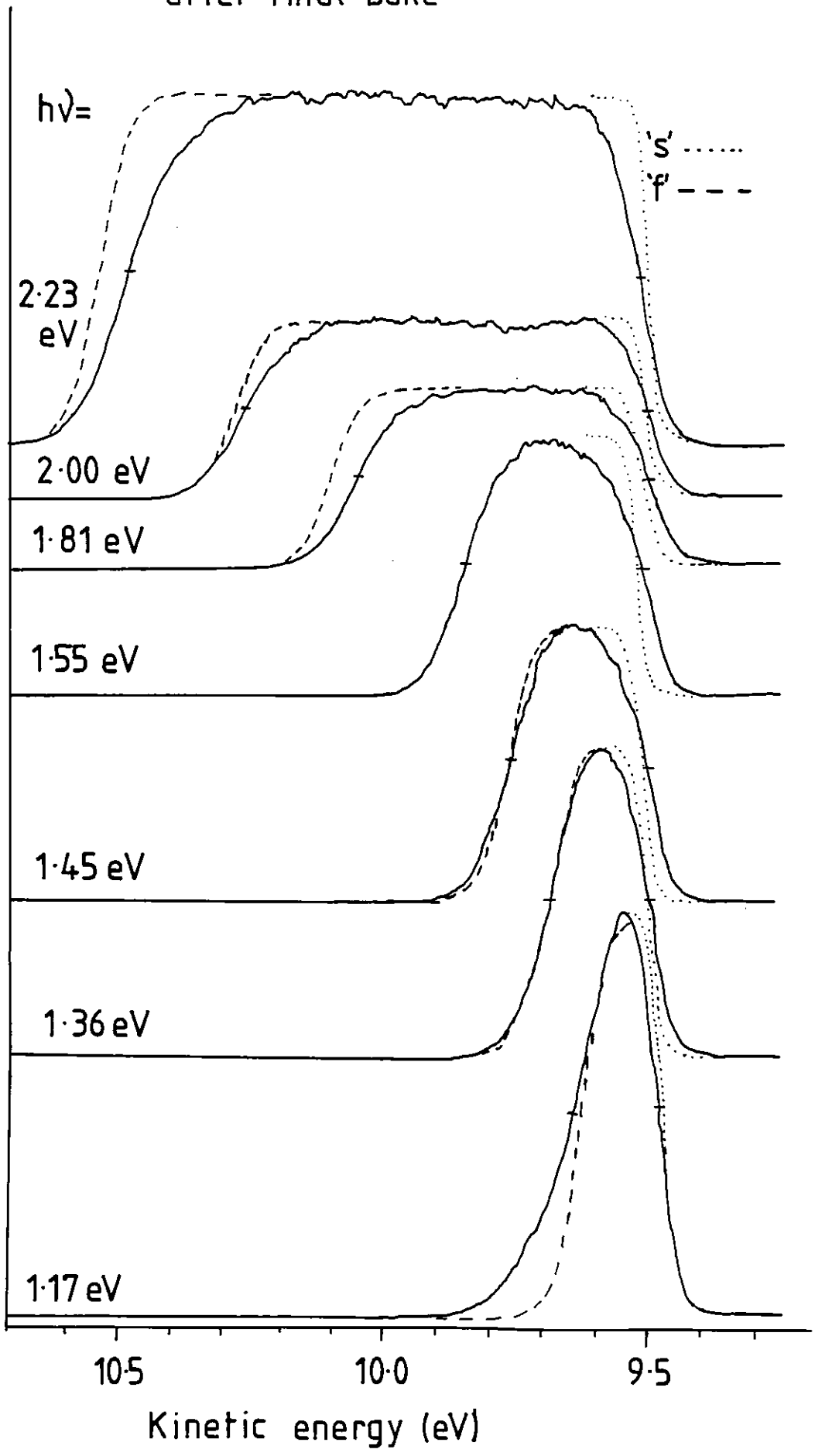


Fig. 6·14(b) S1 EDC's after 2nd silver evaporation.

Fig 6·14 (c) S1 Transmission EDC's after final bake



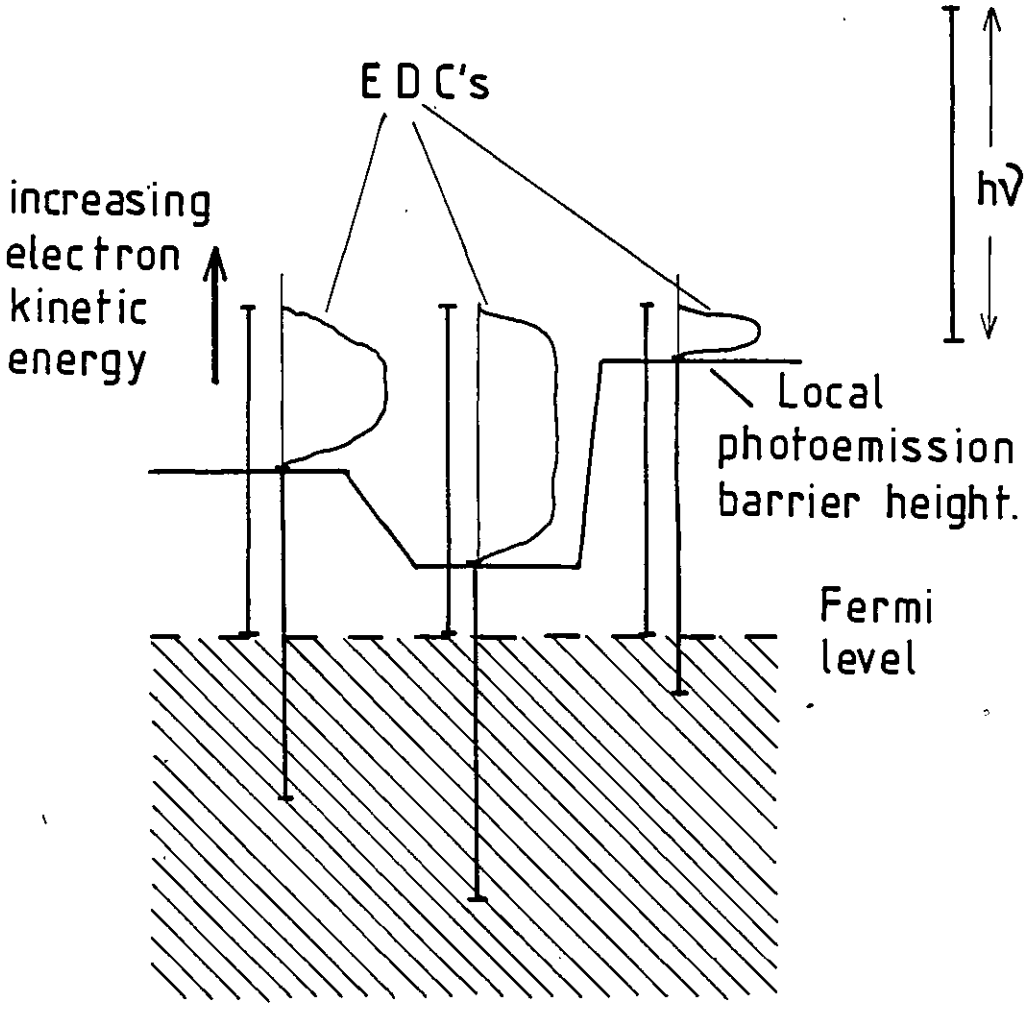


Fig.6·15.

Diagram Showing the Effect of Patchiness
in the Photoemission Barrier Height
on the EDC'S.

exceptions to this phenomenon occurred at wavelengths close to the cathode photoelectric threshold where at all stages in the processing the low energy cut-off was very sharp and was described well by the step convolution curve.

Since the electron spectrometer measures the energies of the photoelectrons relative to the Fermi level in the photocathode, such a gradual tail-off in the low kinetic energy side of the EDC's can be explained in terms of the generally accepted non-homogeneity of the photoelectric work function of the S1 cathode.

Referring to Figure 6.15 it can be seen that if the high energy photoelectrons are being excited from states near the Fermi level then the shape of the high energy cut-off of the EDC's (in the absence of scattering effects) will be independent of the local work function of the cathode. On the other hand the low kinetic energy cut-off region of the EDC consists of photoelectrons which have been excited from well below the Fermi level with only just enough energy to clear the local photoemission threshold limiting barrier (whether this limiting barrier occurs at the Ag-Cs_2O interface or the Cs_2O vacuum interface) and will thus be dependent on the local photoelectric work function.

In the measured EDC's therefore, a patchy photoelectric work function will result in a "smearing-out" of the low energy cut-off. In the case of threshold response EDC's the majority of the photocurrent would be coming from the low photoelectric work function patches, and the EDC shapes would therefore be representative of a much narrower range of surface barrier heights. Inspection of Figure 6.14 shows that a surface photoelectric work function variation of $\sim$ 150 meV would be sufficient to explain the low energy cut-off shapes seen in these EDC's.

On the basis of the arguments outlined above it might be expected that to a first approximation the shapes of the high energy cut-offs of the EDC's should reflect only the energy dependence of the density of states in the region of the Fermi level and be largely independent of photon energy. Generally this is found to be the case and the high energy cut-off was more gradual than would be predicted by the Fermi function curve for all but the lowest photon energies where the fit with the "f" curve was quite good. The one exception to this rule was the EDC for λ = 1.06μm after the final baking stage, where it was suspected that the very small percentage of white light leakage through the interference filter used at the time, coupled with the high relative sensitivity of the cathode to visible light at this stage was giving an artificially extended high energy tail on the EDC.

Attempts were made to calculate photoelectric work function values from the widths of the EDC curves. For this purpose the widths of the EDC's were calculated by measuring the energy interval between a point halfway up the low kinetic energy edge of the EDC (to approximate to an average low energy cut-off for the whole surface), and a point halfway up the high kinetic energy edge (approximating to the kinetic energy of photoelectrons emitted from states at the cathode Fermi level). The points chosen are marked in Figure 6.14.

Substracting the EDC widths measured in this way from $h\nu$ afforded an estimate of the cathode photoelectric work function. The results are tabulated in Figure 6.16, together with the kinetic energies of the points chosen by the procedures outlined above.

Group "a" and group "b" cathodes, as well as differing in their behaviour on processing, showed notable differences in their EDC data. Figure 6.17 shows EDCs from a group "b" photocathode at the

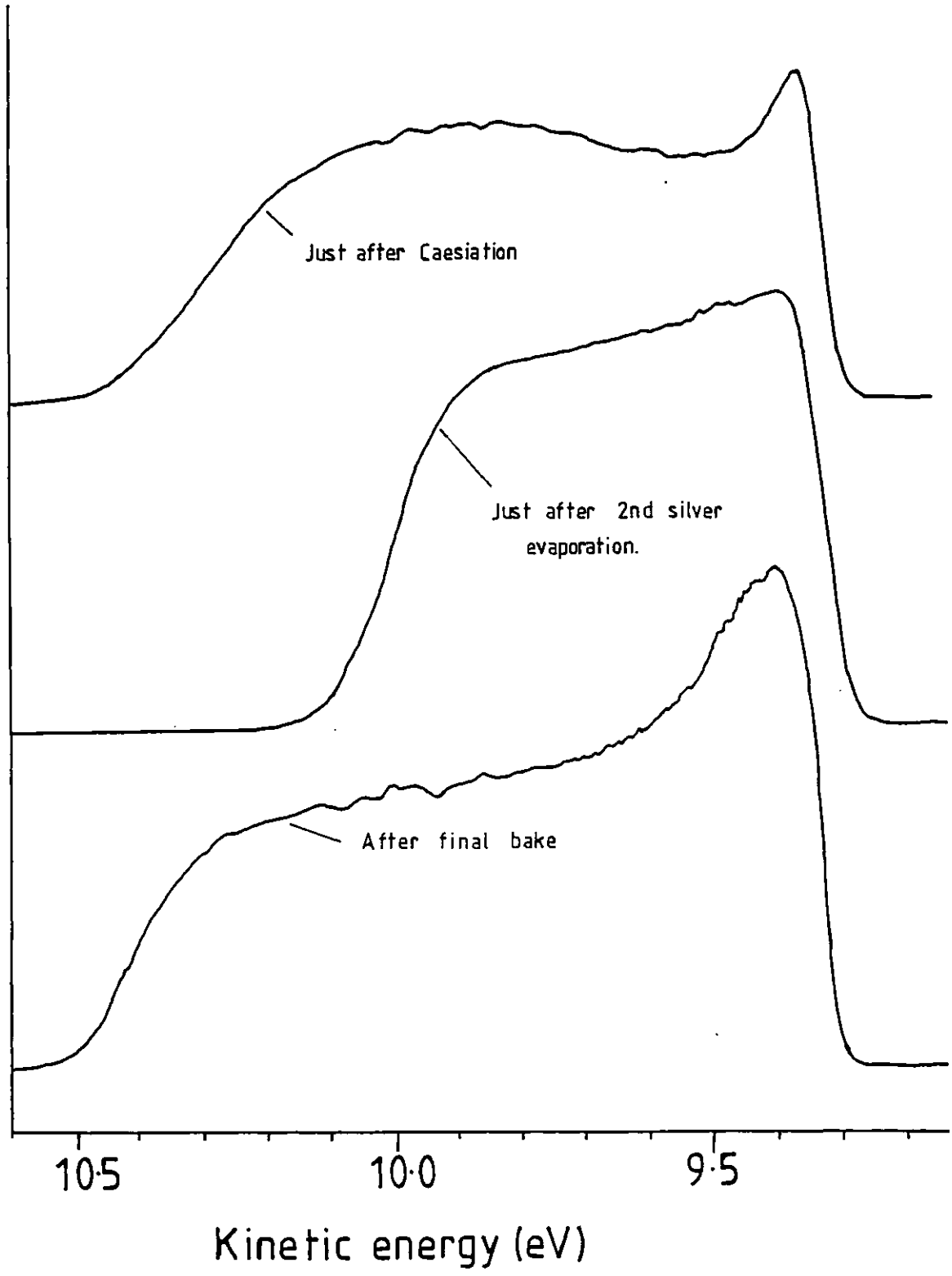


Fig.6·17

Transmission EDC's at hν=2.23eV for a Typical Group "b" Type S1 Photocathode at Various Stages in the Processing.

three stages in the processing schedule as apply to Figure 6.14. The "b" cathodes exhibit lower work functions (∿ 1.2eV after caesiation, 1.55eV after the second silver evaporztion and ∿1.16eV after the final bake) and a prominent peak in the EDC's which occurs at the instrument limited low energy EDC cut-off for all wavelengths. The high energy cut-off of the EDC's are also considerably more gradual than is the case with the group "a" cathodes at similar stages in processing.

Processing Stage		2.23	2.00	1.81	1.55	1.45	1.36	1.17
After step (c) Caesiation	Low KE	9.68	9.69	9.69	9.66	9.58	9.52	9.4
	High KE	10.42	10.22	10.02	9.84	9.78	9.72	9.82
	ϕ (est.)	1.49	1.47	1.48	1.37	1.25	1.16	0.75
After step (d) Second Ag evap.	Low KE	9.77	9.77	9.77	9.77	9.77	9.77	9.77
	High KE	10.45	10.22	10.02	9.91	9.97	9.95	9.90
	ϕ (est.)	1.55	1.55	1.56	1.41	1.25	1.18	1.04
After step (e) Final baking press	Low KE	9.51	9.49	9.49	9.51	9.50	9.49	9.47
	High KE	10.48	10.52	10.04	9.87	9.75	9.68	9.64
	ϕ (est.)	1.26	1.24	1.26	1.19	1.20	1.17	1.00

Figure 6.16 SI Photocathode EDC work function measurement data all figures in eV units.

Figure 6.18 is a reproduction of an EDC produced by a group "a" type photocathode operating in the technologically important threshold spectral region with spectrally pure radiation produced from a 1.3μm laser diode.

The 109 meV FWHM EDC width at this wavelength would result in a very high temporal resolution for such a photocathode in a streak tube. The measured intensity of the thermionic peak (plotted here with a tenfold increase in sensitivity), corresponds to a photocathode noise limited minimum detected intensity of $\sim 0.1\mu W\ mm^{-2}$ CW at this wavelength (such an illumination would give a signal-to-noise ratio of 2:1 at the screen, quite adequate for synchroscan

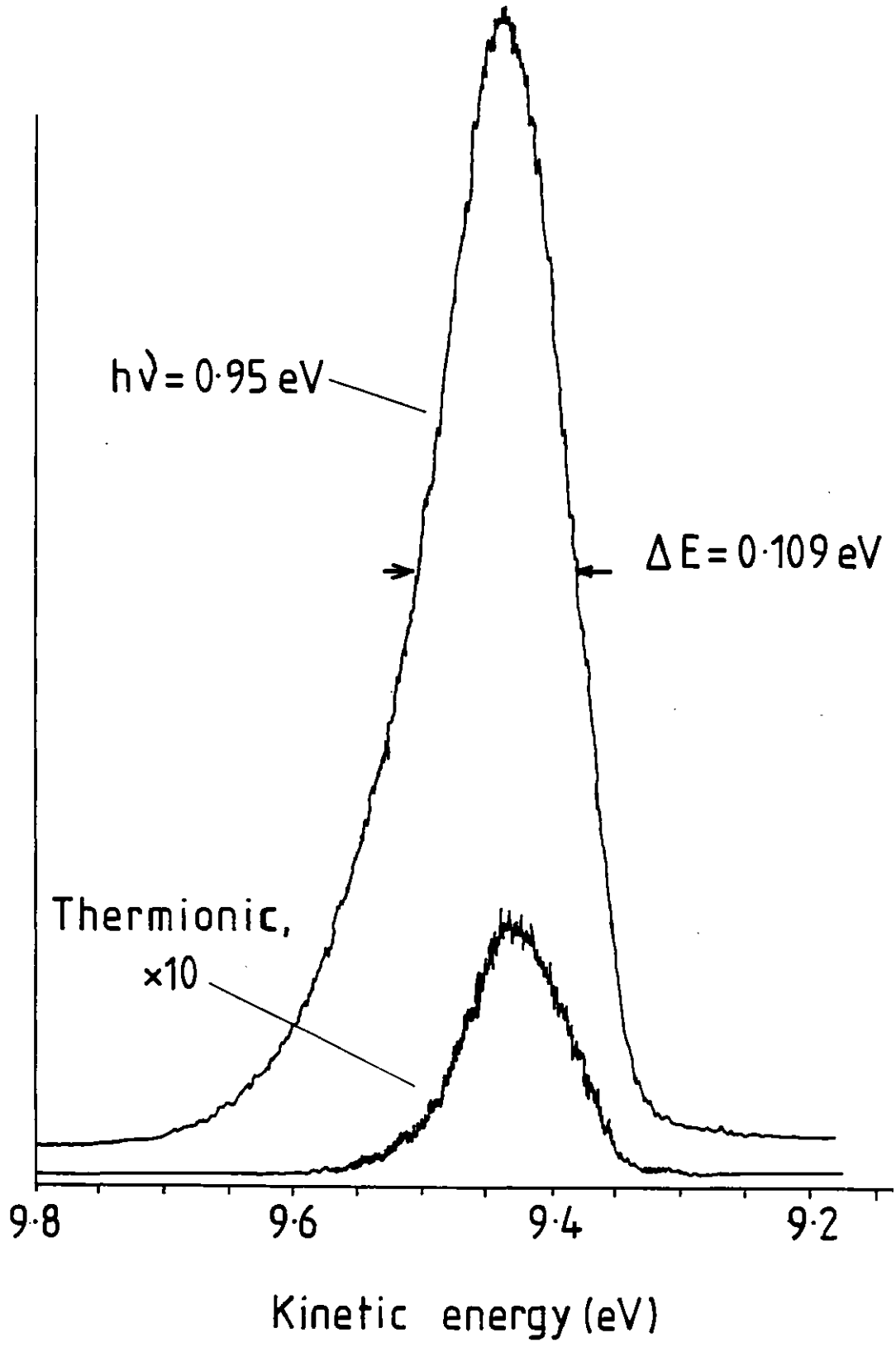


Fig.6·18.

Transmission EDC at λ=910nm for a Group "a" Type Photocathode.

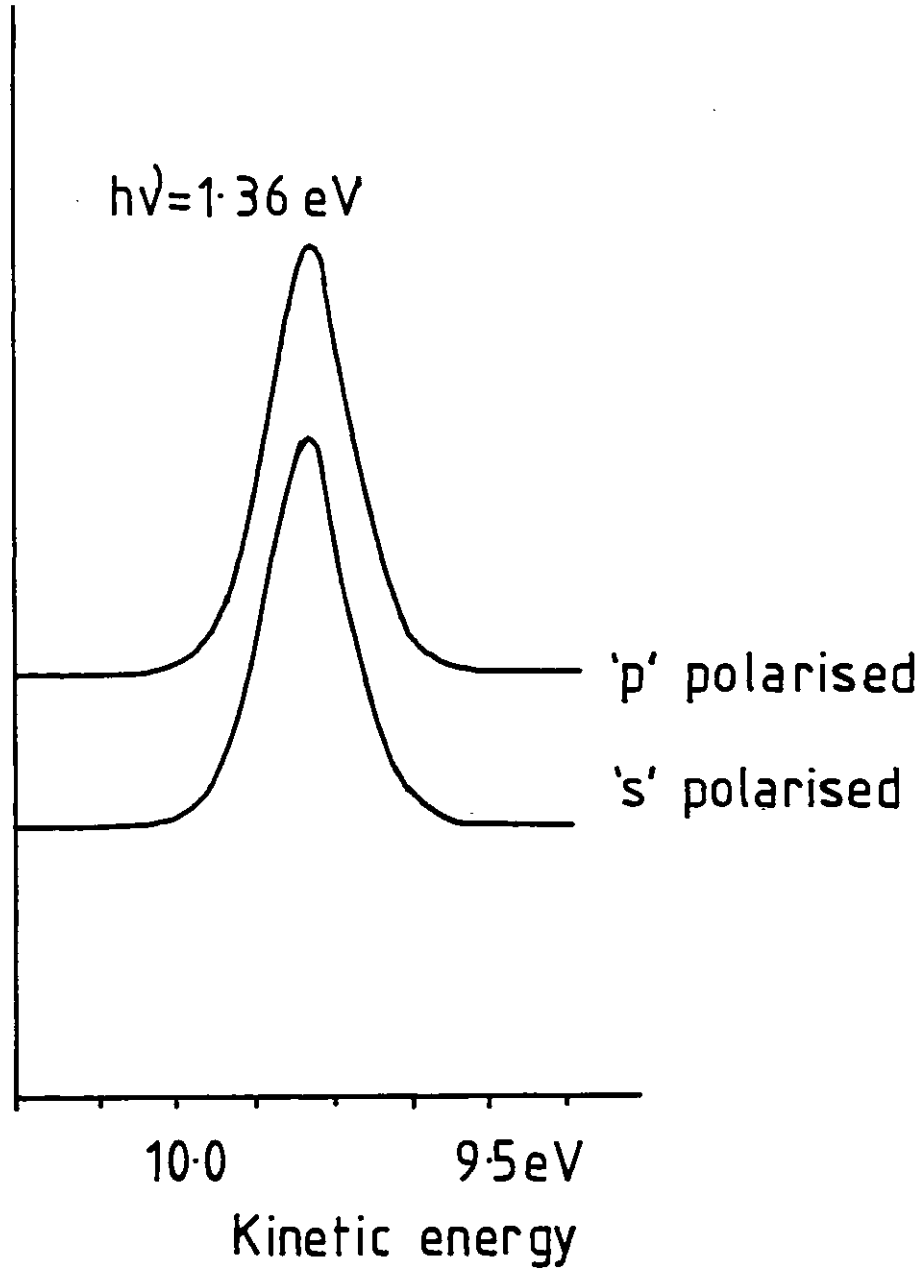


Fig.6·19

Reflection EDC's at = 910nm, with Light Incident at 45° to the Surface Normal of a Typical Group "a" Type S1 Photocathode.

operation where noise effects can be averaged out).

6.3.3 Polarisation dependence of S1 Photocathode sensitivity

In view of the current theoretical models which attempt to explain the threshold response of the S1 cathode in terms of surface plasmon effects, the polarisation dependence of the S1 sensitivity and the polarisation dependence of the EDC shapes was investigated in detail.

Due to the geometry of the UHV equipment the EDC's had to be taken in the reflection mode for these non-normal incidence experiments, and Figure 6.19 shows the EDCs obtained for a representative group "a" cathode at λ = 910 nm, with the light incident at $\sim$ 45° to the vacuum surface normal for both "s" and "p" polarisations.

There was no polarisation dependence of the EDC shape apparent in these curves, or indeed in any of the EDCs at other wavelengths, and the differences in the EDC heights between the two polarisations could easily be accounted for by the polarising effects of the various mirrors used to steer the light onto the photocathode surface.

As a check on this latter conclusion the polarisation dependence of the transmission sensitivity (corrected for reflected radiation) of a small test cell containing a normal commercial type S1 photocathode was measured using the experimental arrangement depicted in Figure 6.20a. The ratio of the reflection corrected photoelectron yields for the "p" and "s" polarisations of the incident illumination, Y_p/Y_s, is plotted as a function of incident wavelength in Figure 6.20.

As the graph shows the measured Y_p/Y_s ratio (the "vector ratio" as defined by Flödstrom et al., 1975) is unity to within the $\sim$ 10% experimental error throughout the S1 photosensitivity wavelength range.

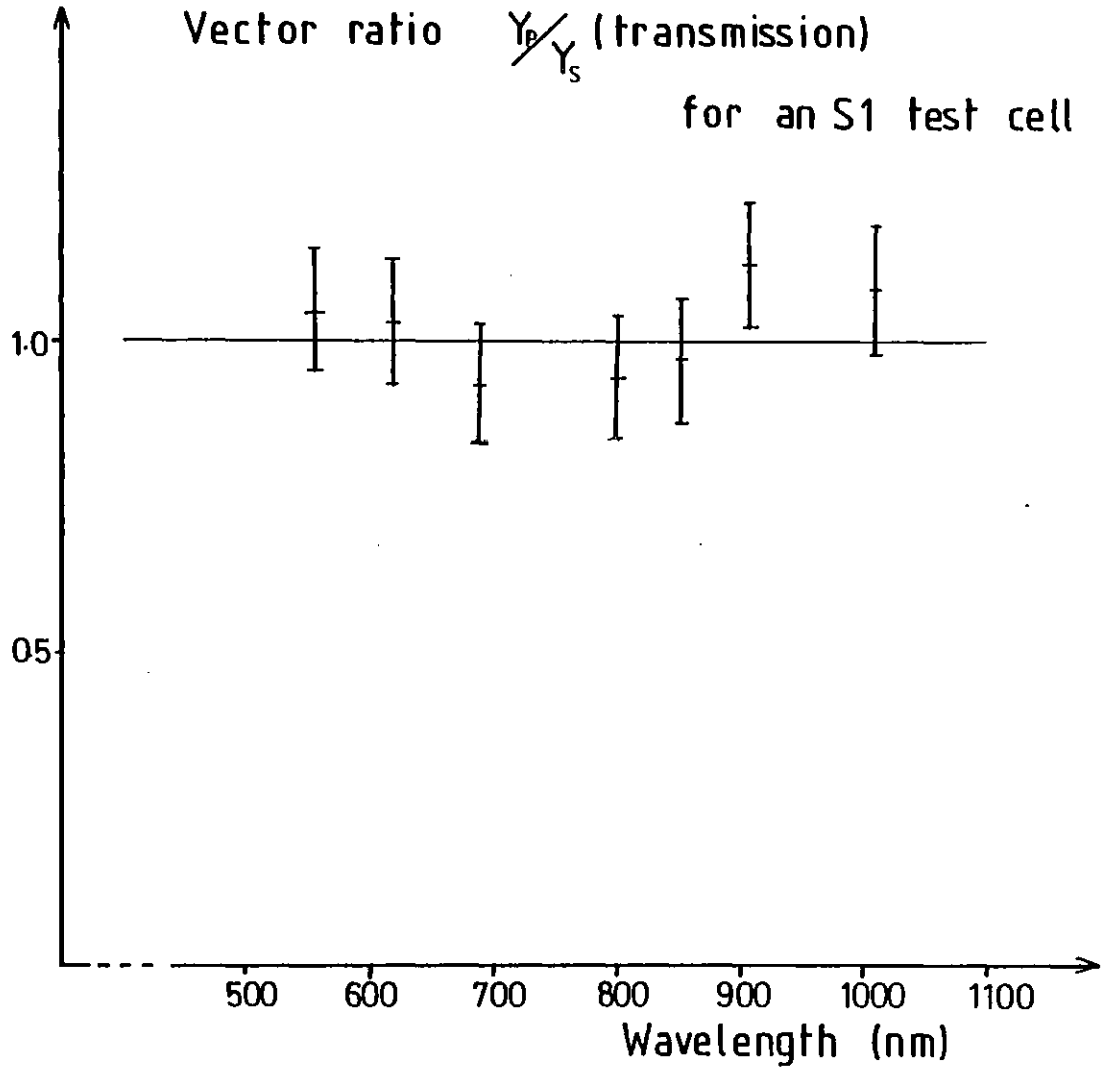

Vector ratio Y_p/Y_s (transmission)
for an S1 test cell
1·0
0·5
500
600
700
800
900
1000
1100
Wavelength (nm)

Fig. 6·20

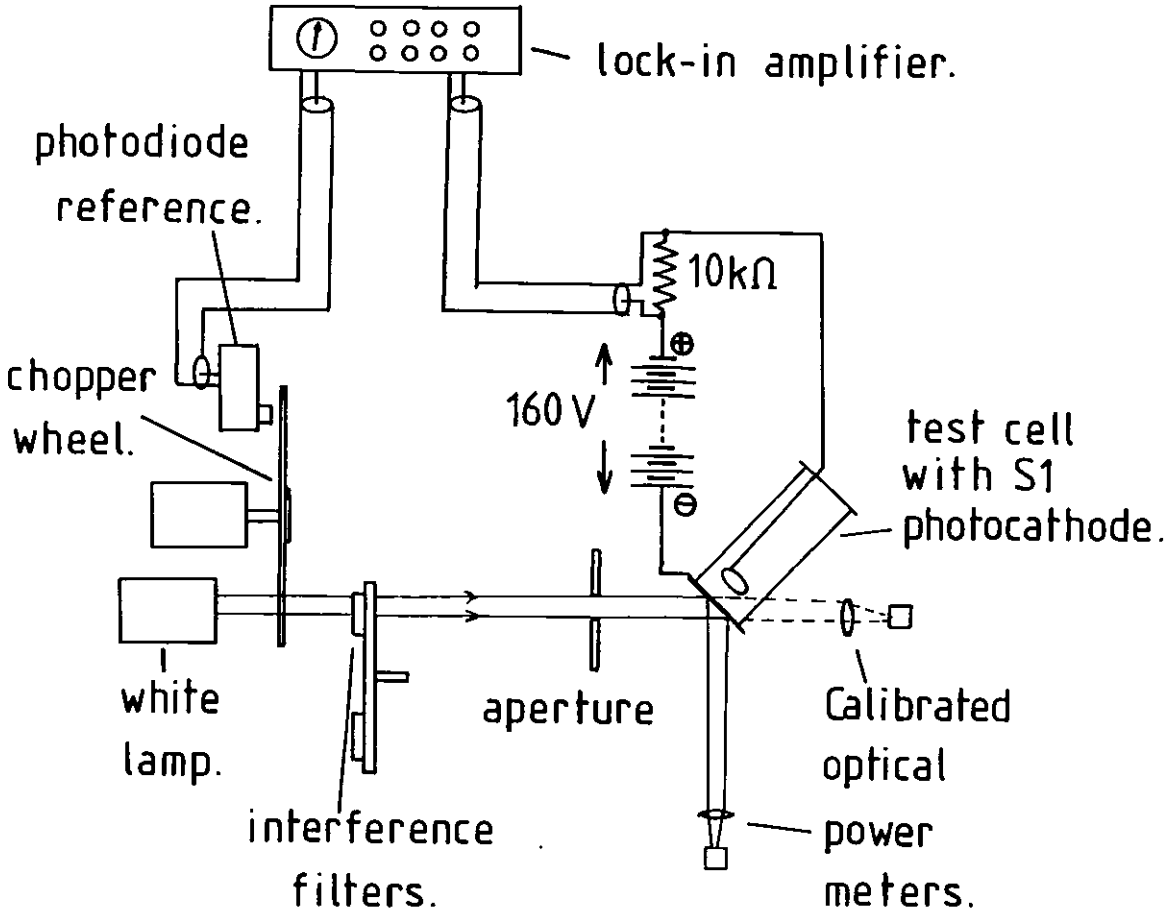


Fig.6·20a

Apparatus used to measure the polarisation dependence of S1 photosensitivity.

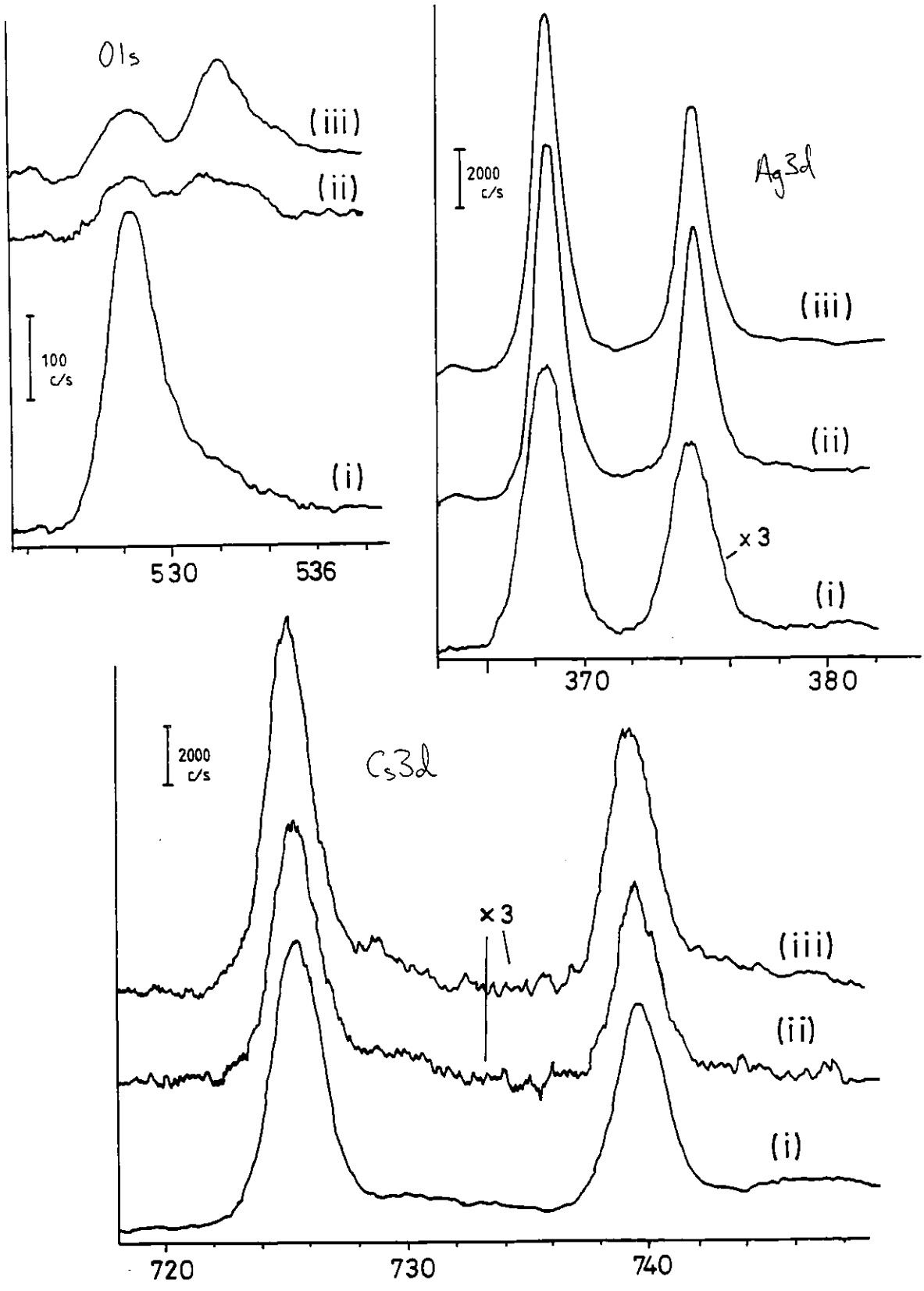


Fig. 6·21.

O take off XPS Spectra for a Typical S1 Cathode at Various stages in the Processing Schedule.

(i) Just after Caesiation.
(ii) Just after the 2nd Silver Evaporation.
(iii) After the Final Bake Process.

6.3.4 S1 Photocathode XPS results

Figure 6.21 shows XPS spectra taken of one of the group "a" type S1 photocathodes at various stages in the processing schedule. The peaks labelled (i) were taken just after caesiation (i.e. step (c) in 4.3.1(b)), at which point the photocathode resistance was high and considerable sample charging problems were encountered. The sample charging voltage also appeared to vary between traces, making accurate binding energy measurements impossible. It was possible however to identify the oxygen 1s peak occurring at this stage as being at a binding energy approximately corresponding to the lower of the split O1s peaks which appeared later on in the processing.

Charging shifts on the other peaks were eliminated by substracting the necessary voltage to make their energies coincide with those of the peaks (ii) which were taken after the second silver evaporation (step (d) in 4.3.1(b)), when the photocathode resistance was very low. The peaks (iii) were taken at the end of the cathode processing schedule and in all cases showed binding energies which were the same (to within the 0.1eV measuring accuracy at this stage) as the peaks (ii)). These experimental binding energy values are tabulated in Figure 6.22.

XPS Peak	Binding energy/eV
O1s (low binding energy)	528.5
O1s (high binding energy)	531.5
$Ag3d^{3}_{2}$	374.5
$Ag3d^{5}_{2}$	368.4
$Cs3d^{3}_{2}$	739.5
$Cs3d^{5}_{2}$	725.4

Figure 6.22 XPS Binding energies for the S1 photocathode

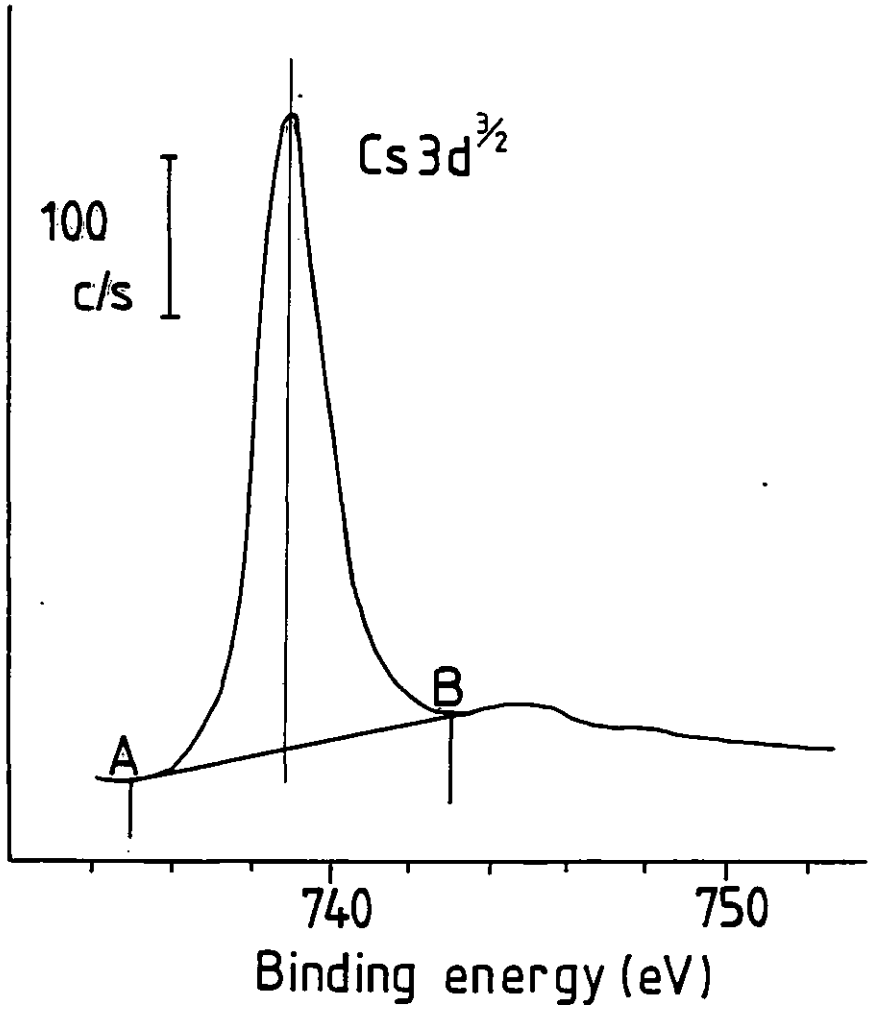


Fig.6·23

Background determination on the Cs $3d^{3/2}$ XPS peak.

The XPS spectra in Figure 6.21 were all recorded at a take off direction perpendicular to the cathode surface, but complimentary spectra, recorded at take-off directions of 30° and 60° to the surface normal showed the same XPS peak energies.

Elemental ratios were derived from the XPS peak intensities using the quantification scheme described in detail in Chapter 5. For this purpose interest was confined to the $3d^{3/2}$ peaks of silver and caesium since the $3d^{5/2}$ peaks also contained X-ray satellite structures of unknown intensity which made background determination difficult. A decision of what constituted the peak area in the case of the $C3d^{3/2}$ peak was further complicated by the existence of a prominent inelastic tail. The peak area in this case was therefore determined by taking the two limiting points (A and B in Figure 6.23) to be 4 eV either side of the peak, so as to exclude the inelastic tail, in accordance with the sampling depth considerations outlined by Seah (1979a). Where a split O1s peak was encountered, the calculated elemental ratios refer to the sum of the intensities of both the split peaks.

For the cathode giving the XPS spectra in Figure 6.20, the measured Cs:O ratio was found to be 2.10 ±10% at each stage in the processing, moreover the measured Cs:O ratio was found to be completely independent of X-ray photoelectron take-off angle. This behaviour was typical of all the "a" type photocathodes, and although the measured Cs:O ratio of other group "a" cathodes ranged between extremes of 2.8 and 1.5 from cathode to cathode, for any particular cathode the ratio remained constant to within ∿ 10% throughout the processing schedule and was independent of take-off angle to the same extent. The mean value of the observed Cs:O ratio, based on a large S1 photocathode population giving > 50 readings, was 2.08±0.36.

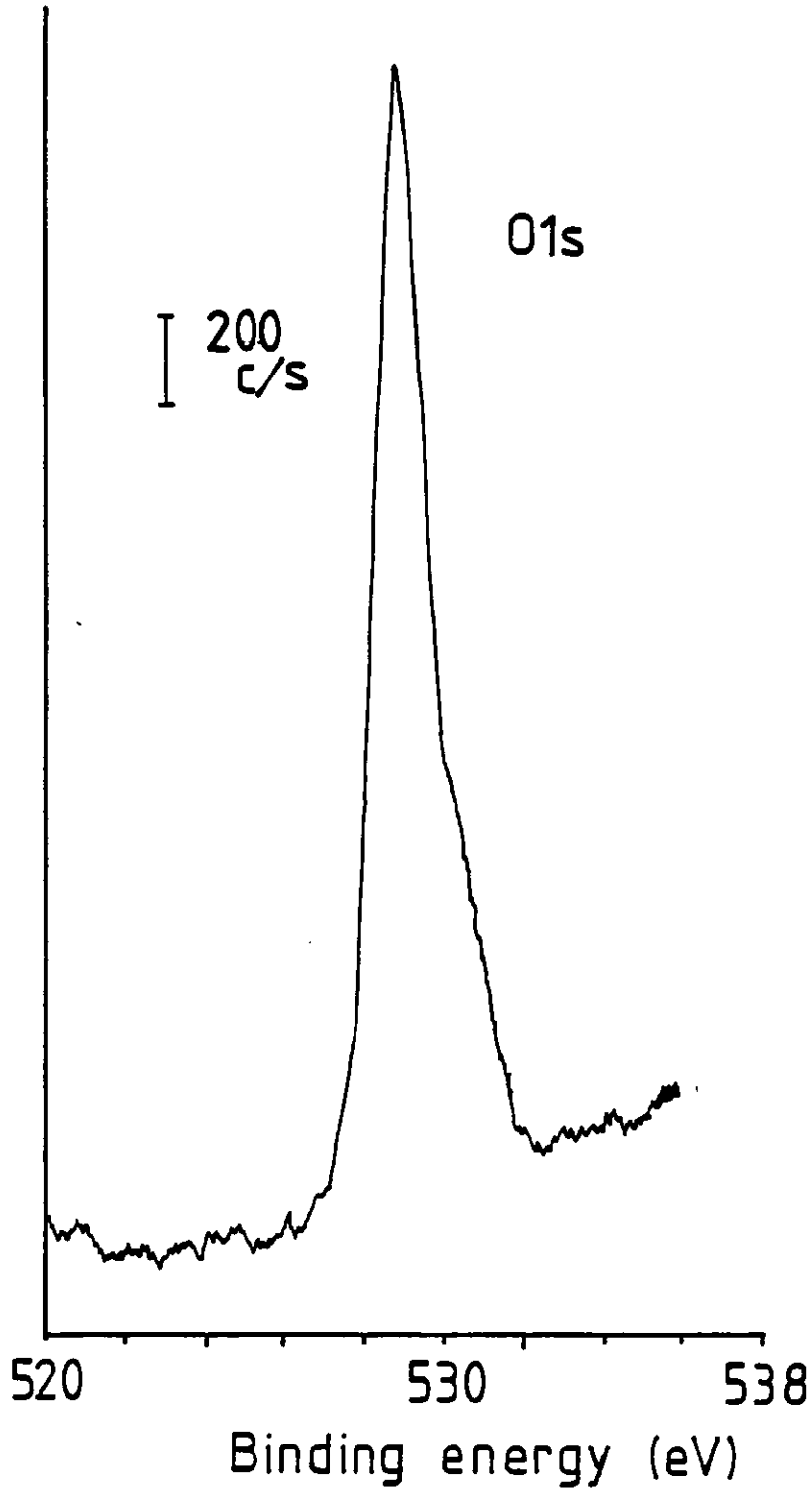


Fig.6·24

O1s XPS Peak from the oxidised solid silver stub.

The Cs:Ag ratio was also calculated from the $Cs3d^{3/2}$ and the $Ag3d^{3/2}$ XPS peak intensities. Again this ratio was found to be independent of XPS take-off angle for the group "a" type cathodes, but varied (not suprisingly) considerably during processing, the cathode population giving values of 0.65±0.08 just after caesiation, 4.1±1 after the second silver evaporation and 2.2±0.8 for the final photocathode.

Attempts had been made to obtain XPS spectra of the oxidised silver base (i.e. directly after step (b) in 4.3.1(b)), but severe charging problems were encountered with the insulating oxide film on the insulating fused silica base. Binding energy measurements proved impossible at this stage, but peak intensity measurements gave a silver:oxygen ratio of 1.5. The presence of small silicon peaks in the wide-scan spectra at this stage however, suggested that perhaps some of the observed O1s signal might be coming from the silica substrate.

To test this theory XPS traces were run of a pure solid silver sample stub which had been argon-ion cleaned, annealed, and then oxidised in a glow discharge for the same length of time and with the same discharge current and voltage as the S1 photocathode base layers. This stub also showed a silver:oxygen ratio of 1.5 for all take off angles. The O1s spectrum of the oxidised stub showed a single oxygen peak at a binding energy of 529.0eV (Figure 6.24).

There was a noticable correlation between the appearance of the high binding energy O1s peak in the cathode film and the increasing silver concentration in the photocathode films as cathode processing progressed. In Figure 6.25 O1s XPS spectra for a number of group "a" cathodes have been arranged in order of increasing Cs:O ratio. Comparing Figures 6.25(a) and 6.25(b) for a particular photocathode it is clear that although there is a

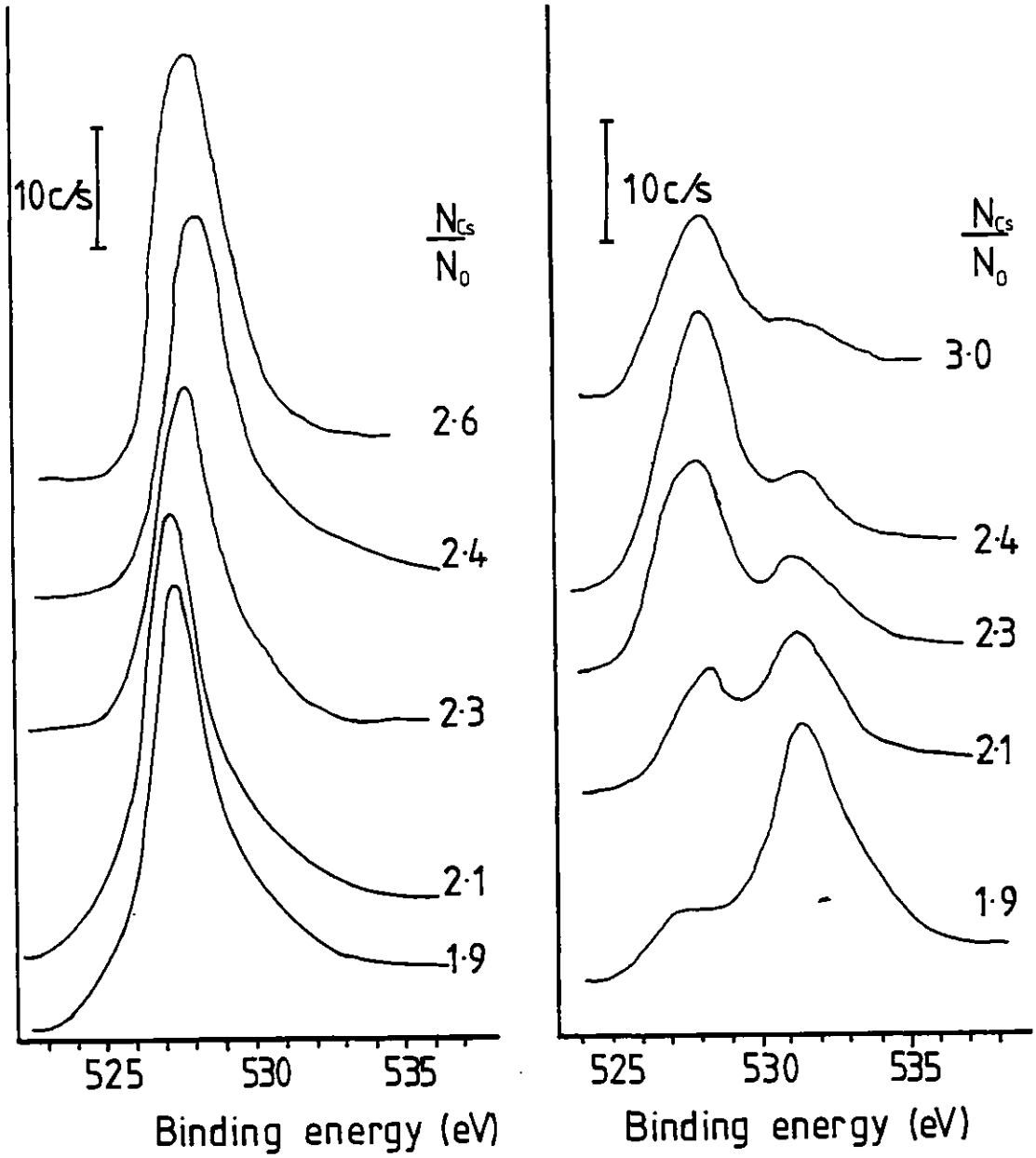


Fig.6·25

O 1s XPS traces from a number of Group "a" Photocathodes at two Different Stages in the the Processing.

considerable variation in the ratios of the two portions of the O1s peak from cathode to cathode, the second silver evaporation and subsequent baking increases the intensity of the higher binding energy O1s peak at the expense of the lower one in all cases, with the magnitude of the higher binding energy peak generally being larger for smaller measured Cs:O ratios.

For a comparison with the Cs_2O overlayer on the GaAs NEA photocathodes the width (FWHM) of the $Cs3d^{5/2}$ peaks from the completed group "a" type S1 films was measured, giving a mean result of 2.09±0.08eV.

6.4 Conclusion

A large volume of original experimental data on both types of infra-red sensitive photocathode has been presented.

In particular it has been shown that under certain circumstances NEA photocathodes can be made with temporal response times as low as 7 ps, implying their potential for use in medium high-speed photography applications in the near infra-red. The EDC's measured from these cathodes have been shown for the first time to be narrow and almost totally wavelength independent essentially "thermalised" electron distributions with widths only just capable of being resolved by the spectrometer.

The results of XPS studies of a large number of S1 photocathodes have also been presented and they show an atomic Cs:O ratio of 2:1. Although there was a noticeable cathode to cathode variation in this ratio, for each cathode it was found to be independent of XPS take-off angle, and constant throughout the processing schedule after the caesiation step.

The Ag:Cs ratio however was found to vary during the processing being 0.65±0.08 after caesiation, 4.1±1 after the second silver evaporation and 2.2±0.8 for the final photocathode. Investigation

of the O1s XPS spectra revealed twin O1s peaks, one occurring at a binding energy of 528.5 eV and the other at 531.5 eV. The relative intensities of these two peaks were found to change during photocathode processing even though the overall caesium:oxygen ratio remained constant. The appearance of the higher binding energy peak correlated well with the introduction of silver into the photocathode film.

Analysis of the EDC's from the S1 cathodes gave photoelectric work function values of $\sim$1.4 after caesiation, $\sim$1.5 after the second silver evaporation and $\sim$1.20 after the final baking process. Qualitative information about S1 cathode photoelectric work function inhomogeneities was deduced from the low energy cut off regions of the EDCs, and the deductions agreed well with the ideas of Soboleva (1959) and Sommer (1968).

CHAPTER 7

CONCLUSIONS DRAWN FROM EXPERIMENTAL DATA

7.1 Introduction

This chapter summarises the conclusions which were drawn about the structures and modes of operation of the photocathodes produced in this series of experiments. An attempt is made to explain the behaviour of both types of photocathode and the surface analytical results from them in terms of simplified electron structure models.

In the case of the GaAs cathodes the physical structure and emission mechanisms are relatively well established, and have been used to explain the phenomena observed in this study quite satisfactorily. In the case of the Si photocathode however, the results of the XPS analysis in particular cannot be explained by any of the currently proposed structure models of the cathode. A revised cathode structure model is advanced which is capable of explaining all the experimental data obtained from this study.

The chapter concludes by assessing the potential areas for application of both types of cathode material in fast-imaging devices, particularly in the light of the discoveries made in this project.

7.2 Conclusions as to the nature of the GaAs Photocathodes produced in these experiments

The fact that all the GaAs photocathodes showed the flat photosensitivity curves (similar in shape to Figure 6.1), and the very narrow almost wavelength independent EDCs as predicted by Scheer

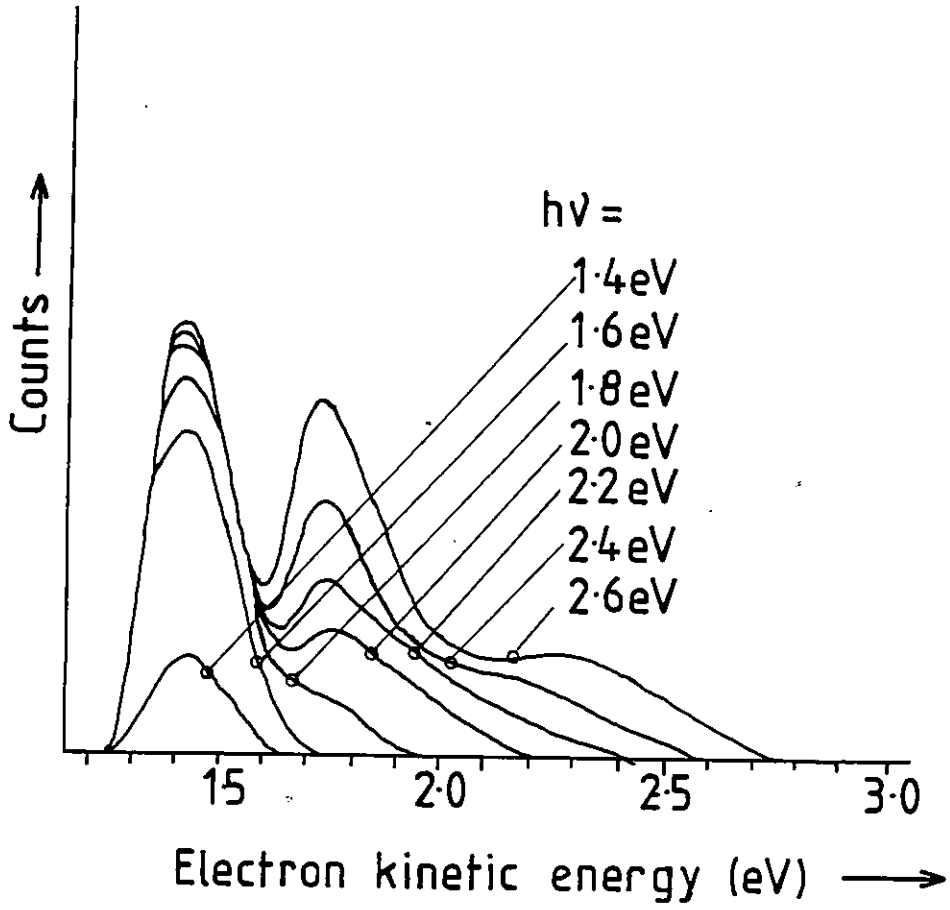


Fig.7·1

EDC's Obtained by James and Moll (1969) from a GaAs-Cs-(O+Cs) Photocathode.

and van Laar (1965) of Figures 6.2 and 6.3 shows that genuine NEA surfaces were in fact being produced.

There are a number of possible reasons for the comparitively low absolute photosensitivitiesobserved. Firstly there was the possibility of unusually high electron-hole recombination velocities at the cathode surface due to defects introduced by the Argon-ion bombardment cleaning. Most other workers (e.g. Allenson et al., 1972) use a heat cleaning process. Secondly inferior bulk crystal quality in the $Ga_xAl_{1-x}As$ substrate layer (due to the fact that it had been bonded on to glass and not epitaxially grown on a single crystal base), may have introduced bulk defect states in the GaAs film causing defect recombination centres in the active layer. Finally there was the possibility that the active GaAs layers in this case were considerably thinner than the optimum thickness of $1\sim2\mu m$.

Of these three possibilities the last is most likely since the substrates were subjected to no less than four of the acid etch cleaning processes of the type described in 4.3.2(b) due to repeated experimental mishaps before the photocathode processing equipment ran smoothly. This conclusion was further reinforced by the correlation between the low cathode photosensitivities and fast temporal responses observed in Section 6.2.3.

The EDC curves observed in this study are quite different in width and overall shape to the reflection EDC curves previously reported by James and Moll (1969) for the (110) face of a GaAs single crystal cleaned in UHV and activated with Cs and O (Figure 7.1). The reason for this discrepancy is not immediately clear. The peaks in the curves in Figure 7.1 are too broad compared with kT to be due to electrons thermalised in the X and Γ minima as claimed by the authors . All the EDCs, especially those at higher photon energies show large amounts of "hot" electron structure at high kinetic energies.

It seems possible in retrospect that the EDCs in Figure 7.1 represent principally "hot electron" spectra from within a few nanometers of a positive electron affinity crystal surface,as opposed to the thermalised distributions which were observed in this study, with nearly all the photoelectrons having thermal energies of $\sim$25 meV in the Γ band minimum. The latter case is the situation one would expect for a true NEA cathode with an emission depth of the order of one micron (Blakemore, 1982; Scheer and van Laar, 1965).

Applying the diffusion model of electron transport (Bell, 1973) to the photocathodes produced in these experiments (the shapes of the EDCs and the spectral sensitivity curves suggest this is reasonable), then the 8psec temporal response of the fastest photocathode would suggest a GaAs active layer thickness of $\sim$ 50nm. The theoretical band bending length in the doped GaAs layer is given by the equation (Bell, 1973)

$$d^2 = \frac{2\varepsilon V_{BB}}{q(N_A - N_D)} \qquad (7.1)$$

Where V_{BB} = Potential difference by which bands are bent

q = average charge on donors/acceptors

N_A = Net acceptor concentration

N_D = Net donor concentration

ε = absolute permittivity of material ($= \varepsilon_o \varepsilon_r$)

Taking ε = 12.85 (from Blakemore, 1982), q=1, N_D=0, $V_{BB} \sim 0.7$eV and $N_A = 10^{18}cm^{-3}$, the equation predicts a band bending distance of d$\sim$10 nm. Considering this fact, together with the 0.8 nm hot electron scattering depth reported by James and Moll (1970) for the GaAs active layer, it can be seen that the GaAs films used in this study were probably almost as thin as was practically possible without destroying the NEA character of the cathode.

The $5x10^{-17}cm^{-3}$ doping of the $\sim$10 μm thick GaAlAs substrate layer implies a bulk resistivity of the order of $1.5x10^{-3}$ Ωm, (using the electron mobility of 8000 $cm^2\ V^{-1}\ sec^{-1}$ from Blakemore, 1982) and consequently even the fastest and least photosensitive of the GaAs films showed no signs of charging (to within the 0.1 eV instrumental resolution of the spectrometer) during XPS, when currents in excess of 100 nA were being drawn from its centre. The calculated resitivity of the substrate of $\sim$50Ω $\square^{-1}$ is on a par with the lowest surface resistivities observed for the S1 photocathode (Hou et al., 1982) and therefore would be expected to result in an excellent dynamic range if it were fitted into a streak tube.

Although this work was done with GaAs with its bandgap limited threshold of $\sim$950 nm (Bell, 1973), the fact that it proved possible to successfully fabricate such thin photocathode films with genuine NEA characteristics and usable infra-red photosensitivities suggests that using some of the known 3-5 ternary compounds with much narrower direct bandgaps may permit the construction of a steak tube with a photoelectric threshold wavelength in excess of 1.5 μm (as reported by Fisher et al., 1972) and a temporal resolution of < 10psec.

As to the nature of the Cs-O overlayer on these NEA cathodes, the Cs:O ratio of 2:1 measured in XPS showed excellent agreement with the exposure measurements of Uebbing and James (1970), and proved to be reproducible to within 10% from one photocathode to another. This was in contrast to the large cathode-to-cathode variation in this ratio observed with the S1 photocathodes, and implies a surface overlayer on the GaAs cathodes with a very well-defined Cs_2O stoichiometry.

In the past two principal models have been advanced to account for the way in which the Cs-O overlayer decreases the work function of the GaAs surface to achieve NEA. In the heterojunction model (Figure 7.2) as featured in the work of e.g. Uebbing and James (1970),

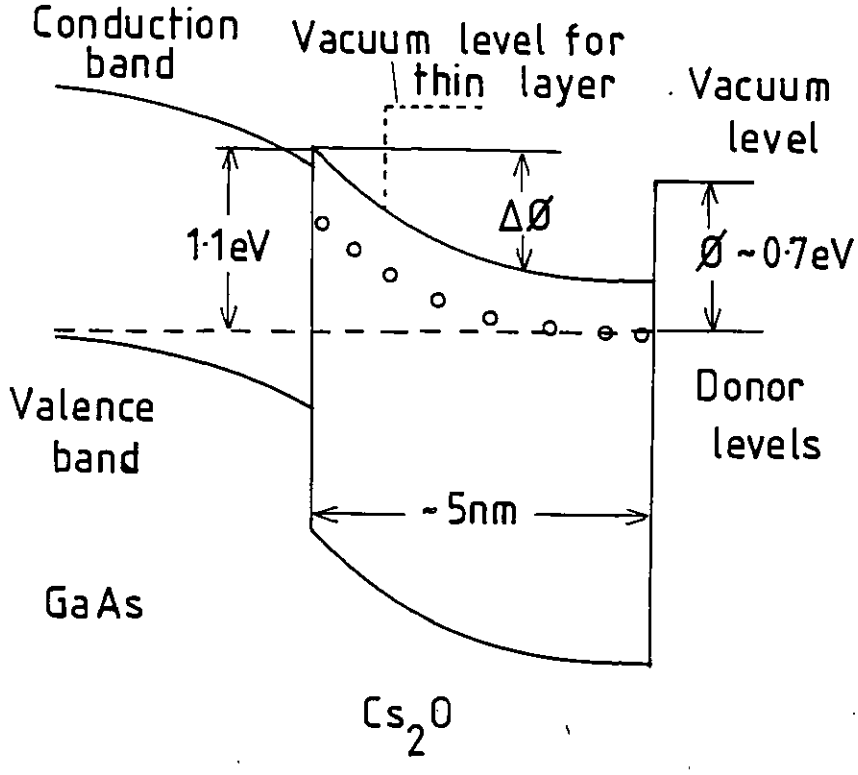


Fig.7·2.

Heterojunction model of the GaAs photocathode surface work function lowering mechanism as proposed by Uebbing and James (1970).

Sonnenberg (1969) and Bell and Spicer (1970) the overlayer is seen as heavily doped n-type semiconducting Cs_2O with a 2eV band gap and band bending throughout its thickness on a scale of 5nm (Uebbing and James, 1970). This band bending means that thicker Cs_2O overlayers result in lower surface workfunctions but higher photoelectron absorption, so that for a given 3-5 material there is an optimum overlayer thickness which respresents the optimum tradeoff between these two considerations. Narrower bandgap materials therefore require thicker overlayers for optimal activation.

In this model there also exists at the interface between the GaAs layer and the Cs_2O layer a potential spike of height equal to the difference between their electron affinities i.e. $\sim$4.4 eV. In the region of this potential spike the potential energy is greater than the photoelectron energy and tunnelling statistics are applicable, although the effect of this on photoelectron escape probability is generally ignored when experimental data is interpreted in terms of this model (e.g. Sonnenberg, 1969).

In the dipole model (e.g. Fisher et al., 1972; Williams and Tietjen, 1971; Sommer et al., 1970), the Cs-O overlayer is conceived of as a single monolayer of Cs_2O on top of a polarised monolayer of Cs ions on the GaAs crystal surface (Figure 7.3). The dipole moment formed by the ionised caesium atom and its image charge is considered to be the principle cause in lowering the height of the interfacial barrier between the two layers to the values of $\sim$1.1 eV which have been deduced from experimental data (e.g. Fisher et al., 1972), and reducing the surface work function.

Clearly one of the main differences between these two models is in the thicknesses they assume for the Cs-O overlayer. Concepts of bulk band diagrams and band bending effects cannot be applied convincingly to Cs-O overlayers only one or two monolayers thick. The experimental data on this subject however is not conclusive.

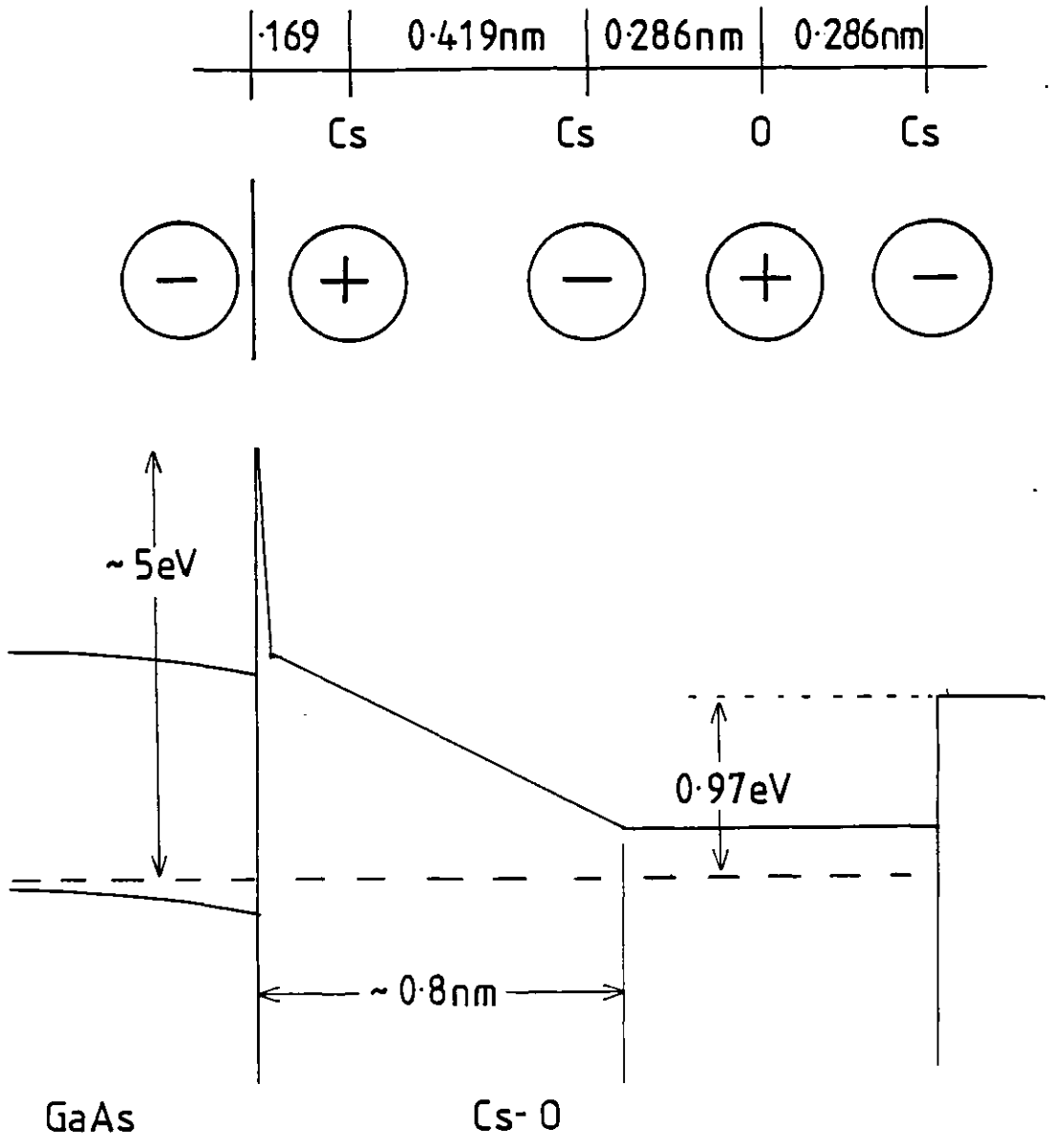


Fig.7·3.

Diploe model of GaAs surface work function lowering mechanism,as proposed by Fisher et al.(1972).

Uebbing and James (1970) for example deduce an optimum photoelectron escape probability on the basis of exposure measurements for a Cs-O monolayer of a thickness corresponding to one Langmuir of O_2. Sommer et al., on the basis of wet-chemical analysis of cathode films deduced a caesium content in the overlayer corresponding to 3 monolayers of caesium. Fisher et al. (1972) deduced an overlayer thickness of $\sim$0.8 nm from an analysis of photosensitivity data, whereas Turnbull and Evans (1968) estimated their overlayers to be between 4 and 10 monolayers thick, agreeing with the "6 layers" deduced by James et al. (1968).

A route out of this confusion was suggested by the work of Uebbing and James (1970). In their experiments with Cs_2O films on evaporated silver they found that increasing numbers of Cs-O exposure cycles reduced the photoemissive threshold down to a value of $\sim$ 1eV, at which point the photoemissive threshold levelled off but the work function of the surface (as measured by a Kelvin CPD probe), carried on decreasing to a minimum of 0.6eV. From this they deduced that for very low workfunction layers the photoemissive threshold was limited by the height of the interfacial barrier between the Cs-O layer and the silver layer, and they deduced that this barrier was $\sim$1.1eV above the Fermi level.

Carrying these results over to the GaAs photocathodes then, it can be seen that if the "effective barrier height" is taken as the electron energy which separates very large electron tunnelling probabilities from very small electron tunnelling probabilities through the interfacial barrier then the vacuum level need only be lowered below this "effective barrier height" to optimise the yield of the photocathode. On the basis of the literature, this optimal Cs-O thickness corresponds to $\sim$1nm of caesium oxide (Bell, 1973), and thicker layers than this will only serve to reduce the yield by virtue of their increased photoelectron absorption, in

spite of their lowered Kelvin work function.

The XPS results obtained from this study, then, are consistent with the GaAs photocathodes having been optimally activated with ∿1nm of Cs_2O on the surface, corresponding to a Cs-O film of approximately monolayer dimensions. However the observed and very reproducible 2:1 Cs:O ratio argues strongly aginst the interfacial layer of ionised caesium hypothesised in the original dipole model of Figure 7.3. A dipole layer structure similar to that observed with Cs-O layers on metallic tungsten (Swanson and Strayer, 1968) and silicon (Goldstein, 1973), with the oxygen atoms bound in the interstices of the GaAs surface, underneath the Cs atoms is more consistent with the results of this study. A dipole layer so formed could reduce the interfacial barrier from the ∿4.4eV expected purely on heterojunction grounds to the 1.1eV observed experimentally by Fisher et al. for a range of 3.5 semiconducting substrates. This conclusion was supported by the fact that the O1s binding energy was seen to be slightly increased to ∿530.1 eV in the GaAs photocathode spectra compared with the O1s binding energy values of 528.5eV identified with oxygen in the bulk Cs_2O matrix in the S1 photocathodes. This indicates a lower ionisation coefficient for the oxygen atom in the Cs_2O overlayer on GaAs than for an oxygen atom in bulk Cs_2O.

7.3 Conclusions as to the Nature of the S1 Photocathodes Produced in this Study

7.3.1 Evidence concerning the physical structure of the S1 Photocathodes

The most valuable clues as to the physical structure of the S1 photocathodes produced in this study emerge from the XPS data presented in Section 6.3.4. The higher binding energy O1s peak (at 531.5eV) which was found to appear as processing progressed

was seen by Yang and Bates (1980) and by Bates (1981). From the binding energy of the higher binding energy (HBE) O1s peak, and on the basis of experiments in which he "varied the angle of observation of photoelectrons and, from a measurement of the areas and the published data for photoionisation cross-sections, established that the $Cs_{11}O_3$ exists as an overlayer on Cs_2O" (Bates, 1981), he ascribed the O1s HBE peak to oxygen in $Cs_{11}O_3$.

Such a conclusion is in sharp disagreement with the experimental evidence obtained in this study. In this work the Cs3d core level spectra observed from completed photocathodes were sharp and symmetrical, in contrast to the broad loss tails seen in the work of Simon (1979) for Cs in $Cs_{11}O_3$ and observed by Yang (1980) in his S1-like surfaces. The cathode caesium to total oxygen ratio of 2:1 (see Section 6.3.4) was constant throughout the processing schedule even although the ratios of the intensities of the two O1s peaks changed as processing was continued (see e.g. Figure 6.25), moreover for each photocathode the Cs:O ratio was independent of take off angle.

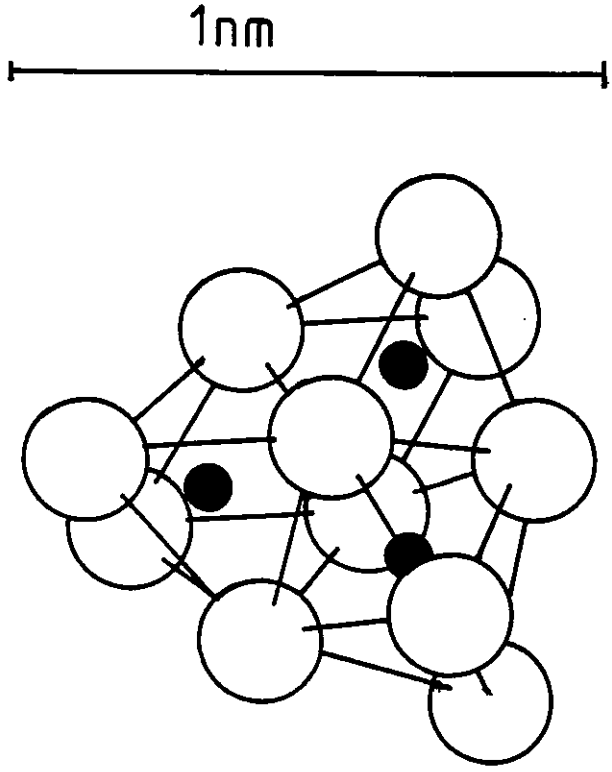
As a more quantitative test of the latter statment the measured Cs:O ratios for take off angles of 0° and 60° were calculated for 15 group "a" type photocathodes after the final baking process. For each photocathode the measured Cs:O ratio for 0° take off was divided by that for 60° take-off to produce an "angular dependence coefficient" for the Cs:O ratio on each photocathode. Such a double ratioing procedure eliminates the effect of any errors in the theoretical XPS SPCs used to calculate the Cs:O ratios. The fifteen coefficients so obtained formed a statistical population with a mean of 1.091 and a standard deviation of 0.146. If the Bates and Yang model were an accurate representation of the photocathode structure, the use of the XPS overlayer attentuation equations 5.5

and 5.6, coupled with the Seah and Dench IMFP Equation 5.11 would predict observed XPS Cs:O ratios of 2.23 at normal takeoff and 2.52 at 60° takeoff, giving a value of 0.88 for the "angular dependence coefficient" for the Cs:O ratio as defined above (see Appendix II).

Thus it can be seen that the "angular dependence coefficient" calculated on the Bates and Yang model of photocathode structure differs from the observed experimental mean by more than 1.4 times the standard derivation apparent in the experimental results, an event which would only occur with a probability of 0.15 if the photocathodes really did have a Bates and Yang type structure.

Another feature of the Bates and Yang overlayer model is that the proposed $Cs_{11}O_3$ overlayer reduces the effective electron affinity of the S1 photocathode to negative values, resulting in high escape probabilities for thermalised photoelectrons, and accounting for the high photocathode sensitivity in the visible and near infrared. Clear evidence that a NEA surface is not required for good S1 photoresponse and longwavelength threshold can be obtained by comparing the S1 EDCs in Section 6.3.2 with the "thermalised" NEA GaAs EDCs in Section 6.2.2. It can be seen that a change in electron affinity to a positive value of only $\sim$100 meV would eliminate nearly all the photosensitivity in the case of the GaAs photocathodes, while such an increase in the case of the S1 photocathodes would only decrease the photosensitivity by a few percent for most of the wavelength range, rising to $\sim$50% at 1.06 μm.

These results, coupled with the intuitive feeling that it is unlikely that a structure as complicated as the proposed $Cs_{11}O_3$ clusters (Figure 7.4) would be energetically favourable in a layer only 1.5 nm thick seem to be sufficient grounds on which to reject the Bates and Yang model of the S1 photocathode structure as being inconsistent with the observed experimental data.



$Cs_{11}O_3$

Fig 7·4.

$Cs_{11}O_3$ cluster, from Simon(1979).

Having decided this an explanation must be advanced to account for the observed presence of the split O1s peaks in all the S1 XPS spectra. The fact that the ratio of the O1s HBE peak intensity to be O1s CBE peak intensity continually changed as the photocathode processing schedule progressed, even though the observed caesium to total oxygen remained unchanged and neither element was being added to the cathode, strongly suggested that the different oxygen peaks came not from oxygen in different caesium oxide stoichiometries, but from oxygen atoms in Cs_2O in differing physical environments.

The consistent increase in the O1s HBE peak intensity (at 531.5eV) as silver was added to the cathode, so obvious in Figure 6.25, suggested that this peak could be due to oxygen atoms in direct contact with silver. Calculations based on the measured Ag:Cs ratio, the measured Cs:O ratio and the relative observed intensities of the two O1s peaks showed that such a hypothesis could comfortably explain all the experimental data if the final cathode were assumed to contain colloidal silver particles of linear dimensions $\sim$2.5 nm distributed homogeneously throughout the $\sim$30 nm thick cathode layer, with an average spacing of $\sim$5.5 nm (see Appendix III for details of these calculations) with the oxygen ions arranged in the interstices present on the surface of the silver particles thereby forming a dipole layer.

Since the silver atom is not as electropositive as the caesium atom, the oxygen atoms in contact with the silver would probably carry a smaller negative charge than their counterparts in the bulk of the Cs_2O matrix, and the resulting coulomb field differences between the two types of oxygen atom could qualitatively explain the observed shift in the O1s binding energy.

Such a Cs_2O-Ag interface structure is of course identical with the dipole layer model proposed in the previous section to account for the observed lowering of the interfacial barrier on GaAs by the absorption of a Cs_2O layer of molecular dimensions, and agrees in the same way with the Cs_2O layer structures observed on tungsten (Swanson and Strayer, 1968) and silicon (Goldstein, 1973).

If such a photocathode structure is applicable to the S1 it could also go some of the way towards explaining the observed critical importance of following the correct photocathode processing schedule during processing. To illustrate this point, what follows is an account, albeit largely conjectural, of the microscopic changes in the structure of the photocathodes in these experiments during processing, which is wholly consistent with the experimental data in this study and with the majority of the results from other workers described in Chapter 3.

During the initial silver evaporation the silver film grows as a series of small islands of linear dimensions $\sim$10-20 nm (as reported in the work of Sennett and Scott) up to a mean thickness, calculated on the basis of a bulk silver density, of about 5 nm.

On oxygen ion bombardment, all of this silver film is oxidised into a non-stoichiometric silver oxide (<u>not</u> the well-defined Ag_2O formula normally assumed at this stage). The silver stub experiments outlined in Section 6.34 made it clear that the Ag:O atomic ratio of 1.5 observed at this stage was a genuine reflection of the surface oxide composition, and not due to a spurious O1s signal originating in the silica substrate. At this stage the layer can be thought of as basically Ag_2O with a stoichiometric excess of oxygen which results from ion implantation during bombardment, and it probably has a surface morphology similar to the original silver film since the percentage volume change on oxidation (based on the bulk densities of

Ag and Ag_2O) is only ∿26%.

As the caesium is deposited on the silver oxide base it reacts forming Cs_2O, and the smaller reduced silver atoms diffuse through the Cs_2O Matrix and aggregate on nucleation centres (5nm-10nm apart on average), into small clusters containing only a few tens of silver atoms each, (providing that the substrate is heated to at least the minimum temperature of ∿120°C found necessary for successful cathode formation). The reaction continues until all of the oxygen in the initial silver oxide base layer has been exhausted. At the end of this stage the mean measured Ag:Cs ratio of 0.65 (Section 6.3.4) agrees well with the value of 0.66 predicted on the basis of Cs_2O formation in a layer with an Ag:O ratio of 1.5. The relatively low concentration of silver in the photocathode at this stage (comprising a volume fraction of only 18%, based on the bulk densities of Ag and Cs_2O), means that very little of the oxygen atoms in the cathode are adsorbed on silver particles, and the intensity of the O1s HBE peak at 531.5 eV is correspondingly low (see Figure 6.20 O1s (i)).

In this complex caesiation process it is likely that the size and distribution of the silver particles throughout the Cs_2O matrix and the correct formation of the dipole layer around them will depend in some incalculable manner on.

a) the overpressure of caesium above the substrate film,

b) the exact temperature of the substrate and hence the diffusion rates of the elemental species within it, and

c) the surface morphology of the silver oxide base

(one could imagine for example silver in a small hemispherical bulge on the surface of the silver oxide film concentrating in a small particle approximately at the centre of the hemisphere as the caesiation

reaction progresses). All of these parameters, in particular the caesium flux, are difficult to control accurately in the majority of experimental procedures.

In the light of the optical conduction resonance theories (see Section 3.3.3) which imply that the distribution of the silver in small colloidal particles of dimensions much smaller than the wavelength of light is crucial to efficient photocathode operation, it can be seen how, if the small silver clusters formed at this stage in the process are seen as nucleation centres for the larger silver particles which are supposed to form as more silver is added to the cathode, the ultimate photosensitivity of a photocathode could be determined by the exact caesiation conditions at this early stage in the processing.

As the caesiated film is subjected to a slow second silver evaporation, its behaviour would seem to be well described by the theories of Asao (1940), in which the silver is seen as increasing the surface work function as it collects on the cathode surface, thereby reducing the photoelectric threshold wavelength, but the added silver which diffuses into the cathode as it is being deposited results in increased photon absorption and photoelectron excitation in the visible region.

As the cathode film is warmed up during the final baking process, excess silver on the cathode surface diffuses inwards, combining with the silver particles already present in the bulk of the cathode film and the low surface work function is restored. This conclusion ties in neatly with the decrease in the mean Ag:Cs ratio from 4.1±1 (with a mean "angular dependence coefficient" of ∿0.77) just after the second silver evaporation to 2.2±0.8 (with a mean angular dependence coefficient of 1.00) for the final photocathode.

The above cathode formation model also qualitatively explains the behaviour of the group "b" photocathodes where the low work function, high thermionic emission and high photoemission after caesiation implied an excess of caesium deposited on the top of the layer containing the collidal silver particles, resulting in a lower work function but increased photoelectron scattering. This behaviour is manifest in the EDC's of Figure 6.17, where the beginnings of a low kinetic energy electron cascade are visible in the low kinetic energy tails of all the EDC's directly after caesiation, and the highest energy photoelectrons have been scattered down into states of lower energy, resulting in comparatively gentle high kinetic energy edges on the EDC's. Similar EDC's are observed again after the second evaporated layer of silver has been baked into the photocathode, implying that the extra silver has diffused right down to the original small Ag crystals present in the lower layers of the photocathode film.

7.3.2 Evidence concerning the Electronic Structure of the S1 Photocathodes produced in this study

The majority of the evidence concerning the nature of the electronic band structure of the photocathodes produced in this study is contained in the EDC's of Figures 6.14 and 6.17. On the basis of the photoelectric work functions derived from these curves it seemed that the group "b" type cathodes showed a lower white light sensitivity combined with a lower photoelectric work function than the group "a" photocathodes. The shapes of the high and low edges of the EDC's for "a" and "b" type cathodes implied that type "a" photocathodes had the more inhomogeneous work function of the two, whereas the effects of electron scattering were more apparent in the EDC's of the "b" type cathodes.

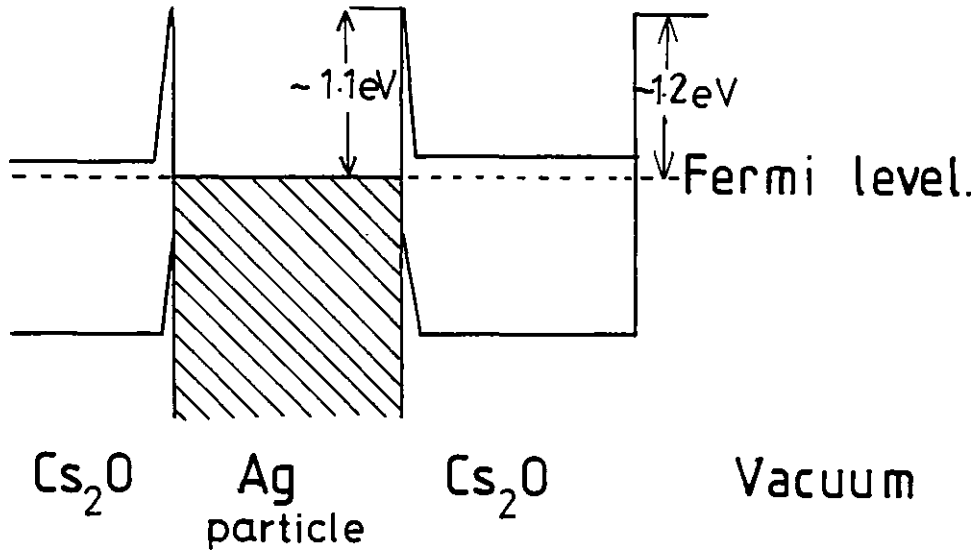


Fig.7·5 (a)

Proposed band structure for type "a" S1 photocathode.

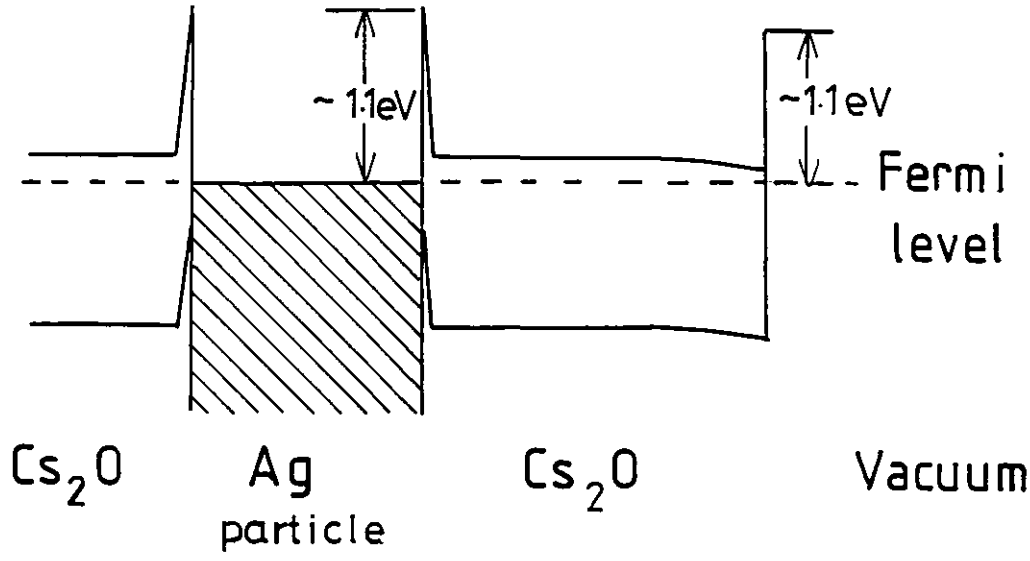


Fig.7·5 (b)

Proposed band structure for type "b" S1 Photocathode.

Previous results e.g. the optical absorption measurements of Cs-O films by Borziak et al (1956), the thermal conductivity measurements of Harper and Choyke and the S1 thermionic emission measurements of Davey (1957) on S1-like films have indicated that the Cs_2O matrix can be thought of as an n-type semiconductor.

This is not to say that the photoemission models which attribute various features in the spectral photosensitivity curves to narrow impurity level photoexcitations can be taken seriously (see e.g. Section 3.3.3), rather that out of the undoubtedly high concentration of defects and impurities in the Cs_2O, the number of defects resulting in n-type carriers (i.e. those with defect states higher than halfway up the band gap) outweigh those defects which result in p-type carrier production. The likelihood of a broad degenerate band of impurity/defect states in the bandgap explains both the difficulty experienced by Davey in establishing a single temperature independent thermionic work function for his photocathodes, and the variation observed by Harper and Choylee (1956) in the slopes of their thermal conductivity Arrhenius plots for Cs-O layers.

Taking this information into account, together with the data for the dipole layer model deduced for the structure of the Ag-Cs_2O from the experimental XPS data in the previous section, it is possible to justify an electronic band diagram for the group "a" type photocathodes of the type shown in Section 7.5(a). In this model the interfacial barrier between the silver and the caesium oxide has been reduced to $\sim$1.0eV above the Fermi level (as measured in the work of Uebbing and James, 1970) by the surface dipole layer. Also the Cs_2O-vacuum interface is assumed to have a low density of surface states so that Fermi level pinning and the associated electrostatic band bending effects at the vacuum interface

are slight and can be ignored, with the result that increasing n-type doping of the Cs_2O will reduce the electron affinity of the film as the surface Fermi level rises towards the vacuum level.

In contrast to the case with the GaAs photocathodes, the Cs_2O layer thicknesses in Sl photocathodes are quite large enough to support the idea of electrostatic band bending as an electron affinity lowering mechanism and consequently the final assumption of the previous paragraph requires some justification.

Since electrostatic band-bending effects arise as a result of the space charge distribution of free carriers near the interfaces in a photocathode film they will affect the binding energies of core level electrons localised in orbits in different part of the photocathode to the same extent that they affect the local total kinetic energy of the free photoelectrons travelling through the solid. The electron spectrometer measures the XPS photoelectron energies relative to the photocathode Fermi level and so, on the basis of the band structure in Figure 7.5, the observed silver XPS binding energies would be expected to be much the same in an Sl photocathode as in bulk silver. In the case of the caesium and oxygen XPS signals however, the binding energy of the XPS signal from an atom in a particular region of the photocathode will be shifted by an amount equal and opposite to the local shift of the Fermi level away from its intrinsic position in the band gap centre.

Absolute binding energy shifts were difficult to measure in these experiments, but XPS peak <u>widths</u> could be measured accurately to within $\sim$0.05eV. Using the surface band bending figure of 0.7 eV postulated by Niel and Mee (1970), in conjunction with the dielectric constant in the Cs_2O overlayer of 5.3 from Goldstein (1973) and a conservative estimate of a net ionised impurity level density in the Cs_2O of $\sim 10^{20} cm^{-3}$, the band bending equation (5.1) was used

to calculate a band bending distance in the Cs_2O overlayer of ~ 2 nm.

Comparison of this figure with the Seah and Dench (1979) electron IMFP figures of 2.97 nm and 2.62 nm for the O1s and $Cs3d^{5/2}$ XPS peaks (using Al kα radiation) implies that any band bending present in an S1 photocathode surface should show as a broadening of the observed $Cs3d^{5/2}$ and O1s XPS peaks.

To test for this effect the FWHM figures of the $Cs3d^{5/2}$ peaks of several different GaAs and group "a" S1 photocathodes were measured and the mean and standard deviation apparent in the spread of the results for each cathode type were calculated. The X-ray FWHM linewidths were then de-convolved from these peak widths, assuming a Gaussian convolution process, using the X-ray linewidths of 0.83 eV (Alkα) and 0.68 eV (MgKα) from p.52 of Cardona and Ley (1978). The results are summarised in Figure 7.6. Using this data the "standard error of the difference", δ_ω, of the two samples was calculated using the formulae in Moroney (1951).

Cathode type	Mean $Cs3d^{5/2}$ FWHM	X-ray linewidth	Deconvolved $Cs3d^{5/2}$ FWHM	Standard deviation, σ, in FWHM measurement	Number of readings
GaAs	2.103eV	0.68eV	1.9638eV	0.1067eV	7
S1	2.091eV	0.83eV	1.9177eV	0.0871eV	15

"Standard error of the difference" $\sigma_\omega = \left[\frac{\sigma_1^2}{n_1} + \frac{\sigma_2^2}{n_2}\right]^{\frac{1}{2}} = 4.48\times10^{-2}$eV

Observed difference in sample means = 4.61×10^{-2}eV.

Figure 7.4 Summary of $Cs3d^{5/2}$ peak width data

On the basis that band bending was not possible in the thin overlayers observed to be present on the GaAs cathodes (see Section 7.2), the presence of a 0.7eV band bending region on the surface of an Al photocathode would result in a mean difference in the sample means of -0.119eV, a figure which differs from the observed difference in sample means by $3.6\ \sigma_{\omega}$.

This implies that if surface band bending of 0.7eV were present on the Sl photocathode the experimental $Cs3d^{5/2}$ peak widths results observed would only occur with a probability of $< 1\%$ on a chance basis. If the same degree of surface band bending were present in both types of photocathode film, the observed experimental results would occur with a probability of $\sim 66\%$. Hence from these results it seems fair to conclude that electrostatic band bending is not an important mechanism in lowering the work function of the group "a" type photocathodes, and that the degree of Fermi level pinning at the cathode surface is small.

The Sl photocathode band structure of Figure 7.5 can also be used to qualitatively explain the observed behaviour of the group "b" type Sl photocathodes. If the surface of these latter photocathodes were more heavily n-type doped than the average doping level in the group "a" cathodes (conceivably due to excess caesium atoms having been introduced during caesiation), then in the absence of Fermi level pinning (as justified above), the surface Fermi level of the cathode would rise towards the vacuum level as in Figure 7.5 (b), decreasing the effective electron affinity for photoelectrons excited in the silver particles and thereby increasing the observed EDC widths. Such a Cs-O film is likely to show increased impurity scattering and will be thicker than the Cs-O films in the group "a" cathodes resulting in lower photoelectron escape probabilities and thereby explaining the lower overall photosensitivity in spite of the lower work function observed with these photocathodes.

7.3.3 Evidence concerning the Photoemissive Mechanism of the S1 Photocathodes produced in this study

The XPS information presented in 7.3.1 alone suggests that the $Cs_{11}O_3$ layer which has been supposed to support the 1.55 eV surface plasmon oscillations which result in the infra-red photoemission (Ebbinghaus et al., 1976) is not present on S1 photocathode surfaces. Even so it is likely that the Cs-O layer is capable of supporting some form of surface plasmon oscillations although of unknown energy, which could contribute to the photosensitivity in the visible and near infra red regions, as claimed by Endritz (1974). The most relevant evidence on this topic comes from the results of the experiments on the polarisation dependence of the photoyield and the EDC's described in 6.3.3.

In a detailed review of surface plasmon field properties Raether (1977) shows that in the idealised case of a plane infinite interface between two materials it is impossible to excite non-radiative plasmons (the type which may decay by the Landau damping mechanism to excite a single electron) with S-polarised incident light because "the E-fields parallel to the interface are continuous and no surface charges are produced". This polarisation dependence has been verified in numerous experimental studies (see e.g. Swalen et al., 1980 for an elegant demonstration of this effect).

In the case of the surface roughness assumed to be present in an S1 however, photon-plasmon coupling is generally assumed to take place via a surface roughness mediated coupling mechanism (simple models of which have been proposed by e.g. Crowell and Richie, 1970), and the position is not so clear.

A careful examination of the work of Crowell and Ritchie however, reveals that the surface plasmon modes used in the model are all S-polarised radiative plasmon oscillations. Whereas these modes could be expected to have significant effects on the optical reflectivity

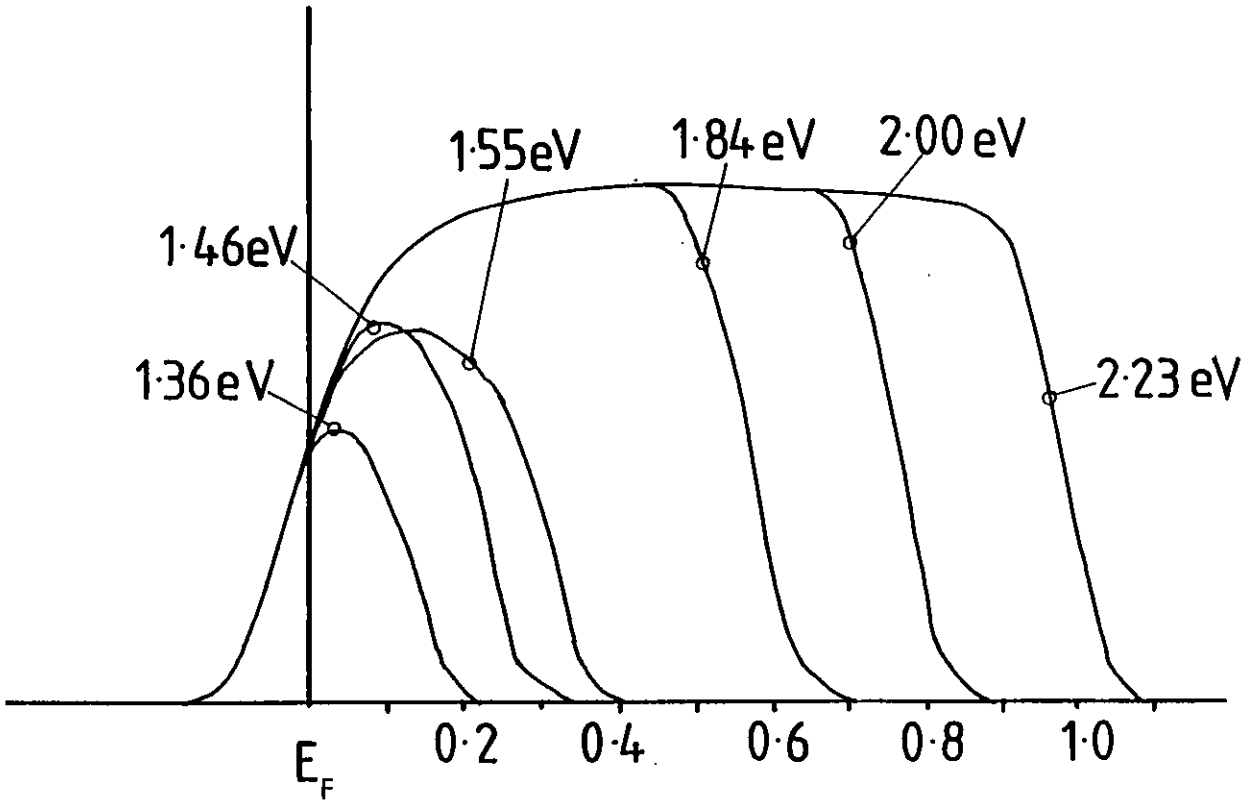


Fig.7·7

Transmission EDC's for a range of photon energies for a typical "a" type photocathode plotted on a reduced energy scale.

properties of the surface (the principal problem the authors were attacking) they would not give rise to strong single electron photoemission effects due to their short radiation damped lifetimes.

It is justified then, even in the absence of complete theoretical understanding of the effect, to say that if a plasmon decay photoemission mechanism is important for the photocathode film, then the cathode photosensitivity to "p" polarised light should be much enhanced over that for "s" polarised light.

On the basis of the above discussion the yield ratio for the two polarisations of unity observed throughout the S1 photosensitivity range in the experiments described in 6.3.3 suggests that in normal S1 photocathodes surface plasmon decay photoemission is responsible for at most a negligible contribution to the overall photosensitivity.

The close correlation between the photosensitivity in the visible-NIR spectral region and the overall content of silver deduced to be in colloidal form in the photocathode from the XPS results (7.3.1) together with the interpretation of the photoemissive characteristics of the "a" and "b" type photocathodes agrees well with the body of previous work on the subject (see e.g. 3.3.3) which attributes the visible and infra red sensitivity to photoelectron excitation within the colloidal silver particles.

In Figure 7.7 the EDCs from the group "a" cathode which featured in Figure 6.14 are replotted on an energy scale where the kinetic energy position of each EDC is shifted by an amount equal to the energy of the photon which produced it, and the heights of all the EDCs are scaled so as to coincide at the point labelled "E_F". The point E_F was designated as the kinetic energy of unscattered photoelectrons excited from the photocathode Fermi level because it closely approximated to the reduced energies of the points half way up the high kinetic energy cut-offs of the EDCs for $h\nu$ = 2.23, 2.00 and 1.81 eV.

As can be seen from the figure, the EDC's shapes and energies are consistent with the photocurrent for all photon energies between 1.36eV and 2.23 eV having been excited in an emitting species with a density of states with no sharp structure over an energy range ~2.2eV either side of the Fermi level, as judged by the flat EDC's observed at even the high photon energies.

At photon energies in the visible-NIR part of the spectrum, as an inspection of the silver band diagrams in Koyama and Smith (1970) and Christensen (1972) shows, direct interband transitions in silver are impossible, and the most likely method of photoexcitation in the silver particles is by indirect interband transitions. Although a complete theory for predicted EDC shapes for these conditions is unavailable at present, for a particular photon energy the EDC's under the circumstances would to a first approximation be expected to follow the joint bulk density of states for silver averaged over the Brillouin zone.

On this basis the agreement between the smooth flat EDC's observed in this study, and the bulk density of states for silver (as reported by Lässer, Smith and Benbow, 1981 and Christensen 1976) is striking and must be considered as strong evidence that the majority of photosensitivity in the visible and NIR spectral regions originates in indirect optical transitions in the metallic silver particles.

7.4 Conclusions as to the Best Type of Photocathode for Future use in Infra-red Ultrafast Imaging Devices

The sucesssful activation of semitransparent 3-5 glass bonded AIB cleaned substrates to NEA in this study has shown for the first time the possibility of cleaning and activating an NEA type photocathode in-situ in a streak tube. This represents a major

advance over previous techniques which involve processing the photocathode in a separate UHV system and then sealing it into the tube body, whilst still under UHV, with an indium cold welding technique.

These practical considerations, in conjunction with the already established potential for efficient photoemission in excess of 1.55 μm, would appear to make the 3-5 NEA cathodes an attractive choice in the future for NIR photochronography. The new EDC measurements in this study (reported in 6.2.2), show EDC's which are considerably narrower than those observed with conventional photocathodes operating in the visible region of the spectrum (including the S1), and would give much reduced transit time dispersion figures in present streak tube designs.

The NEA photocathodes, however, generally suffer from a much poorer "intrinsic emission time uncertainty" than their S1 counterparts. Even although the temporal response measurements (reported for the first time in 6.2.3) indicate that with suitable substrate treatment, response times as low as ∿10psec can be achieved this figure is still almost two orders of magnitude slower than the overall temporal resolutions available with the latest streak tube designs.

NEA cathodes though would be eminently suitable for the latest generation of electron-optical framing cameras. In these devices the electron-optical design currently has a limiting temporal resolution of ∿ 100psec alone, and the fractional additional degradation to this figure introduced by using a moderately thin NEA cathode would be a small price to pay for the possibility of a much increased infra-red threshold and sensitivity.

For sub-picosecond infra-red studies with the latest generation of streak camera devices however, it seems that there is still no other material capable of providing the combination of negligible "intrinsic

emission time uncertainty" and usable infra-red sensitivity available with the Sl. The progress made in the understanding of the structure and operation of this comparatively poorly understood material as a result of these experiments has suggested numerous avenues of further research with the aim of reliably producing Sl photocathodes with high infra-red sensitivities and extended long wavelength thresholds.

In particular a controlled investigation into the effects of substrate temperature and the caesium overpressure during the photocathode caesiation process step may provide valuable information leading to the reliable reproduction of the high infrared sensitivity and $\sim$1.4 μm longwavelength threshold demonstrated by Hou et al. for this emitter.

APPENDIX I

ENHANCEMENT OF PHOTOEMISSION FROM SMALL SILVER SPHERES

The calculations presented here describe two idealised photoemitting systems, one a plane semi-infinite silver surface and the other a set of small silver spheres, packed in a square lattice on a non-emitting substrate. In each system photoelectrons are assumed to be excited homogenously and isotropically throughout the volume of the silver, and the photoelectron scattering losses are approximated for by taking an electron IMFP, λ, obtained from Seah and Dench (1979).

The photoelectrons are assumed to have an infinite IMFP and unity probability of being photoemitted once they have left the silver. Account is taken of the refraction limit for electron emission (arising from refraction of the photoelectrons at the surface as a result of the crystal inner potential), by performing the integrals up to a value of θ max calculated from the photoelectron kinetic energy above the Fermi level and the average inner potential for silver.

For a semi-infinite silver surface in which photoelectrons are being excited at a rate q per unit time per unit volume, then a slab of silver in a depth range d, d+δd below the surface (Figure AI.1) produces a flux q δd per unit time per unit photocathode area, of which electrons in the angular range θ, θ +$\delta\theta$ comprise a fraction

$$\frac{2\pi(z^2-d^2)^{\frac{1}{2}} \cdot (z\delta\theta)}{4\pi z^2} \qquad \text{(AI.1)}$$

It follows that the total flux of photoelectrons emitted per unit area of the silver surface, F, will be given by

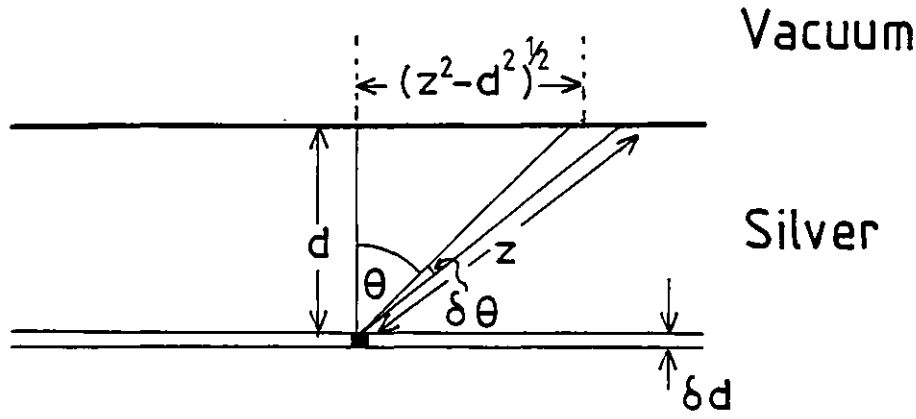


Fig. AI·1.

Geometry of photoemission calculation for a plane silver surface.

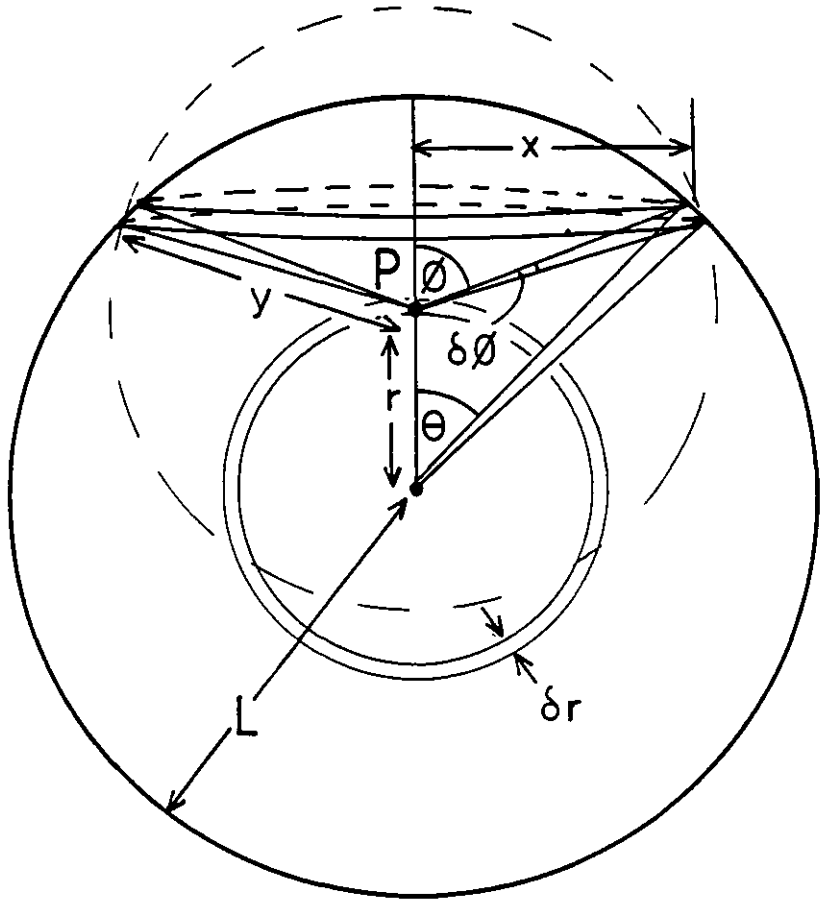


Fig. AI·2

Geometry for photoemission calculation in a small silver sphere.

$$F = q \int_{d=0}^{\infty} \int_{\theta=0}^{\theta_{max}} \frac{(d^2-z^2)^{\frac{1}{2}} \exp(-z/\lambda)}{2z} \, dz d\theta \qquad \text{(AI.2)}$$

where θ_{max}, the maximum angle a photoelectron can be travelling to the surface and still be emitted, is given by

$$\theta_{max} = \sin^{-1} \left[\frac{E}{E+E_F+\phi} \right] \qquad \text{(AI.3)}$$

where E_F is the Fermi energy for silver (5.48eV), ϕ is the work function of the silver surface, and E is the photoelectron kinetic energy once outside the solid.

To evaluate the emission from the small spheres, each sphere was split into a number of spherical shells. A shell in the radius range r, r+dr will have $q.4\pi r^2 \delta r$ photoelectrons excited in it. Spherical symmetry arguments indicate that all the points in this shell are equivalent with regard to the escape probabilities of the photoelectrons excited on them, so the total emission from the sphere can be calculated by considering the average escape probability of photoelectrons from an isotropic point source of unit intensity a distance r from the sphere centre, and multiplying this average escape probability by the total number of photoelectrons excited in the spherical shell of that radius.

Taking the isotropic point source P in Figure AI.2, electrons emitted into the angular range $\phi, \phi+\delta\phi$ occupy a solid angle

$$\frac{(2\pi x)y \, \delta\phi}{4\pi y^2} \qquad \text{(AI.4)}$$

and they will be attenuated by a factor $\exp(-y/\lambda)$. So the total

photocurrent emitted by the sphere will be given by

$$S = q \int_0^L \int_{\phi \text{ s.t. } |\theta-\phi|<\theta_{max}} \frac{4\pi r^2 x \exp(-y/\lambda)\, dr d\phi}{2y} \qquad \text{(AI.5)}$$

Multiplying S by the number of spheres per unit area on the particle photocathode gives the total photoelectron flux per unit area, and dividing this by F, (the photoelectron flux per unit area for the flat plane) gives an "Enhancement Factor" for the particle system.

The integrals were evaluated numerically on a microcomputer for a number of different silver sphere radii, and enhancement factors were calculated for

a) Pure uncoated silver, with a work function of 4.48eV, and photon energies of 5.39eV (λ=2.0nm) and 5.5eV (λ=7.0nm) and

b) A coated silver surface with a much lowered work function of 1.1eV (the photoelectrons were still assumed to have a unity probability of being emitted from the cathode structure once they had left the silver) and photon energies of 2.2eV (λ=2.0nm) and 2.0eV (λ=2.5nm).

The results of these computations are plotted in Figure AI.3, where it can be seen that although this mechanism can go at least part of the way towards explaining the high enhancement factors of $\sim$ 100 observed by Schmitt-Ott et al. (1980) with microscopic silver particles in an aerosol, the lower photon energies and correspondingly longer electron IMFP's in the case of an Sl mean that this mechanism

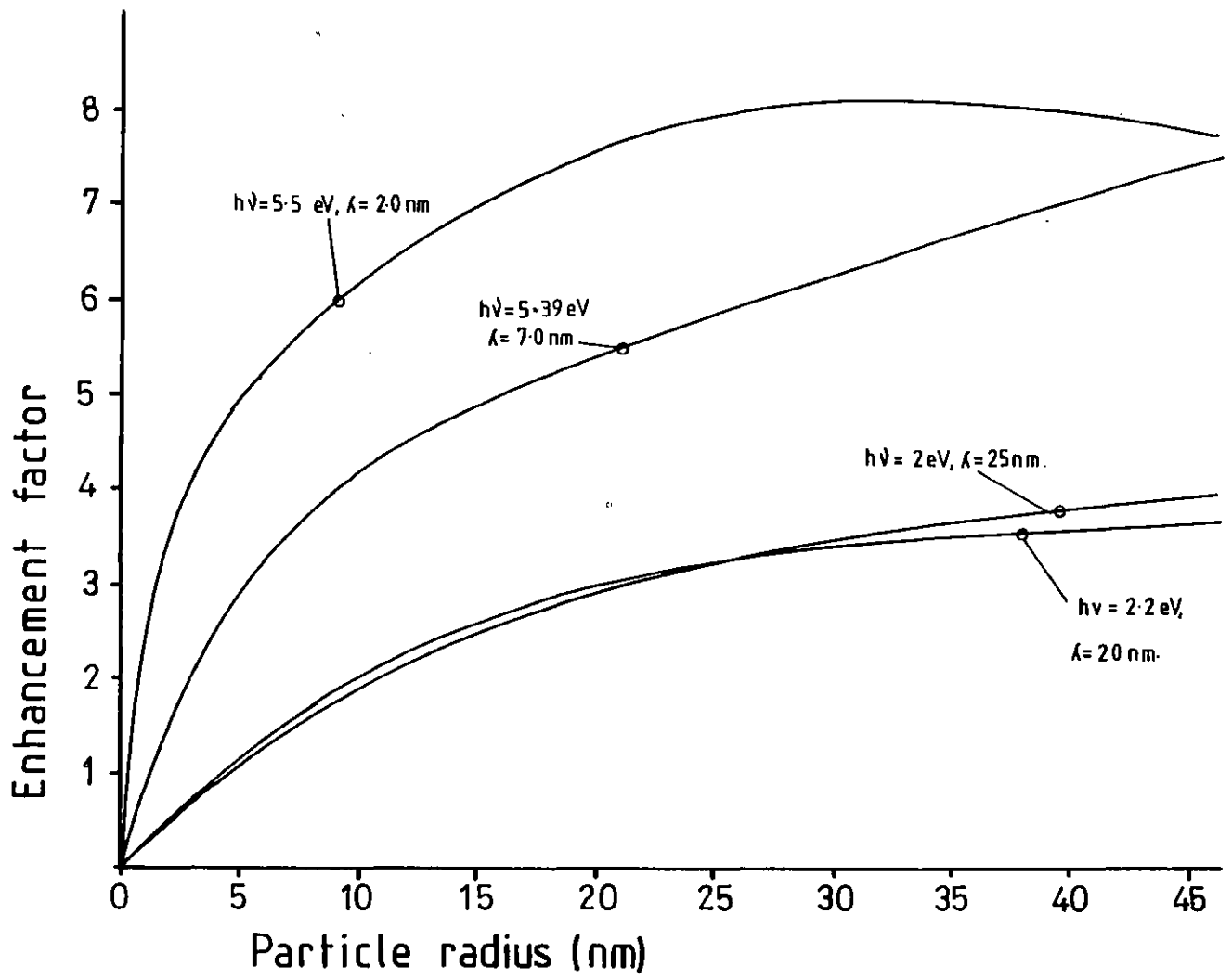

Enhancement factor
Particle radius (nm)
hν=5·5 eV, λ= 2·0 nm
hν=5·39 eV
λ= 7·0 nm
hν= 2eV, λ=25nm.
hv = 2·2 eV,
λ= 20 nm.
0
5
10
15
20
25
30
35
40
45
1
2
3
4
5
6
7
8

Fig. A1·3

would only explain the enhancement in a colloidal S1 type cathode structure if the silver particles were very large. Even in the latter case one would expect the enhancement effect to decrease at longer wavelengths as the electron IMFPs increase.

APPENDIX II

CALCULATED Cs:O XPS RATIOS IN THE S1 PHOTOCATHODE

$Cs_{11}O_3$ OVERLAYER MODEL

In the $Cs_{11}O_3$ overlayer model of the S1 photocathode (Bates, 1981; Bates and Yang, 1980), the photocathode is supposed to consist of silver particles in a Cs_2O matrix, covered with a layer of more or less pure $Cs_2O > 4nm$ thick and a layer of $Cs_{11}O_3$ 1-2 nm on top of that (Figure AII.1).

Using the Seah and Dench electron IMFP equation (Equation 5.11) for inorganic compounds gives values of 2.97 nm and 2.57 nm for the electron IMFP at the O1s and $Cs3d^{3/2}$ kinetic energies respectively, and these figures can be used in conjunction with the overlayer attenuation equations (5.5 and 5.6) to calculate the XPS Cs:O ratios one would expect to observe if the Bates and Yang model were an accurate representation of the photocathode structure.

For the purposes of this calculation, the following bulk number densities for the elements in the different oxides were used. The $Cs_{11}O_3$ data were taken from Simon (1979) and the Cs_2O data were taken from Tsai et al. (1956).

$$N_o(Cs_2O) = 9.83\times10^{21}cm^{-3}$$
$$N_{cs}(Cs_2O) = 1.96\times10^{22}cm^{-3}$$
$$N_o(Cs_{11}O_3) = 3.15\times10^{21}cm^{-3}$$
$$N_{cs}(Cs_{11}O_3) = 1.15\times10^{22}cm^{-3}$$

If one defines I_{cs} and I_o as the $Cs3d^{3/2}$ and O1s intensities which would result from an infinitely thick layer of pure Cs_2O, then

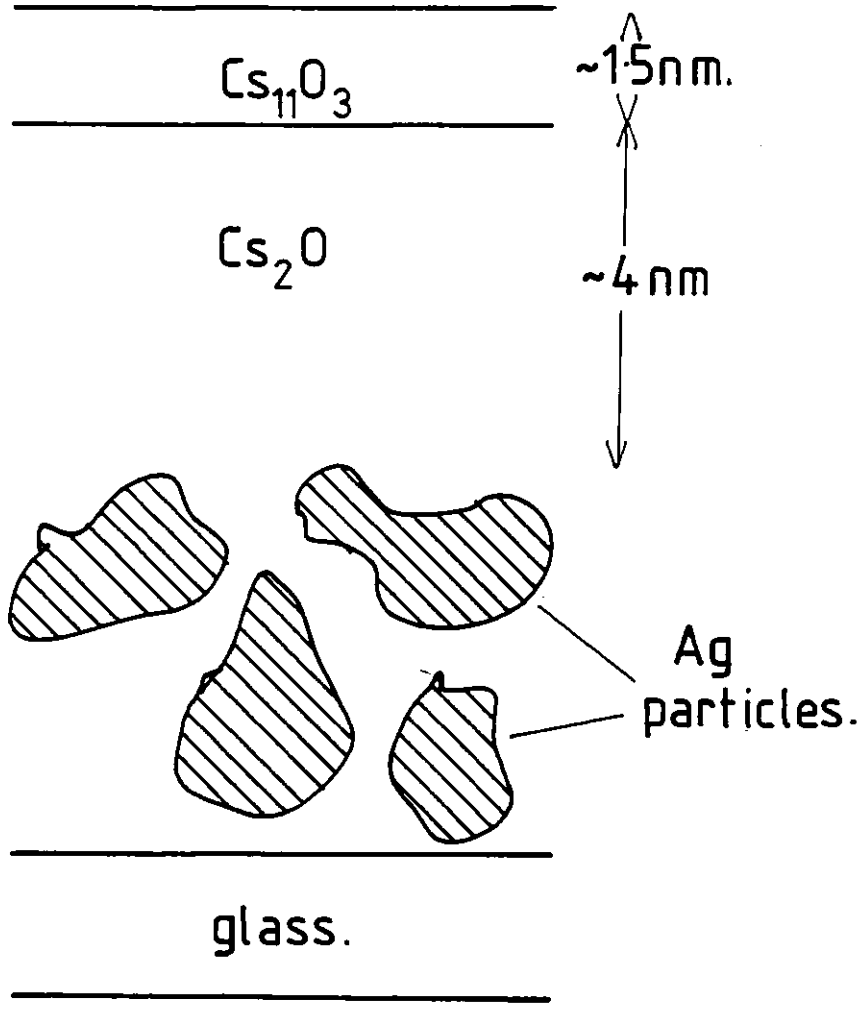


Fig. AII·1.

Schematic representation of the S1 photocathode structure as proposed by Bates and Yang (1980).

the $Cs3d^{3/2}$ and O1s XPS intensities expected from a Bates and Yang photocathode structure are given by

$$Cs3d^{3/2}\ \text{Intensity} = I_{cs}\left[\frac{N_{cs}(Cs_{11}O_3)[1-\exp(^{-1.5}/_{2.57\cos\theta})]}{N_{cs}(Cs_2O)} + \exp(^{-1.5}/_{2.57\cos\theta}\right.$$

$$O1s\ \text{Intensity} = I_o\left[\frac{N_o(Cs_{11}O_3)\ [1-\exp(^{-1.5}/_{2.97\cos\theta})]}{N_o(Cs_2O)} + \exp(^{-1.5}/_{2.97\cos\theta})\right.$$

where θ is the angle between the X-Ray photoelectron take-off direction and the sample normal. Evaluation of these expressions for $\theta = 0°$ and $\theta = 60°$ gives a predicted measured $Cs3d^{3/2}$ intensity:O1s intensity ratio of

$$1.119 \times \frac{I_{cs}}{I_o} \quad \text{for} \quad \theta=0°$$

and

$$1.260 \times \frac{I_{cs}}{I_o} \quad \text{for} \quad \theta=60°$$

Taking the ratio of the figures for these two different take off angles yields an "angular dependence coefficient" (as defined in 7.3.1) of 0.88.

APPENDIX III

COLLOIDAL SILVER PARTICLE SIZE CALCULATED FROM SI XPS RESULTS

On the basis of the discussion in 7.3.1 the XPS spectra obtained in this study were consistent with a cathode structure which comprised sub-microscopic colloidal silver particles dispersed homogenously throughout a matrix of Cs_2O. The mean ratio of the O1s low binding energy XPS peak to the high binding energy XPS peak suggested that in a typical S1 photocathode ~50% of the oxygen atoms are in contact with the surface of the silver particles, while the measured Ag:Cs ratio indicated a mean volume fraction of silver of 40%.

The number density of Cs_2O molecules, from the data presented by Tsai et al. on a pure single crystal Cs_2O sample is $9.21 \times 10^{21} cm^{-3}$, i.e. each Cs_2O molecule occupies a volume equivalent to a cube of side 0.48 nm. If it is assumed that every Cs_2O molecule in contact with a silver particle is orientated so that its oxygen atom is in sufficiently intimate contact with the silver particle (see 7.2) to change its binding energy from the lower to the higher of the two binding energy peaks observed, then to a first approximation the Cs_2O molecules contributing to the high binding energy O1s peak can be thought of as forming a skin around each silver particle, of thickness 0.48 nm and with one oxygen molecule adsorbed per 0.23 nm^2 of silver particle surface.

If the photocathode structure is modelled by considering smooth silver spheres of radius r, distributed throughout the Cs_2O matrix on a simple cubic type lattice, with a lattice constant R, then by considering a unit cell of this lattice the following relations

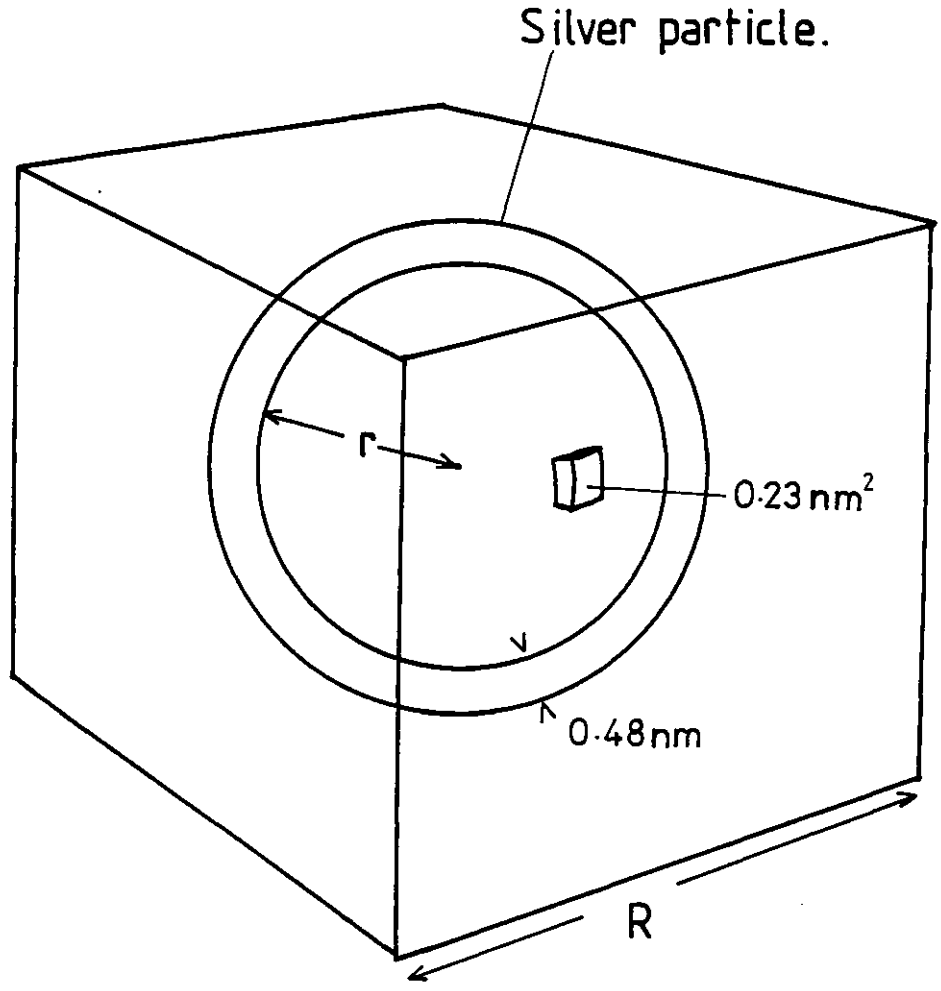


Fig.AIII·1.

"Unit Cell" containing one silver Particle,as used in the Particle size calculations.

can be derived (Figure AIII.1)

$$\frac{R^3 - \frac{4}{3}\pi r^3}{\frac{4}{3}\pi r^3} = 1.5 \qquad \text{(AIII.1)}$$

from the volume fraction of silver in the photocathode, and

$$\frac{4\pi r^2}{(0.48)^2} = \frac{R^3 - \frac{4\pi}{3}(r+0.48)^3}{0.109}$$

from the ratio of Cs_2O molecules in contact with silver to those not in contact with silver. Solving the resultant cubic equations gives the only physically meaningful pair of roots $r \approx 2.5$nm and $R \approx 5.5$nm.

Of the simplifications involved in this calculation probably the most important is the one involved in treating the silver particles as smooth spheres. It is likely that the real shapes of the silver particles in the cathode will be far more irregular and have a higher surface area to volume ratio than these smooth spheres. Such irregular particles would have larger radii and separations for the same mean Ols lower binding energy: higher binding energy XPS peak intensity ratio.

REFERENCES

ALLEN, G.A., "The Performance of Negative Electron Affinity Photocathodes", J. Phys. D. App. Phys. 4, 308 (1971).

ALLENSON, M.B., King, P.G.R., Rowland, M.C., Steward G.J. and Syms, C.H.A., "An Improved GaAs Transmission Photocathode", J. Phys. D. App. Phys. 5, 138 (1972).

ANTYPAS, G.A. and Edgecumbe, J., "Glass-sealed GaAs-AlGaAs Photocathode" App. Phys. Lett. 26(7), 371 (1975).

ANTYPAS, G.A., Escher, J.S., Edgecumbe, J. and Enck, R.S., "Broad-band GaAs Transmission Photocathode", J. App. Phys. 49(7), 4301 (1978).

ARSEN'EVA-GEĬL', A.N. and Kask, A.A., "Photoemission of Electrons from F-Type GaAs", Soviet Phys. Solid State 7(4), 952 (1965).

ASAO, S, "Behaviour of Foreign Metal Particles in the Composite Photocathode", Proc. Phys. Math. Soc. Japan 22, 448 (1940).

ASAO, S. and Suzuki, M. "Improvement of Thin Film Photoelectric Tube", Proc. Phys.-Math. Soc. Japan 12, 247 (1930).

ATTWOOD, D.J. and Coleman, L.W., "Picosecond X-Ray Spectral Studies", Proc. 12th Int. Conf. on High Speed Photog. pp. 318-324 (1976).

BALLU, Y., "High Resolution Electron Spectroscopy", Adv. in Elec. and Elec. Phys. Suppl. 138, 257 (1980).

BARRIE, A. and Street, F.J., "An Auger and XPS Study of Sodium Metal and Sodium Oxide", JESRP, 7, 1 (1977).

BATES, C.W. "Photoemission from Ag-O-Cs" Phys. Rev. Lett. 47 (3), 204 (1981).

BELL, R.L., "Negative Electron Affinity Devices", Clarendon Press Oxford (1973).

BELL, R.L. and Spicer, W.E., "3-5 Compounds: A New Family of Photoemitters with Greatly Improved Performance", Proc. IEEE 58, 1788 (1970).

BENTON, A.F. and Drake, L.C. "Dissociation Pressure of Silver Oxide Below 200C", J. Amer. Chem. Soc. 54, 2186 (1932).

BERGLUND, C.N. and Spicer, W.E. "Photoemission Studies of Cu and Ag: Theory" and "Photoemission Studies of Cu and Ag: Experiment", Phys. Rev. A136, 1030 and 136, 1044 (1964).

BERTHOU, H. and Jørgensen, C.K., "Relative Photoelectron Signal Intensities Obtained with a Magnesium X-Ray Source", Anal. Chem. 47, 482 (1975).

BLAKEMORE, J.S., "Semiconducting and Other Major Properties of GaAs", J. Appl. Phys. 53 (10), R123 (1982).

BORZIAK, P.G., Bibik, V.F. and Kramerenko, G.S., "Distinctive Characteristics of the Photoeffect in Cs-O-Ag Photocathodes", Bull. Acad. Sci. USSR, Phys. Ser. 20, 939 (1956).

BRADLEY, D.J. and Sibbett, W., "Subpicosecond Chronoscopy", App. Phys. Lett. 27 (7), 382 (1975).

BRADLEY, D.J., Bryant, S.F., Taylor, J.R. and Sibbett, W., "Intensity Dependent Time Resolution and Dynamic Range of Photochron Picosecond Streak Cameras", Rev. Sci. Inst. 49, (2), 215 (1978).

BRILLSON, L.J. and Caesar, G.P. "X-Ray Photoionisation Cross-sections for Quantitative Analysis", Surf. Sci. 58, 457 (1976).

BULGYIN, V.S., Drozhbin, Yu.A. and Stepanov, B.M., "Photoelectric Limit on the Time Resolution in Electron Optical Photochronography", Sov. Phys. Tech. Phys., 21 (4), 479 (1976).

BUTSLOV, M.M., Zavoysky, Ye.K. and Fanchenko, S.D., "Multistage Image Converter Tubes for Studying High Speed Phenomena", Opt. Tech. 39 (8), 494 (1972).

CAMPBELL, N.R., Phil. Mag. 6, 633 (1928).

CAMPBELL, N.R., "The Photoelectric Emission of Thin Films", Phil. Mag. 12, 173 (1931).

CARDONA, M. and Ley, L., "Photoemission in Solids I", Springer-Verlag Topics in Applied Physics 26 (1978).

CHANG, C.C., "Auger Electron Spectroscopy", Surf. Sci. 25, 53 (1971).

CHECHIK, N.O., Feinstein, S.M. and Lifshits, T.M., "Electron Multipliers", p.40 M.-L. (1954).

CHINEN, K., Niigaki, M. Miyao, M. and Hagino, M., "GaAs Transmission Photocathode Grown by MBE", Jap. J. App. Phys. 19 (11), 703, (1980).

CHRISTENSEN, N.E., "The Band Structure of Silver and Optical Interband Transitions", Phys. Stat. Sol. 54, 551 (1972).

CHRISTENSEN, N.E. Proc. Int. Symp., Photoemission Ed. Willis, R.F. et al., ESA Special Publication No. SP118 (1978), Noordwijk, Holland.

CHUNG, M.F. and Jenkins, L.H., "Auger Electron Energies of Outer Shell Electrons", Surf. Sci. 22, 479 (1970).

CROWELL, J. and Ritchie, R.H., "Surface Plasmon Effect in the Reflectance of a Metal", J. Opt. Soc. Am. 60, (6), 794 (1970).

CSORBA, I.P., "Transit-Time-Spread Limit time Resolution of Image Tubes in Streak Operation", RCA Review 32, 650 (1971).

DAVEY, J.E., "Thermionic and Semiconducting Properties of (Ag)-Cs_2O,Ag,Cs", J. App. Phys., 28 (9), 1031 (1957).

DINAN, J.H., Galbraith, L.K. and Fischer, T.E., "Electronic Properties of Clean Cleaved (110) GaAs Surfaces", Surf. Sci. 26, 587 (1971).

DOBRETSOV, L.N., "Electronic and Ionic Emission", p.204, M.-L (1952).

EBBINGHAUS, G., Braun, W. and Simon, A., "Photoemission from Metallic Caesium Oxide Films", Phys. Rev. Lett. 37 (26), 1770 (1976).

ECKHART, F., "Measurement of the Dark Current of a Secondary Electron Photomultiplier with an (Ag)-Cs_2O,Cs,Ag Photocathode", Ann. Phys. 16, 323 (1955).

ENDRITZ, J.G., "Surface Waves and Grating Tuned Photocathodes", App. Phys. Lett. 25 (5), 261 (1974).

ERTL, G.A. and Küppers, J., "Low Energy Electrons and Surface Chemistry", Verlag Chemie Weinheim (1974).

EVANS, S., Pritchard, R.G. and Thomas, J., "Relative differential Subshell Photoionisation Cross-sections from Li to Ur", JESRP, 14, 341 (1978).

EVANS, S., Pritchard, R.G. and Thomas, J.M., "Escape Depths of X-Ray (Mgkα) Induced Photoelectrons and Relative Photoionisation Cross-sections for the 3P Subshell of the Elements of the first Long Period", J. Phys. C. Sol. State Phys. 10, 2483 (1977).

FADLEY, C.S., "Instrumentation for Surface Studies: XPS Angular Distributions", JESRP, 5, 725 (1974).

FADLEY, C.S., "Photoelectron Cross-Sections and Multielectron Transitions in the Sudden Approximation" Chem. Phys. Lett. 25, 225 (1974).

FADLEY, C.S., Kono, S., Peterson, L-G., Goldberg, S.M., Hall, N.F.T., Lloyd, J.T. and Hussain, Z., "Determination of Surface Geometries from Angular Distributions of Deep Core Level X-ray Photoelectrons", Surf. Sci. 89, 52 (1979).

FAUST, R.C., "An Interferometric Study of Some Optical Properties of Evaporated Silver Films", Phil. Mag. 41, 1238 (1950).

FISHER, D.G., Enstrom, R.E., Escher, J.S. and Williams, B.F. "Photoelectron Surface Escape Probability of (GaIn)As:Cs-O in the 0.9-1.6 μm Range", J. App. Phys. 43, 3815 (1972).

FLÖDSTROM, S.A., Hansson, G.V., Hagstrom, S.B.M. and Endritz, J.G., "Photoemission with Polarised Light from Free-Electron and Transition Metals" Surf. Sci. 53, 156 (1975).

FRIMER, A.I. and Gerasimova, A.M., "Electron Microscopic Investigation of the Structure of Photoelectric Cathodes", Sov. Phys. Tech. Phys., 1, 705 (1956).

GARBE, S. and Frank, G., "Efficient Photoemission from GaAs Layers", Sol. Stat. Comm. 7, 615 (1969).

GOLDSTEIN, B., "LEED, Auger and Plasmon Studies of Negative Electron Affinity on Si Produced by the Adsorption of Cs and O" Surf. Sci. 35, 227 (1973).

GREGORY, P.E. and Spicer, W.E., "UPS Photoemission Studies of Caesium Oxide Films on GaAs", J. App. Phys. 47 (2), 510 (1976).

GREGORY, P.E., Escher, J.S., Saxena, R.R. and Hyder, S.B., "Field Assisted Photoemission to 2.1 microns from a Ag/p-$In_{0.77}Ga_{0.23}As$ Photocathode", App. Phys. Lett. 36 (8), 639 (1980).

GUGEL, B.M., Melamid, A.Ye and Stepanov, B.M., "The Structure of the Silver-Oxygen-Caesium Photocathode" Radio Eng. Electron. Phys. 22, 101 (1977).

HALL, P.M. and Morabito, J.M., "Matrix Effects in Quantitative Auger Analysis of Dilute Alloys", Surf. Sci. 83, 391 (1979).

HARPER, W.J. and Choyke, W.J., "The Resistance of Semitransparent Photocathodes", J. App. Phys. 27 (11), 1358 (1956).

HELMER, J.C. and WEICHERT, "Enhancement of Sensitivity in ESCA Spectrometers", App. Phys. Lett. 13 (8), 266 (1968).

HENKE, B.L., "Ultrasoft X-Ray Reflection, Refraction and Production of Photoelectrons (100eV-1000eV Region)", Phys. Rev. A. 6, 94 (1972).

HOENE, E.L. and Saggau, B. ,Z. Angew. Phys. 20, 502 (1966).

HOLLAND, L. "Thin Film Microelectronics", Chapman and Hall p.205, (1965).

HOU, X., Sibbett, W. and Weekly, B., "Palladium-Silver-Oxygen-Caesium Photocathode", Rev. Sci. Inst. 52 (10), 1487 (1981).

HOU, X., Sibbett, W. and Weekly, B., "Surface Resistivity Measurements of S1 Photocathodes", J. App. Phys. 53 (4), 3243 (1982).

HUGHES, A.E. and Phillips, C.C., "An Experimental and Theoretical Study of the Transmission of a Commercial Hemispherical Electron Energy Analyser", Surf. Inter. Anal. 4 (5), 220 (1982).

JAMES, L.W. and Moll, J.L., "Transport Properties of GaAs Obtained from Photoemission Measurements" Phys. Rev. 183 (3), 740 (1969).

JAMES, L.W., Moll, J.L. and Spicer, W.E., "Gallium Arsenide" Proc. 2nd Int. Symp. Dallas p.230 (1968) (Unpublished).

KALIBJIAN, R. "High-Intensity Laser-beam Effects on the Spatial Resolution of a Streak Camera Tube", J. App. Phys. 46 (11), 4875 (1975).

KHLEBNIKOV, N.S., Zhur. Tekh. Fiz. 16, 745 (1946).

KIRSCHNER, J. "Electron Excited Core Level Spectroscopies", Ch. 3 Topics in Current Physics 4 ed. Bach, H.I., "E.S.C.A.", Springer-Verlag (1977).

KOLLER, L.R., "Photoelectric Emission from Thin Films of Caesium", Phys. Rev. 36, 1639 (1930).

KOYAMA, R.Y. and Smith, N.V. "Photoemission Properties of Simple Metals", Phys. Rev. B. 2 (8), 3049 (1970).

KRAUSE, M.O., J. Phys. (Paris), Colloque C4, Suppl. 10, 32 C4-67 (1971).

KROLIKOWSKI, W.F., Ph.D. Thesis Stanford Univ. (1967).

LASSER, R., Smith, N.V. and Benbon, R.L., "Empirical Band Calculations of the Optical Properties of d-Band Metals, I.Cu.Ag and Au", Phys. Rev. B. 24 (4), 1895 (1981).

LEWIS, R.T. and Kelly, M.A. "Binding Energy Reference in XPS of Insulators" JESRP 20, 105 (1980).

MADEY, T.E. and Yates, J.T., "Electron Stimulated Desorption as a Tool for Studies of Chemisorption: A Review", J. Vac.Sci. Tech. 8 (4), 525 (1971).

MARTON, J.P. and JORDAN, B.D., "Optical Properties of Aggregated Metal Systems: Interband Transitions", Phys. Rev. B. 15 (4), 1719 (1977).

MARTON, J.P. and LEMON, J.R., "Optical Properties of Aggregated Metal Systems 1, Theory", Phys. Rev. B. 4 (2), 271 (1971).

MAXWELL-GARNETT, J.C., "Colours in Metal Glasses and in Metallic Films", Philos. Trans. Roy. Soc. London 203, 385 (1904) and 205, 247 (1906).

MAY, P.G., Sibbett, W., Smith, K., Taylor, J.R. and Willson, J.P., "Simultaneous Autocorrelation and Synchroscan Streak Camera Measurement of Cavity Length Detuning Effects in a Synchronously Pumped CW Dye Laser", Opt. Comm. 42 (4), 285 (1982).

MENZEL, D. and Gomer, R.,"Electron-Impact Desorption of CO from Tungsten", J. Chem. Phys. 41 (11), 3329 (1964).

MIDWINTER, J.E., "Optical Fibres for Transmission" Wiley Series in Pure and Applied Optics (1979).

MORABITO, J.M., "Scanning Electron Microscopy", Ed. Johari, O. (IIT Res. Inst., Chicago), p.221 (1976).

MORONEY, M.J., "Facts from Figures", Ch. 13 Penguin Books (1951).

MOSS, H., "Narrow Angle Electron Guns and Cathode Ray Tubes" Adv. Elec. and Elec. Phys. Series, Academic Press (1968).

McGUIRE, G.E., "Auger Electron Spectroscopy Reference Manual" Plenum Press (New York and London) (1979).

NEIL, K.S. and Mee, C.H.B., "The Mechanism of Emission from the Silver-Oxygen-Caesium Photocathode", Phys. Stat. Sol (a) 2, 43 (1970).

NIU, H. and Sibbett, W., "Theoretical Analysis of Space Charge Effects in Photochron Streak Cameras", Rev. Sci. Inst. 52 (12), 1830 (1981).

NIU, H., Sibbett, W. and Baggs, M.R., "Theoretical Evaluation of the Temporal and Spatial Resolutions of Photochron Streak Image Tubes", Rev. Sci. Inst. 53 (5), 563 (1982).

P.E.I. "Handbook of Auger Electron Spectroscopy", (1972).

PAKHOMOV, M.T., "On Determining the Activation Energy of the Cs Impurity Donors in Ag-O-Cs Photocathodes" Bull. Acad. Sci. USSR 35 (2), 289 (1971).

PAKHOMOV, M.T., "Temperature Dependence of the Work Function of a Silver-Oxygen-Caesium Photocathode" Bull. Acad. Sci. USSR 33 (3), 478 (1969).

PAKHOMOV, M.T. and Melamid, A. Ye., "Mechanism Governing the Effect of Additional Silver on the Properties of the Silver-Oxygen-Caesium Photocathode", Bull. Acad. Sci. USSR 35 (3), 562 (1971).

PAKHOMOV, M.T., Melamid, A. Ye. and Gerchikov, Ya. B., "The Effect of Colloidal Silver Prticles on the Effectiveness of Optical Methods of Increasing the Sensitivity of the Ag-O-Cs Photocathode" Radio Eng. Elec. Phys. 20 (9), 147 (1975).

PAYNE, D.N. and Gambling, W.A., "Zero Material Dispersion in Optical Fibres", Electron. Lett. 11, 176 (1975).

PENN, D.R., "Quantitative Chemical Analysis from ESCA" JESRP 9, 29 (1976).

PIEDMONT, J.R. and Pollehn, H.K., "High Modulation Transfer (MTF) Phosphor Screens", SPIE Vol. 99 3rd European Electron-Optics Conf. p.155 (1976).

POWELL, C.J., "Attenuation Lengths of Low Energy Electrons in Solids" Surf. Sci. 44, 29 (1974).

POWELL, C.J., "Cross-sections for Ionisation of Inner Shell Electrons by Electrons", Rev. Mod. Phys. 48 (1), 33 (1976).

POWELL, C.J. and Larson, P.E., "Quantitative Surface Analysis by XPS", App. Surf. Sci. 1, 186 (1978).

RAETHER, H., "Surface Plasma Oscillations and their Applications", Phys. Thin Films, 9, 145 (1977).

RCA Photocathode Wallchart.

REILMAN, R.F., Msezane, M. and Manson, S.T., "Relative Intensities in Photoelectron Spectroscopy of Atoms and Molecules", JESRP, 8, 389 (1976).

RODDIE, A.G., Edwards, J.G., Murphy, T. and Maisey, S., "Development of a Miniaturised Picosecond Streak Camera Part 1: Cathode

Stability and Initial Electrode Design", NPL Report DES 72 (October 1981).

ROY, D. and Carette, J.D., "Design of Spectrometers for Surface Analysis", Topics in Current Physics 4 Ed. BACH H I "E.S.C.A." Springer-Verlag Berlin (1977).

SAYAMA, Y., "Vapour Pressure of the Caesium-Oxide Photocathode", J. Phys. Soc. Japan 1, 13 (1946).

SCHEER, J.J. and van Laar, J., "GaAs-Cs: A New Type of Photoemitter" Sol. Stat. Commu. 3, 189 (1965).

SCHMITT-OTT A., Schurtenberger, P. and Siegmann, H.C., "Enormous Yield of Photoelectrons from Small Particles", Phys. Rev. Lett. 45 (5), 1284 (1980).

SCOFIELD, J.H., "Hartree-Slater Subshell Photoionisation Cross-sections at 1254 eV and 1487 eV" JESRP 8, 129 (1976).

SEAH, M.P., "Quantitative AES, via the Energy Spectrum or the Differential?", Surf. Inter. Anal. 1, 86 (1979).

SEAH, M.P., "Quantitative AES: Modulating the Spectrometer", Surf. Inter. Anal. 1, 91 (1979a).

SEAH, M.P., "The Quantitative Analysis of Surfaces by XPS: A Review", Suff. Inter. Anal. 2 (6), 222 (1980).

SEAH, M.P. and Dench, W.A., "A Standard Database for Electron Inelastic Mean Free Paths in Solids", Surf. Inter. Anal. 1 (1), 2 (1979).

SENNETT, R.S. and Scott, G.D., "Structure of Evaporated Metal Films and Their Properties", J. Opt. Soc. America 40 (4), 203 (1950).

SEVIER, K.D., "Low Energy Electron Spectrometry", Wiley-Interscience (1972).

SIBBETT, W., Baggs, M.R. and Niu, H., "A Picosecond Framing Image Tube", SPIE Vol. 348, p.267 Proc. 15th Int. Cong. on High Speed Photog. and Photonics, San Diego (1982).

SIBBETT, W., Baggs, M.R., Eagles, R.T. and Sleat, W.E., "Subpicosecond Chronoscopy using a Photochron IV Streak Camera" Proc. 8th Symp. on Photoelectronic Imaging Devices (1983) to be published by SPIE.

SIBBETT, W., Niu, H. and Baggs, M.R., "A Femtosecond Streak Image Tube", p.271 SPIE Vol. 348, 15th ICHSP Dan Diego (1982).

SIBBETT, W., Niu, H. and Baggs, M.R., "Photochron IV Subpicosecond Streak Image Tube", Rev. Sci. Inst. 53 (6), 758 (1982).

SIBBETT, W., Sleat, W.E., Taylor, J.R. and Willson, J.P., "Internally Intensified Photochron II Streak Tube", p. 2175 SPIE Vol. 348 15th ICHSP San Diego (1982).

SIEGBAHN, K., Nordling, C., Fahlman, R., Nordberg, R., Hamrin, K., Hedman, J., Johansson, G., Bergmark, T., Karlsson, S.E., Lindgren, I. and Linberg, B., "ESCA" Alquist and Wiskells, Uppsala (1967).

SIMON, A., Struct. and Bonding 36, 81 (Berlin 1979).

SOBOLEVA, N.A., "The Causes of Anomalous Behaviour of Caesium-Oxide Photocathodes in a Spherical Condenser System", Radio Eng. Electron. 4 (11), 204 (1959).

SOBOLEVA, N.A., Shefov, A.S. and Tolmasova, V.N., Bull. Acad. Sci. USSR, 26, 1393 (1962).

SOMMER, A.H., RCA Review, 28, 543 (1967).

SOMMER, A.H., "Hypothetical Mechanism of Operation of the Ag-O-Cs(S1) Photocathode Involving the Peroxide Cs_2O_2", J. App. Phys. 51 (2), 1254 (1980).

SOMMER, A.H., "Photoemissive Materials, Preparation, Properties and Uses", Wiley, New York (1968).

SOMMER, A.H., Whitaker, H.H. and Williams, B.F., "Thickness of Cs and Cs-O Films on GaAs(Cs) and GaAs(Cs-O) Photocathodes" App. Phys. Lett. 17 (7), 273 (1970).

SONNENBERG, H., "Low Work Function Surfaces for Negative Electron Affinity Photoemitters" App. Phys. Lett. 14 (9), 289 (1969).

SPICER, W.E., "Negative Electron Affinity 3-5 Photocathodes: Their Physics and Technology" App. Phys. 12, 115 (1977).

SPICER, W.E., "Photoemissive, Photoconductive and Optical Absorption Studies of Alkali-Antimony Compounds" Phys. Rev. 112 (1), 114 (1958).

SPICER, W.E. and WOOTEN, F., "Photoemission and Photomultipliers" Proc. IEEE51, 1119 (1963).

SPICER, W.E., Lindau, I., Su, C.Y., Chye, P.W. and Pianetta, P., "Core-level Photoemission of the Cs-O Adlayer of NEA GaAs Photocathodes", App- Phys. Lett. 33 (11), 934 (1978).

STAHL, H.A., "Compound Formation upon Sensitising Semitransparent Oxidised Silver Layers by Caesium Vapour", J. App. Phys. 43 (4), 2002 (1972).

STOCKER, B.J., "AES and LEED study of the Activation of GaAs-Cs-O NEA Surfaces", Surf. Sci. 47, 501 (1975).

SUNJIC, M., Sokcevic, D. and Lucas, A., "Inelastic Effects in XPS", JESRP, 5, 963 (1974).

SWALEN, J.D., Gordon II J.G., Philpott, M.R., Brillante, A., Pockrand, I. and Santo, R., "Plasmon Surface Polariton Dispersion by Direct Observation", Am. J. Phys. 48 (8), 669 (1980).

SWANSON, L.W. and Strayer, R.W., "Field-Electron-Microscopy Studies of Caesium Layers on Various Refractory Metals: Work Function Change", J. Chem. Phys. 48 (6), 2421 (1968).

SZAJMAN, J., Jenkin, J.G., Leckey, R.C.G. and Liesgang, J., "Subshell Photoionisation Cross-sections, Electron Mean Free Paths and Quantitative X-Ray Photoelectron Spectroscopy", JESRP 19, 393 (1980).

TAYLOR, N.J., "Resolution and Sensitivity Considerations of an Auger Electron Spectrometer Based on Display LEED Optics",

Rev. Sci. Inst. 40 (1), 792 (1969).

TIMAN, H., "On the Relationship of Optical Data and Emission in Thin Film Photocathodes", IEEE Trans. Nuc. Sci. Vol. NS-28 (1), 652 (1981).

TSAI, K.R., Harris, P.M. and Lassettre, E.n., "The Crystal Structure of Caesium Monoxide", J. Phys. Chem. 60, 338 (1956).

TURNBULL, A.A. and Evans, G.B., "Photoemission from GaAs-Cs-O", Brit. J. App. Phys. (J. Phys.D) Ser. 2 1, 155 (1968).

UEBBING, J.J. and James, L.W., "Behaviour of Caesium Oxide as a Low Work Function Coating", J. App. Phys. 41 (11), 4505 (1970).

WAGNER, C.D., "Factors Affecting Quantitative Determination by XPS" Anal. Chem. 49 (9), 1282 (1977).

WAGNER, C.D., Davis, L.E. and Riggs, W.M., "The Energy Dependence of the Electron Mean Free Path", Surf. Inter. Anal. 2 (2), 53 (1980).

WAGNER, C.D., Davis, L.E., Zeller, M.V., Taylor, J.A., Raymond, R.H. and Gale, L.H., "Empirical Atomic Sensitivity Factors for Quantitative Analysis by ESCA", Surf. Inter. Anal. 3 (5), 211 (1981).

WENTZEL, G. ,Z. Phys. 43, 524 (1927).

WILLIAMS, B.F. and TIETJEN, J.J., "Current Status of Negative Electron Affinity Devices" Proc. IEEE 59 (10), 1489 (1971).

WILLSON, J.P., Ph.D. Thesis London Univ. (1982) pp.164-167.

WILLSON, J.P., Sibbett, W. and Sleat, W., "Pulse Width and Interpulse Jitter Measurements of a Passively Mode-locked CW Ring Dye Laser", Opt. Comm. 42 (3), 208 (1982).

YAMAGUCHI, T. YOSHIDA, S. and KINBARA, A., "Effect of Retarded Dipole-Dipole Interactions between Island Particles on the Optical Plasma Resonance of a Silver Island Film", J. Opt. Soc. Am. 64 (11), 1563 (1974).

YANG, S.J., Ph.D. Thesis Stanford Univ. (1980).

YANG, S.J. and Bates, C.W., "The Role of Caesium Suboxides in Low Work Function Surface Layers Studied by X-Ray Photoelectron Spectroscopy: Ag-O-Cs", App. Phys. Lett. 36 (8), 675 (1980).

ZAVOISKY, E.K. and Fanchenko, S.D., "Image Converter High-Speed Photography with 10^{-9} - 10^{-14} sec Time Resoolution", App. Opt. 4 (9), 1155 (1965).

A C K N O W L E D G E M E N T S

I'd like to take the chance to extend my thanks to ...

Alun Hughes and Wilson Sibbett (my supervisor), for all the stimulating discussions and support with this project.

Roy Taylor and Bill Sleat, for all their help setting up the dye laser system and RF electronics for the streak cameras.

Mike Allenson for supplying the GaAs substrates.

Martin Baggs for the electron optical design of the miniature electron gun used in the ATF measurements.

Basil Weekley for his enthusiastic willingness to share the benefits of his knowledge of the black art of Sl photocathode processing.

Dave Yarwood, the glassblower, for his illimitable patience and humour whilst repeatedly rebuilding the glass caesiation chamber.

EMI Ruislip for financial support and invaluable help constructing the miniature ATF gun and the glassware for the UHV streak camera.

Joe for proofreading the script.

Sarah for typing it so speedily

and all the other friends, colleagues and family who in the labs, pubs and places of leisure made the last four years the fun that they were.

An Experimental and Theoretical Study of the Transmission Function of a Commercial Hemispherical Electron Energy Analyser†

A. E. Hughes and C. C. Phillips
Imperial College of Science and Technology, Optics Section, The Blackett Laboratory, Prince Consort Road, London SW7 2BZ, UK

The electron energy analyser transmission (peak area/incident current) of a VG Scientific ESCALAB has been measured as a function of kinetic energy, analyser energy and source position for a point source of electrons in the sample plane (produced using a specially designed mini electron gun). Results have been obtained in both CAE (constant analyser energy) and CRR (constant retard ratio) modes. The results are extrapolated to give the energy dependence of the analyser transmission for an extended current source, such as encountered in routine XPS analysis applications. A detailed theoretical study explains the rationale behind this data extrapolation and predicts an analyser transmission in fair agreement with experimental results, possible causes for the discrepancies between theory and experiment are discussed.

INTRODUCTION

XPS has now reached the stage where routine quantitative analysis is possible. The analysis can proceed via one of two routes, (1) internal calibration by measuring spectra of known chemical compounds containing the elements to be analysed, (2) using tabulated core level photoionization cross-sections and mean free paths of electrons. In the latter case, one must also know the way in which the transmission function of the spectrometer varies with kinetic energy and other instrumental variables. Hence we have measured the transmission of a commercial electron spectrometer (VG Scientific, ESCALAB) for a point source of electrons as a function of kinetic energy, analyser energy and source postition.

EXPERIMENTAL PROCEDURE

A schematic diagram of the spectrometer is shown in Fig. 1. Electrons of kinetic energy E_K from a point on the sample, (or electron gun) S, are brought to a focus by a multi-element electrostatic lens on to the earthed mesh, M1, they then pass through a planar retarding field between M1 and M2 (which is at the retarding voltage) before they are incident on the entrance aperture E1 of the 150° hemispherical sector analyser, (M1 and M2 have a ~90% optical transmission). The analyser can be operated in one of two modes, either (i) constant analyser energy mode, CAE, in which the analyser pass energy E_0 is held constant during a kinetic energy scan ($E_0 = HV$ where H is a constant for the analyser and V is the voltage difference between the hemispheres), or (ii) constant retard ratio mode, CRR, when the ratio of kinetic energy to analyser pass energy is held constant, that is when $E_K/E_0 = C_R$, the retard ratio.

The electron source is provided by the electron gun shown in Fig. 2, which produces a divergent conical beam of electrons, of half angle 9°, from a cross-over situated a few mm in front of the final anode. The gun has an indirectly heated Ba0/Sr0 planar cathode.

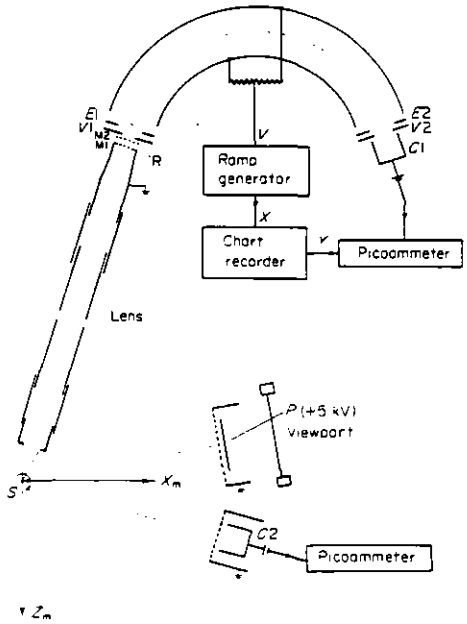


Figure 1. Schematic diagram of spectrometer and experimental set up. V_1 = variable entrance aperture, V_2 = variable exit aperture, M1 = earthed mesh, M2 = retard mesh, S = sample or electron gun source. X_m, Y_m (out of plane of paper), Z_m = manipulator coordinates. E1 = fixed entrance aperture, E2 = fixed exit aperture.

† Paper presented at the International Conference on Quantitative Surface Analysis held at the National Physical Laboratory, Teddington, UK, 24–25 November 1981.

CCC–0142–2421/82/0004–0220 $03.50

© Wiley Heyden Ltd, 1982

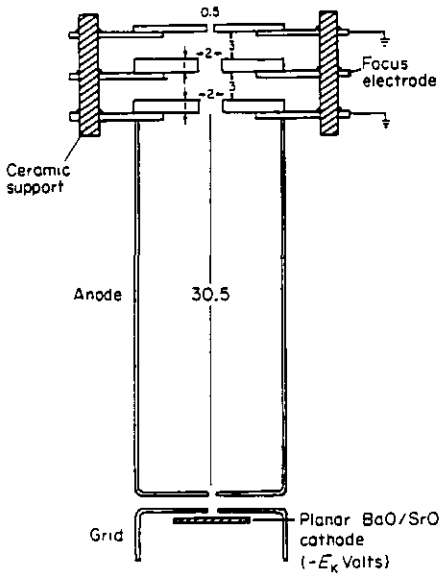


Figure 2. Miniature electron gun. Dimensions in mm.

The gun was attached to the spectrometer's high precision specimen manipulator (HPTI) which allows movement in the X_m, Y_m and Z_m directions and rotation θ about the Y axis (Fig. 1). The gun could be rotated to face (1) a phosphor screen at +5 kV mounted behind an earthed mesh (2) a Faraday cup collector with an earthed mesh shield—the collector, which accepts a cone of semi-angle 6° from the electron gun, was biased at +150 V to minimize emission of low energy secondaries (3) the entrance aperture of the spectrometer lens, which also accepts a cone of semi-angle 6° from the gun.

The voltages on the gun electrodes were kept in constant ratio to the kinetic energy of the electrons it produced, by using a voltage divider network, with the result that the beam stayed in focus throughout the energy range. The gun current (as measured by C2) varied as $E_K^{3/2}$ and for the experiments presented here covered the range from 2×10^{-9} to 10^{-7} A. The uniformity of the electron beam was checked by observing it on the phosphor screen and was found to be good throughout the energy range.

An energy spectrum (transmitted current as a function of kinetic energy) was obtained for a given electron kinetic energy E_K by ramping the retarding voltage V_R. A picoammeter was used to measure the transmitted current ($I_{C1} \approx 10^{-8} \rightarrow 10^{-10}$ A) and gave a direct voltage output proportional to this current, which was connected to the Y input of the chart recorder. The X axis was ramped in synchronism with V_R. Having run a spectrum the gun was then rotated to face C2 and the beam current was measured.

Areas under the energy spectra were measured by copying the graphs onto tracing paper, cutting out and weighing. The area was expressed in Amp-eV units by weighing a normalizing area, resulting in transmission values given by

$$T = \frac{\text{Area of transmitted peak}}{I_{C2}} \qquad (1)$$

If the transmission $T_{2\pi}$ for an isotropic source emitting into 2π is required then

$$T_{2\pi} = \frac{\text{solid angle acceptance of lens}}{2\pi} \times T = 0.03T \qquad (2)$$

RESULTS

Point source on axis

CAE mode. Figure 3 (crosses) shows the transmission T(peak area/collector current [I_{C2}]) vs kinetic energy on a log-log scale for analyser energies $E_0 = 5$, 10, 20 and 50 eV. The results were obtained for values of the collector current I_{C2} ranging from 2×10^{-9} A to 10^{-7} A.

From the results of Fig. 3, T can be plotted against E_0 for constant E_K, this shows that T varies as E_0^m where m depends on kinetic energy, changing from 1.5 at $E_K = 50$ eV to 1.75 at $E_K = 1500$ eV.

CRR mode. The transmission as a function of kinetic energy is shown for retard ratios $E_K:E_0$ of 2:1, 4:1 and 10:1 in Fig. 3 (black dots). The results were obtained for values of the collector current I_{C2} ranging from 2×10^{-9} A to 10^{-7} A.
In Fig. 4 the peak height transmission v. kinetic energy for different retard ratios is shown for comparison.

Point source off axis

The transmission was measured for different positions of the electron source in the place of the sample by varying either X_m or Y_m (altering X_m moves the image

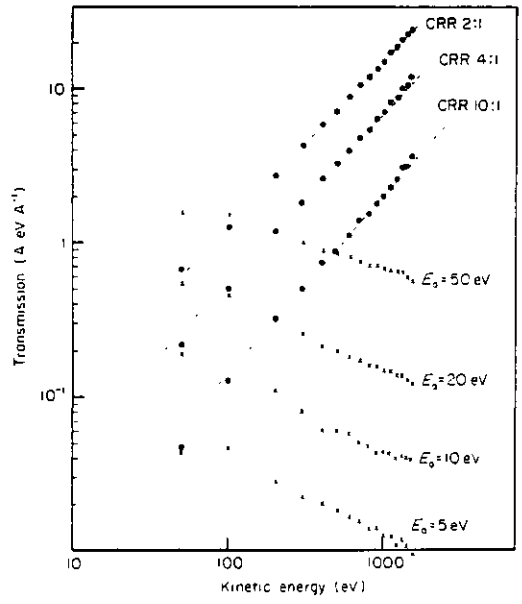


Figure 3. Experimental area transmission CAE mode (crosses) CRR mode (dots) vs kinetic energy.

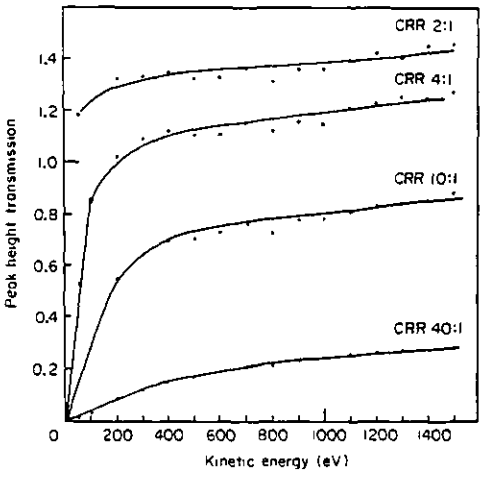


Figure 4. Experimental peak height transmission in CRR mode vs kinetic energy for different retard ratios. Lines through data points drawn by eye. $T_p = I_{C1}(\text{peak}) \div I_{C2}$.

of the electron source across the width of the variable aperture V_1, altering Y_m moves the image along the length of V_1). The measurements were made at energies of 50 eV and 100, 200 ... 1500 eV. The transmission vs E_K for $X_m = 2$ mm, $Y_m = Z_m = 0$ in the CAE mode with $E_0 = 20$ eV are shown in Fig. 5 (crosses). The transmission vs X_m for $Y_m = Z_m = 0$ and vs Y_m for $X_m = Z_m = 0$ is shown for $E_K = 500$ eV in Fig. 6.

DISCUSSION

The transmission of the spectrometer is determined by the combined effects of the lens, of pre-retardation and of the hemispherical analyser. To calculate the transmission it is necessary to find first the current distribution incident on the entrance slit of the analyser and then determine the response of the analyser to this distribution. Accordingly we discuss first the effect of the lens and of pre-retardation on the transmission.

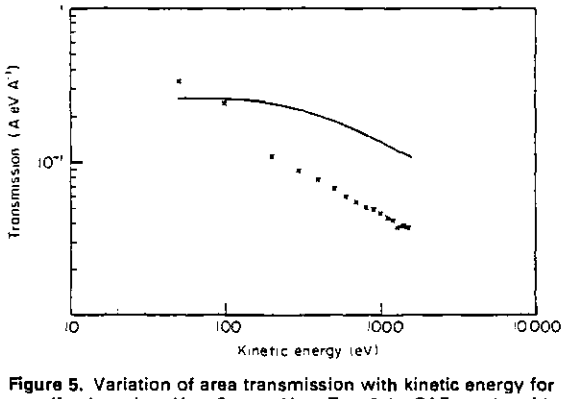


Figure 5. Variation of area transmission with kinetic energy for an off-axis point. $X_m = 2$ mm, $Y_m = Z_m = 0$ in CAE mode with $E_0 = 20$ eV (crosses). Theoretical transmission (solid line).

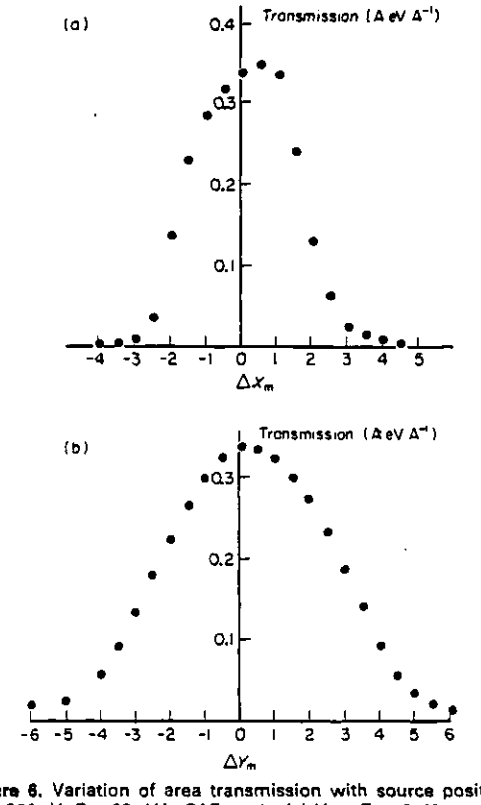


Figure 6. Variation of area transmission with source position $E_K = 300$ eV, $E_0 = 20$ eV in CAE mode, (a) $Y_m = Z_m = 0$. X_m varied, (b) $X_m = Z_m = 0$. Y_m varied.

Lens

The entrance aperture of the electrostatic lens accepts a conical beam of electrons of half-angle ~6° from a point on the sample. The lens voltage L is varied such that the ratio $E_K : L$ remains constant, thus the trajectories of the electrons are the same for all E_K. The lens affects the transmission only by defining the accepted solid angle.

Electron trajectories through the lens to the earth mesh were computed for electrons emitted from $S(X_m = Y_m = Z_m = 0)$ at angles $\theta = 0°, 1°, \ldots, 6°$ to the axis of the lens. The computations showed that the electrons are not brought to a point focus at the earthed mesh, but that the displacements from the axis there are < 1 mm. The maximum angle made by the electrons to the axis at the mesh is 4°.

Pre-retardation

The effect of pre-retardation on the transmission of electron spectrometers has been discussed by Helmer and Weichert,[1] Nöller *et al.*[2] and recently by Seah.[3] An electron incident at an angle θ to a planar retarding field will emerge from that region at an angle of θ' to the field given by

$$\sin\theta' = \left(\frac{E_K}{E_K - V_R}\right)^{1/2} \sin\theta \qquad (3)$$

i.e. retardation diverges the incident beam of electrons.

Analyser

The transmission of dispersive analysers is discussed by Sevier.[4] For the hemispherical analyser, the dispersion equation, which relates the radial co-ordinates of the electron in the plane of the entrance and exit apertures (r_1 and r_2, respectively), is

$$E_K - V_R - E_0 = \left(\frac{x_1 + x_2}{2r_0} + \alpha^2\right) E_0 \qquad (4)$$

where $x_1 = r_1 - r_0$; $x_2 = r_2 - r_0$; r_0 = radius of central ray; E_K = kinetic energy before retardation; V_R = retarding voltage; E_0 = kinetic energy of central ray; α = half-angle in plane of dispersion.

The electron is either transmitted ($|x_2| < \omega_2/2$) or falls outside the exit aperture ($|x_2| > \omega_2/2$), where ω_2 is the exit slit width. An electron of energy E_K incident at x_1, α is transmitted over a range of V_R from $V^{+\omega_2/2}$ to $V^{-\omega_2/2}$ where

$$V_R^{\mp\omega_2/2} = E_K - E_0 - E_0 \frac{x_1}{2r_0} - E_0\alpha^2 \pm E_0 \frac{\omega_2}{4r_0} \qquad (5)$$

Therefore the analyser impulse response function $T_\delta(V_R)$ is a rectangle function of unit height and of width $E_0\omega_2/2r_0$ as shown in Fig. 7, i.e.

$$T_\delta(V_R) = \Pi\left(\frac{V_R - E_K + E_0 + E_0(x_1/2r_0 + \alpha^2)}{E_0\omega_2/2r_0}\right) = \Pi(\eta) \qquad (6)$$

where

$$\Pi(\eta) = \begin{cases} 0, & |\eta| > \frac{1}{2} \\ \frac{1}{2}, & |\eta| = \frac{1}{2} \\ 1, & |\eta| < \frac{1}{2} \end{cases}$$

For an illumination $B(E_K - V_R, x_1, y_1, \alpha, \beta)$ of the entrance aperture where B is the brightness (current/unit area/unit solid angle). The current transmitted for any value of V_R is given by

$$I(V_R) = \int_{-\omega_1/2}^{\omega_1/2} dx_1 \int_{-l_1/2}^{l_1/2} dy_1 \int_{\alpha_1}^{\alpha_2} d\alpha \int_{\beta_1}^{\beta_2} d\beta \int_{E_1}^{E_2} dE_K \; B(E_K - V_R, x_1, y_1, \alpha, \beta)\Pi(\eta) \qquad (7)$$

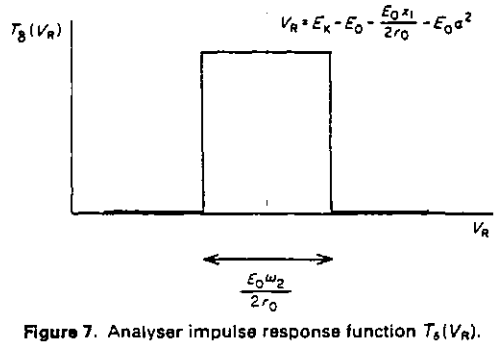


Figure 7. Analyser impulse response function $T_\delta(V_R)$.

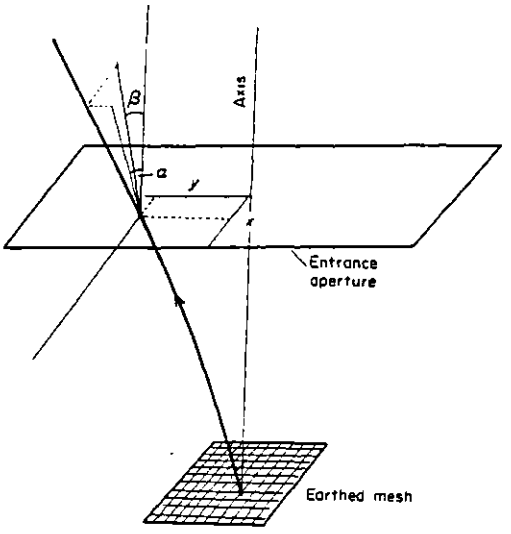


Figure 8. Definition of angular coordinates α and β.

where $\alpha_1\ \beta_1\ x_1$ and y_1 are defined in Fig. 8, ω_1 and l_1 are, respectively, the width and the length of the entrance aperture (for the present system $\omega_1 = 4.76$ mm, $l_1 = 77$ mm, aperture V_1 has $w = 4$ mm, $l = 10$ mm). α_1, α_2, β_1, β_2 give the range of α and β due to the finite extent of the source (Fig. 9); E_1 and E_2 are the energy limits between which the brightness is non-zero.

For illumination of the entrance aperture from a point source at the earthed mesh emitting uniformly into a cone of semi-angle θ,

$$B(E_K - V_R, x_1, y_1, \alpha, \beta) = B(E_K - V_R)\delta(\alpha - \alpha(x_1))\delta(\beta - \beta(y_1)) \qquad (8)$$

where $\alpha(x_1)$ is the value of α at x_1, $\beta(y_1)$ is the value of β at y_1, then $I(V_R)$ is the overlap integral of the brightness function (which is narrow in E_K) with a top-hat function of width $E_0\omega_2/2r_0$. This integral will tend to a maximum when $E_0\omega_2/2r_0$ is much greater than the width of $B(E_K)$, as is seen in Fig. 4.

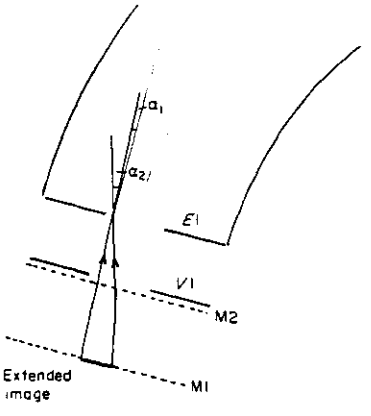


Figure 9. Angular limits for an extended source.

The area under $I(V_R)$ is of course given by

$$A = \int_0^\infty I(V_R)\,dV_R \tag{9}$$

the integral over V_R can be performed first to give

$$A = \frac{E_0\omega_2}{2r_0}\int_{-\omega_1/2}^{\omega_1/2} dx_1 \int_{-l_1/2}^{l_1/2} dy_1 \int_{\alpha_1}^{\alpha_2} d\alpha \int_{\beta_1}^{\beta_2} d\beta \int_{E_1}^{E_2} dE_K\, B(E_K - V_R) \tag{10}$$

$$= \frac{E_0\omega_2}{2r_0}. \text{ (current incident on entrance aperture)} \tag{11}$$

Kuyatt and Rudd (1963) showed that Eqn (11) is valid even when the current is distributed over the entrance slit and over the angles α and β in an arbitrary manner, provided that the distribution over the entrance slit is independent of energy. Details of this work are discussed by Sevier.[4]

Considering the system as a whole

The lens images a point source of electrons in the sample plane to the earthed mesh, the image emitting into a cone of semi-angle θ, and this cone is diverged by the retarding field. The entrance aperture of the analyser is rectangular in α and β, thus in CAE mode the transmission displays different kinetic energy variations depending on which of the following happens: (i) the whole of the incident beam falls inside the entrance aperture; (ii) the incident beam fills the entrance aperture in the α but not in the β directions; (iii) the incident beam fills the entrance aperture in both the α and β directions.

In case (i), the transmission will be given by

$$T = 0.81\,\frac{E_0\omega_2}{2r_0}\,\text{A eV A}^{-1} \tag{12}$$

where the factor 0.81 arises from the transmission of the meshes (each mesh has 90% optical transmission). In cases (ii) and (iii), the transmission will be given by

$$T = 0.81F\,\frac{E_0\omega_2}{2r_0}\,\text{A eV A}^{-1} \tag{13}$$

where F is the fraction of the incident current which passes through the entrance aperture. Referring to Fig. 10, we see how F can be calculated for a point source

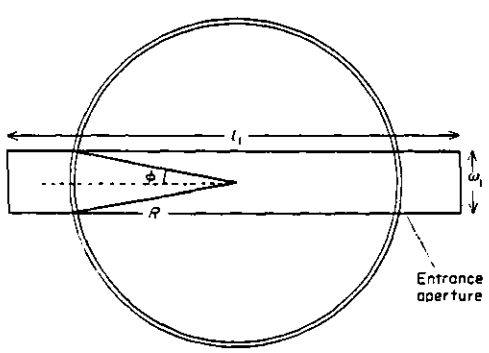


Figure 10. Illustrating the calculation of F the fraction of current entering the hemispherical analyser.

radiating uniformly into a cone of semi-angle θ_{max}. Electrons emitted initially into the angular range between θ and $(\theta + d\theta)$ occupy a solid angle $2\pi\theta\,d\theta$ (in the small angle approximation which is valid here). If we divide θ_{max} into N small intervals, $\theta_{n-1,n}$ where $n = 1$ to $N(\theta_{0,1} = 0 \rightarrow \theta_1,\ \theta_{1,2} = \theta_1 \rightarrow \theta_2,\ \theta_{N-1,N} = \theta_{N-1} \rightarrow \theta_N)$ such that each interval contains $1/N$ of the total current, then θ_n is given by

$$\theta_n = \left(\frac{n}{N}\right)^{1/2}\theta_{max} \tag{14}$$

The radius of the nth annulus, R_n, which is the projection of the interval $\theta_{n-1,n}$ in the plane of the entrance aperture is given by

$$r = \frac{2d\sin\theta_n}{\cos\theta_n + (E_0/E_K - \sin^2\theta_n)^{1/2}} + \frac{D\sin\theta_n}{(E_0/E_K - \sin^2\theta_n)^{1/2}} \tag{15}$$

where d is the distance between the earthed mesh and the retarding mesh (10 mm), D is the distance between the retarding mesh and the plane of the entrance aperture (25 mm). The first term on the right-hand side of Eqn (15) is the distance travelled perpendicular to the lens axis in the retarding region, the second term is the distance travelled perpendicular to the lens axis between the retarding mesh and the analyser entrance aperture.

The following conditions determine F

(a) $r_n < \omega/2$, each interval contributes a fraction $1/N$ of the incident current to F.
(b) $l_1/2 < r_n > \omega/2$, each interval contributes a fraction $(1/N)2\phi/\pi \sin^{-1}\omega_1/2r_n$ of the incident current to F.
(c) $r_n > l_1/2$, no contribution is made to F.

The transmission was computed using Eqns (12)–(15), subject to conditions (a)–(c) above for E_K from 50 eV to 1500 eV, both in CAE mode (for $E_0 = 5$, 10, 20 and 50 eV) and in CRR mode (for retard ratios of 2:1, 4:1 and 10:1). The results for $\theta_{max} = 6°$ (solid lines) are plotted in Fig. 11, together with the experimental values for comparison.

In CAE mode, experiment and theory are in close agreement, except for $E_0 = 5$ eV, where the experimental values are somewhat smaller than predicted by theory. Although the analyser is enclosed in a mumetal shield, it is possible that the residual magnetic field is affecting the transmission at this low pass energy by deflecting the electrons inside the analyser. Another possibility is that space charge repulsion within the analyser is responsible for the discrepancy. The effects of space charge repulsion within the hemispherical analyser have been discussed by Kuyatt and Simpson[5] and more recently by Ballu.[6] The latter author shows that when the current incident on the analyser reaches a critical value given by

$$I_{crit} = 3.3\times10^{-5}\left(\frac{\omega_1}{2r_0}\right)E_0^{3/2}\,\text{A} \tag{16}$$

the effect of space charge repulsion are sufficiently strong that the convergence of the dispersive system is then exactly compensated for by the divergence from the space charge fields. The present system has $\omega_1 = 4.76$ mm, $R_0 = 100$ mm giving $I_{crit} = 8.35$, 23.6, 66.8 and 264×10^{-7} A for $E_0 = 5$, 10, 20 and 50 eV respectively.

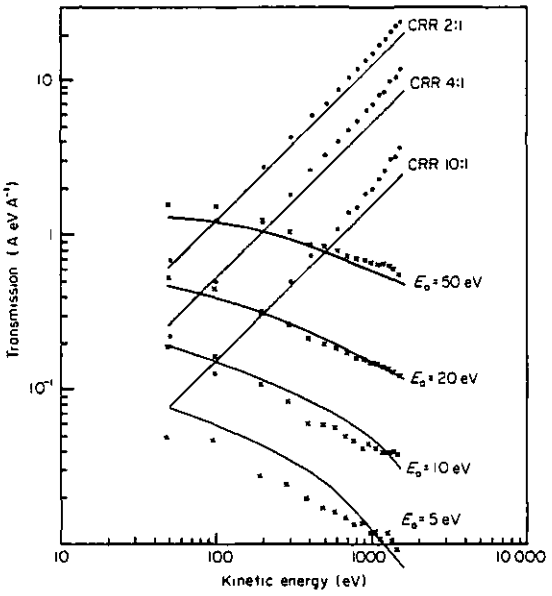


Figure 11. Comparison of the experimental area transmission vs the kinetic energy in CAE mode (crosses) and in CRR mode (dots) with theoretical calculations (solid lines).

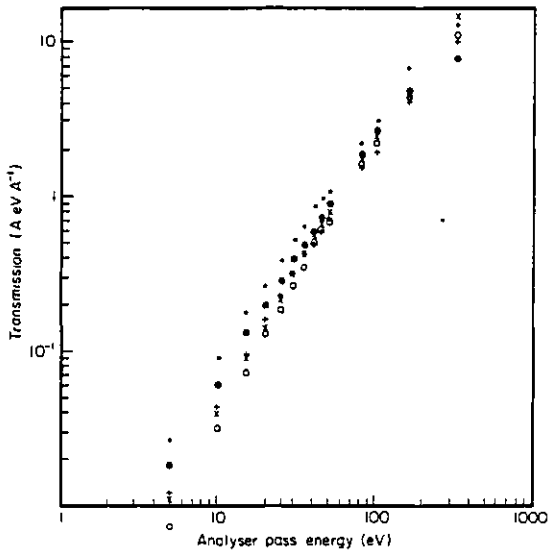


Figure 12. Peak area transmission vs E_0 for XPS peaks of different E_K.
· Cu2p$_{1/2}$ with MgKα radiation, E_K = 300 eV
● Cu2p$_{1/2}$ with AlKα radiation, E_K = 540 eV
+ Ols with AlKα radiation, E_K = 945 eV
× Cu3s with MgKα radiation, E_K = 1130 eV
○ Cu3s with AlDα radiation, E_K = 1360 eV

In the present experiments, the current incident on the entrance aperture, I_e, is given by

$$I_e = FI_{C2} \qquad (17)$$

I_{C2} varies from 2×10^{-9} A to 10^{-7} A as E_K increases from 50 to 1500 eV. This gives $I_e < 0.2$, 0.7, 1.5 and 2.5×10^{-8} A for $E_0 = 5$, 10, 20 and 50 eV, respectively. Giving $I_e/I_{crit} < 5\times10^{-3}$ which suggests that space charge will have a negligible effect in these experiments.

In CRR mode theory predicts that the transmission depends linearly on E_0 (hence on E_K) whereas experimentally it is found to vary as $E_K^{1.14}$ (or as $E_0^{1.14}$) for a retard ratio of 10:1 and as $E_K^{1.07}$ ($E_0^{1.07}$) for retard ratios of 4:1 and 2:1.

For an extended source

Measurements were made of the variation of peak areas of various XPS peaks as a function of analyser pass energy (from 5 eV→320 eV). The samples used were argon ion bombarded and annealed SiO_2 and freshly evaporated copper, from which the peaks listed in the caption of Fig. 12 were measured.

The measured areas were normalized at $E_0 = 20$ eV to the corresponding electron gun transmission values and these normalized values taken as the absolute values i.e. (XPS area transmission at $E_0 = 20$) = (electron gun transmission at $E_0 = 20$ eV and E_K of peak), the results are shown in Fig. 12.

The variation of the transmission with E_0 for a given XPS peak over the range from $E_0 = 5$ eV to 50 eV, agrees with that obtained with the electron gun at the same kinetic energy. The transmission was calculated at $E_K = 300$ eV and 1360 eV using Eqns (12)–(15) and the results are shown in Fig. 13 for comparison. For large values of E_0 a higher transmission is found experimentally than predicted theoretically. This is probably due to the increased width of the XPS peaks which results in additional signal due to inelastically scattered core electrons being included in the measurements.

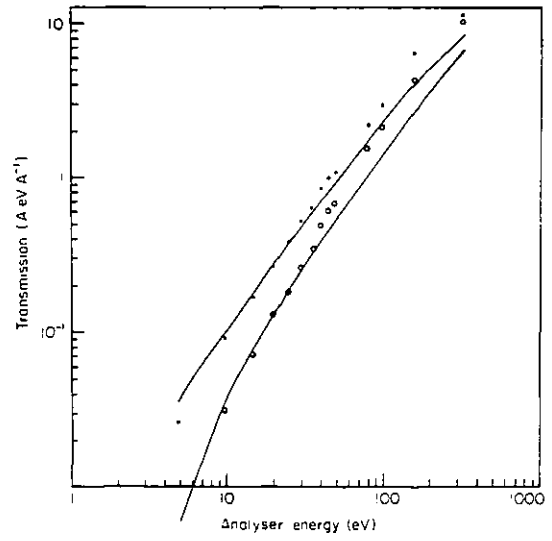


Figure 13. Comparison of the experimental results of Fig. 12 for E_K = 300 eV (dots) and E_K = 1360 eV (open circles) with the theoretical results (solid lines).

When considering an extended source, the effect of the variable slit V_1, which limits the area from which the signal is accepted by the analyser, must be taken into account. The signal from a point off-axis will be partially or completely blocked by V_1 (see Fig. 1). Thus, in Fig. 6, the fall off in transmission as $|\Delta X_m|$ and $|\Delta Y_m|$ increase is due to aperturing by V_1.

Following the same procedure, the transmission was calculated for the source at different off-axis positions ($X_m \neq 0$), taking into account the effect of V_1; the same type of energy dependence is observed as for an on-axis point, with transmission varying according to conditions (i), (ii) and (iii) above. The calculated transmission is shown in Fig. 5 for a point $\Delta X_m = 2$ mm and $E_0 = 20$ eV in CAE, together with the experimental results for comparison. As a result of the above, the kinetic energy dependence of the transmission for an extended source is expected to be the same as for a point source on axis. There is no significant difference between the energy dependence for an off-axis and on-axis point (except for $E_k < 100$ eV) also the near axis points make the major contribution to the signal.

CONCLUSIONS

The variation with pass energy, kinetic energy and sample position of the transmission of a VG Scientific Escalab analyser has been measured experimentally. Most of the behaviour observed is explained in terms of a simple theory which calculates the fraction of the current which is incident on the entrance plane of the analyser that is transmitted through the analyser. However, some discrepancies exist which are not explained by the theory, e.g. in CRR mode, the transmission is predicted to increase linearly with E_0, whereas it increases as $E_0^{1.17}$ for a retard ratio of 10:1 and as $E_0^{1.07}$ for a retard ratio of 2:1. The discrepancies may be explained by the existence of residual magnetic field or by fringing field effects.

Acknowledgements

We would like to thank M. P. Seah (National Physical Laboratory, Teddington), E. Munro and M. Baggs (Imperial College) and EMI Ruislip for their help.

REFERENCES

1. J. C. Helmer and N. H. Weichert, *Appl. Phys. Lett.* **13**, 266 (1968).
2. H. G. Nöller, H. D. Polaschegg and H. Schillalies, *J. Electron. Spectros. Relat. Phenom.* **5**, 705 (1974).
3. M. P. Seah, *Surf. Interface Anal.* **2**, 222 (1980).
4. K. D. Sevier, *Low Energy Electron. Spectroscopy*, Wiley, N.Y. (1972).
5. C. E. Kuyatt and J. A. Simpson, *Rev. Sci. Instrum.* **38**, 103 (1967).
6. Y. Ballu, *A.E.E.P. Supplement* **13B** (1980).
7. C. E. Kuyatt and M. E. Rudd, *Bull. Am. Phys. Soc.* **8**, 336 (1963).